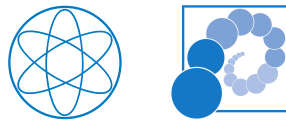




Dissertation

# Relating Morphology and Function in Low-Bandgap Polymer-Based Solar Cells

Franziska Carina Löhner



Technische Universität München

Physik-Department

Lehrstuhl für Funktionelle Materialien



TECHNISCHE UNIVERSITÄT MÜNCHEN

Physik-Department  
Lehrstuhl für Funktionelle Materialien

# Relating Morphology and Function in Low-Bandgap Polymer-Based Solar Cells

Franziska Carina Löhner, M. Sc.

Vollständiger Abdruck der von der Fakultät für Physik der Technischen Universität München zur Erlangung des akademischen Grades eines

**Doktors der Naturwissenschaften (Dr. rer. nat.)**

genehmigten Dissertation.

Vorsitzender: Prof. Dr. Martin Zacharias  
Prüfer der Dissertation: 1. Prof. Dr. Peter Müller-Buschbaum  
2. apl. Prof. Dr. Martin Brandt

Die Dissertation wurde am 17.09.2021 bei der Technischen Universität München eingereicht und durch die Fakultät für Physik am 05.11.2021 angenommen.



## Abstract

The present work investigates the relationship between structural properties of photoactive layers in polymer-based organic solar cells and their efficiency and stability. Its focus lies on observing structural changes in situ during the application of metal electrodes or during radiation-induced degradation using various spectroscopy, microscopy, and X-ray scattering methods. Differences between the photoactive polymers PTB7 and PTB7-Th and their effect on the gold layer applied by sputter deposition are examined. The substitution of oxygen by thiophene rings leads to a significant change in gold layer growth and to smaller grain sizes in later growth stages. Additionally, the influence of the morphology of active layers based on PTB7-Th and PC<sub>71</sub>BM on the gold growth is investigated. The addition of the solvent additive DIO leads to a smoother layer with PTB7-Th enrichment and thus enhances the gold contact quality. Changes in the photovoltaic performance of solar cells based on PTB7-Th are correlated with radiation-induced chemical and morphological aging processes in the active layer. These findings offer detailed insights into the functionality of organic solar cells.

## Zusammenfassung

Die vorliegende Arbeit untersucht den Zusammenhang zwischen strukturellen Eigenschaften photoaktiver Schichten in polymerbasierten organischen Solarzellen und deren Effizienz und Stabilität. Der Fokus liegt auf der Beobachtung struktureller Veränderungen beim Aufbringen von Metallelektroden oder strahlungsinduzierter Alterung mittels verschiedener Spektroskopie-, Mikroskopie- und Röntgenstreuungsmethoden. Es werden Unterschiede zwischen den photoaktiven Polymeren PTB7 und PTB7-Th und ihr Einfluss auf die durch Sputterdeposition aufgebrachte Goldschicht untersucht. Die Substitution von Sauerstoff durch Thiophenringe führt zu einer signifikanten Veränderung des Schichtwachstums und kleineren Korngrößen in späteren Wachstumsstadien. Außerdem wird der Einfluss der Morphologie aktiver Schichten auf Basis von PTB7-Th und PC<sub>71</sub>BM auf das Goldwachstum untersucht. Die Zugabe des Lösungsmittelzusatzes DIO führt zu einer glatteren Schicht mit PTB7-Th-Anreicherung und somit zu einer besseren Kontaktqualität. Veränderungen der photovoltaischen Leistung von Solarzellen basierend auf PTB7-Th werden mit strahlungsinduzierten chemischen und morphologischen Alterungsprozessen in der aktiven Schicht korreliert. Diese Ergebnisse bieten detaillierte Einblicke in die Funktionsweise organischer Solarzellen.



# Contents

|  |            |
|--|------------|
| <b>Abstract</b>  | <b>i</b>   |
| <b>List of Abbreviations</b>                                     | <b>vii</b> |
| <b>1 Introduction</b>  | <b>1</b>   |
| <b>2 Theoretical Aspects</b>                                     | <b>5</b>   |
| 2.1 Polymer Fundamentals . . . . .                               | 5          |
| 2.1.1 Basic Principles . . . . .                                 | 6          |
| 2.1.2 Polymer Blends . . . . .                                   | 7          |
| 2.1.3 Conductive Polymers . . . . .                              | 9          |
| 2.2 Organic Solar Cells . . . . .                                | 14         |
| 2.2.1 General Principles . . . . .                               | 14         |
| 2.2.2 Loss Mechanisms . . . . .                                  | 20         |
| 2.2.3 Degradation of Photoactive Layers . . . . .                | 21         |
| 2.3 Polymer-Metal-Interfaces . . . . .                           | 23         |
| 2.3.1 Metal Nanostructures at Polymer-Metal Interfaces . . . . . | 24         |
| 2.3.2 Sputter Deposition . . . . .                               | 24         |
| 2.3.3 Processes at Polymer Surfaces . . . . .                    | 26         |
| 2.3.4 Layer Growth Models . . . . .                              | 27         |
| 2.4 X-ray Scattering . . . . .                                   | 28         |
| 2.4.1 Basic Principles . . . . .                                 | 28         |
| 2.4.2 X-Ray Reflectivity . . . . .                               | 31         |
| 2.4.3 Grazing-Incidence Small-Angle X-ray Scattering . . . . .   | 32         |
| 2.4.4 Grazing-Incidence Wide-Angle X-ray Scattering . . . . .    | 34         |
| <b>3 Sample Preparation</b>                                      | <b>39</b>  |
| 3.1 Materials . . . . .  | 39         |
| 3.1.1 Functional Materials . . . . .                             | 40         |
| 3.1.2 Solvents . . . . .   | 41         |
| 3.1.3 Substrate Types . . . . .                                  | 42         |
| 3.2 Thin Film Preparation . . . . .                              | 43         |
| 3.2.1 Substrate Cleaning . . . . .                               | 44         |
| 3.2.2 Solution Preparation . . . . .                             | 44         |
| 3.2.3 Film Deposition . . . . .                                  | 45         |

|          |  |            |
|----------|--|------------|
| 3.3      | OPV Device Assembly . . . . .  | 46         |
| 3.3.1    | Substrate Preparation . . . . .  | 47         |
| 3.3.2    | PEDOT:PSS Layer . . . . .  | 49         |
| 3.3.3    | Active Layer . . . . .   | 49         |
| 3.3.4    | Electrode Deposition . . . . .   | 49         |
| <b>4</b> | <b>Sample Characterization</b>   | <b>51</b>  |
| 4.1      | Spectroscopic and Electrical Characterization . . . . .  | 51         |
| 4.1.1    | UV-Vis Spectroscopy . . . . .  | 52         |
| 4.1.2    | FTIR Spectroscopy . . . . .  | 54         |
| 4.1.3    | Electrical Characterization . . . . .  | 56         |
| 4.2      | Structure Investigation in Real Space . . . . .  | 58         |
| 4.2.1    | Optical Microscopy . . . . .   | 59         |
| 4.2.2    | Scanning Electron Microscopy . . . . .   | 60         |
| 4.2.3    | Height Profilometry . . . . .  | 62         |
| 4.2.4    | Atomic Force Microscopy . . . . .  | 63         |
| 4.2.5    | Nano-IR mapping combined with AFM (AFM-IR) . . . . .   | 65         |
| 4.3      | Structure Investigation in Reciprocal Space . . . . .  | 66         |
| 4.3.1    | X-ray Reflectometry . . . . .  | 67         |
| 4.3.2    | Grazing-Incidence X-ray Scattering (GIXS) . . . . .  | 68         |
| 4.3.3    | Grazing-Incidence Small-Angle X-ray Scattering (GISAXS) . . . . .                                  | 71         |
| 4.3.4    | Grazing-Incidence Wide-Angle X-ray Scattering (GIWAXS) . . . . .                                   | 73         |
| <b>5</b> | <b>Influence of Polymer Side Chains on the Growth of Gold Electrodes during Sputter Deposition</b> | <b>75</b>  |
| 5.1      | Introduction . . . . .   | 76         |
| 5.2      | Experimental Details . . . . .   | 77         |
| 5.3      | In-situ Characterization . . . . .   | 80         |
| 5.3.1    | Evolution of Crystallinity . . . . .   | 80         |
| 5.3.2    | Film Thickness Evolution . . . . .   | 84         |
| 5.3.3    | Morphological Evolution . . . . .  | 91         |
| 5.4      | Conclusion . . . . .   | 102        |
| <b>6</b> | <b>Effects of the Active Layer Morphology on the Gold Layer Growth</b>                             | <b>105</b> |
| 6.1      | Introduction . . . . .   | 105        |
| 6.2      | Experimental Details . . . . .   | 107        |
| 6.3      | Morphology of the Organic Thin Films . . . . .   | 109        |
| 6.4      | In-Situ Characterization . . . . .   | 113        |
| 6.4.1    | Island Growth . . . . .  | 113        |
| 6.4.2    | Layer Growth . . . . .   | 120        |
| 6.4.3    | Gold Layer Crystallinity . . . . .   | 123        |
| 6.5      | Ex-Situ X-ray reflectometry (XRR) . . . . .  | 126        |

---

|          |  |            |
|----------|--|------------|
| 6.6      | Growth Model . . . . .   | 129        |
| 6.7      | Conclusion . . . . .   | 131        |
| <b>7</b> | <b>Light-Induced and Oxygen-Mediated Aging Processes in PTB7-Th-based Photoactive Layers</b> | <b>133</b> |
| 7.1      | Introduction . . . . .   | 134        |
| 7.2      | Experimental Details . . . . .   | 135        |
| 7.3      | In-Operando Solar Cell Characterization . . . . .  | 139        |
| 7.3.1    | Development of the Photovoltaic Properties . . . . .   | 139        |
| 7.3.2    | In-Operando GISAXS Measurement . . . . .   | 141        |
| 7.4      | Following the Light-Induced Aging of Thin-Film Samples . . . . .                             | 145        |
| 7.4.1    | Optical Absorption . . . . .   | 145        |
| 7.4.2    | Chemical Structure . . . . .   | 153        |
| 7.4.3    | Surface Morphology and Chemistry . . . . .   | 158        |
| 7.5      | Conclusion . . . . .   | 160        |
| <b>8</b> | <b>Conclusion &amp; Outlook</b>  | <b>161</b> |
|          | <b>Bibliography</b>  | <b>165</b> |
|          | <b>List of Publications</b>  | <b>197</b> |
|          | <b>Acknowledgments</b>   | <b>203</b> |



# List of Abbreviations

|        |  |
|--------|--|
| AFM    | atomic force microscopy                        |
| BDT    | benzodithiophene                               |
| BHJ    | bulk-heterojunction                            |
| CB     | chlorobenzene                                  |
| DA     | decoupling approximation                       |
| DC     | direct current                                 |
| DESY   | Deutsches Elektronen-Synchrotron               |
| DI     | deionized                                      |
| DIO    | 1,8-diiodooctane                               |
| DOS    | density of states                              |
| DPDAK  | Directly Programmable Data Analysis Kit        |
| DWBA   | distorted-wave Born approximation              |
| EBL    | electron blocking layer                        |
| EIA    | effective interface approximation              |
| FF     | fill factor                                    |
| FTIR   | Fourier-transform infrared                     |
| FWHM   | full width at half maximum                     |
| GISAXS | grazing-incidence small-angle X-ray scattering |
| GIWAXS | grazing-incidence wide-angle X-ray scattering  |
| GIXS   | grazing-incidence X-ray scattering             |
| HBL    | hole blocking layer                            |

## List of Abbreviations

---

|                                |  |
|--------------------------------|--|
| HCl                            | hydrochloric acid  |
| HOMO                           | highest occupied molecular orbital   |
| H <sub>2</sub> SO <sub>4</sub> | sulfuric acid  |
| HTL                            | hole transport layer   |
| I/V                            | current-voltage  |
| IR                             | infrared light   |
| ITO                            | indium-doped tin oxide   |
| LCAO                           | linear combination of atomic orbitals  |
| LED                            | light-emitting diode   |
| LMA                            | local monodisperse approximation   |
| LUMO                           | lowest unoccupied molecular orbital  |
| MiNaXS                         | Micro- and Nano-focus X-ray Scattering   |
| MPP                            | maximum power point  |
| o-DCB                          | ortho-dichlorobenzene  |
| OPV                            | organic photovoltaic   |
| P3HT                           | poly(3-hexyl-thiophene)  |
| PC <sub>71</sub> BM            | [6,6]-phenyl-C <sub>71</sub> butyric acid methyl ester   |
| PA                             | polyacetylene  |
| PCBM                           | [6,6]-phenyl-C <sub>61</sub> butyric acid methyl ester   |
| PCE                            | power conversion efficiency  |
| PCPDTBT                        | poly[2,6-(4,4-bis-(2-ethylhexyl)-4H-cyclopenta[2,1-b;3,4-b']-dithiophene)-alt-4,7(2,1,3-benzothiadiazole)] |
| PEDOT                          | poly(3,4-ethylene dioxythiophene)  |
| PEDOT:PSS                      | poly(3,4-ethylene dioxythiophene):poly(styrene sulfonate)  |
| PL                             | photoluminescence  |
| PPV                            | poly(phenylene-vinylene)   |

|         |  |
|---------|--|
| PS      | polystyrene  |
| PSS     | poly(styrene sulfonate)  |
| PTB7    | poly[[4,8-bis[(2-ethylhexyl)oxy]benzo[1,2-b:4,5-b']dithiophene-2,6-diyl][3-fluoro-2-[(2-ethylhexyl)carbonyl]thieno[3,4-b]thiophenediyl]]   |
| PTB7-Th | poly[[4,8-bis(5-ethylhexylthienyl)benzo[1,2-b:4,5-b']dithiophene-2,6-diyl][3-fluoro-2-[(2-ethylhexyl)carbonyl]thieno[3,4-b]thiophenediyl]] |
| PTFE    | polytetrafluoroethylene  |
| PVDF    | polyvinylidene fluoride  |
| rms     | root mean square   |
| ROI     | region of interest   |
| rpm     | revolutions per minute   |
| RPSD    | radial power spectral density  |
| SAXS    | small-angle X-ray scattering   |
| SDD     | sample-to-detector distance  |
| SEM     | scanning electron microscopy   |
| SLD     | scattering length density  |
| SSH     | Su-Schrieffer-Heeger   |
| TT      | thienothiophene  |
| US      | ultrasonic   |
| UV      | ultraviolet  |
| UV/vis  | ultraviolet/visible  |
| XRR     | X-ray reflectometry  |



# CHAPTER 1

## Introduction

With a growing population and an increasing living standard, the world's demand for sustainable energy is rising. Alternative energy sources such as solar, wind, or hydropower already contribute significantly to the energy supply in Germany.<sup>[1]</sup> However, they are typically limited to static, large-scale applications. Organic photovoltaics (OPV) have received pronounced attention in recent years as a viable alternative to conventional solar cells.<sup>[2-4]</sup> The discovery of electrical conductivity in polymers upon doping by the groups of Heeger, MacDiarmid, and Shirakawa in 1977 initiated a whole new field of potential applications in organic electronics.<sup>[5-7]</sup> Using polymers as active materials for energy conversion has a variety of potential advantages.<sup>[8-12]</sup> Photoactive polymers can be synthesized from low-cost, abundant precursor materials and enable the formation of thin, light-weight, and flexible films with tunable absorption. The devices can be produced via roll-to-roll processing, an easily up-scalable and thereby low-cost production technique. Due to these advantages, OPV devices can be integrated into a wide range of applications, combining functionality with design in fields as diverse as mobility, architecture, or clothing. Recent research efforts focus on enhancing the photovoltaic performance to make organic solar cells feasible for industrial purposes. This has led to the development of low band-gap materials with reported power conversion efficiencies surpassing the industrially important limit of 10%.<sup>[13]</sup> Record efficiencies for single-junction or tandem solar cells have frequently been reported based on new materials.<sup>[14,15]</sup> Still, the comparably low initial efficiency and insufficient long-term stability of purely organic devices remain issues hindering their widespread use.<sup>[16-18]</sup>

Important factors contributing to the efficiency of organic solar cells are the chemistry and morphology of the photoactive layer as well as the contact to and quality of the applied electrode.<sup>[10,19–26]</sup> One way to enhance the efficiency is tuning the optical bandgap of the photoactive materials by modifying their chemical structure.<sup>[21]</sup> Especially for polymers, this can be achieved by slight changes in their side groups, thereby creating families of polymers with an identical backbone, but varying bandgaps. Another way to increase the efficiency is the use of solvent additives during the preparation of the photoactive layer.<sup>[27,28]</sup> In organic solar cells, the photoactive layer consists of at least two materials, as the material interfaces are needed to create free charge carriers. For practical purposes, active layers are mainly created out of a mixed solution of both materials, with the solvent additives leading to a more beneficial arrangement of the material phases. Aside from the active layer, the contact to the applied electrode – often made of metal – is of high importance for the solar cell efficiency. The created interface between the back electrode and the organic film influences the charge carrier extraction and thereby the device efficiency.<sup>[21,25]</sup> Enhancing the initial power conversion efficiency is a necessary, yet not sufficient step towards potential applications, as the devices also need to show long-term stability.<sup>[16–18]</sup> All these features are interconnected and depend on the respective material system, yet are far from being understood in detail. Chapter 2 gives an overview of the most important theoretical concepts needed to understand the systems and processes investigated in the present thesis. The respective model material systems are prepared according to routines described in Chapter 3.

To acquire a deeper understanding of the properties of organic solar cells defining their efficiency and stability, a range of suitable characterization methods are applied in the scope of this work, as presented in Chapter 4. Chemical properties are probed using different spectroscopic methods sensitive to the chemical structure, environment, and optical bandgap of the investigated materials. The photovoltaic behavior of solar cells during operation is tracked by recording their current-voltage characteristics. Several microscopy methods give information about the surface morphology of the investigated samples on different length scales and with varying sensitivity to changes in height, composition, absorption, or defects. In particular, when combining infrared spectroscopy with atomic force microscopy, structure information can be obtained on a nanoscale. While microscopy is an important tool to understand the film morphology, it is mostly restricted to small areas and film surfaces. To obtain statistically relevant information about structures within the sample film, X-ray scattering techniques have to be applied. In the scope of this work, they are performed in reflection geometry to increase the probed sample volume and get information about the vertical film profile of the investigated thin film samples. Especially grazing-incidence small-angle X-ray scattering (GISAXS) and grazing-incidence wide-angle X-ray scattering (GIWAXS) are used to investigate the very thin – or even newly forming – films, yielding information about structures in a range between 1 Å and 1 µm. Using synchrotron radiation with

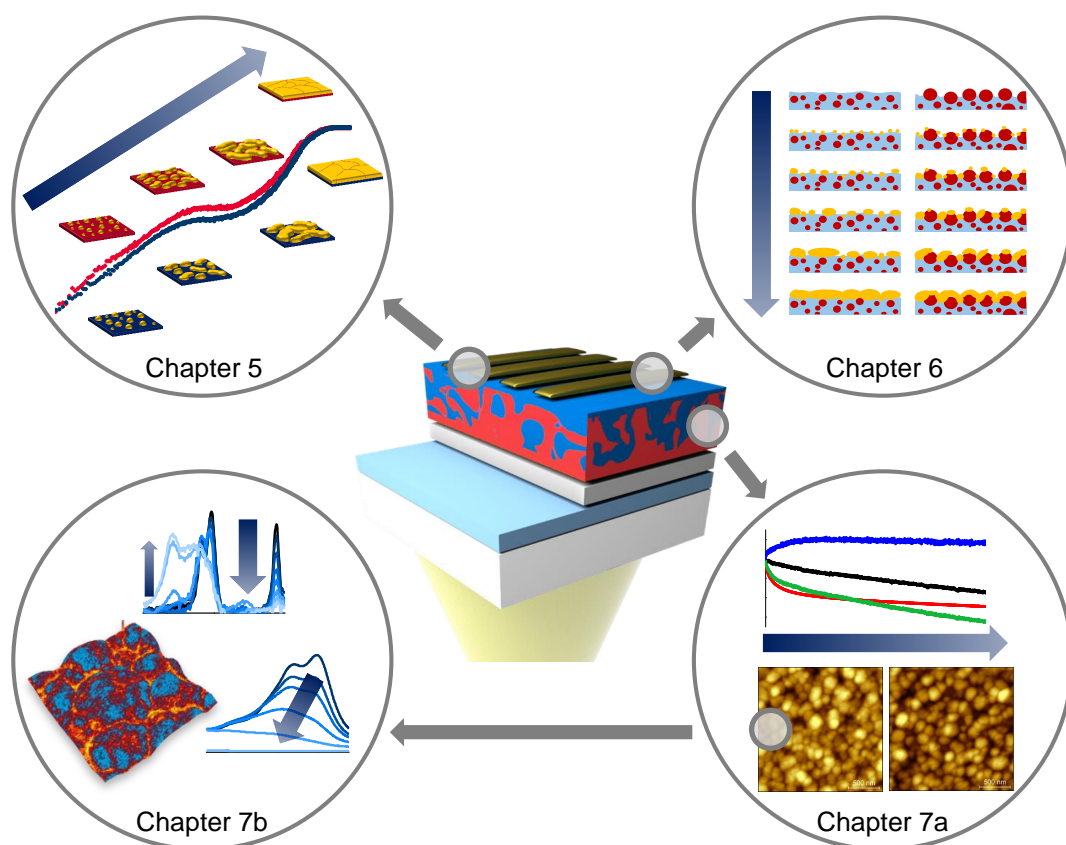


**Figure 1.1**

Overview of the topics covered in the present work. Chapter 5 focuses on the effect of side-chain engineering of pure polymer films on the formation of applied gold layers. The effect of morphology and film roughness of active layer films on applied gold layers is presented in Chapter 6. Chapter 7 discusses the effects and mechanisms involved in the photodegradation of the active layer, with the first part focusing on morphology and solar cell efficiency and the second part exploring structural changes during photooxidation.

high intensity, these methods offer the additional advantage of enabling time-resolved measurements during certain processes, such as the deposition of thin films or morphological changes during solar cell operation. Several complementary methods are combined to describe the processes and properties of the material systems introduced in this work. Figure 1.1 gives an overview of the investigated effects and processes.

Organic photovoltaic devices are based on mostly organic materials, yet their back electrodes are often made from metals due to their unparalleled electrical conductivity. For industrial purposes, the back electrodes are typically applied using large-scale methods such as sputter deposition.<sup>[29,30]</sup> However, the effects of different characteristics of organic films on the metal film formation are not fully understood. These characteristics include differences in the chemistry and the morphology of the used organic materials.

Chapter 5 discusses the film formation of a sputter-deposited gold electrode on thin films of the photoactive polymers PTB7<sup>1</sup> and PTB7-Th<sup>2</sup> with slight differences in their side chains.<sup>[31]</sup> While side-chain engineering has a significant impact on the optical bandgap and solar cell device efficiency, the effect on the formation of the gold contact has not been investigated in detail. To obtain an in-depth knowledge of the actual processes defining the polymer-metal interface in dependence of the chemical structure in the side chains, the formation is investigated in situ using GISAXS and GIWAXS.

Building on the findings for the pure polymers, Chapter 6 explores the formation of a gold electrode on mixed photoactive layers of the polymer PTB7-Th with the fullerene-derivative PC<sub>71</sub>BM<sup>3</sup> prepared with and without solvent additive. As mentioned above, solvent additives are used to enhance the active layer morphology and thereby the efficiency of organic solar cells. The question remains, if and in what way the changed active layer morphology and surface roughness affect the formation of a sputter-deposited gold contact. After investigating differences in the initial film morphology and surface roughness, the layer formation is tracked via GISAXS and GIWAXS. Additionally, the influence of the surface topology on the formed contact is probed using X-ray reflectometry.

Solar cells based on low-bandgap polymers are sensitive to various degradation processes, which strongly decrease their lifetime. Chapter 7 is focused on the chemical and physical changes occurring within the active layer of PTB7-Th and PC<sub>71</sub>BM during irradiation-induced aging. The active layer morphology is investigated before, during, and after irradiation using real-space and scattering methods. GISAXS is used to follow morphological changes within the active layer of a working solar cell *in operando*. Structural changes happening on a molecular scale are probed with spectroscopy methods to evaluate the extent of light-induced oxidation processes potentially leading to degradation.

With these findings, a thorough understanding of the electrode formation process is found and detailed growth models are derived. The investigation of the influence of chemical and morphological features of the organic layer on the electrode formation supports the industrialization of the process in a wide range of applications. For reliable operation of the devices, the understanding provided from the investigations of the aging mechanism is of utmost importance. All these findings are summarized in Chapter 8, which concludes this work and gives an outlook to future research questions.

---

<sup>1</sup>PTB7: poly[[4,8-bis((2-ethylhexyl)oxy)benzo[1,2-b:4,5-b']dithiophene-2,6-diyl][3-fluoro-2-[(2-ethylhexyl)carbonyl]thieno[3,4-b]thiophenediyl]]

<sup>2</sup>PTB7-Th: poly[[4,8-bis(5-ethylhexylthienyl)benzo[1,2-b:4,5-b']dithiophene-2,6-diyl][3-fluoro-2-[(2-ethylhexyl)carbonyl]thieno[3,4-b]thiophenediyl]]

<sup>3</sup>PC<sub>71</sub>BM: [6,6]-phenyl-C<sub>71</sub> butyric acid methyl ester

# CHAPTER 2

## Theoretical Aspects

The following chapter introduces theoretical aspects important for understanding the research discussed in the present thesis. Section 2.1 describes the basics of polymer physics with a focus on polymer blends and conductive polymers. Both phenomena play a vital role for organic solar cells which are presented in Section 2.2. Apart from the general working principles of organic solar cells, typical loss mechanisms and degradation pathways are explained. While based mostly on organic materials, organic solar cells often depend on metal electrodes and, therefore, exhibit polymer-metal interfaces which are introduced in Section 2.3. After describing the general features of metal-polymer interfaces, the surface processes and layer growth modes during the metal layer deposition are addressed. X-ray scattering methods form the basis of the investigations for this work and are presented in Section 2.4. Aside from a short overview of the basic principles, the three main characterization techniques are introduced. As this chapter can only give a brief overview of the fundamentals of organic photovoltaics and scattering techniques, the reader is referred to the cited literature for further details.

### 2.1 Polymer Fundamentals

This work's focus lies on investigating photoactive, conductive polymers. In this section, a short introduction of general concepts within polymer physics is given, followed by an overview of the most important processes in conductive polymers such as the electronic band structure and charge transport phenomena.

### 2.1.1 Basic Principles

Polymers are macromolecules formed by a sequence of repeating units called monomers. Organic monomers typically consist of small molecules based on carbon in combination with other main group elements. Carbon offers the unique advantage of easily creating long, branching networks due to its ability to build up to four covalent bonds with other atoms. The polymer behavior is defined by several factors, some of which will be mentioned in the following.<sup>[32]</sup> The length of a polymer chain is given by the number of monomeric units described by the degree of polymerization  $N$  and can significantly change the properties of the respective macromolecule. For short chains (low  $N$  up to 20), the molecules are called oligomers. With increasing  $N$ , the ratio between the functional groups at the chain ends and the monomers in the middle decreases, leading to a decreasing impact of the chain ends on the overall behavior. A glossary of basic terms in polymer science was defined by the International Union of Pure and Applied Chemistry (IUPAC).<sup>[33]</sup>

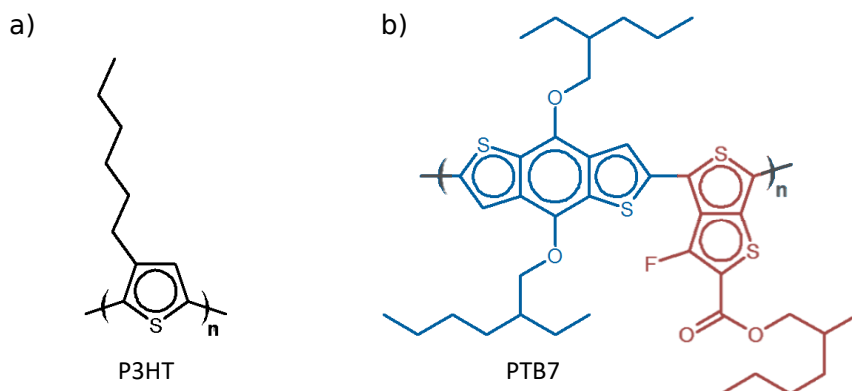
Through a process called polymerization, the monomers are bound covalently to build the polymer. Depending on the exact reaction mechanism to achieve the desired material, the chemical reactions involved lead to a more or less pronounced statistical distribution of chain lengths around a certain degree of polymerization. Polymers are therefore defined not only by their average length or molar mass but also by the distribution of lengths or molar masses around an average value.

While most polymers are based on small monomers consisting of only a few atoms, special applications require more complex polymers consisting of larger monomers or the combination of different units to achieve certain properties. The polymers investigated in the scope of the present thesis address several requirements, namely a certain conductivity, light absorption behavior, and ordering within a film. All these and other properties are closely linked to the type and arrangement of monomers within the polymer chains. Figure 2.1 illustrates differences between simple and more complex polymers via two exemplary polymers used for organic solar cells. The rather simple polymer P3HT<sup>1</sup> with a single monomer unit (= homopolymer) is compared to the more complex polymer PTB7<sup>2</sup> based on two different, larger monomer units. The two monomer units may be arranged in different ways to build either a statistical, alternating, or block copolymer. Within the scope of the present thesis, a focus lies on polymers based on two alternating monomer units with different functionalities, as explained in Section 3.1.1. Apart from the type of monomer, also the conformation of side groups is of interest. Especially monomers with large side chains or functional groups may show a certain ordering of the side groups due to sterical or electronic reasons during the reaction, which influences the ordering of the polymer chains within

---

<sup>1</sup>P3HT: poly(3-hexyl-thiophene)

<sup>2</sup>PTB7: poly[[4,8-bis[(2-ethylhexyl)oxy]benzo[1,2-b:4,5-b']dithiophene-2,6-diyl][3-fluoro-2-[(2-ethylhexyl)carbonyl]thieno[3,4-b]thiophenediyl]]

**Figure 2.1**

Typical monomer unit of a) P3HT in comparison to b) the more complex PTB7 with two monomer units.

the film. Polymers can change their local conformation and therefore their overall shape to a certain extent by rotation of chain segments or functional groups around single bonds. Depending on the environment, the polymer will exhibit different shapes.<sup>[32]</sup> In a good solvent with the Gibb's free energy favoring a mixing of the polymer and the solvent molecules, the chains are relaxed or even stretched to enable the polymer-solvent interaction. In a poor solvent, polymer-polymer interactions are more favorable leading to a collapse of the polymer chains and thereby to phase separation. This leads to different characteristic length scales of the same polymer depending on the solvent environment. The length of the completely stretched polymer chain is not observed in reality and therefore rarely used to describe it. Coiled structures can be determined by the end-to-end distance  $R_e$  between two end groups of a polymer chain. However, this does not give information about the shape and volume of the coiled polymer. One typical measured property is the radius of gyration  $R_g$  which describes the radius of the polymer in a Gaussian coil conformation as a sphere around its center of mass

$$R_g^2 = \frac{1}{M} \sum_i m_i |\vec{r}_i - \vec{r}_c|^2 \quad (2.1)$$

with the average distance of the monomers to the center of mass  $\vec{r}_c$ , the molar mass  $M$ , and the mass  $m_i$  and position  $\vec{r}_i$  of the  $i$ -th component.

### 2.1.2 Polymer Blends

As will be discussed in Section 2.2, the photoactive systems investigated in the scope of this work are usually based on polymer:fullerene blends. These blends are characterized not only by the properties of the individual materials but also by the way the

two (or more) materials intermix. Phase separation is vitally important for organic photovoltaics, as the material interfaces are needed to separate the strongly bound excitons.<sup>[34]</sup> Additionally, the morphology needs to address the short lifetimes and therefore short diffusion length of excitons, while still allowing the separated charge carriers pathways to the respective electrodes.

To describe the thermodynamic behavior of polymer blends in terms of phase separation and intermixing, the Gibbs free energy of mixing  $\Delta G$  needs to be considered. Using a mean-field approach, the well-established Flory-Huggins theory can be used to explain the behavior of polymers in a polymer solution.<sup>[35,36]</sup> The theory states that the difference in the Gibbs free energy  $G_{AB}$  of the fully intermixed phase compared to the energy  $G_A + G_B$  of two isolated components  $A$  and  $B$  yields the Gibbs free energy upon mixing  $\Delta G$

$$\Delta G = G_{AB} - (G_A + G_B). \quad (2.2)$$

For  $\Delta G > 0$ , phase separation is favored, while  $\Delta G < 0$  leads to an intermixing of the components.  $\Delta G$  is related to the change in entropy  $\Delta S$  and enthalpy  $\Delta H$  upon mixing the components at a certain temperature  $T$

$$\Delta G = -T\Delta S + \Delta H. \quad (2.3)$$

Mixing leads to an increase of entropy, while the change in enthalpy depends on the chemical and physical interactions between the components.

The entropy depends on the number of possible arrangements  $\Omega$  and is calculated via  $S = k_B \ln(\Omega)$  with the Boltzmann constant  $k_B$ . The change in entropy upon mixing  $\Delta S = S_{AB} - (S_A + S_B)$  can, therefore, be obtained by calculating

$$\Delta S = -k_B n \left( \frac{\Phi_A}{N_A} \ln \Phi_A + \frac{\Phi_B}{N_B} \ln \Phi_B \right) \quad (2.4)$$

using the degree of polymerization  $N_{A,B}$  and the volume ratio  $\Phi_{A,B}$  of component  $A$  and  $B$ , and the total number of molecules  $n$  on the lattice. The summed volume ratios of the single components add up to  $\Phi_A + \Phi_B = 1$ .

Enthalpic contributions arise from the interaction of the monomers of the components with each other. Mixing two components  $A$  and  $B$  leads to a change in enthalpy  $\Delta H$  given by

$$\Delta H = nk_B T \chi \Phi_A \Phi_B \quad (2.5)$$

with  $\chi$  the Flory-Huggins interaction parameter describing the miscibility of the two materials.

Therefore, the Gibbs free energy upon mixing  $\Delta G$  can be reformulated to

$$\Delta G = RT \left( \frac{\Phi_A}{N_A} \ln \Phi_A + \frac{\Phi_B}{N_B} \ln \Phi_B + \chi \Phi_A \Phi_B \right) \quad (2.6)$$

with  $R = k_B N$  and Avogadro's number  $N$ .

Using the mean-field formalism of the Flory-Huggins model, the Flory-Huggins interaction parameter  $\chi$  originates from purely enthalpic considerations. Empirical data, however, show that entropy also plays a role, contributing to  $\chi$  so that the equation needs to be corrected to

$$\chi = \frac{\chi_H}{T} + \chi_S \quad (2.7)$$

with the enthalpic and entropic contributions  $\chi_H$  and  $\chi_S$ , respectively. Generally, the miscibility of two materials increases with decreasing  $\chi$ . This also explains the enhanced solubility of most polymers with increasing temperatures due to the reduction of  $\chi$  at elevated temperatures.

### 2.1.3 Conductive Polymers

Organic semiconductors are based on conductive organic molecules, often polymers. Polymers are commonly known for their insulating properties. However, as was first discovered in 1997, doping can decrease their resistance to make them electrically conductive.<sup>[5]</sup> Chemical doping under iodine vapor exposure increased the electrical conductivity of the simple polymer polyacetylene (PA) by seven orders of magnitude, making the formerly insulating polymer semi-conducting. This discovery enabled a whole new branch of research into organic electronics based on polymers.<sup>[37–39]</sup> The following section introduces the electronic band structure formation as well as charge carrier creation and transport processes within conductive polymers.

#### Band Structure

Conductivity requires a delocalization of electrons to enable charge transport. The delocalization is based on  $\pi$ -electrons found in conjugated  $\pi$ -electron systems within the molecule, i.e. chain segments with alternating single and double bonds. The atomic orbitals occupied by the  $\pi$ -electrons overlap to create a large delocalized orbital wherein electrons can move freely. The  $\pi$ - $\pi$ -bonds lead to two solutions of the Schrödinger equation, namely the bonding  $\pi$ - and anti-bonding  $\pi^*$ -band. They are called highest occupied molecular orbital (HOMO) and lowest unoccupied molecular orbital (LUMO), respectively, and are comparable to the valence and conduction band in inorganic semiconductors. Typical semiconducting polymers exhibit a conjugated carbon backbone with the representative PA serving as an ideal model system due to its simple structure.

Atomic and molecular orbitals are quantum mechanical wave functions describing the probability density and behavior of electrons in atoms or molecular bonds. In the linear combination of atomic orbitals (LCAO) picture, molecular orbitals can be described by a linear combination of atomic orbitals. By combining the atomic orbitals, the overlap can lead to constructive or destructive interference, forming bonding or

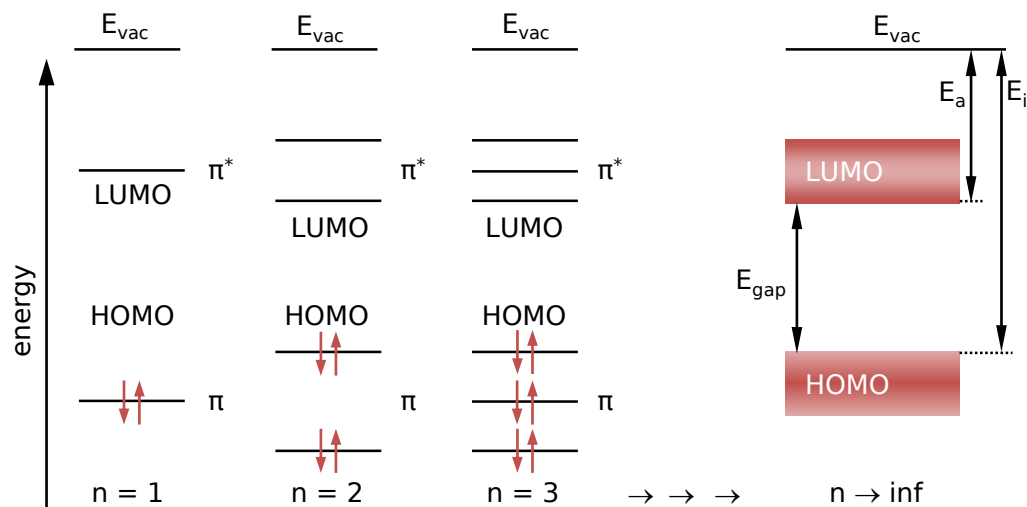


**Figure 2.2**

The LCAO for molecules with increasingly conjugated  $\pi$ -systems, illustrating the creation of energy bands for elongated polymers with a high number of coupled monomers  $n$ . The energy gap  $E_{gap}$  between the bands influences the light absorption behavior and conductivity. The first ionization energy  $E_i$  denotes the energy needed to fully remove an electron from the HOMO level to the vacuum energy  $E_{vac}$ , while the electron affinity  $E_a$  is a measure of how easily an atom or molecule will take up an electron.

anti-bonding orbitals, respectively. Via LCAO, the forming of occupied, bonding  $\pi$ -orbitals and empty, anti-bonding  $\pi^*$ -orbitals for conjugated  $\pi$ -systems with delocalized electrons can be described. Figure 2.2 illustrates the LCAO for molecules with increasingly conjugated  $\pi$ -systems. For a single  $\pi$ -bond, the HOMO and LUMO are distinct energy levels divided by a certain energy gap  $E_{gap}$ . If another  $\pi$ -bond is in close vicinity, the  $\pi$ -orbitals will overlap, thereby narrowing the HOMO-LUMO gap. Consequently, if a large enough number of  $\pi$ -orbitals overlap, the energy levels will cease to be distinct and instead form a band. This band-like structure is the origin of conductivity in conductive polymers. For a combination of  $n$  molecular orbitals, the bonding and anti-bonding states merge and form the band-like structures at the HOMO and LUMO levels that enable the conductivity of charge carriers.

For an ideal, infinitely  $\pi$ -conjugated, linear chain, all bonds in the polymer backbone are placed at a periodic distance  $a$  with  $\pi$ -electrons distributed equally over the chain (see Figure 2.3a). As the band would be half-filled up to the Fermi level  $E_F$ , the chain would behave like a 1D metal. However, any slight disturbance of the ideal chain such as atomic oscillations will lead to a distortion of the periodic lattice. According to Peierl's theorem, a 1D chain of atoms with a periodic distance  $a$  and each atom contributing a single electron is unstable. This instability is schematically illustrated in Figure 2.3b) and further explains the occurrence of band structures in polymers

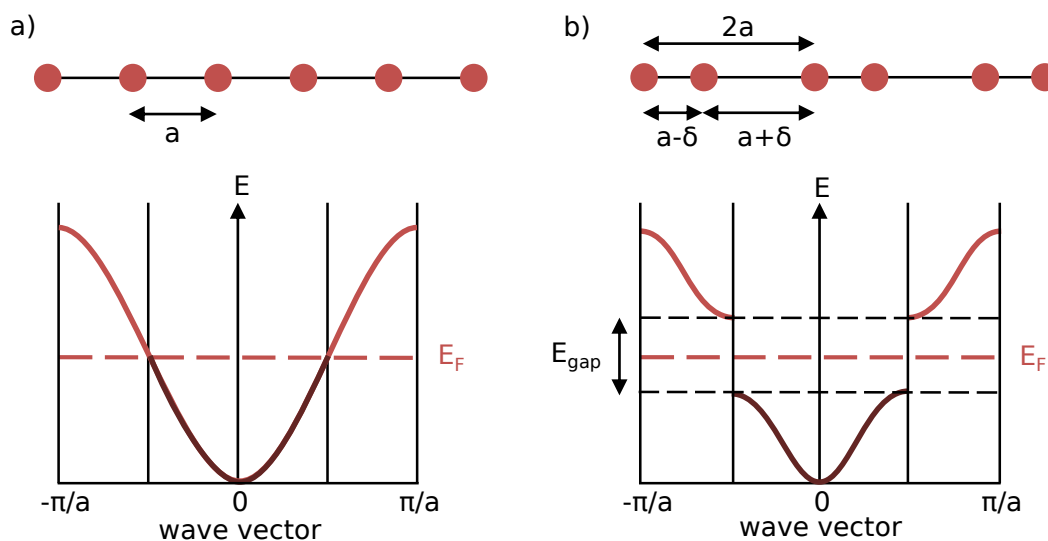


**Figure 2.3**

Electronic structures compared for an ideal chain vs. a real chain considering Peierl's instability theorem: a) an ideal 1D chain with undisturbed periodic distances  $a$  exhibits an energy band filled up to the Fermi Energy  $E_F$ , behaving like a perfect 1D metal. b) A real 1D chain undergoes slight disturbances that lead to a superstructure of periodicity  $2a$  with an energy gap  $E_{gap}$ .

with a conjugated backbone. Already small distortions  $\delta$  of the lattice lead to the formation of alternating bonds with a length  $a \pm \delta$  and, therefore, to a new periodicity of  $2a$ . This periodic superstructure reduces the total energy of the system. As the system still has the same number of electrons, the created lower band (based on  $\pi$  orbitals) is completely filled, while the upper band ( $\pi^*$  orbitals) is empty. This lattice distortion leads to the formation of a bandgap and hence an insulating behavior, as the Fermi level is not affected and lies within the bandgap. This metal-insulator-transition and the resulting bandgap can be influenced by several factors such as the polymer structure, the degree of polymerization, or additional doping. For typical semiconducting polymers, the bandgap is in the range of 1.5 eV – 3.0 eV.<sup>[40–42]</sup> A low bandgap of 1.5 eV is desirable for photovoltaics, as this would allow the most efficient harvesting of photons in the visible region.<sup>[43]</sup>

### Charge Transport

In contrast to inorganic systems, charges in conductive polymers are not simply carried via electrons or holes. In inorganic lattices, the atoms show only limited movement in pronounced potential wells around certain positions, while for polymers, the chains can move comparably freely even without any solvent. This leads to additional polarization effects that have to be taken into account by introducing quasi-particles combining

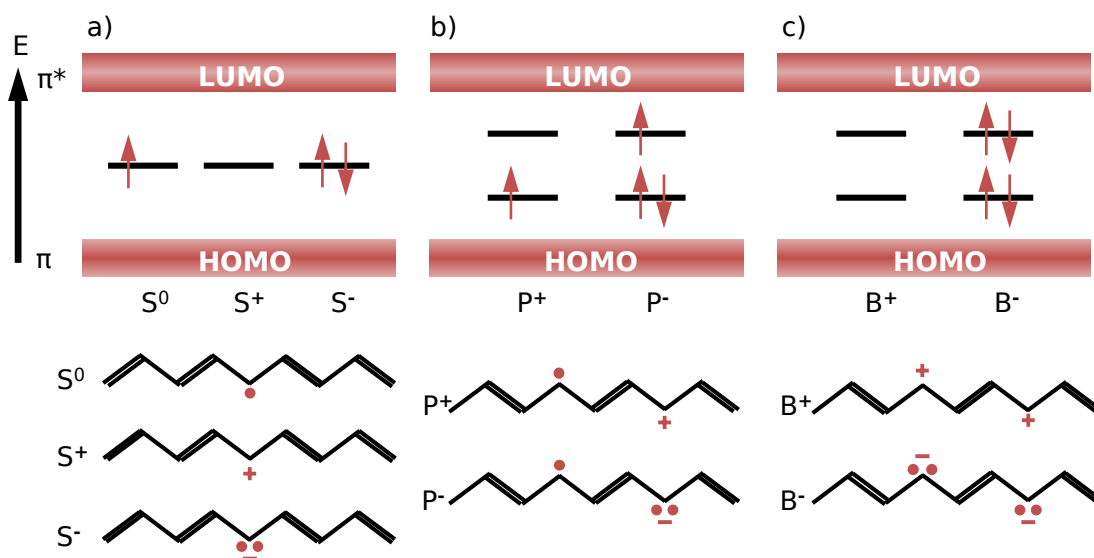


**Figure 2.4**

Different quasi-particles can act as charge carriers in polymers. Shown are the three types of quasi-particles with respective energetic levels and structural representations. Single, unpaired electrons are represented with dots, while net charges are marked with + or - signs. a) Solitons can be either neutral ( $S^0$ ,  $S^+$  and  $S^-$ ), while b) polarons exhibit a single positive  $P^+$  or negative  $P^-$  state. c) Bipolarons are doubly charged ( $B^+$  or  $B^-$ ).

charges and lattice distortions. Three different quasi-particles can be differentiated, namely solitons, polarons, and bipolarons. The quasi-particles are distributed over several atoms of the polymer, for example over 14 carbon atoms in the case of the model system PA.<sup>[44]</sup> According to the Su-Schrieffer-Heeger (SSH) theory, the created quasi-particle states are located in the energy gap between the HOMO and LUMO.<sup>[44]</sup> The respective energetic states and schematic representation for the model system PA are illustrated in Figure 2.4. The two degenerated ground states of PA – swapping double and single bonds – allow the presence of neutral solitons  $S^0$  with an unpaired electron at the meeting point of both states, leading to spin 1/2. As the  $S^0$  state lies between the HOMO and LUMO level, the unpaired electron provides only a singly occupied state and thereby electrical conductivity. Chemical doping or excitation via light can create charged solitons  $S^+$  and  $S^-$ , which – in contrast to electrons or holes – do not have a spin. Polarons combine the spin 1/2 of an unpaired electron with a positive or negative charge, while bipolarons are spin-less and charged. Due to the lattice polarization, the latter are stable despite the repulsive Coulomb interaction between the charges. Quasi-particles can combine, leading to the formation of new quasi-particles or their annihilation. Combining two  $S^0$  or polarons of opposing charges

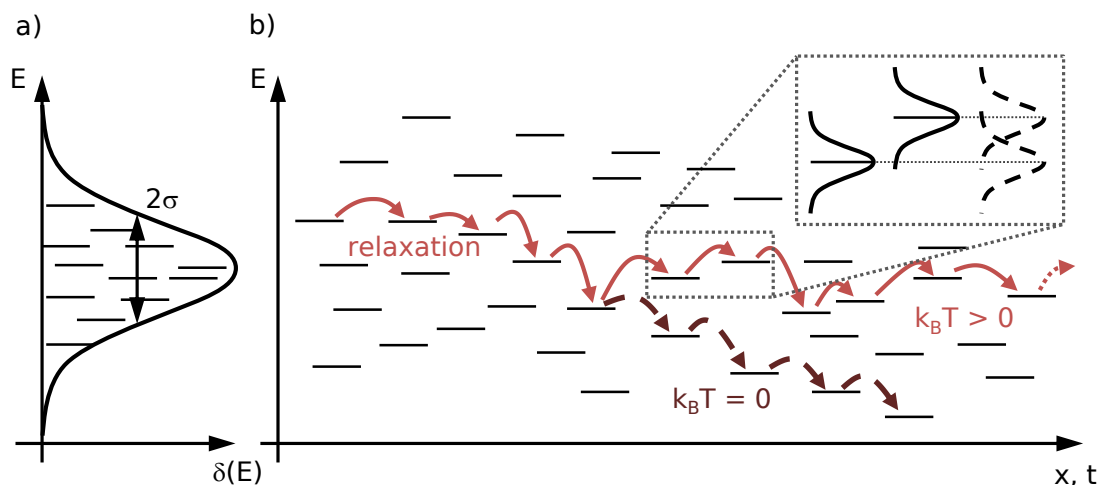


**Figure 2.5**

Charge transport in polymers happens via a hopping mechanism. a) All possible energetic states in the material – marked with thin lines – make up the total density of states (DOS) with Gaussian disorder and width  $2\sigma$ . b) Energetic states plotted over distances  $x$  (or equivalently over time  $t$ ). Hopping transport in an external electric field may generally happen in two ways: Without thermal activation ( $k_B T = 0$ ), the relaxation leads to a loss of energy until a trapped state is reached. Thermal activation ( $k_B T > 0$ ) is needed to allow the hopping towards energetically higher states which is enabled by the smearing of energy levels, as shown in the inset figure.

leads to annihilation, while combining  $S^0$  with  $S^+$  or  $S^-$  creates  $P^+$  or  $P^-$ , respectively. Bipolarons are formed by a combination of polarons of the same net charge.

Charge transport in organic semiconductors shows low charge carrier mobilities and strong polaronic effects. Charges are transported either along a conjugated polymer backbone or by hopping from one polymer chain to the next. While the transport along a chain is a rather efficient band-like process within the delocalized  $\pi$ -bands according to the SSH theory, macroscopic charge transport needs the transition of charges between polymer chains. Interchain transport is achieved via hopping processes, in which charges tunnel between neighboring energetic states if they overlap, as described by the Bässler model.<sup>[45–48]</sup> The spatial and energetic disorder in the system leads to Gaussian smearing of the energetic states, benefiting the tunneling probability.<sup>[49,50]</sup> Figure 2.5 illustrates the schematic processes in the Gaussian disorder model, as introduced by Deibel et al.<sup>[51]</sup> The total density of states (DOS) for a given, disordered system shows a Gaussian distribution. Charge transport happens when a charge is moving in time and space along an electric field. Without thermal activation ( $k_B T = 0$ ), charge carriers relax to lower energetic states. Thermal activation ( $k_B T > 0$ ) is needed to reach energetically higher states, meaning that the conductivity of semiconductors increases with temperature. While the additionally needed thermal activation might pose a dis-

advantage for some systems, it is beneficial for applications in photovoltaics. The solar irradiation leads to typical operation temperatures well above room temperature and therefore higher electrical conductivity.

## 2.2 Organic Solar Cells

Independent of the exact material system, photovoltaic devices generally convert sunlight into electrical energy. The conversion includes several steps, namely the absorption of light, generation of free charge carriers, and charge transport to the electrodes. In contrast to inorganic solar cells, at least two components are needed to create an efficient organic solar, with interfaces between the different phases playing a vital role in the generation of free charge carriers. The following sections introduce the main working principles of solar cells as well as typical loss mechanisms and degradation pathways. For a comprehensive overview of basic principles in organic solar cells, the reader is referred to helpful review articles.<sup>[51–53]</sup>

### 2.2.1 General Principles

Several layers are needed to create a fully functioning solar cell.<sup>[52]</sup> Aside from the (photo)active layer, at least two electrodes are needed, one of which should exhibit high transparency to visible light. Other functional layers are usually introduced to block charge carriers from reaching the wrong electrode, thereby increasing the overall efficiency. An exemplary organic photovoltaic (OPV) layer stack and the corresponding energy level diagram are illustrated in Figure 2.6. The so-called active layer consists of at least two materials and delivers the essential processes needed for light absorption and charge carrier generation. It is sandwiched between the two electrodes in combination with blocking layers introduced to hinder the charge carriers from reaching the wrong electrode. Experimentally, the layer stack is created on a substrate that – at least for this solar cell architecture – needs to be transparent as well. While the shown solar cell is built in the normal configuration with transparent anode and metal cathode, the inverted configuration with transparent cathode and metal anode is equally possible. The active layer consists of (at least) one electron donor and one electron acceptor.

A schematic of the energy levels involved in the energy conversion is shown in Figure 2.6.<sup>[52]</sup> Illustrated are the HOMO and LUMO levels of the two photoactive materials and the working functions of the anode and cathode. Additionally, the five steps of photon absorption

- (I) photon absorption and exciton generation
- (II) exciton diffusion to a donor-acceptor interface
- (III) exciton dissociation into free charge carriers

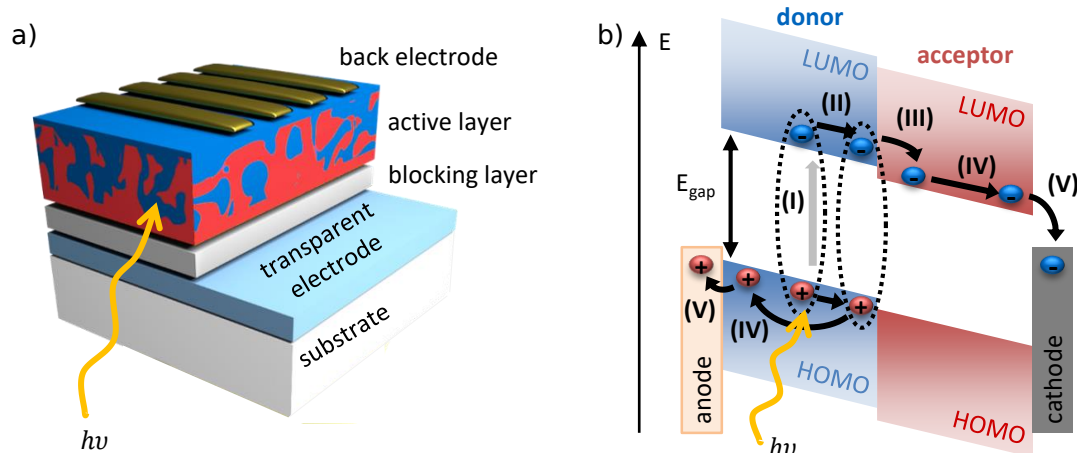


**Figure 2.6**

Exemplary solar cell device stack and corresponding energy level diagram. a) Schematic layer stack of an organic solar cell. The active layer consists of an electron donor material (blue phase) and electron acceptor material (red phase). Light can penetrate the transparent substrate, electrode and charge-carrier blocking layer, before being absorbed within the active layer. b) Typical processes of charge carrier generation are visualized in a simplified energy level diagram (without blocking layers): (I) Absorption of a photon with energy  $h\nu \geq E_{\text{gap}}$  by the donor and creation of a strongly bound electron-hole pair (exciton). (II) Exciton diffusion to the donor-acceptor interface. (III) Dissociation into free charge carriers at the interface with a transfer of the electron to the acceptor. (IV) Charge transport to the respective electrodes. (V) Charge carrier extraction at the electrodes and current generation.

(IV) charge transport to the respective electrodes

(V) charge extraction

are depicted in energetic terms, showing the excitation of an electron to a LUMO level of the donor material as well as the charge separation due to the difference in LUMO levels between the donor and the acceptor material. The different steps are also illustrated in more detail in Figure 2.7 and explained in the following. Incoming photons are absorbed with a certain probability by the electron donor. Each absorbed photon excites an electron from the HOMO to the LUMO, resulting in a strongly bound electron-hole pair called exciton. To split the exciton into free charge carriers, it has to reach the donor-acceptor interface within its lifetime. The difference in LUMO levels between the acceptor and donor material provides the energy needed to split the exciton. Subsequently, the separated charge carriers can be transported to the electrodes where they are extracted. Two main competing factors define an optimal donor-acceptor morphology. While the short exciton diffusion length calls for a highly intermixed active layer with a large interface, the separated charge carriers need interconnected pathways in one phase to reach the respective electrodes. Commonly,

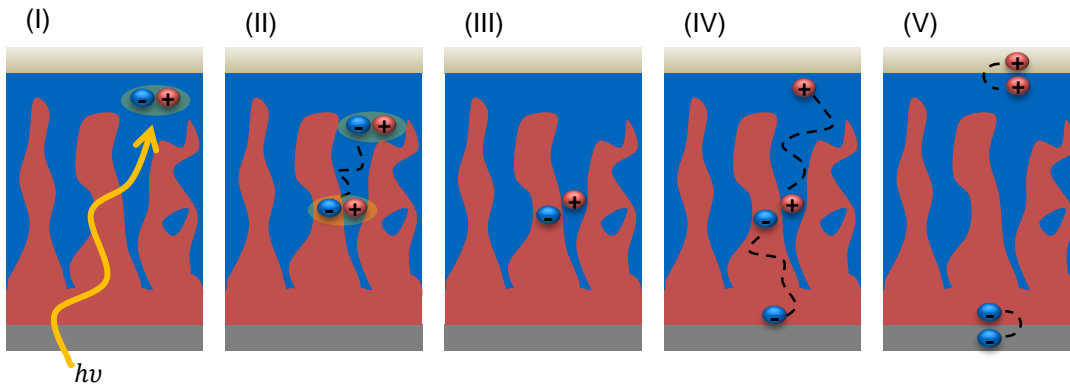


**Figure 2.7**

Active layer profile with the five process steps needed for the conversion of light into an electrical current. (I) Absorption of an incoming photon with energy  $h\nu \geq E_{\text{gap}}$  in the donor phase (blue) and creation of an exciton. (II) Diffusion of the exciton to a donor-acceptor interface and (III) dissociation into free charge carriers with a transfer of the electron to the acceptor phase (red). (IV) Transport of the free charge carriers within the respective phases. (V) Extraction of the charge carriers at the respective electrodes and current generation through an external load.

this problem is addressed successfully by introducing a so-called bulk-heterojunction (BHJ) simply created out of solution of both materials. While providing a much higher interface in contrast to a bilayer, it still is a simple, comparably cheap method that can be tuned by various experimental factors to achieve the desired morphology.

**Absorption:** According to the Beer-Lambert law, the absorption of light in a thin film can be determined by measuring the intensity of transmitted light  $I_T$  in comparison to the one of the incident beam  $I_0$

$$I_T(\lambda) = I_0(\lambda) \exp^{-\alpha(\lambda)d} \quad (2.8)$$

with  $\alpha$  the absorption coefficient and  $d$  the thickness of the material. Absorption in a material takes place when an incident photon has enough energy to excite an electron from a lower to a higher energy level. For polymers, this means that the photon needs an energy  $E_{\text{photon}}$  equal to or larger than the bandgap energy  $E_{\text{gap}}$  between its HOMO and LUMO level

$$E_{\text{photon}} = h\nu = \frac{hc}{\lambda} \geq E_{\text{gap}} = E_{\text{LUMO}} - E_{\text{HOMO}} \quad (2.9)$$

with the Planck's constant  $h$ , the speed of light  $c$ , the frequency  $\nu$ , and the wavelength of the photon  $\lambda$ . The exact absorption of a polymer depends on the type of functional units within the monomer units, degree of polymerization, and chain conformation. Vibronic excitations lead to an additional splitting in the energy levels,

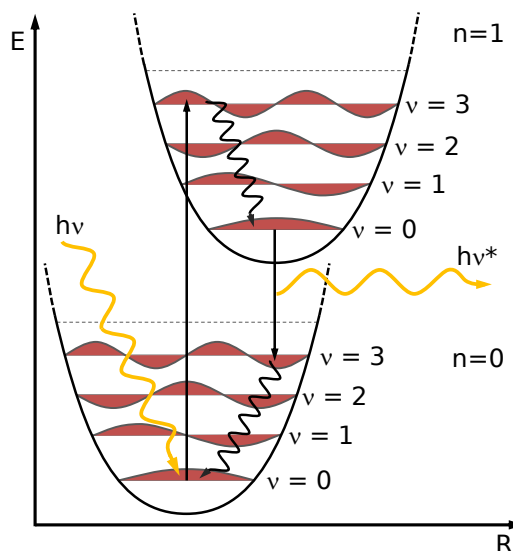


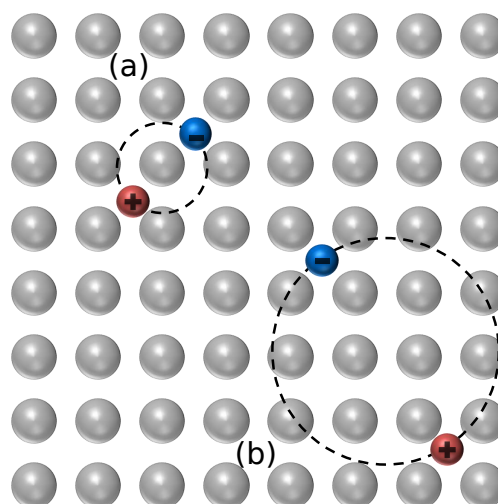
**Figure 2.8**

Visualization of the Franck-Condon principle for the absorption of light. Shown are the two lowest electronic states  $n = 0$  (ground state) and  $n = 1$  (first excited state) as a function of the nuclear distance  $R$ . Different vibronic levels  $\nu$  for each electronic state are illustrated with their respective wave functions. Both electronic transitions of the electron are visualized by vertical lines, as these processes are considerably faster than nuclear motions. (Non-radiative) relaxations to lower vibrational states follow the quick electronic transitions.

which again leads to broadened absorption peaks. Two electronic states with their respective vibrational excitation levels are illustrated in Figure 2.8. Absorption of a photon with energy  $h\nu$  excites an electron from the ground state ( $n = 0, \nu = 0$ ) to an excited state ( $n > 0, \nu > 0$ ) following the Franck-Condon principle. As the electron transition is significantly faster than the motion of nuclei, the atoms can be assumed to be static during this process. The probability to reach a certain vibronic state depends on the vibration wave functions of the two levels. The higher their overlap, the higher the probability that the electron will transition to the respective vibronic state at the excited electronic state, as also illustrated in Figure 2.8. Typically, the most probable transition from the electronic ground state to the first electronic excited state will include a transition to  $\nu = 2$ . Having reached the excited electronic state, the electron then relaxes to the lowest vibronic state ( $\nu = 0$ ), thereby non-radiatively dissipating some energy to the material. The subsequent relaxation to the electronic ground state under emission of a photon with decreased energy  $h\nu^*$  again follows the Franck-Condon principle, reaching a vibronic state with similar local vibronic wave function (in this case  $\nu = 2$ ). The relaxation to the vibronic ground state will again happen non-radiatively. The total energy transferred into vibrations during the whole process can be calculated from the difference in energy of the absorbed and emitted photon ( $h\nu - h\nu^*$ ).

**Figure 2.9**

Depending on the environment, two types of excitons can be differentiated. a) In typical organic materials, Frenkel excitons are localized at a certain atomic position, exhibiting a small size and high binding energy, as the organic material's low dielectric constant has a low shielding effect. b) Weakly bound Wannier-Mott excitons in inorganic materials expand over several atoms, as the higher dielectric constant leads to considerable shielding.



The excitation of an electron to the LUMO leaves a hole in the HOMO. Coulombic interactions lead to attractive forces between the electron and the hole, thereby creating a strongly coupled electron-hole pair called exciton. In contrast to inorganic semiconductors, excitons in organic semiconductors show a significantly stronger electron-hole binding. While the dielectric constant for inorganic semiconductors is above  $\epsilon_r > 10$ , it lies in the range of  $\epsilon_r \approx 3 - 4$  for organic materials, leading to a lower shielding effect and therefore stronger attraction.<sup>[54,55]</sup> Hence, the thermal energy of  $k_B T = 25$  meV alone cannot dissociate the charge carriers in organic materials so that additional sources of energy are needed. Depending on their binding energies and sizes, excitons are generally differentiated into Wannier-Mott or Frenkel excitons, as illustrated in Figure 2.9. Typical for inorganic semiconductors are weakly coupled Wannier-Mott excitons expanding over several distances. In contrast, small, strongly bound Frenkel excitons are located at a certain atomic positions for organic semiconductors due to the low dielectric shielding.<sup>[56]</sup>

**Exciton diffusion:** To contribute to the charge transport, the charge carriers of the exciton have to be separated. As the thermal energy is not sufficient to dissociate the strongly bound Frenkel excitons, an interface of the electron donor and electron acceptor material is needed to induce an external electric field. To reach the interface, the exciton has to diffuse through the donor phase via energy transfer processes. Amongst several pathways, the most important are photon reabsorption and the Förster transfer. During photon reabsorption, the exciton recombines under emission of a photon that gets directly reabsorbed by another molecule in the neighborhood creating a new exciton. The Förster transfer is also called fluorescent resonance energy transfer (FRET) and the dominant process for short distances. Via dipole-dipole coupling, the exciton is transferred non-radiatively from a donor to an acceptor.<sup>[57,58]</sup> Exciton diffusion happens without preferential direction in a random hopping process. The

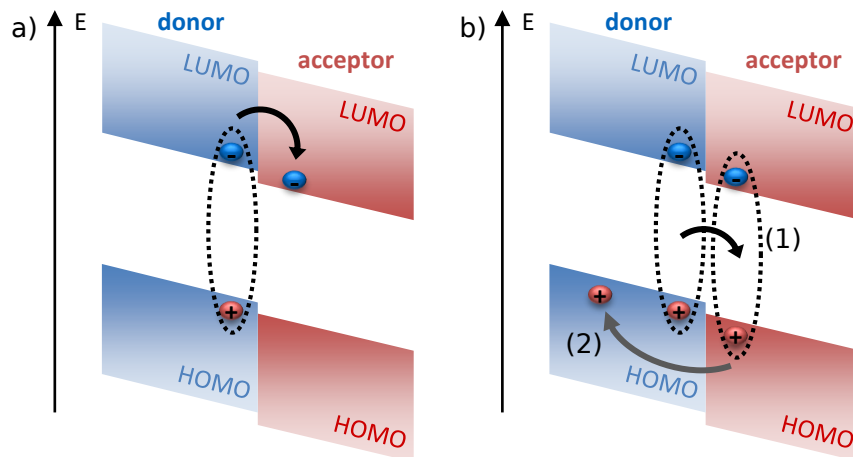


**Figure 2.10**

Exciton dissociation at a donor-acceptor interface can happen in two pathways: a) Direct transfer of the excited electron from the LUMO of the donor phase (blue) to the LUMO of the acceptor phase (red). b) Two-step process with (1) a Förster energy transfer followed by (2) a back-transfer of the hole to the donor phase.

diffusion propagation is characterized by the diffusion length  $l_d$  in all three dimensions and linked to the exciton lifetime  $\tau$  via

$$l_d = \sqrt{\frac{\sum dL_i^2}{N}} = \sqrt{2dD\tau} \quad (2.10)$$

with the diffusion coefficient  $D$  and the dimensionality of diffusion  $d$ . In photoactive polymers, typical exciton lifetimes are only in the range of nanoseconds, leading to diffusion lengths of around 10 nm – 30 nm.<sup>[51,59]</sup> These short distances pose limitations on the optimal donor-acceptor morphology. The donor phase should be formed in such a way as to allow excitons to reach the next interface within their lifetime.

**Exciton dissociation:** Close to the donor-acceptor interface, the exciton is stabilized by the external electric field and is now called exciplex. The acceptor material increases the lifetime and decreases the binding energy of the electron-hole pair. In principle, the exciplex can be split into two potential pathways schematically illustrated in Figure 2.10. A direct charge transfer happens by the electron moving from the LUMO of the donor material to the LUMO of the – more electronegative – electron acceptor. Also possible is a two-step process for which a Förster transfer of the whole exciplex to the acceptor material is followed by a hole transfer from the HOMO of the acceptor back to the HOMO of the donor. Regardless of the pathway, this process needs to happen quickly enough to avoid charge recombination.

**Charge carrier transport:** The freshly separated charge carriers can subsequently move to the respective electrodes. Several factors have to be taken into account for successful charge transport. The charge carriers need to find fully interconnected pathways within one phase to the correct electrode, which has to be reflected in the morphology. Holes and electrons can only move in their respective hole- or electron-conducting material. The charge transport – characterized by comparably low mobilities and strong polaronic effects – is described in more detail in Section 2.1.3.

**Charge extraction:** Charge carrier extraction happens at the interface between the organic semiconductors and respective electrodes. This process depends on the device architecture as well as the charge carrier concentration and correlated recombination rate. Imbalanced electron and hole mobilities and surface recombination influence the charge carrier extraction.<sup>[51,60]</sup> Using a model of Sokel and Huges, the photocurrent can be determined depending on the voltage across the device.<sup>[61]</sup>

A device's total power conversion efficiency (PCE)  $\eta$  can be calculated via

$$\eta = \eta_{\text{absorption}}\eta_{\text{diffusion}}\eta_{\text{dissociation}}\eta_{\text{transport}}\eta_{\text{extraction}} \quad (2.11)$$

as the product of the efficiencies of the individual processes. However, a range of potential loss mechanisms may decrease the efficiency significantly.

## 2.2.2 Loss Mechanisms

Ideally, all created excitons would lead to free charge carriers being extracted at the respective electrodes. In practice, however, several factors influence the whole process and lead to losses at each of the steps. The choice of an optimized combination of donor and acceptor materials with suitable work functions is crucial, yet not sufficient to prevent other loss mechanisms. Five main origins of efficiency losses – all related to recombination or trapping of charges – are illustrated in Figure 2.11.<sup>[51]</sup>

**I) Recombination within the donor phase:** The created exciton may directly recombine within the donor material if it does not reach a donor-acceptor interface within its limited lifetime. Losses can be reduced by optimizing the active layer morphology and keeping the average distances to the next donor-acceptor interface smaller than the exciton diffusion length.

**II) Recombination at the donor-acceptor interface:** Already dissociated charge carriers may recombine at the interface if charge transport is too slow in comparison to the recombination times. In particular, defects, chain end groups, or side groups have a lower charge carrier mobility and will slow down the charge transport, thereby increasing the recombination probability. Hence, a high overall charge carrier mobility in the respective materials is beneficial.

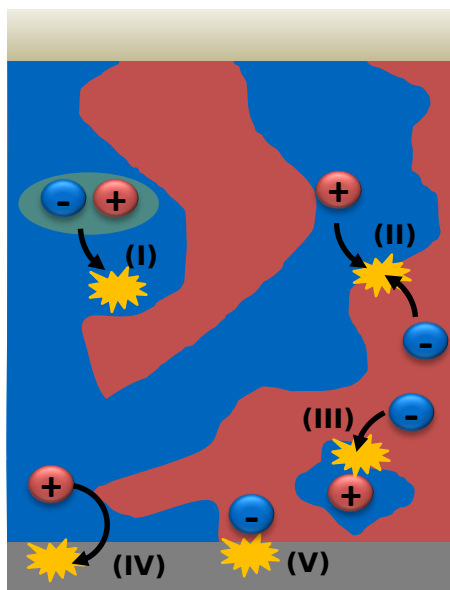


**Figure 2.11**

Potential loss mechanisms in organic solar cells. I) Exciton recombination within the donor phase. II) Recombination of dissociated charge carriers at the donor-acceptor interface III) Charge trapping on isolated domains with potential recombination at the interface IV) Recombination of charge carriers at the wrong electrode V) Surface recombination at the correct electrode.

**III) Charge trapping in isolated domains:** Charges may get trapped in isolated material domains. Without closed percolation paths to the electrodes, the charges will either lead to defects or recombine with another mobile charge carrier at the interface to the other material.

**IV) Recombination at the wrong electrode:** For non-optimized BHJ blends, a material phase may not only be connected to the respective desired electrode but may also have a connection to the other electrode. Without a significant driving force like an external electric field, charge carriers may therefore reach the wrong electrode, thereby not contributing to the current generation. Apart from improving the active layer blend, additional charge carrier blocking layers can prevent this pathway.

**V) Surface recombination at the electrode:** Even when reaching the correct electrode, charges may recombine at the interface instead of contributing to the external current.<sup>[60]</sup>

Thus, morphology plays a vital role in several of the described pathways, with competing restrictions from different mechanisms. Controlling the morphology is of utmost importance and still under investigation in various settings.<sup>[62–70]</sup>

### 2.2.3 Degradation of Photoactive Layers

Organic photovoltaics in general are prone to aging, leading to significantly reduced lifetimes in contrast to conventional solar cells based on inorganic materials. This holds especially true for low-bandgap polymers that are even more sensitive to degradation.<sup>[16–18]</sup>

Encapsulated devices show typical lifetimes in the order of a few thousand hours of operation, while non-encapsulated solar cells often deteriorate in a matter of mere hours.<sup>[4,71–75]</sup>

Potential degradation pathways are typically distinguished by their extrinsic or intrinsic origins.<sup>[20,24,26]</sup> Extrinsic degradation can be triggered by environmental factors such as temperature, electromagnetic radiation, mechanical influences, or the reaction with pollutants, while intrinsic aging is caused by morphological changes and/or modification of the chemical structure within the respective materials. For an extensive discussion of the different degradation routes and mechanisms, the reader is referred to the cited literature.<sup>[16–18,76,77]</sup> An overview of the most prominent pathways of aging is given in the following.

Several sources of external degradation are connected to materials outside the photoactive layer, such as mechanical failures, the oxidation of electrodes, or intrusion of electrode components into the active layer. Especially brittle components of solar cells such as oxide-based electrode materials can experience mechanical failure due to bending. In some solar cell designs, non-noble metals such as aluminium or calcium have to be used as back electrodes due to specific requirements on their work functions. The low work function – while needed for charge extraction – greatly increases the risk of oxidation which has been investigated in detail in various settings.<sup>[78–83]</sup> Oxidation may affect the electrode itself by increasing its resistance. More important, however, are the degradation and delamination of the contact due to the formation of hydrogen or other reaction products of the decomposition which increase the serial resistance and reduce the fill factor. Material from the electrodes can also intrude the active layer and lead to impurities with the respective side effects such as the creation of trap states or changes in the local electronic structure.<sup>[84,85]</sup>

As the present work focuses on aging processes within the photoactive layer, two main pathways are of interest, namely morphological changes and photooxidation. The morphological degradation of various material systems for use in organic solar cells has been investigated using various imaging and scattering techniques.<sup>[63,66,67,71,86–88]</sup> In particular, the morphological aging process during operation of the respective solar cells was followed *in operando* using X-ray scattering methods in earlier works of our group.<sup>[65,68–70,89–91]</sup> Depending on the studied systems, different origins and pathways of morphological degradation were found. For the typical model system P3HT<sup>3</sup> : PCBM<sup>4</sup> in conventional device architecture, an increase of polymer domain sizes and distances causes a loss in the donor-acceptor interface, thereby reducing the chance of exciton splitting.<sup>[65]</sup> The device architecture plays a vital role, as inverting the device structure was found to stabilize the morphology under otherwise similar process parameters.<sup>[89]</sup> In contrast to the P3HT-based system, low-bandgap solar cells show very different

---

<sup>3</sup>P3HT: poly(3-hexyl-thiophene)

<sup>4</sup>PCBM: [6,6]-phenyl-C<sub>61</sub> butyric acid methyl ester

morphological aging. In low-bandgap solar cells based on PCPDTBT<sup>5</sup> or PTB7-Th<sup>6</sup> the evaporation of the processing additive led to a decrease in the domain sizes and formation of islands and traps, significantly reducing the PCE.<sup>[68,70]</sup>

The chemical stability of organic solar cells has been investigated in various settings and for different systems.<sup>[74,92–94]</sup> Especially photon-induced oxidation processes play a prominent role in chemical degradation due to the desired absorption behavior of the photoactive materials. It was shown that the polymer P3HT of the model system P3HT:PCBM is sensitive to combinations of light with either oxygen or moisture, while comparably stable during exposure to only one of these factors.<sup>[95–101]</sup> Different pathways are possible depending on the exact material composition of a system, leading to changes in the local electronic structure, breaking of bonds, trap formation, polymer cross-linking, breaking of the conjugation or even chain scission and other deteriorating effects.<sup>[16,93,95,96,98,102–104]</sup> While many aspects of degradation are connected to the donor polymer due to its high absorption, the electron acceptor can also significantly influence its photochemical stability. The addition of fullerene derivatives was found to stabilize P3HT and poly(phenylene-vinylene) (PPV)-based polymers,<sup>[71,105]</sup> but accelerate the aging of PCPDTBT.<sup>[93]</sup> Several interconnected causes have been proposed, amongst them the stabilizing radical-scavenging properties of the fullerene derivative as well as the difference in electronegativity between the materials having a stabilizing or destabilizing effect.<sup>[106]</sup> In the present work, PTB7-Th is discussed as a stand-in for a range of irradiation-sensitive low-bandgap polymers.<sup>[67,88,93,107–111]</sup> A pronounced degradation under ultraviolet (UV) light was already shown for several systems.<sup>[110–113]</sup> However, as discussed further in Chapter 7, even red light can be harmful to low-bandgap materials.

## 2.3 Polymer-Metal-Interfaces

One of the main features investigated in the scope of this work is the polymer-metal interface created between the metal back electrode and the photoactive layer of organic photovoltaics. Apart from the electrode's electrical conductivity, the polymer-metal interface plays a vital role in the performance of organic electronics. Understanding the formation of the polymer-metal interface during the deposition is of utmost importance for optimized, reproducible, and scalable organic electronic devices. In the following, the most important concepts regarding structures, processes, and growth modes at polymer-metal interfaces are introduced. For more detailed descriptions of important processes at polymer-metal interfaces, the reader is referred to the cited literature.<sup>[114–118]</sup>

<sup>5</sup>PCPDTBT: poly[2,6-(4,4-bis(2-ethylhexyl)-4H-cyclopenta [2,1-b;3,4-b']dithiophene)-alt-4,7(2,1,3-benzothiadiazole)]

<sup>6</sup>PTB7-Th: poly[[4,8-bis(5-ethylhexylthienyl)benzo[1,2-b;4,5-b']dithiophene-2,6-diyl][3-fluoro-2-[(2-ethylhexyl)carbonyl]thieno[3,4-b]thiophenediyl]]

### 2.3.1 Metal Nanostructures at Polymer-Metal Interfaces

Metals are elements characterized by free electrons leading to a whole range of collective properties such as their high electrical and thermal conductivity. However, these properties undergo pronounced changes when reducing the dimensions of the respective material from the bulk towards nanoparticles or even clusters of only several atoms, leading to a whole range of potential size-dependent applications. While nanostructures above 10 nm still show mostly typical metallic behavior, quantum confinement will significantly change the properties of structures below this limit. Very small clusters of only several atoms are extremely mobile, with clusters up to a radius  $R \leq 1.3$  nm considered to behave liquid-like.<sup>[119,120]</sup> Similar to the features discussed for polymers in Section 2.1.3, the linear combination of atomic orbitals (LCAO) can explain the creation of a bandgap between fully occupied and unoccupied energetic states when reducing the metal particle size, leading to a size-induced metal-insulator transition for nanostructures below about 10 nm.<sup>[121]</sup> For this transition, drastic changes in various related properties were observed, for example in the electrical conductivity, the dielectric function, or the optical absorption behavior.<sup>[122–125]</sup> As the metal layers investigated in the scope of this work should act as electrode materials, a certain minimum electrical conductivity is required. This conductivity necessitates a minimum layer thickness and full percolation paths for electrons to reach the external circuit. Apart from affecting the electrode conductivity itself, the morphology at the polymer-metal interface also changes the energy bands of the materials close to the interface, leading to a bending of energy levels.<sup>[126]</sup> Therefore, the fine-tuning of the structures at polymer-metal interfaces is of high importance for the optimization of the device performance.

Metals typically used as electrode materials include noble metals for their unrivaled conductivity and chemical inertness as well as cheaper, more reactive metals such as aluminium<sup>[127,128]</sup> due to their abundance and availability. The evolution of the metal nanostructures on polymer films during sputter deposition has been investigated for various materials such as aluminium,<sup>[128]</sup> copper,<sup>[129]</sup> silver,<sup>[130]</sup> and gold<sup>[131–134]</sup>. Most studies focus on simple polymer substrates, for example on polystyrene (PS) to study the general concepts of structure formation,<sup>[131,133]</sup> whereas some follow the film deposition on more complex polymers used for organic photovoltaics<sup>[128,132]</sup>, batteries<sup>[129]</sup> or as templating structures<sup>[130,134]</sup>. This work focuses on gold as a promising material for thin electrodes needed for flexible organic solar cells due to its high conductivity and inertness as well as the tunability of its properties depending on the exact nanostructures within the layer.<sup>[135–137]</sup>

### 2.3.2 Sputter Deposition

A whole range of preparation techniques allows the creation of thin metal films on organic substrates. For many research purposes regarding organic photovoltaics, the

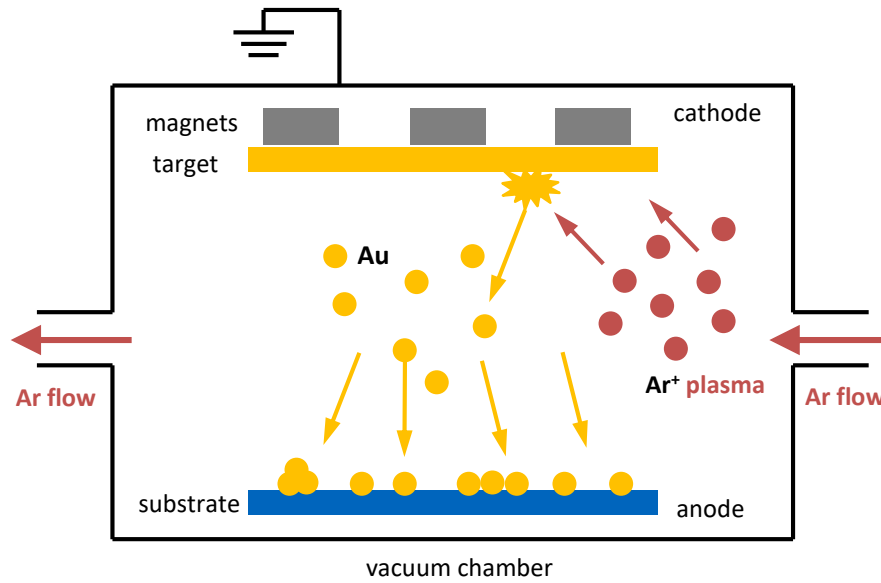


**Figure 2.12**

Schematic of the sputter deposition process. The sputter chamber is evacuated, before starting a low-pressure argon gas flow. A voltage is applied between the target and the substrate, creating an argon plasma and accelerating the positive Ar ions towards the negatively charged cathode. Their impact on the target leads to the ejection of gold atoms which subsequently are deposited on the substrate surface. Magnets inserted into the cathode enhance the efficiency of the process.

back electrodes are applied using lab-scale methods, for example thermal evaporation, as described in Section 3.3.4. In industry, however, mostly large-scale techniques like chemical or physical vapor deposition are preferred.<sup>[29,30,133,138]</sup> The method of choice to create the polymer-metal interface investigated in the present work is direct current (DC) magnetron sputter deposition, as discussed in more detail in the cited literature.<sup>[133,139,140]</sup>

Sputtering describes the process of creating a plasma with highly energetic ions which bombard a target, thereby ejecting atoms from it. The plasma is usually created in an evacuated chamber via a glow discharge by applying an electric potential to a noble gas under low working pressure. The electric field accelerates the noble gas ions towards the target material acting as the cathode. Through the bombardment with energetic ions, atoms of the target material are emitted into the gas phase and deposited as a thin film on a substrate. This process creates highly controllable layers and is sketched in Figure 2.12. The properties of the deposited film depend on a whole range of parameters.<sup>[139]</sup> Especially the surface mobility of the sputtered atoms – mainly defined by the working gas pressure, substrate temperature, and sputter rate – has a significant influence on the structures created during deposition.<sup>[141,142]</sup>

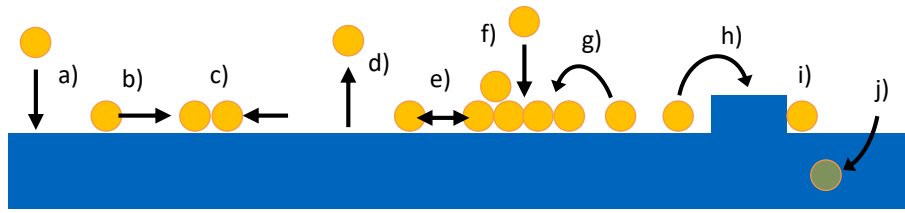


**Figure 2.13**

Typical surface processes during the sputter deposition of gold on a polymer substrate: a) condensation, b) surface diffusion, c) binding, d) (re-)evaporation, e) dissociation, f) adhesion, g) inter-layer jump, h) jump on a step in the substrate, i) capture at a defect, j) diffusion into the substrate, based on literature discussions.<sup>[114,143]</sup>

### 2.3.3 Processes at Polymer Surfaces

A whole range of competing processes takes place during the deposition of metal atoms on any film surface. They are affected by various parameters and create a complex system of interdependent kinetic and thermodynamic phenomena described in more detail in the literature cited in the following. While at any given moment, many or all of the processes take place, some dominate certain phases of the layer growth depending on the investigated material system. Some aspects of the growth can at least generally be described with models developed for immobilized clusters in equilibrium.<sup>[114]</sup> However, growth kinetics further complicate the matter so that a more empiric approach has to be used to describe the growth-defining processes.<sup>[117,118]</sup>

All processes depend on the exact system and local variations in the binding energies due to imperfections in the film leading to different condensation and diffusion rates. The rate  $R_i$  of a process  $i$  can be described by a Boltzmann distribution

$$R_i \propto \exp\left(-\frac{E_{A,i}}{k_B T}\right) \quad (2.12)$$

with an activation energy  $E_{A,i}$ , Boltzmann constant  $k_B$  and temperature  $T$ .<sup>[117]</sup> This holds true for the typical, thermally activated phenomena described in the following. Figure 2.13 illustrates the most common surface processes.<sup>[114,143]</sup> Sputtered atoms are deposited on the surface via condensation (a). Without any competing processes, this would lead to a statistical and therefore homogeneous distribution on the surface. However, atoms and small clusters are often highly mobile and might diffuse (b) on the surface, before meeting and binding to another atom or cluster of atoms (c). In principle, re-evaporation into the gas phase (d) and dissociation of atoms from clusters (e) are also possible, albeit thermodynamically inhibited. For longer deposition times, more and more surface area is covered, increasing the possibility of gold atoms to directly deposit on clusters via adhesion (f). Diffusing atoms may also bind to clusters after an inter-layer jump from the surface (g). With growing size, the clusters lose

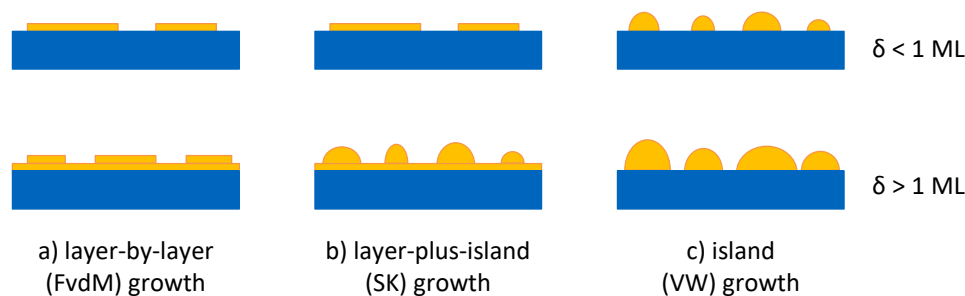


**Figure 2.14**

Depending on the difference in surface tension between substrate and sputtered species, three typical growth modes are distinguished. They are illustrated for effective thicknesses  $\delta$  below or above one monolayer (1 ML): a) Frank-van-der Merwe (FvdM) or layer-by-layer growth, b) intermediate Stranski-Krastanow (SK) or layer-plus-island growth, and c) Volmer-Weber (VW) or island growth.

their mobility.<sup>[117]</sup> As the surface is usually not completely flat, atoms may also jump on steps (h) or be captured at defect sites (i). Another highly important process is the diffusion of atoms into the substrate film (j)<sup>[29,144]</sup> which plays a significant role in the performance of the respective device.

### 2.3.4 Layer Growth Models

As mentioned before, the characteristics of surface processes depend on the exact interactions between the used materials. The difference in binding energies of atoms to atoms of the same or other materials result in variations in the growth behavior.<sup>[114]</sup> Depending on the metal's affinity to the polymer, significant differences in growth behavior occur. Generally, three modes of layer growth (illustrated in Figure 2.14) can be differentiated depending on the affinity of the respective deposited material onto the substrate material.<sup>[115,145]</sup> Metals with a high affinity to the polymer typically exhibit a layer-by-layer or Frank-van der Merwe (FvdM) growth. Layer-by-layer growth requires the interactions of metal atoms with the substrate to outweigh the interactions between each other. This behavior is seen for aluminium on P3HT with metal atoms forming chemical bonds to the polymer, thereby preventing further diffusion.<sup>[127,128]</sup> For certain circumstances, the layer-by-layer growth is disturbed, leading to a layer-plus-island or Stranski-Krastanow (SK) growth behavior. Above a critical wetting layer, island growth is preferred due to induced lattice strains or changes in the surface energy.

The opposite behavior to layer-by-layer growth is seen for metals with a low affinity to the polymer, resulting in an island or Volmer-Weber (VW) growth. Especially noble metals such as gold show a pronounced tendency to form clusters and islands rather than monolayers. Deposited atoms stay mobile and diffuse until meeting with other

metal atoms to build small clusters called nuclei. This leads to a 3D growth of islands until immobilized larger clusters merge into a larger, granular layer.

Gold shows a typical island growth behavior on various templates.<sup>[131–133,146]</sup> A general growth model for the sputter deposition of a gold layer on a silicon substrate was developed by Schwartzkopf et al. and expanded to its growth on PS films.<sup>[133,142,146]</sup> The growth can be divided into typical phases dominated by different processes depending on the effective deposited gold layer thickness, namely nucleation, diffusion, adsorption, coalescence of clusters, and creation of percolation pathways<sup>7</sup>.<sup>[133,146]</sup>

## 2.4 X-ray Scattering

Morphology and crystallinity play a vital role in several of the aspects discussed previously, namely charge transport (Section 2.1.3), solar cell efficiency (Section 2.2) and degradation (Section 2.2.3) as well as polymer-metal interfaces (Section 2.3). To investigate the structural features of a film, X-ray scattering can be applied. Methods based on X-ray scattering offer a whole range of advantages in comparison to other investigation techniques, probing the inner film structures with high statistical relevance. The described techniques are all based on elastic scattering for which the incident photon energy is preserved. After introducing the basic principles of elastic X-ray scattering, the different methods used in the present work are introduced.

### 2.4.1 Basic Principles

X-rays are electromagnetic radiation with wavelengths  $\lambda$  in the pm up to the nm range and interact with the electrons in a sample material.<sup>[147]</sup> Generally, an electromagnetic wave is described by its electric field vector at a position in space  $r$

$$\vec{E}(\vec{r}) = \vec{E}_0 e^{i\vec{k}_i \vec{r}} \quad (2.13)$$

with the constant amplitude  $|\vec{E}_0|$ , the wave vector  $\vec{k}_i$ , and position vector  $\vec{r}$ . The modulus of the incoming wave  $k$  can be calculated via

$$k = |\vec{k}_i| = \frac{2\pi}{\lambda}. \quad (2.14)$$

Utilizing the wave modulus of the electromagnetic wave traveling through a medium with refractive index  $n(\vec{r})$  can be described by the Helmholtz equation

$$\Delta \vec{E}(\vec{r}) + k^2 n^2(\vec{r}) \vec{E}(\vec{r}) = 0. \quad (2.15)$$

---

<sup>7</sup>Full percolation is reached when all islands are interconnected so that charge carriers find percolation pathways throughout the layer.

The refractive index  $n(\vec{r})$  is related to the dispersion  $\delta(\vec{r})$  and absorption  $\beta(\vec{r})$  via<sup>[147,148]</sup>

$$n(\vec{r}) = 1 - \delta(\vec{r}) + i\beta(\vec{r}) = 1 - \frac{\lambda^2}{2\pi}\text{Re}(SLD) + i\frac{\lambda^2}{2\pi}\text{Im}(SLD), \quad (2.16)$$

with  $\delta(\vec{r})$  connected to the real part of the scattering length density (SLD) and  $\beta(\vec{r})$  connected to the imaginary part. Both the absorption and dispersion can be calculated using the Fourier transform of the electron density called the atomic scattering form factor, which can be expressed as<sup>[149]</sup>

$$f_j = f_j^0 + f_j'(E) + f_j''(E) \quad (2.17)$$

where  $f_j^0$  depends on  $\vec{q} = \vec{j}_f - \vec{j}_i$  and  $\vec{j}_i$  and  $\vec{j}_f$  are the wave vectors of the incident wave and exiting wave, respectively.<sup>[148,150]</sup> The respective absorption and dispersion are, therefore, expressed as<sup>[151]</sup>

$$\delta(\vec{r}) = \frac{\lambda^2}{2\pi}r_e\rho(\vec{r}) \sum_{j=1}^N \frac{f_j^0 + f_j'(E)}{Z} \quad (2.18)$$

$$\beta(\vec{r}) = \frac{\lambda^2}{2\pi}r_e\rho(\vec{r}) \sum_{j=1}^N \frac{f_j''(E)}{Z} = \frac{\lambda}{4\pi}\mu(\vec{r}) \quad (2.19)$$

with the total number of electrons  $Z$ , where  $Z = \sum_j Z_j$  is the sum of the number of electrons of each component  $j$ .  $\delta(\vec{r})$  is always positive. The term  $r_e$  is given as

$$r_e = \frac{e^2}{4\pi\epsilon_0 c^2} \quad (2.20)$$

is the so-called Thompson scattering length of an electron or simply the electron radius.  $\rho(\vec{r})$  is the electron density as a function of space, while  $\mu(\vec{r})$  gives the linear absorption. For elastic scattering for which a change in momentum occurs without energy loss, the momentum transfer can be described by the scattering vector  $\vec{q}$  as the difference between the final and the incident wave vector<sup>[152]</sup>

$$\vec{q} = \vec{k}_f - \vec{k}_i. \quad (2.21)$$

For small incident angles, the momentum transfer vector  $\vec{q}$  is small and therefore  $f_j^0 \approx Z_j$ . Therefore, for homogeneous media and far away from absorption edges, equation (2.16) can, therefore, be simplified to<sup>[147]</sup>

$$n = 1 - \frac{\lambda^2}{2\pi}r_e\rho + i\frac{\lambda}{4\pi}\mu. \quad (2.22)$$

For hard X-rays,  $\delta$  typically is in the range of  $10^{-6}$  and one or two orders of magnitude larger than  $\beta$  so that only very little radiation is absorbed, leading to only slight deviations of  $n$  from 1. The higher the difference in SLD between two materials, the better is the scattering contrast, as described by

$$|\Delta n|^2 = \Delta\delta^2 + \Delta\beta^2. \quad (2.23)$$

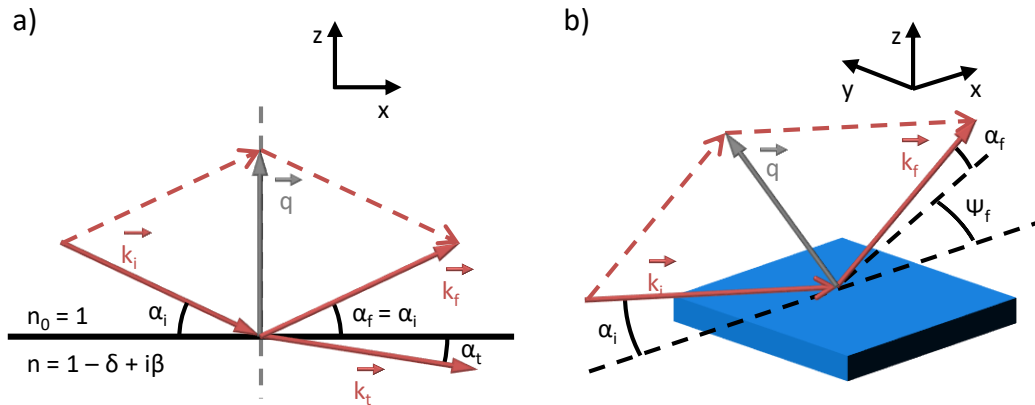


**Figure 2.15**

General definitions and geometries for specular and diffuse scattering. a) Specular reflection within the plane of the incident beam exhibits a momentum change only in  $z$ -direction. b) Diffuse or off-specular scattering leads to an additional momentum transfer in  $y$ -direction with an angle  $\Psi_f$ .

For small incident angles, total reflection occurs at or below the material-specific critical angle  $\alpha_c$  which can be approximated as<sup>[147,153]</sup>

$$\alpha_c \approx \sqrt{2\delta}. \quad (2.24)$$

$\alpha_c$  plays a crucial role in scattering. Yoneda first observed anomalous surface scattering from films probed under shallow angles due to the critical angle of the respective material.<sup>[154]</sup> Therefore, the region around  $\alpha_c$  of a material is called its Yoneda region and allows conclusions about material-specific structural features within blends of materials.

In principle, scattering can be further divided into specular and diffuse scattering. The most important geometrical parameters for both regimes are shown schematically in Figure 2.15 for an X-ray beam impinging the sample under a shallow angle. The incident X-ray beam  $\vec{k}_i$  hits the sample under a grazing incident angle  $\alpha_i$  towards the sample surface and is reflected ( $|\vec{k}_f|$ ) with an exit angle  $\alpha_f$  in the vertical direction. Specular reflection leads to an exiting beam with  $\alpha_f = \alpha_i$  in the  $xz$ -plane which is also referred to as the scattering plane. Diffuse or off-specular scattering also leads to a momentum transfer in the  $y$ -direction so that  $\vec{k}_f$  also possesses an angle  $\Psi_f$  in the  $xy$ -plane so that  $\alpha_f \neq \alpha_i$ .

### 2.4.2 X-Ray Reflectivity

The specular reflection can be used to probe the vertical film composition via a technique called X-ray reflectometry (XRR). Keeping both the incident beam and detector at equal angles ( $\alpha_f = \alpha_i$ ) within the scattering plane, only the specular scattering is detected. The out-of-plane angle is  $\Psi_f = 0$ . For elastic scattering, the modulus remains constant and is given as  $k = \frac{2\pi}{\lambda}$  and the scattering vector  $\vec{q}$  consists only of the  $q_z$  component

$$q_z = \frac{4\pi}{\lambda} \sin(\alpha_i). \quad (2.25)$$

Reflection occurs when the incident beam meets a change in refractive index, for example at interfaces between materials of different SLD. According to Snell's law, the angles  $\alpha_i$  of the incident beam and  $\alpha_t$  of the transmitted beam are connected via

$$\frac{\cos(\alpha_t)}{\cos(\alpha_i)} = \frac{n_0}{n_1}. \quad (2.26)$$

As the amplitude of the transmitted beam is connected to the Fresnel reflection  $r_F$  and transmission coefficient  $t_F$ , the reflectivity and transmission are defined by  $R_F = |r_F|^2$  and  $T_F = |t_F|^2$ .

The vertical structure of a sample can be modeled by theoretically placing the film between an infinite substrate and an infinite air layer. For the most simple film, based on one material of even density, reflection would occur only due to the two interfaces present in the sample, namely the interfaces of the film with the infinite substrate layer below the film and the infinite air layer above it. For modeling, the film is sliced into  $k$  layers of thickness  $d_k$ , refractive index  $n_k$ , and roughness  $\sigma_{rms,k}$ . Each layer has a certain ratio of reflection and transmission, from which an overall reflectivity of the layer stack can be calculated by using formalisms such as the Abeles matrix method or Paratt's recursive method to compute all contributions.<sup>[155–158]</sup> In practice, layers are not perfectly flat, but exhibit a certain surface roughness. The interface between layers can be expressed in terms of the root mean square (rms) roughness  $\sigma_{rms,j}$ , as calculated from the deviation from the mean height  $r_j$  for all considered sampling points  $N$  via

$$\sigma_{rms} = \sqrt{\frac{1}{N} \sum_{j=1}^N r_j^2}. \quad (2.27)$$

This roughness is taken into account by applying an exponential function to the Fresnel coefficient assuming a Gaussian distribution of heights.<sup>[159]</sup> Total reflection is observed for incident angles  $\alpha_i$  smaller than the critical angle  $\alpha_c$ . Above the critical angle of a respective material, some intensity will be lost due to transmission, which is visible in the critical edge in the reflectivity curve. The intensity decreases with  $q^{-4}$  at higher

angles (equivalent to higher  $q_z$  values). The so-called Kiessig-fringes visible in the reflectivity curve are oscillations related to the Film thickness  $d$  via<sup>[160]</sup>

$$d \approx \frac{2\pi}{\Delta q_z} \quad (2.28)$$

with  $\Delta q_z$  being the distance between neighboring maxima or minima. An increase in roughness will not only reduce the overall intensity but also dampen the Kiessig-fringes. From the modeled data, SLD values for all layers depending on the film depth can be determined. A higher roughness, porosity or intermixing of different materials leads to a smearing of SLD values between adjacent layers.

### 2.4.3 Grazing-Incidence Small-Angle X-ray Scattering

While XRR is based purely on specular reflection, diffuse scattering can be used to obtain even more structural information about a sample. Diffuse scattering methods are conventionally performed in transmission mode, which is not suitable for the very thin films investigated in the scope of this work due to the small probed scattering volume. To increase the scattering volume and thereby the statistical relevance, a shallow angle below  $1^\circ$  is chosen, resulting in a larger footprint of the beam on the sample. Additionally, by varying the incident angle  $\alpha_i$  the penetration depth can be adjusted to change the sensitivity of the measurement towards the surface or bulk.<sup>[161]</sup> For so-called grazing-incidence X-ray scattering (GIXS) experiments, the diffuse scattering is recorded by a 2D detector. GIXS methods offer the unique advantage of simultaneously probing lateral and vertical structures within the thin film. Depending on the given sample-to-detector distance (SDD) and detector and pixel size, the detector will resolve smaller or larger angles which can be translated to the scattering vector  $\vec{q}$  via<sup>[162]</sup>

$$\vec{q} = \begin{pmatrix} q_x \\ q_y \\ q_z \end{pmatrix} = \frac{2\pi}{\lambda} \begin{pmatrix} \cos(\alpha_f) \cos(\psi_f) - \cos(\alpha_i) \\ \cos(\alpha_f) \sin(\psi_f) \\ \sin(\alpha_f) + \sin(\alpha_i) \end{pmatrix}. \quad (2.29)$$

This work focuses on two GIXS methods, namely grazing-incidence small-angle X-ray scattering (GISAXS) and grazing-incidence wide-angle X-ray scattering (GIWAXS), which differ in the used SDD and thus also in the accessible scattering angles and  $q$ -range. GISAXS is discussed in the following and GIWAXS will be explained in the next section. For a more detailed discussion on these and similar X-ray scattering techniques, the reader is referred to the cited literature.<sup>[147,163-169]</sup>

Developed as a tool by Levine et al. in 1989 to specifically study the growth of thin films, GISAXS was first used to analyze soft matter films by Müller-Buschbaum et al. in 1997.<sup>[171]</sup> The method is used to investigate structural features on the mesoscale, such as the island growth in the deposition of gold layers (Chapter 5 and Chapter 6) or typical phase separation in organic films (Chapter 6 and Chapter 7). Placing the

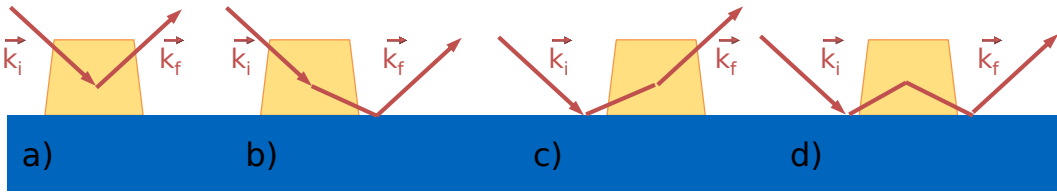


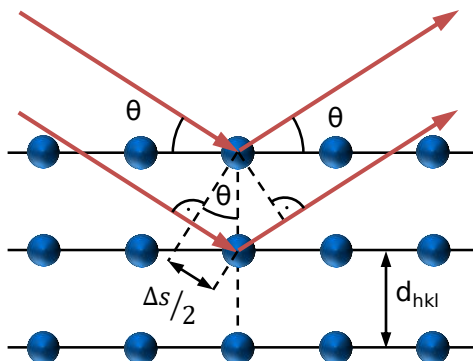
**Figure 2.16**

Contributions of different combinations of scattering and reflection events to the DWBA. Illustrated are the four simplest contributions, although more complex combinations of multiple reflection and scattering events are typically accounted for in simulations. The incoming beam  $\vec{k}_i$  may experience a) direct scattering to the outgoing wave  $\vec{k}_f$ , b) scattering with subsequent reflection at the substrate, c) reflection at the substrate with subsequent scattering, or d) reflections at the substrate before and after the scattering event.

detector at a larger SDD, small scattering angles and therefore  $q$ -values up to typically  $2 \text{ nm}^{-1} - 5 \text{ nm}^{-1}$  can be resolved, translating into real-space distances of around  $1 \text{ nm} - 100 \text{ nm}$ . In contrast to conventional small-angle X-ray scattering (SAXS) performed in transmission mode, scattering in GISAXS is further complicated by reflections at the sample and the substrate. To account for additional reflection events, the distorted-wave Born approximation (DWBA) is implemented into the scattering model as a first-order perturbation of the Born approximation.<sup>[172,173]</sup> The additional contributions are illustrated in Figure 2.16. The resulting complex 2D scattering pattern can be simulated using a range of analysis tools.<sup>[162,174-176]</sup> To reduce the computational time for data analysis, the 2D data can be reduced to line cuts by integration over a certain region of interest (ROI). Typically, horizontal line cuts are performed at the Yoneda position of a material of interest to obtain more information about lateral structures of this material within the film. This approach enables the use of the effective interface approximation (EIA) in which only lateral correlations in the film are considered, keeping  $q_z$  constant.<sup>[164,177]</sup> The scattering is influenced by the differential scattering cross-section of a certain area  $A$

$$\frac{d\sigma}{d\Omega}|_{diff} = \frac{A\pi^2}{\lambda^4} (1 - n^2)^2 |T_i|^2 |T_f|^2 P_{diff}(\vec{q}) \quad (2.30)$$

with the Fresnel transmission coefficients  $T_{i,f}$  for the incident and outgoing beam and the diffuse scattering factor  $P_{diff}(\vec{q})$  as a direct measure of the scattered intensity.<sup>[151,162]</sup> Horizontal intensity profiles can be modeled using a certain number  $N$  of scattering objects of a particular size, form, and spatial distribution. The size and form of an object are defined by the Fourier transform of its electron density distribution called form factor  $F(\vec{q})$ . A structure factor  $S(\vec{q})$  describes the spatial arrangement of the ob-

**Figure 2.17**

Bragg diffraction of X-rays (red) impinging a 2D lattice under an incident angle  $\Theta$ . The horizontal lattice planes are distanced by  $d_{hkl}$ . According to the Bragg condition, constructive interference occurs for path differences  $\Delta s$  equaling  $n\lambda$ .

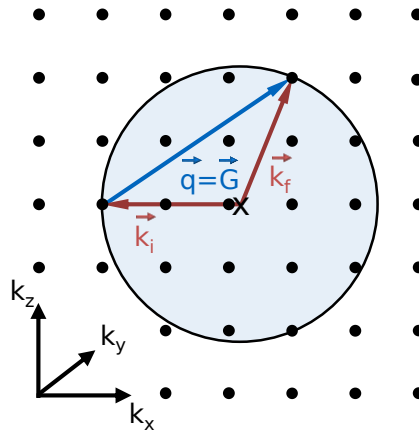
jects via an interference function.<sup>[178]</sup> Therefore, the diffuse scattering can be calculated via<sup>[153,164,179]</sup>

$$P(\vec{q}) \propto N |F(\vec{q})|^2 S(\vec{q}). \quad (2.31)$$

For the disordered, organic systems investigated in the present work,  $F(\vec{q})$  is assumed to be cylindrical to account for the rotational symmetry of the system and a 1D paracrystalline lattice is used as  $S(\vec{q})$  to induce a certain short-range order. Independent of the orientation, the lattice is, therefore, invariant towards rotation.<sup>[180]</sup> The model is based on several form factors with respective structure factors. The objects are assumed to scatter only with objects of the same type, but not with those of other forms and spatial distributions, as explained in detail in the thesis of Christoph Schaffer.<sup>[181]</sup> This assumption is implemented into the model in form of the local monodisperse approximation (LMA) or decoupling approximation (DA) with the final intensity calculated as the sum of intensities from each contributing form and structure factor.<sup>[162,182]</sup>

#### 2.4.4 Grazing-Incidence Wide-Angle X-ray Scattering

With a typical SDD of less than 1 m, GIWAXS is used to investigate the crystalline structure of a thin film, for example following the crystallization of gold clusters during sputter deposition (Chapter 5 and Chapter 6). The X-rays are scattered at different lattice planes ( $hkl$ ) with a distance  $d_{hkl}$ . The resulting difference in the beam path length is  $\Delta s$ , as illustrated in Figure 2.17. The scattering takes place due to periodic changes in the electron density cloud around the lattice of atoms, as discussed for the atomic scattering factor in Equation 2.17.<sup>[148]</sup> Depending on the incident angle  $\theta$

**Figure 2.18**

Ewald sphere illustrating off-specular scattering for X-rays (red arrows) impinging a 2D lattice with a wave vector  $\vec{k}_i$ . According to the Laue condition, constructive interference is observed for intersections of the reciprocal lattice with the Ewald sphere around  $x$  with a radius of  $|\vec{k}_i|$ .

and the orientation of the lattice planes to the beam, the scattered X-rays experience constructive or destructive interference. According to the Bragg condition,

$$n\lambda = 2d_{hkl}\sin(\theta) \quad (2.32)$$

has to be fulfilled for constructive interference under specular conditions. However, for off-specular scattering,  $\vec{q}$  does not only have a  $z$ -component and each scattering point is the origin of an elementary wave (Huygens' principle). Therefore, constructive interference only occurs if the momentum transfer is equal to a reciprocal lattice vector and fulfills the Laue condition

$$\vec{q} \equiv \vec{G}_{hkl} = \vec{k}_f - \vec{k}_i. \quad (2.33)$$

For elastic scattering, the energy is conserved so that  $|\vec{k}_i| = |\vec{k}_f|$ . An Ewald sphere illustrates this phenomenon, as shown in Figure 2.18. Diffraction can only be observed if a reciprocal lattice point intersects the Ewald sphere's surface, as only there the momentum is conserved. For any given incident wave  $\vec{k}_i$ , the scattered wave  $\vec{k}_f$  will contain contributions of  $k_x$  or  $k_y$  in addition to the  $k_z$ -component, which cannot be neglected, as the small-angle approximation does not hold for GIWAXS. Thus, the scattering in the specular plane ( $k_y = 0$ ) has contributions from  $k_z$  as well as  $k_x$  and the information cannot be decoupled from each other. As 2D detectors represent a projection of the allowed Bragg reflexes of the Ewald sphere, a certain range of scattering features cannot be accessed.

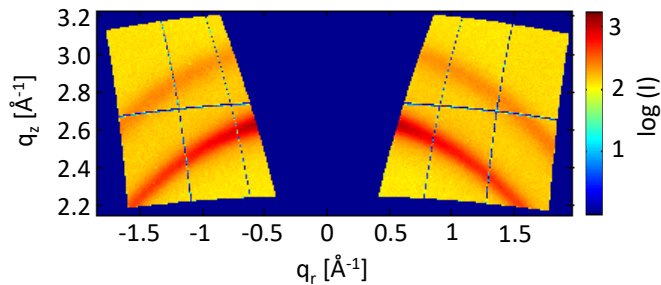


**Figure 2.19**

Reshaped 2D GIWAXS data of a thin gold film on a polymer substrate. Apart from the clear intensity rings arising due to the gold crystal structure (explained in more detail in Chapter 5), the so-called missing wedge is a prominent feature.

This area is also called missing wedge and illustrated in Figure 2.19 with reshaped 2D GIWAXS data of a thin gold film on a polymer substrate, as explained in more detail in Chapter 5.

Before data analysis, several corrections have to be applied. The corrections and their effects on the scattering pattern are described in detail in the literature, especially in the work of Jiang in 2015, and are, therefore, just listed shortly in the following.<sup>[166,167,169]</sup>

- The flat field correction addresses the variation in sensitivity of different pixels and is often already implemented into the measurement routine. The dark field correction additionally excludes dead or hot pixels.
- Depending on the exact structure of the film and experimental setup, the photons are scattered at different angles. This leads not only to a difference in pathways between the scattering center and the detector area but also to the scattered photons hitting the detector pixels under different angles. Both effects are taken into account by so-called efficiency corrections.
- Polarization corrections implement the linear polarization of synchrotron radiation to compensate for the reduced intensities for small scattering angles.
- Pixels on a flat detector are of the same size but cover different angles. This purely geometrical effect is corrected via the solid angle correction.
- Further geometric corrections may have to be addressed in case of special experimental setups such as a tilting of the detector.

The scattering pattern yields information about several structural parameters. As described above, the lattice parameters translate into peak positions. The peak intensity corresponds to the amount of crystallites in comparison to non-crystalline material. Additionally, the peak width is affected by the size of the crystallites, with larger crystals leading to sharper peaks. Using the Scherrer equation, the full width at half

maximum (FWHM)  $\Delta(2\theta_{hkl})$  of a diffraction peak at a certain diffraction angle  $2\theta_{hkl}$  gives the lower limit of the crystallite size  $D_{hkl}$

$$D_{hkl} = \frac{K\lambda}{\Delta(2\theta_{hkl})\cos(\theta_{hkl})}, \quad (2.34)$$

with the Scherrer constant  $K$ . The constant has a value of around 0.9 as derived from the original publication<sup>[165]</sup>

$$K = 2 \left( \frac{2\ln(2)}{\pi} \right)^{\frac{1}{2}} \approx 0.93. \quad (2.35)$$

As GIWAXS data are analyzed in reciprocal space, the formula becomes

$$\Delta q_{hkl} = \frac{4\pi}{\lambda} \left[ \sin \left( \frac{2\theta_{hkl} + \frac{\Delta(2\theta_{hkl})}{2}}{2} \right) - \sin \left( \frac{2\theta_{hkl} - \frac{\Delta(2\theta_{hkl})}{2}}{2} \right) \right] \quad (2.36)$$

$$= \frac{4\pi}{\lambda} 2\cos(\theta_{hkl}) \sin \left( \frac{\Delta(2\theta_{hkl})}{4} \right). \quad (2.37)$$

In most cases, the approximation  $\sin(\theta) \approx \theta$  is valid, as the FWHM is in general rather small. Thus, the simplified Scherrer equation for reciprocal space can be written as

$$D_{hkl} = \frac{2\pi K}{\Delta q_{hkl}}. \quad (2.38)$$

It is important to note that the experimental setup and size distributions in the crystallites will induce additional peak broadening. The Scherrer equation can thus only give an estimate of the lower limit of the crystallite size.



# CHAPTER 3

## Sample Preparation

In the following chapter, the materials and processing routines used for the samples investigated within this thesis are described. Details for each experiment are noted at the beginning of the respective chapter. Section 3.1 introduces the physical and chemical properties as well as important technical details of the mainly used materials and solvents. The preparation of thin film samples using various techniques is described in more detail in Section 3.2, including additional steps such as the required substrate cleaning. Organic photovoltaic (OPV) devices were fabricated based on the standard procedure discussed in Section 3.3. This section discusses the required special patterning and cleaning routine for the used substrates as well as the deposition of blocking layers and back electrodes.

### 3.1 Materials

The materials used in this thesis can be divided into three groups. Section 3.1.1 discusses the photoactive materials mainly investigated in this thesis as well as other conductive or blocking materials applied in solar cell devices. The used solvents are given in Section 3.1.2, while the required different substrate materials are introduced in Section 3.1.3

### 3.1.1 Functional Materials

The following section presents the functional materials used for the present thesis. A focus is set on the investigated electron donors, the polymers PTB7 and PTB7-Th. They are combined in the photoactive layer with their counterpart and electron acceptor, the fullerene derivative PC<sub>71</sub>BM. PEDOT:PSS acts as an electron blocking layer. The materials' chemical structures are illustrated in Figure 3.1.

#### PTB7

PTB7<sup>1</sup> is a photoactive polymer that has been commonly applied as an electron donor for OPV in the last years. It serves as a well-known example for a whole range of low-bandgap, hole-conducting polymers based on similar structural units. The polymer is based on two alternating functional units, the electron donor thienothiophene (TT) and the acceptor benzodithiophene (BDT). PTB7 exhibits a hole mobility in the range of  $1 \times 10^{-3} \text{ cm}^2 \text{ V}^{-1} \text{ s}^{-1}$  and a bandgap of 1.85 eV, as derived from its lowest unoccupied molecular orbital (LUMO) of  $-3.3 \text{ eV}$  and highest occupied molecular orbital (HOMO) of  $-5.15 \text{ eV}$ .<sup>[183–185]</sup> The PTB7 investigated in the present work is purchased from 1-Material Inc., Canada.

#### PTB7-Th

PTB7-Th<sup>2</sup> – also known as PBDTTT-EFT or PCE10 – is a sister polymer to PTB7, derived from the latter by substitution of oxygen in the side-chains of the BDT units with thiophene rings. Its LUMO of  $-3.64 \text{ eV}$  and HOMO of  $-5.22 \text{ eV}$  result in a bandgap of around 1.58 eV.<sup>[185–188]</sup> In comparison to PTB7, PTB7-Th exhibits a fivefold higher electron mobility.<sup>[185]</sup> The PTB7-Th investigated for this work is purchased from 1-Material Inc., Canada.

#### PC<sub>71</sub>BM

Derivatives of the buckminsterfullerenes have been widely applied as electron accepting photoactive materials in organic photovoltaics. For the investigated polymers PTB7 and PTB7-Th, PC<sub>71</sub>BM<sup>3</sup> is the most commonly used fullerene-based acceptor material. PC<sub>71</sub>BM exhibits an electronic bandgap of 2.0 eV, resulting from the difference in its LUMO and HOMO level at  $-3.9 \text{ eV}$  and at  $-5.9 \text{ eV}$ , respectively.<sup>[189,190]</sup> Its comparably high electron mobility of around  $1 \times 10^{-3} \text{ cm}^2 \text{ V}^{-1} \text{ s}^{-1}$  originates from the large number of delocalized  $\pi$ -orbitals.<sup>[183,191]</sup> PC<sub>71</sub>BM is purchased from 1-Material Inc., Canada.

<sup>1</sup>PTB7: poly[[4,8-bis[(2-ethylhexyl)oxy]benzo[1,2-b:4,5-b']dithiophene-2,6-diyl][3-fluoro-2-[(2-ethylhexyl)carbonyl]thieno[3,4-b]thiophenediyl]]

<sup>2</sup>PTB7-Th: poly[[4,8-bis(5-ethylhexylthienyl)benzo[1,2-b:4,5-b']dithiophene-2,6-diyl][3-fluoro-2-[(2-ethylhexyl)carbonyl]thieno[3,4-b]thiophenediyl]]

<sup>3</sup>PC<sub>71</sub>BM: [6,6]-phenyl-C<sub>71</sub> butyric acid methyl ester

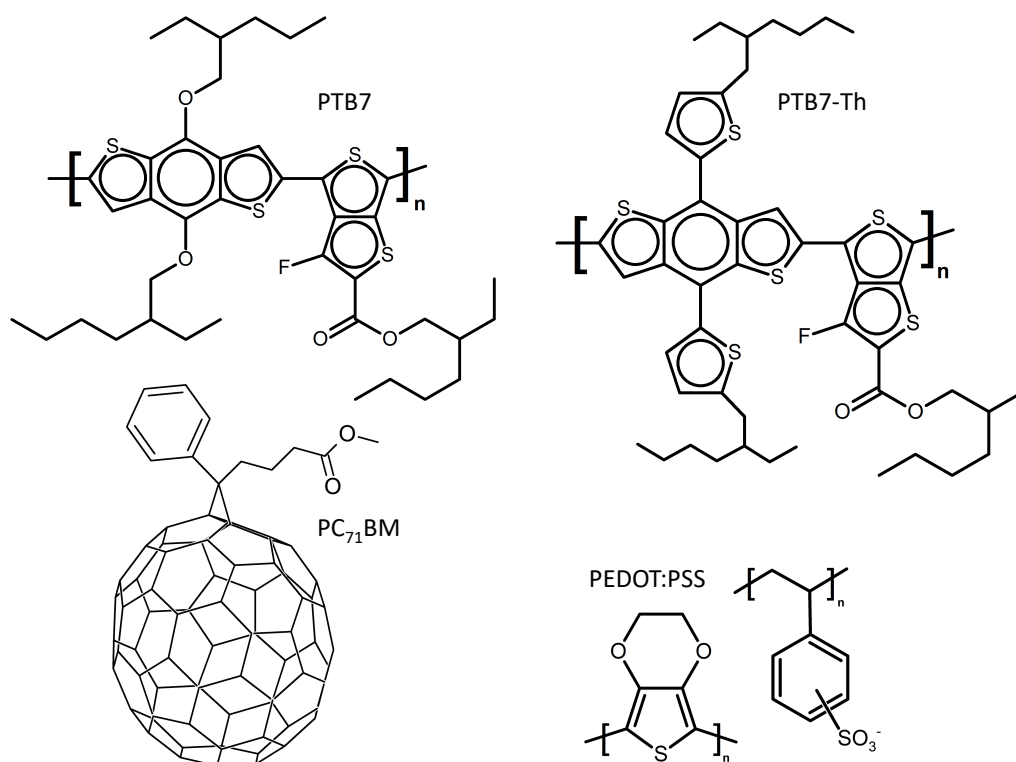


**Figure 3.1**  
Chemical structures of the investigated materials.

### PEDOT:PSS

In different fields of organic electronics, the polymer mixture PEDOT:PSS is used as versatile conductive and transparent material for electrodes or blocking layers. It consists of two functional polymers: the hydrophobic, hole-conducting poly(3,4-ethylene dioxythiophene) (PEDOT) and the water-soluble, insulating poly(styrene sulfonate) (PSS). PEDOT:PSS is nearly transparent in the visible wavelength region and therefore a suitable electron blocking layer (EBL) for solar cells prepared in conventional architecture. A ready-made aqueous solution of PEDOT:PSS (PEDOT:PSS ratio 1:6, 1.3 – 1.7 wt.%, AI 4083, Heraeus Clevios<sup>TM</sup>) is provided by Ossila Ltd, UK and stored in the refrigerator at 4 °C.

### 3.1.2 Solvents

The solvents and acids used for the preparation of thin-films and devices are described in the following. Active layer materials are typically dissolved in the host solvents chlorobenzene (CB) or ortho-dichlorobenzene (o-DCB). Solvents such as 1,8-diiodooctane (DIO) and methanol are used to enhance certain properties of the photoactive

films. Deionized (DI) water and certain acids and the respective solvents are used for cleaning purposes.

### Deionized Water

Clean tap water has to be further cleaned and deionized using the high-purity water system Purelab Chorus 1 (Veolia). The thereby purified water has a resistance of above 18.2 M $\Omega$  cm and can subsequently be used for sample preparation.

### Chlorobenzene

For typical thin films of the active materials discussed in this work, the chlorinated aromatic compounds CB and o-DCB are used as solvents. CB (C<sub>6</sub>H<sub>5</sub>Cl) has a boiling point of 131 °C and a density of 1.11 g mL<sup>-1</sup> at 25 °C. It is purchased from Carl Roth GmbH + Co. KG with a purity of  $\geq 99.5\%$ .

### ortho-Dichlorobenzene

In comparison to the monochlorinated CB, o-DCB (C<sub>6</sub>H<sub>4</sub>Cl<sub>2</sub>) shows two adjacent chlorine substituents, leading to a higher boiling point of 180 °C and density of 1.31 g mL<sup>-1</sup> at 25 °C. It is purchased from Carl Roth GmbH + Co. KG with a purity of  $\geq 98\%$ .

### 1,8-Diiodooctane

DIO (I(CH<sub>2</sub>)<sub>8</sub>I) is commonly used as a processing solvent additive to increase the performance of OPV devices due to its selective solubility of fullerene derivatives.<sup>[192]</sup> It exhibits a relatively high boiling point of 332 °C and density of 1.84 g mL<sup>-1</sup> at 25 °C. DIO is purchased from Sigma-Aldrich and added to the respective sample solutions in small quantities.

### 3.1.3 Substrate Types

Different substrates have to be used for the sample preparation depending on the chosen investigation technique. For this work, three substrate types are mostly used, namely pristine or indium-doped tin oxide (ITO)-covered glass substrates and silicon wafers. Most optical measurements are performed on pristine glass substrates, except when stated otherwise. Devices are prepared on patterned ITO-covered glass substrates. X-ray and Fourier-transform infrared spectroscopy (FTIR) investigations are usually performed on samples deposited on silicon wafers, except when stated otherwise.

### Glass Substrates

Initial tests for preparation routines and most optical measurements are performed on simple glass substrates due to their optical transparency and electrically insulating properties. Microscopy glass slides with optical quality ( $76 \times 26 \text{ mm}^2$ , 1 mm thickness, Carl Roth GmbH + Co. KG) are cut to the required substrate form and size using a diamond cutter. The substrates are cleaned via a hot acid bath, as described in more detail in Section 3.2.1.

### Silicon Substrates

Most X-ray and FTIR measurements are performed on substrates prepared from silicon wafers. The p-doped, round wafers (diameter 100 mm, thickness 0.5 mm, Silicon Materials (Kaufering, Germany)) exhibit a resistivity of  $10 \Omega \text{ cm} - 20 \Omega \text{ cm}$ . Their polished side is aligned with the  $\langle 100 \rangle$  crystal direction, achieving a very low surface roughness of  $R_q < 0.5 \text{ nm}$ . Substrates of the desired size and form are cut along the crystal directions using a diamond cutter. Especially for X-ray measurements using grazing incidence geometry, particular care has to be taken to avoid additional scattering by the edges. For this purpose the substrates are partially cut with the diamond cutter on their non-polished side and placed over a sharp edge of an aluminum plate, before breaking them along the crystal planes, creating well-defined, sharp edges. Analogously to the glass substrates, the silicon substrates are cleaned via a hot acid bath (see Section 3.2.1).

### Indium-doped Tin Oxide (ITO) Substrates

Solar cell devices are prepared on ITO-covered glass substrates ( $25 \cdot 25 \cdot 1.1 \text{ mm}^3$ , ITOSOL30, Solems (Palaiseau, France)). The substrates are bought covered with a conductive ITO layer of 100 nm thickness, which provides a sheet resistance of  $25 \Omega \square^{-1} - 35 \Omega \square^{-1}$ . In contrast to glass and silicon substrates, the ITO substrates have to be cleaned using a different, less aggressive routine to avoid destruction of the ITO layer (see subsection 3.3.1).

## 3.2 Thin Film Preparation

For this thesis, most investigations are performed on thin films of the respective materials. To create homogeneous and reproducible films, a fabrication routine has to be established. The individual steps of this routine are explained in the following.

### 3.2.1 Substrate Cleaning

Prior to thin-film deposition, the glass and Si substrates are cleaned using a hot acid bath. This procedure is based on a standard ionic silicon wafer cleaning protocol common in the semiconductor industry, using a modified piranha bath.<sup>[193]</sup> A clean beaker is placed inside a water bath in a larger beaker on a heating plate with a magnetic stirrer. Deionized water ( $\text{H}_2\text{O}$ ), hydrogen peroxide ( $\text{H}_2\text{O}_2$ , 30%), and concentrated sulfuric acid (sulfuric acid ( $\text{H}_2\text{SO}_4$ ), 95% – 98%) are subsequently and carefully filled into the beaker to avoid overheating due to the exothermic reaction taking place. The used amounts are listed in Table 3.1. The solution is covered with a watch glass and heated to 80 °C. For the bath, custom-built acid-resistant polytetrafluoroethylene (PTFE) holders are used to separate the substrates from each other and the beaker walls. After washing off potential contaminants, the holders with the substrates are inserted into the hot acid bath and left there for 15 min. The sample holder is subsequently rinsed excessively, before taking out individual substrates and rinsing them again. Residual water is dried under a continuous nitrogen flow. The hot acid treatment creates a hydrophobic  $\text{SiO}_x$  surface layer on the substrates. If hydrophilicity is required (particularly for PEDOT:PSS layers), the substrates can be subjected to additional oxygen plasma treatment, as detailed in subsection 3.3.1.

**Table 3.1**

Composition of the hot acid bath for substrate cleaning.

| chemical                | amount [ml] |
|-------------------------|-------------|
| DI $\text{H}_2\text{O}$ | 54          |
| $\text{H}_2\text{O}_2$  | 84          |
| $\text{H}_2\text{SO}_4$ | 198         |

### 3.2.2 Solution Preparation

Most samples discussed for this thesis are thin films of the pristine active layer materials or their blends. As the materials are sensitive to oxygen and water, especially under light exposure, all following preparation steps are usually performed under inert nitrogen atmosphere in a glovebox (M. Braun Inertgas-Systeme GmbH). The atmosphere is continuously filtered to eliminate oxygen and water that may be introduced via materials, solvents, or tools. The respective materials are dissolved in either CB or o-DCB with concentrations in the range of  $5 \text{ mg mL}^{-1}$  –  $30 \text{ mg mL}^{-1}$ , depending on the required viscosity of the solution. Detailed values are mentioned in the related experimental sections. Before the solution preparation, the required glass vials are rinsed with the respective solvent and dried under oil-free nitrogen flow. Using an analytical microbalance (Sartorius AG), the desired amount of material is weighed

into a cleaned glass vial. After measuring the exact mass of the weighed material, the corresponding amount of solvent is calculated and added using a microliter pipette to create a solution of the desired concentration. Usually, the solutions are prepared one day in advance and constantly stirred at 60 °C in the glass vials sealed with Parafilm™ to allow a complete dissolution. As the polymers exhibit a significantly lower solubility as compared to the fullerene derivatives, the fabrication of blend solutions usually consists of two steps: first dissolving only the polymer and letting it stir for a certain amount of time, before adding the fullerene derivative and stirring the blend solution for another few hours. Details are described in the related experimental sections.

### 3.2.3 Film Deposition

The sample films are prepared via depositing the respective solution on a substrate using either spin-casting or drop-casting, as detailed in the following. For investigations of polymer-metal interfaces, metal layers are also deposited via a sputtering process, as explained in Section 2.3 and Section 5.2.

#### Spin Coating

Most samples investigated within this thesis are prepared using spin-casting, as this technique generates homogeneous thin films with high control over the thickness in the sub- $\mu\text{m}$  range. The spin coater has a substrate holder rotating in a well-defined, controllable manner to create an environment, in which the volatile solvents can evaporate, leaving a well-defined even film behind. Substrates can be fixed by applying vacuum or by placing them in a respective mold. For this work, different instruments were used, as detailed in the respective sections. Several parameters such as the rotational speed (in revolutions per minute (rpm)), acceleration rate, and total rotation time can be adjusted as needed. The sample solution is quickly dispersed on a cleaned substrate until it covers it completely (80  $\mu\text{L}$  – 200  $\mu\text{L}$ , depending on the viscosity and substrate size), before immediately starting the spin-coating process. Initially, excess solution is removed from the revolving substrate. Subsequently, the solvent starts to evaporate, leaving a film of defined thickness  $d$  behind.<sup>[194]</sup> The thickness  $d$  depends on several parameters, namely the molecular mass  $M_W$ , the initial concentration  $c_0$ , and the angular velocity  $\omega$ . It can be calculated using the Schubert equation<sup>[195]</sup>

$$d = C c_0 \omega^{-1/2} M_w^{1/4}, \quad (3.1)$$

taking into account a scaling factor  $C$ , which includes environmental parameters such as humidity, temperature, and the spin-coater type. Within certain limits, a linear correlation between the concentration of the solution and the resulting film thickness can be assumed, when neglecting viscosity effects.<sup>[195]</sup> With higher concentrations, however, viscosity plays a more dominant role, so that the parameters have to be carefully

investigated to find optimal values for the desired film thickness. Typical parameters for spin-casting active layer films involve rotation speeds of 1000 rpm – 2000 rpm with an initial acceleration time of ~6 s and total rotation time of 20 s – 60 s, with the standard values listed in Table 3.2. The thereby prepared films are left to dry overnight before they can be investigated.

**Table 3.2**

Typical spin-coating parameters used for the functional layers.

| <b>material/layer</b> | $\omega$ [rpm] | <b>time</b> [s] |
|-----------------------|----------------|-----------------|
| PEDOT:PSS             | 3000           | 60              |
| active layer          | 1000           | 40              |
| methanol treatment    | 1000           | 120             |

### Drop Casting

To generate high-resolution FTIR data, drop-casting is preferred over spin-casting. An aluminum block is aligned horizontally inside the glovebox, before placing a clean silicon substrate on it. A droplet of the respective solution (30  $\mu\text{L}$ ) is dropped on the substrate and left to dry for one day. This creates a thicker film in the range of several  $\mu\text{m}$  with a thickness gradient, which enhances the absorption of infrared light (IR) light and decreases interference effects, as described in more detail in Section 4.1.2.

## 3.3 OPV Device Assembly

The present thesis addresses the chemical and structural characteristics of photoactive materials typically used in OPV devices. While the optimization of devices is not in the focus of this work, exemplary devices are built to investigate their behavior with regard to the above-mentioned chemical and structural changes upon operation. The following section gives a detailed fabrication routine for the OPV devices examined for the present thesis. The patterning and cleaning of the used substrates are discussed in Section 3.3.1. Section 3.3.2 deals with the preparation of the PEDOT:PSS hole blocking layer (HBL), while Section 3.3.3 describes the solution preparation for the active layer and its deposition via spin casting. The metal back electrode is deposited, as explained in Section 3.3.4. The complete fabrication routine is illustrated in figure Figure 3.2.

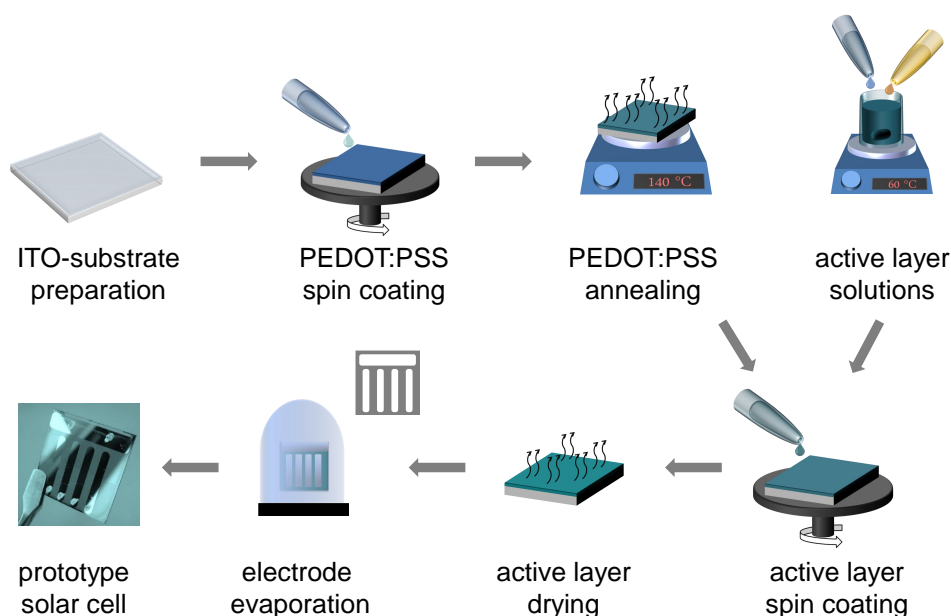


**Figure 3.2**

A typical OPV device assembly procedure consists of several steps. The ITO-coated glass substrate is partly etched, cleaned, and treated with oxygen plasma. The electron blocking layer based on PEDOT:PSS is deposited via spin coating and annealed via heating. For the photoactive layer, a solution of PTB7-Th and PC<sub>71</sub>BM is spin-cast onto the PEDOT:PSS-coated substrate and left to dry overnight. Thermal evaporation is performed to deposit a thin Al layer as the back electrode to create a functional OPV device. A shadow mask (illustrated in the inset) is used to form the desired electrode pattern.

### 3.3.1 Substrate Preparation

As explained in Section 2.2, OPV devices are based on a photoactive layer – usually in combination with other functional layers – stacked between two electrodes. At least one of those needs to be partly transparent to make the photoactive layer accessible for incoming photons. For standard geometry solar cells also fabricated for the present thesis, ITO-covered glass substrates are commonly used as electrodes. The ready-made substrates have to be patterned, cleaned, and treated with oxygen plasma before depositing further layers of the OPV device stack.

#### Electrode patterning

To avoid shortcuts from the metal back electrodes through the organic layers to the ITO electrode during operation, the latter has to be partially removed from the glass substrate. Typically, the middle of a substrate is covered with adhesive tape (Tesafilm<sup>®</sup>, 10 mm width), leaving out regions on two sides for the etching process. The unpro-

tected regions are etched using a combination of Zn powder and a diluted hydrochloric acid (HCl) solution, with Zn acting as a catalyst for the reaction. The HCl solution is prepared by mixing concentrated HCl (37%) with DI H<sub>2</sub>O in a volume ratio of 1:1. The Zn powder is distributed on the unprotected area, before dropping a diluted HCl solution onto it using a pipette, which starts the reaction. Using a cotton swab, the reaction products are wiped off mechanically. Potential residues are rinsed off repeatedly using deionized water, before removing the adhesive tape. The substrates are further cleaned from potential adhesive residues using an Alconox<sup>®</sup> detergent solution (16 g L<sup>-1</sup>) and wiped off, before rinsing them again with deionized water.

### Organic Cleaning

The patterned ITO substrates have to be further cleaned before depositing the functional organic layers on top. As the harsh acid cleaning discussed for pristine glass substrates would etch the ITO layer, a gentler cleaning protocol is chosen. The process consists of several cleaning steps with solvents of decreasing polarity to address different potential contaminants, namely Alconox<sup>®</sup> detergent solution (16 g L<sup>-1</sup>), DI water, ethanol, acetone, and isopropanol. The substrates are placed in a custom-built acid-resistant PTFE holder. For each step of the cleaning process, the holder and substrates are first rinsed and then placed in a beaker filled with the respective solution or solvent. The beaker is placed in an ultrasonic (US) bath (Badelin SONOREX RK100H) for 10 minutes, before rinsing the holder and substrates again and turning to the next solvent. After the final rinse with isopropanol, the substrates are dried under nitrogen flow.

### Oxygen plasma

The clean substrate surface can be further functionalized using an oxygen plasma, thereby simultaneously removing all organic traces and enhancing the surface hydrophilicity. The latter will increase the surface wetting needed for the deposition of the water-based PEDOT:PSS solution. The plasma treatment is performed using a Nano Plasma Cleaner (Diener Electronic). The samples are placed in the vacuum chamber which is first evacuated to around 0.2 mbar to remove contaminants from the air. Afterward, the chamber is flooded with oxygen with a working pressure of 0.4 mbar. The oxygen plasma is created by applying a power of ~250 W with a frequency of 40 kHz for 10 min. Driven by the emitted ultraviolet (UV) radiation, organic compounds react with the produced oxygen radicals. After extracting the resulting reaction products by applying a vacuum, the chamber is refilled with ambient air.

### 3.3.2 PEDOT:PSS Layer

PEDOT:PSS is a polymer mixture typically used as a hole transport layer (HTL)/EBL between the transparent electrode and the active layer to define the current direction of the device. The polymer mixture is purchased as a ready-made aqueous solution. However, as the polymers tend to form agglomerates, the mixture has to be further treated before its application. The PEDOT:PSS stock solution is filled in a clean glass vial placed into an ultrasonic (US) bath for 15 min to break up agglomerates. Residual agglomerates are subsequently removed via filtering the solution through a polyvinylidene fluoride (PVDF) filter with a pore size of 0.45  $\mu\text{m}$  (Altmann Analytik) into a clean glass vial. The filtered PEDOT:PSS solution is then spin-cast onto the cleaned ITO substrates with a rotational speed of 3000 rpm for 60 s, resulting in a film thickness of about 40 nm (Delta 6 RC TT spin coater, Süß MicroTec Lithography GmbH). To remove the remaining water and optimize the film structure, the samples are thermally annealed for 10 min on a heating plate. For this thermal treatment, a copper block is attached to an RCT basic heating plate (IKA<sup>®</sup>) and heated to 140 °C. After the annealing step, the samples are placed on a cool metal plate, before transferring them into the glovebox for the next preparation steps.

### 3.3.3 Active Layer

Based on literature reports for optimized performance values, the devices investigated for this work focus on a blend of PTB7-Th and PC<sub>71</sub>BM in o-DCB with a weight ratio of 1:1.5 and total concentration of 35 mg mL<sup>-1</sup>.<sup>[196–198]</sup> As mentioned in Section 3.2.2 and discussed in further detail in Chapter 7, the photoactive materials are sensitive to light in combination with ambient air, so that all steps involving them have to be performed under inert nitrogen atmosphere in a glovebox. A small amount of solvent additive DIO is added to the solvent o-DCB (3%), before dissolving PTB7-Th with a concentration of 14 mg mL<sup>-1</sup> and stirring the mixture for 2 h at 70 °C. Subsequently, the solution is added to a corresponding amount of PC<sub>71</sub>BM (21 mg mL<sup>-1</sup>) to achieve the total concentration of 35 mg mL<sup>-1</sup> and stirred overnight at 70 °C. The solution is now ready for deposition via spin-coating, as described in subsection 3.2.3, using a rotation speed of 1000 rpm for 40 s, resulting in a film thickness of about 100 nm – 120 nm. After spin-coating, the samples are left to dry for one day, before depositing the electrode material.

### 3.3.4 Electrode Deposition

To complete the device and measure its performance, back electrodes are applied on top of the active layer. As they are on the backside of the layer stack, there is no need for transparency, so that metals are typically preferred due to their outstanding electrical conductivity. For the devices investigated for the present thesis, aluminum (ChemPUR,

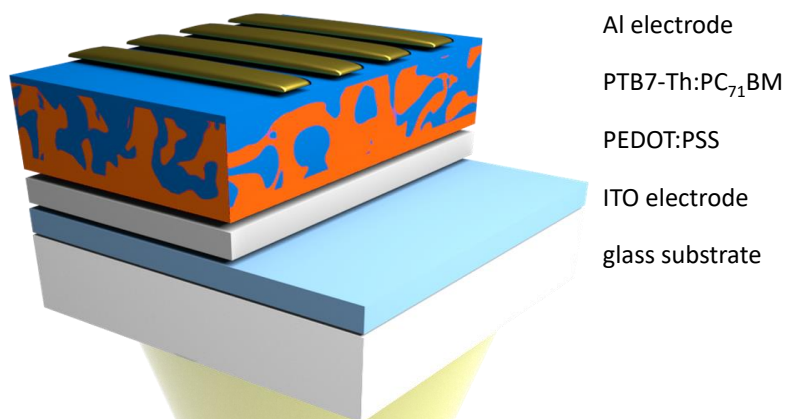


**Figure 3.3**

Schematic OPV device layer stack showing from bottom to top: the transparent glass substrate, transparent ITO electrode, PEDOT:PSS electron blocking layer, photoactive layer based on PTB7-Th:PC<sub>71</sub>BM, and aluminium back electrode.

99.99 % purity) is evaporated and applied on top of the sample via physical vapor deposition. A shadow mask (illustrated in the inset of Figure 3.2) is used to define the size, position, and form of the desired electrodes. For the deposition process, the samples are placed upside down on the shadow mask in a custom-built setup (implemented by Dr. Robert P. Meier<sup>[199]</sup>). About 60 mg – 80 mg of aluminum is placed in a tungsten boat (BD482000-T, Leybold Oerlikon) below the mask. The setup is evacuated to a working pressure of 1 mbar to  $5 \times 10^{-5}$  mbar. Using a high current of ~90 A (~180 A), the aluminum evaporates and is deposited on the sample, creating a film with a thickness of ~100 nm for a functional device (see Figure 3.3). After venting the chamber, the devices can be measured immediately.

# CHAPTER 4

## Sample Characterization

A main focus of the present work lies on the connection of functionality with structural parameters which can be investigated in real or reciprocal space. The following chapter introduces the characterization techniques used to investigate the physical and chemical properties of the samples. Spectroscopy and electrical characterization techniques are discussed in Section 4.1. The structural investigation is performed in real space using different microscopy methods (Section 4.2) and in reciprocal space using X-ray scattering techniques (Section 4.3). Aside from the general working principles, the used instruments and respective data analysis protocols are described.

### 4.1 Spectroscopic and Electrical Characterization

Depending on its energy, electromagnetic radiation interacts in different ways with materials, which can be used to characterize samples due to their behavior under illumination. One important measure for the photoactive functionality of the investigated samples is their light absorption behavior, which is measured using ultraviolet/visible (UV/vis) spectroscopy and discussed in Section 4.1.1. This absorption is greatly influenced by the respective chemical structure of the materials, which can be probed using Fourier-transform infrared (FTIR) spectroscopy (see Section 4.1.2). The materials are also implemented into exemplary organic photovoltaic (OPV) devices to investigate their stability during operation, as detailed in Section 4.1.3.

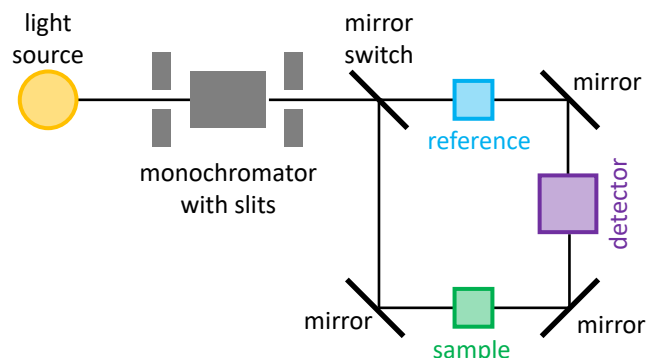


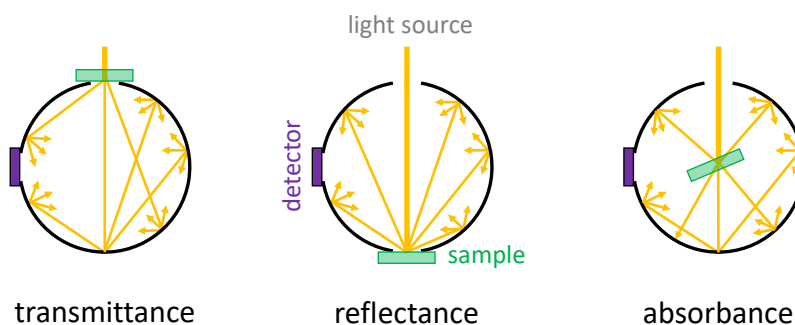
**Figure 4.1**

Schematic of the optical paths within the UV-vis spectrometer. A light source provides light which is focused by a slit, before reaching the monochromator that selects a desired wavelength. Passing a second slit, the monochromatic light is split into two paths guided via mirrors through the reference (blue) or the sample (green), before being guided to the photodetector (purple). For clarity, not all optics are illustrated, which additionally filter, collimate and focus the light.

### 4.1.1 UV-Vis Spectroscopy

As discussed in more detail in Section 2.2, solar cells are inherently based on light-absorbing materials to transfer the photon energy into electrical energy. With ultraviolet/visible (UV/vis) spectroscopy, key optical characteristics such as wavelength-dependent absorption or transmission of samples can be probed. From the onset of absorption, the respective optical bandgap can be determined. Shifts in absorbance maxima give information about the chemical structure and the inter- and intramolecular ordering of the investigated materials. Figure 4.1 schematically depicts the optical paths within a UV/vis spectrometer. For the light source, two different lamps are used to provide a wavelength range of around  $\lambda \approx 190 \text{ nm} - 900 \text{ nm}$ : a tungsten halogen lamp for the near-infrared to the visible region and a deuterium lamp for the ultraviolet (UV) region – switching the light source at around 320 nm. The spectra are recorded with a scanning speed set to  $266 \text{ nm min}^{-1}$ . The light is filtered and collimated (not shown) as well as focused via a slit (2 mm width) on the monochromator which selects the desired wavelength. After passing a further focusing slit (1 mm width), the monochromatic light is then split into two paths and guided to the sample (green) or used as reference (blue). Depending on the exact experiment, the transmitted and/or reflected light is then guided to the photodetector, which compares its intensity  $I$  to the initial intensity  $I_0$ .

Measurements are typically performed on thin films on quartz glass substrates using a Lambda 650 S spectrometer (PerkinElmer, Germany). The spectrometer offers a so-called integrating sphere (Spectralon R highly reflective 150 mm spherical cham-

**Figure 4.2**

Schematic of the integrating sphere used for UV-vis spectroscopy. Transmittance is measured by placing the sample in front of the entrance of the sphere. For reflectance measurements, the sample is placed in front of a blackened holder opposite the entrance. Placing the sample on a sample holder within the integrating sphere, the absorbance can be determined.

ber) that collects all scattered light. To enable the selective measurement of either transmission, reflection, or absorption, the sample can be placed at different positions within or in front of the integrating sphere, as illustrated in Figure 4.2. The integrating sphere is coated with a highly reflective material to direct light from all different angles to the detector. Transmission-only measurements are achieved by placing the sample in front of the sphere and capturing all transmitted light but not absorbed or reflected radiation. Absorption is measured using a sample holder placed within the sphere to acquire all transmitted, scattered, and reflected light. The absorbed intensity can be calculated from the difference to the initial light intensity. The sample holder can be rotated to take angle-dependent measurements. Reflectivity measurements are possible by placing the sample – typically deposited on a silicon substrate – at the back of the sphere in front of a blackened sample holder. Aside from the light absorbed by the sample itself, all scattered and transmitted radiation is absorbed by the sample holder behind it so that only reflected light will be captured by the detector.

Data points are measured for every wavelength from 900 to 270 nm. Depending on the measurement, different background measurements are needed to normalize the data. These include measuring the detected light intensity for a blocked path (to define 0% transmission) and free path (i.e. 100% transmission), as the light intensity varies slightly depending on the wavelength, the lamp life, and environmental factors such as external lighting in the laboratory. Additionally, reference samples are measured to determine the absorption of a certain substrate or the pristine materials in a mixed sample.

In general, the light reaching the detector has a certain intensity  $I$  which is compared to the intensity  $I_0$  that would reach the detector when completely unobscured, as measured for the 100% transmission background. This ratio is defined as the transmit-

tance  $T(\lambda)$  of the material and described by the Beer-Lambert law (see Equation 2.8) to be

$$T(\lambda) = \frac{I(\lambda)}{I_0(\lambda)} = \exp^{-\alpha(\lambda)d}, \quad (4.1)$$

with the absorption coefficient  $\alpha$  and the sample film thickness  $d$ . Additionally, the substrate's transmittance can be extracted from a respective reference measurement and subtracted from the total transmittance:

$$T(\lambda) = \frac{T_{\text{raw}}(\lambda)}{T_{\text{ref}}(\lambda)}, \quad (4.2)$$

with the measured transmittance  $T_{\text{raw}}$  and the substrate contribution  $T_{\text{ref}}$ . The absorbance  $A(\lambda)$  can be deduced from the transmittance by

$$A(\lambda) = -\log_{10} T(\lambda) = \frac{\alpha(\lambda)d}{\ln 10}, \quad (4.3)$$

with the absorption coefficient  $\alpha$  as a function of the absorbance or transmittance.  $\alpha$  is a material-specific parameter independent of the sample thickness  $d$ . As only photons with an energy exceeding the excitation energy  $E$  of the absorbing material are absorbed, the relation

$$E = \frac{hc}{\lambda} \quad (4.4)$$

with the Planck constant  $h$  and the speed of light  $c$ , can be used to determine the bandgap of the probed material.<sup>[200]</sup> The optical bandgap energy  $E_{\text{gap}}$  is related to the absorption coefficient  $\alpha$  via the Tauc equation

$$(\alpha E)^n = B(E - E_{\text{gap}}) \quad (4.5)$$

with the constant  $B$  for different transitions and the exponent  $n = 0.5$  for allowed indirect transitions and  $n = 2$  for allowed direct transitions. To obtain  $E_{\text{gap}}$ ,  $(\alpha E)^n$  is plotted against the photon energy  $E$  and linearly extrapolated at its highest slope.<sup>[201]</sup>

### 4.1.2 FTIR Spectroscopy

FTIR spectroscopy is applied to identify specific molecular bonds and thereby characterize the studied materials within a sample. The technique is based on infrared light (IR) radiation exciting molecular vibrations characteristic for the chemical structure and environment of the respective functional unit. The resulting absorption spectrum can be recorded using different techniques and is usually plotted over the wavenumber  $\tilde{\nu}$ , given in  $\text{cm}^{-1}$ .  $\tilde{\nu}$  is directly proportional to the photon energy  $E$  and frequency  $\nu$  and reciprocal to the wavelength  $\lambda$ :

$$E = h\nu = h\frac{c}{\lambda} = hc\tilde{\nu}. \quad (4.6)$$

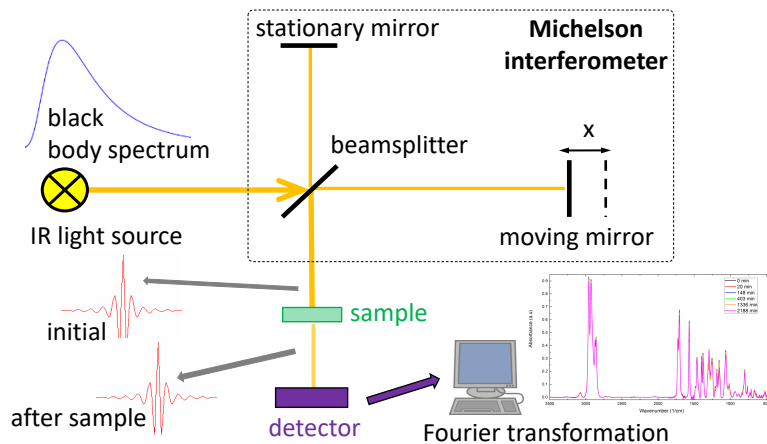


**Figure 4.3**

Schematic FTIR setup showing the light path from a broad-band IR source through a Michelson interferometer. The interferometer is based on splitting the initial light beam and reflecting the split beams with a stationary and a moving mirror to create an initial interferogram once the beams are combined again. The combined radiation passes through a sample and is then detected with a photodetector. By comparing the interferograms before and after the absorbing sample and Fourier transforming the subtracted data, a full IR spectrum can be obtained.

Similar to UV/vis spectroscopy, the sample could be irradiated sequentially with monochromatic light of different photon energies. However, this is a rather slow process, so that most experiments are performed based on the so-called Fourier-transform infrared method using a thermal light source emitting broad-band IR radiation. A Michelson interferometer is used to illuminate the sample and collect the interferogram, as illustrated schematically in Figure 4.3. The IR radiation emitted from the light source is split by a semi-transparent mirror acting as a beamsplitter. Both split beams are reflected by mirrors and sent back to be recombined at the beamsplitter. While one mirror is stationary, the other one can be moved to induce slight path differences between both split beams. These path differences result in interference effects of the recombined light waves and therefore fluctuations in the total light intensity. The resulting initial interferogram as a function of the path difference can be recorded by a photodetector to obtain information about the black body spectrum of the IR source. A black body radiates a broad spectrum characterized by Planck's law, with the spectral radiance  $B(\tilde{\nu}, T)$  given as

$$I(\tilde{\nu}, T) = \frac{2hc^2\tilde{\nu}^3}{\exp\left(\frac{hc\tilde{\nu}}{k_B T}\right) - 1}, \quad (4.7)$$

with the wavenumber  $\tilde{\nu}$ , the temperature  $T$ , the Planck constant  $h$ , the speed of light  $c$ , and the Boltzmann constant  $k_B$ . The interferogram can be used to characterize the

respective used light source. Placing a sample in the path of the recombined beam, a second interferogram can be recorded, showing changes depending on the sample's absorption behavior. After subtracting the initial measurement, the interferogram is Fourier transformed to obtain an absorption spectrum as a function of the wavenumber. Absorption peaks arise from the energy transfer of the IR light to certain functional groups within the material, with characteristic peak positions and shapes for different molecular bonds and vibration or rotation modes.

FTIR data are taken using the FTIR-Spectrometer Equinox 55 (Bruker, Germany). IR radiation is emitted by a rod of ceramic silicon carbide heated electrically to a temperature above 1200 °C while using additional air-cooling to keep the spectrum constant. The beam splitter within the Michelson interferometer consists of a thin germanium film sandwiched between two potassium bromide (KBr) windows. To obtain reproducible results, the sample holder's temperature is controlled. Additionally, the sample compartment has to be purged with dry, CO<sub>2</sub>-free air to reduce the noise from the strongly absorbing H<sub>2</sub>O and CO<sub>2</sub> molecules. A background measurement is performed to eliminate contributions from the sample environment and the instrument itself. Using the OPUS software (Bruker), the measurements were controlled, with time-dependent measurements performed using a macro. Spectra are recorded from 400 cm<sup>-1</sup> – 6000 cm<sup>-1</sup> with a resolution set to  $\tilde{\nu} = 2 \text{ cm}^{-1}$  and an aperture diameter set to 2 mm. Depending on the film thickness, several hundred scans are averaged per measurement to achieve a high signal-to-noise ratio. Before the data analysis, a baseline correction has to be performed to reduce the contributions from the non-perfect sample and measurement setup.

While IR spectroscopy has traditionally been restricted to a spatial resolution in the  $\mu\text{m}$  range, combining it with atomic force microscopy (AFM) measurements gives new insights into the surface chemistry of samples, as discussed in Section 4.2.5 .

### 4.1.3 Electrical Characterization

The performance of exemplary organic photovoltaic (OPV) devices can be investigated by tracking their photovoltaic performance during operation. To probe this performance, the so-called current-voltage (I/V) characteristics are tracked, whereby the electric current density flowing through a solar cell both under dark conditions and under simulated sunlight is measured as a function of the applied bias. Solar cell devices are illuminated with a standardized irradiation spectrum simulating the air mass 1.5 global (AM1.5G, international standard ASTM G-173-03) solar irradiance.<sup>[202,203]</sup> For standard tests under static conditions, a SolarConstant solar simulator (K.H. Steuernagel Lichttechnik GmbH) is applied, while in-situ grazing-incidence small-angle X-ray scattering (GISAXS) experiments at the synchrotron X-ray source are performed using the mobile, custom-built setup PocketSolar (for details see the description by Christoph Schaffer).<sup>[68]</sup> The PocketSolar setup uses a 150 W Xenon lamp (Perkin Elmer PX5),

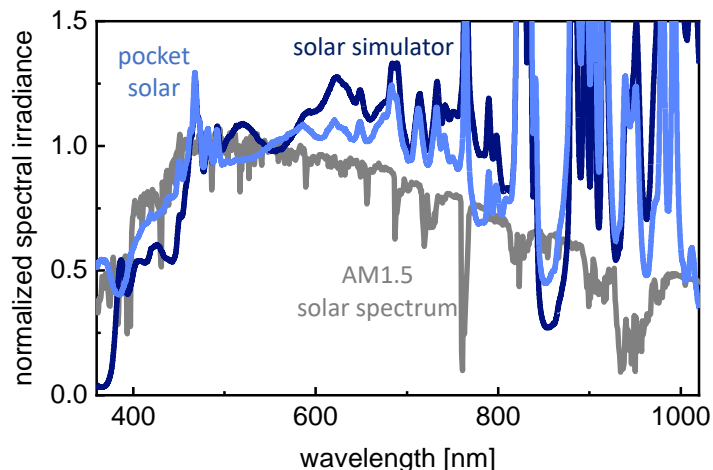


**Figure 4.4**

Comparison of the wavelength-dependent spectral irradiance of sunlight under AM1.5G conditions (standard reference, grey) with the two used solar simulators. The standard simulator SolarConstant (dark blue) is used for all experiments, except when performing experiments at the synchrotron source with the mobile PocketSolar simulator (light blue). The simulated irradiation is calibrated in intensity to match the AM1.5G spectrum.

can be evacuated to a pressure of about  $2 \times 10^{-1}$  mbar and the sample holder temperature can be controlled using a Peltier element to keep the device at a constant temperature upon illumination. Figure 4.4 illustrates the irradiation spectra of the standard AM1.5G (grey) in comparison to the used standard solar simulator (dark blue) and mobile PocketSolar (light blue). Characteristic lines visible in the AM1.5G solar spectrum are due to element-specific absorption in the earth's atmosphere.

The solar simulator is set to an intensity of  $100 \text{ mW cm}^{-2}$  with a calibrated standard silicon solar cell (ReRa Solutions BV). For measuring the I/V curves, a Keithley 2400 SourceMeter unit is used to apply a bias voltage in a range from  $-1 \text{ V}$  to  $1 \text{ V}$  while simultaneously recording the flowing current. Figure 4.5 shows typical I/V curves recorded in the dark (grey curve) and under illumination (light blue). The current  $I$  is normalized to the pixel size, which is confined using a mask during illumination, resulting in the current density  $J$ . The mask size is set to  $0.1 \text{ cm}^2$  for small standard solar cells. Typical solar cell parameters are extracted from the recorded I/V curves under illumination, including the open-circuit voltage  $V_{oc}$  at  $J = 0$ , the short circuit current density  $J_{sc}$  for  $V = 0$ , and the maximum power point (MPP), where the power density  $P = JV$  reaches its maximum. The fill factor (FF) of a solar cell is defined as the ratio of the power at the MPP and the maximum power possible as the product of  $J_{sc}$  and  $V_{oc}$  depicted as rectangles in Figure 4.5:

$$FF = \frac{U_{MPP} J_{MPP}}{V_{oc} J_{sc}} = \frac{P_{max}}{V_{oc} J_{sc}}. \quad (4.8)$$

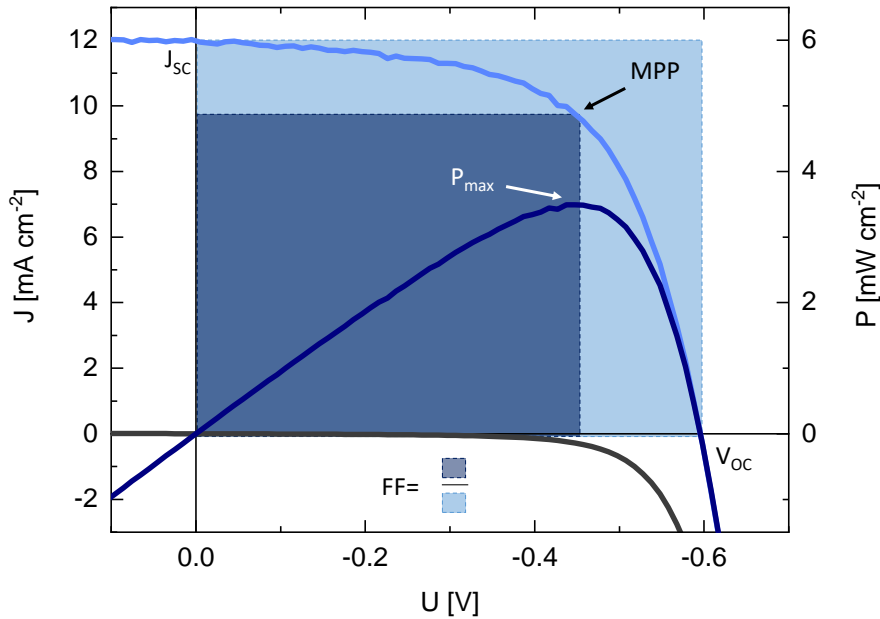


**Figure 4.5**

Typical current-voltage characteristics of a polymer-based solar cell. The solar cell is measured in dark conditions (grey curve) and under simulated AM1.5G illumination (light blue). The power-voltage curve (dark blue) exhibits a maximum absolute value at the MPP. The open-circuit voltage  $V_{oc}$  and the short circuit current density  $J_{sc}$  define the maximum theoretically possible power output  $J_{sc}V_{oc}$ . The FF is calculated as the ratio of the measured maximum power  $P_{max}$  at the MPP and  $J_{sc}V_{oc}$ .

In contrast to an ideal solar cell with an almost rectangular curve and FF close to 100 %, certain factors described in more detail in Section 2.2 reduce the FF. For maximizing the efficiency, the serial resistance of a solar cell, as determined from the slope at  $J_{sc}$ , should be as low as possible. On the other hand, charge leakage should be prevented to increase the shunt resistance, as determined from the slope at  $V_{oc}$ . The solar cell power conversion efficiency (PCE) – also called  $\eta$  – depends on the combination of all these parameters and is defined as the ratio of the extracted power  $P_{out}$  to the incident power  $P_{in}$  during illumination:

$$PCE = \eta = \frac{P_{out}}{P_{in}} = \frac{V_{oc}j_{sc}FF}{P_{in}} \quad (4.9)$$

with the incident power set to  $P_{in} = 100 \text{ mW cm}^{-2}$ .

## 4.2 Structure Investigation in Real Space

The structural characterization of the investigated thin films in real space is performed using different microscopy techniques. Optical microscopy gives insights into

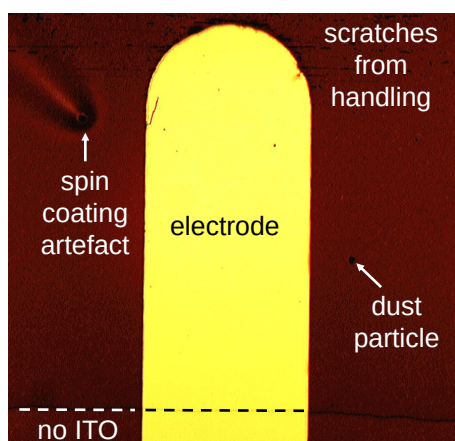


**Figure 4.6**

Exemplary optical micrograph of an aluminium electrode (bright area) on a polymer-based solar cell device (dark area). The line near the bottom illustrates the edge resulting from a partial etching of ITO. Artefacts from spin coating and scratches due to sample handling and dust particles are illustrated for this investigated device.

the homogeneity of films and pixel size of OPV devices (see Section 4.2.1). Lateral structures of the sputter-deposited metal electrodes presented in Chapter 5 are investigated using scanning electron microscopy (SEM) (Section 4.2.2). Height profilometry (Section 4.2.3) and AFM (Section 4.2.4) are applied to determine the surface topology and thickness of the thin films. AFM can be combined with local, nano-scale, IR spectroscopy to give a nano-IR mapping of the sample surface, as discussed in Section 4.2.5.

### 4.2.1 Optical Microscopy

Optical microscopy is a quick and easy-access method to evaluate the film homogeneity on a micrometer scale and determine the size of macroscopic features such as the dimensions of electrodes or processing artefacts. An Axiolab A microscope by Carl Zeiss is used to obtain microscopy images with a magnification between  $M = 1.25\times$  and  $100\times$ . As some of the investigated films or substrates are non-transparent, a reflection geometry is chosen to investigate all samples. Using a PixeLink PL-S621CU CMOS sensor ( $1280 \times 1024 \text{ px}^2$ , 8.52 mm sensor diagonal) digital micrographs can be recorded. Figure 4.6 shows an optical micrograph of an aluminium electrode on a photoactive film. It should be noted that here, a microscopy image with significant artefacts was specifically chosen to illustrate the technique. The electrode material seems highlighted due to its high reflectivity, while the organic film looks significantly darker. Artefacts from spin coating typically show meteor-like tails resulting from dust particles or unresolved material during the processing. Further dust particles and

scratches can be acquired during later sample handling and can be investigated and measured via optical microscopy.

Depending on the used magnification lense, certain transformation factors can be deduced to measure the distances in the micrographs. The resolution limit in the focal plane depends on the respective wavelength  $\lambda$  and used numerical aperture  $NA$  and is given by the Rayleigh criterion:

$$R = \frac{1.22\lambda}{2NA}. \quad (4.10)$$

For this work,  $\lambda$  is assumed to be 700 nm, while the  $NA$  is given by the microscopy setup. The pixel size for each objective is obtained and listed in Table 4.1 along with the resolution calculated from equation 4.10 for a wavelength of 700 nm. The recorded images are processed and analyzed using the open-source software ImageJ.<sup>[204,205]</sup>

**Table 4.1**

Available magnifications  $M$  for optical microscopy images with corresponding numerical aperture  $NA$ , spatial resolution  $R$ , and empirically determined transformation factor from pixel size to real space length.  $R$  is calculated according to Equation 4.10 for  $\lambda = 700$  nm.

| $M$  | $NA$  | $R$ [ $\mu\text{m}$ ] | factor [ $\mu\text{m px}^{-1}$ ] |
|------|-------|-----------------------|----------------------------------|
| 1.25 | 0.035 | 12.2                  | 6.258                            |
| 2.5  | 0.075 | 5.7                   | 3.2                              |
| 10   | 0.20  | 2.1                   | 0.8                              |
| 50   | 0.70  | 0.61                  | 0.16                             |
| 100  | 0.75  | 0.57                  | 0.08                             |

## 4.2.2 Scanning Electron Microscopy

While optical microscopy gives a good overview of features in the  $\mu\text{m}$ -range, the structures investigated for the present work are typically in the range of nm and cannot be resolved by visible light. For this reason, further structural investigations are performed by applying scanning electron microscopy (SEM). The de Broglie wavelength of electrons depends on their momentum  $p$  which depends on the applied acceleration voltage. Accelerating electrons with a typical voltage of  $V = 5$  keV leads to a very low de Broglie wavelength

$$\lambda = \frac{h}{p} = \frac{hc}{\sqrt{2m_e c^2 eV + (eV)^2}} \approx 17.3 \text{ pm} \quad (4.11)$$

with Planck's constant  $h$ , the speed of light  $c$ , the rest mass of an electron  $m_e$  and its elementary charge  $e$ , making a sub-nanometer resolution – at least in theory – possible. However, the measurements can be only performed on conducting samples to prevent electrostatic charging and the measurement has to be performed under a high vacuum.

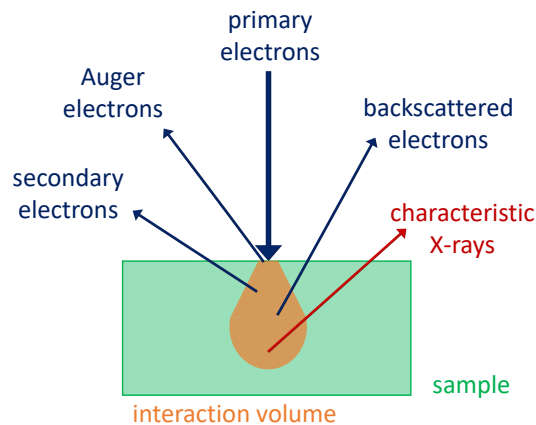


**Figure 4.7**

Typical signals used for SEM measurements. The primary electrons interact with atoms in the sample, leading to elastic (back)scattering or inelastic scattering creating secondary electrons, Auger electrons, or characteristic X-rays. While backscattered electrons can leave deeper regions of the sample due to their higher energy, secondary electrons can only emerge from near-surface areas.

Figure 4.7 illustrates some of the typical interactions of accelerated electrons with materials close to their surface. The incident or so-called primary electrons of an electron beam penetrate the sample to a certain extent, before meeting and interacting with the shell electrons of atoms. Those interactions take place in a certain interaction volume called scattering plume and lead to elastic or inelastic scattering, resulting in several characteristic effects. Secondary electrons are created by inelastic scattering of primary electrons at electron shells and show significantly lower energies ( $\approx 10\text{ eV} - 50\text{ eV}$ ). They can only emerge from regions very close to the surface and are therefore typically used to get the best resolution. Elastically backscattered electrons show only a little loss in energy and emerge from deeper regions of the sample which reduces the lateral resolution. However, as the scattering strongly depends on the atomic number, they can yield a high material contrast. Further material contrast and chemical mapping can be achieved by additionally detecting Auger electrons or characteristic X-rays.

The primary electrons are typically generated using a thermally assisted field emission gun to provide a sharp electron beam of high flux with a stable, well-defined energy using low acceleration voltages below 5 kV). While the electron's de Broglie wavelength in principle could resolve sub-nanometer structures, the actual resolution is limited by the electron beam diameter and the size of the generated interaction volume within the sample. Experimental resolutions of around 1 nm – 10 nm can typically be achieved. Similar to light optics, the electron beam is condensed by a set of electromagnetic lenses and cut down by an aperture to a specified beam size. Using scan coils, the beam can be directed to the desired position on the sample and scanned over a

certain region of interest (ROI), while detecting the scattered and generated electrons and/or photons with different detectors placed within the measurement chamber. The most important factor for the image quality is the respective signal contrast. While secondary electrons are especially sensitive to surface structures and less so to different materials, backscattered electrons will show a significantly higher material contrast, but less resolution regarding surface topography.

For the present work, secondary electrons are chosen to investigate the surface structure of homogeneous metal films, with a focus on the contrast created by the topology. Electrically conductive samples with conducting substrates have to be used to prevent the depletion of electrons from the sample's surface. Measurements are performed using the high-resolution field emission SEM Gemini NVision 40 FIB-SEM by Zeiss with 5 kV at 3.6 mm distance. A small beam size is created by choosing the smallest aperture of 10  $\mu\text{m}$ . Using the software ImageJ v1.44p, the images are further processed to adjust the contrast.<sup>[205]</sup> Dominant structure sizes and distances are identified using the Fourier transformation of a chosen ROI and performing a radial integration to get a radial power spectral density (RPSD).

### 4.2.3 Height Profilometry

Profilometry is a quick and efficient method to determine the surface profile of a sample. For the present thesis, it is used to investigate the thickness gradient and homogeneity of drop-cast films as well as the thickness of thin films. Thickness measurements are performed by scratching or partly removing the film and scanning perpendicularly to the resulting edge or scratch. For the present thesis, the Stylus Profiler DektakXT (Bruker, Germany) is used. The contact profilometer is based on a diamond tip (radius: 2  $\mu\text{m}$ ) placed on the sample with a contact pressure corresponding to 1 mg. The sample is scanned by moving the  $xy$ -stage with a certain scan rate below the stylus. Simultaneously, the contact pressure is kept constant by adjusting the stylus height position to the sample height. The vertical deflection of the probe is recorded and translated into a height profile. Typical measurements are performed over a scan range of 350  $\mu\text{m}$  with a scan speed of 35  $\mu\text{m s}^{-1}$ , obtaining a lateral resolution of 120 nm pt<sup>-1</sup>. For spin-cast films, the thickness is determined by averaging over at least 3 spots per scratch and several scratches on different positions on the sample. Aside from simply measuring the film thickness, the surface profile can be investigated by automatically scanning the samples over a larger area. Figure 4.8 shows an exemplary scan perpendicular to a scratch in a thin film. From the scan, several data can be acquired using the software Vision64 included in the instrument. The film thickness can be determined from the average step height (ASH) between the upper and lower plateau to be about  $(174 \pm 8)$  nm, with a root mean square (rms) roughness  $R_q = 10$  nm (as can be calculated via Equation 2.27 introduced in Section 2.4.2).

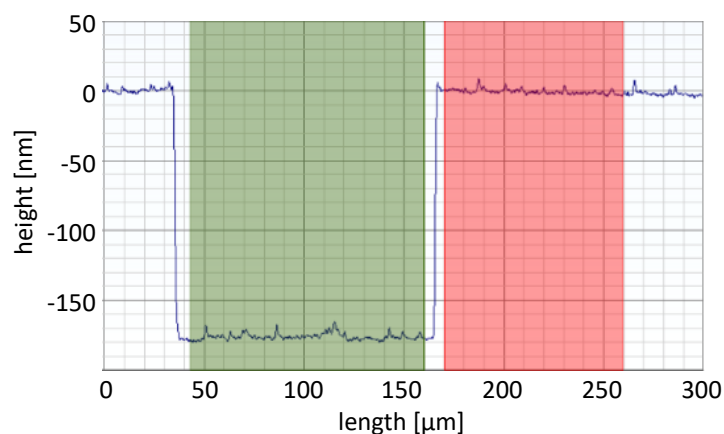


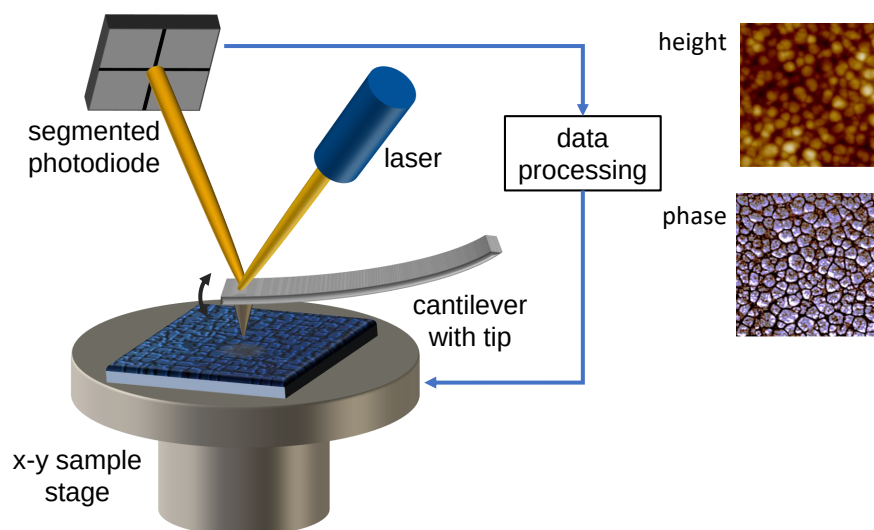
**Figure 4.8**

Exemplary height profile scanned across a scratch in a spin-cast organic thin film. From the absolute height difference between the film surface and the scratch surface, the film thickness is calculated. For this purpose, height data are integrated over a certain region for both the film surface (red) and the scratch surface (green). Additional values such as the average roughness  $R_q$  can be determined.

Several drawbacks have to be taken into account, when interpreting the profilometry data. While the technique delivers fast estimates for the film thickness and gives a first impression on the surface profile of films, the constant contact with the sample may lead to issues regarding some samples. Soft polymer films may be penetrated by the tip or lead to contamination of the diamond tip. Scanning rough surfaces too quickly or with too much contact pressure might lead to damage to the film or stylus. In combination with potential material residues in the scratched area, those drawbacks can lead to an underestimation of the film thickness.

#### 4.2.4 Atomic Force Microscopy

Similar to the profilometry discussed before, but with a significantly higher resolution in the nm-range, atomic force microscopy (AFM) probes the surface topology of a sample. Depending on the exact setup and technique used, additional surface characteristics such as stiffness or certain chemical and electric properties can be probed. A very sharp tip attached to a flexible cantilever is placed on the sample and moved via piezo-electric elements to scan the sample surface. While scanning the sample, the tip is subjected to different forces depending the surface structure which results in the bending of the cantilever. A laser beam focused on the cantilever is reflected to a segmented photodiode. Deflections of the cantilever result in a shift of the reflected laser beam which is detected by the photodiode and corrected via the feedback electronics. Figure 4.9 depicts the schematic AFM setup and working principles. AFM is based on the interaction of the nm-sized tip with the atoms at the sample surface. The tip

**Figure 4.9**

Schematic AFM setup and general working principles. A cantilever with a very sharp tip is moved across a sample with the tip being influenced by attractive or repulsive forces from the sample structure. The resulting deflection of the cantilever changes the reflection of a laser beam monitored with a segmented photodiode. Typical data obtained via AFM are height profiles and phase information, as illustrated with an exemplary polymer-fullerene blend film.

of the cantilever is placed at a certain distance from the sample surface to feel the inter-atomic forces present in the so-called Lennard-Jones potential. This potential results from a combination of attractive and repulsive forces between the sample and the cantilever tip, with attractive forces dominating for larger distances and a strong repulsion at very small distances arising from the Pauli principle. This allows for three different modes of operation, namely contact, dynamic-contact (i.e. tapping), and non-contact mode. In contact mode, the tip is placed in direct contact with the sample and kept in a region of repulsive forces, usually by adjusting the cantilever height to keep the force constant. However, the close contact can lead to a damage of soft materials and to a contamination or breaking of the measuring tip when investigating rough surfaces. Therefore, the so-called tapping mode is usually preferred for soft matter samples, with the tip oscillating between the different regimes in the Lennard-Jones potential, thereby periodically tapping the surface. The cantilever is stimulated by an external, periodic force to oscillate at or close to its resonance frequency depending on the forces from the sample surface. All forces on the cantilever will result in changes in the resonance frequency, amplitude, and phase. Variations in the amplitude will be recorded by the changed reflection on the photo-diode and translated into height information. Via a feedback loop, this information is used to keep the amplitude constant by adjusting the tip-to-sample distance. Using piezoelectric actuators, the cantilever

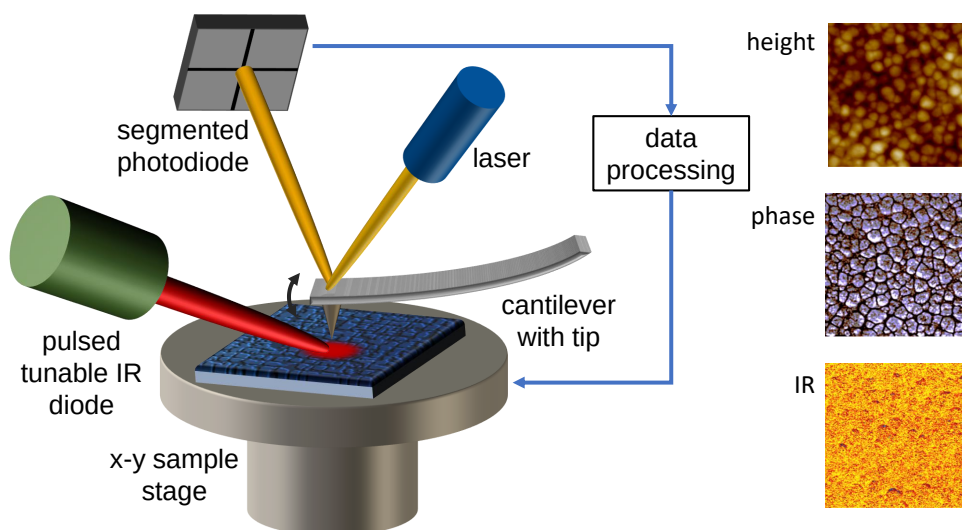
is scanned line-by-line over the sample to map the topographic information within the sample area in the  $\mu\text{m}$ -range. The recorded changes in frequency, amplitude, and phase give information about the topography and the surface material composition.

AFM measurements are performed using the nanoIR2-FS instrument with a quantum cascade laser (Anasys Instruments US). The images are processed and analyzed using the software Gwyddion v2.45.<sup>[206]</sup> Image processing includes leveling the data to reduce tilt and subtracting a polynomial background. Line cuts are performed to extract height profiles and local topological parameters. Dominating surface structure sizes and distances can be determined by obtaining the radial power spectral density (RPSD) of a certain area.

### 4.2.5 Nano-IR mapping combined with AFM (AFM-IR)

Depending on the used tip, measurement mode, sample environment, and other parameters, AFM can be combined with other techniques to obtain additional information about the chemical or physical properties of a sample surface on a nanoscale. For the present work, additional IR spectroscopy is performed on a nanoscale by using a specific AFM-IR measurement setup schematically shown in Figure 4.10. The technique was invented by Dazzi et al. in 2005 and enhanced by using a quantum cascade laser with resonance-enhanced mode.<sup>[207–211]</sup> The theory and working principles of AFM-IR are described in detail by Centrone.<sup>[212]</sup> While traditional IR spectroscopy is limited to resolutions in or above the  $\mu\text{m}$  range due to the optical diffraction limit, AFM-IR can yield spatial resolutions below 10 nm.<sup>[213]</sup> By introducing an additional, pulsed, tunable IR laser (shown in red), molecular vibrations can be excited in close proximity to the cantilever tip. The absorbed photon energy will lead to local heating which results in a local thermal expansion that is detected by changes in the oscillations of the cantilever. These additionally induced oscillations show a characteristic decay depending on their amplitude and frequency, which can be extracted using Fourier transformations.

In principle, two measurement modes are possible. Keeping the cantilever at a constant position, the tunable IR source can scan a whole range of photon energies to create a full IR spectrum similar to one obtained for conventional FTIR spectroscopy for a larger sample area. This gives the option to check the material composition at specific points of interest with a high spatial resolution. However, even more interesting is the possibility to create a map overlaying spectroscopic data over the topology of a certain sample area. For this purpose, the IR source is kept at a constant wavenumber of interest while simultaneously scanning the sample area with the cantilever to get information about the height, phase, and absorption behavior on a nanoscale. AFM measurements with IR mapping are performed using the nanoIR2-FS instrument with a quantum cascade laser (QCL) with a variable repetition rate and using a gold-covered tip (Anasys Instruments, US). Multiple spectra are acquired, averaged, and smoothed

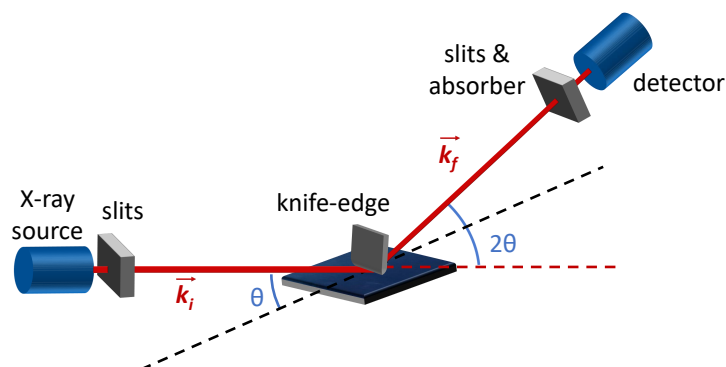
**Figure 4.10**

Schematic AFM setup combined with nanoscale IR mapping. In addition to the AFM measurement described before, a pulsed laser of a tunable wavelength in the mid-IR region is focused on the sample area close to the cantilever tip. Absorption due to excitation of certain molecular vibrations leads to local heating of the materials, which again leads to a change in the cantilever oscillation that can be measured. In addition to the height and phase information, an additional map of the IR absorption at a specific wavenumber can be obtained.

using the Savitzky-Golay filter, with a range of  $1000\text{ cm}^{-1} - 1900\text{ cm}^{-1}$  at  $2\text{ cm}^{-1}$  data point spacing.

### 4.3 Structure Investigation in Reciprocal Space

In contrast to real-space techniques, X-ray scattering techniques yield averaged information on a larger sample volume and can also probe structures within a film, thereby complementing microscopy methods. Furthermore, they allow a non-destructive structure investigation, paving the way towards in-situ or in-operando techniques that follow dynamic processes in real-time. For the present thesis, thin films are probed, making scattering methods using very low incident angles particularly useful. The vertical film profile, including layer roughness and scattering length density (SLD), is probed using X-ray reflectometry (XRR) (Section 4.3.1). GISAXS is applied to investigate the lateral morphology and composition of the thin films in the range of  $1\text{ nm} - 100\text{ nm}$  (Section 4.3.3). Crystal structures in the range of  $0.1\text{ nm} - 5\text{ nm}$  are probed using grazing-incidence wide-angle X-ray scattering (GIWAXS) (Section 4.3.4).

**Figure 4.11**

Schematic XRR setup with X-rays ( $\vec{k}_i$ ), generated by a Cu-K $_{\alpha}$  anode, impinging the sample surface under the angle  $\theta$ . The specular reflection ( $\vec{k}_f$ ) under the angle  $2\theta$  with respect to the incident beam is recorded by a scintillation detector. A knife-edge prevents over-illumination of the sample.

### 4.3.1 X-ray Reflectometry

Using X-ray reflectometry (XRR) structural information about the vertical film profile such as its thickness, roughness, and composition in terms of scattering contrast can be determined. Like all X-ray-based methods, the technique is sensitive towards differences in the SLD within the film, depending on the respective local electron density and therefore differences in material composition and density. Films with distinct layers with differences in the electron density in vertical direction such as layered structures are especially suited for this technique. The schematic setup and working principle of XRR is shown in figure Figure 4.11 The monochromatic X-rays hit the sample under a (usually small) angle  $\theta$  and are specularly reflected under an angle of  $2\theta$  with respect to the incoming beam. The reflected X-rays are detected by a scintillation detector. To restrict the footprint of the beam, a metal knife-edge is positioned a few micrometers above the sample surface. By moving both the X-ray source and the detector, a range of  $\theta$  angles can be scanned while always keeping the  $\theta/2\theta$  configuration. The X-ray photons are scattered elastically and the reflected intensity is recorded as a function of  $\theta$ . As will also be of relevance for the grazing incidence experiments discussed in the next section, for angles smaller than the material-dependent critical angle  $\theta < \alpha_c$  total reflection occurs. As soon as the critical angle is surpassed, a certain amount of X-rays will penetrate the film which leads to a significant decrease in intensity. According to Fresnel's theory (Section 2.4.1), the beam is split into a reflected and transmitted part at each interface with a change in refractive index  $n$ . The superposition of multiple reflected and refracted waves results in characteristic Kiessig fringes of the reflectivity

pattern which yield information about the thickness  $d$  of the respective layer determined from the distance between adjacent fringes  $\Delta q_z$  according to Equation 2.28:

$$d \approx \frac{2\pi}{\Delta q_z}, \quad \text{with } \Delta q_z = |q_{z,1} - q_{z,2}|.$$

The vertical structure can be investigated by dividing the probed film into a model stack of layers with distinct refractive index, thickness, and roughness. Using the Paratt algorithm, a vertical SLD profile can be obtained.<sup>[156]</sup> Detailed information about XRR with a focus on soft-matter thin films can be found in the introduction to *X-Ray Scattering from Soft-Matter Thin Films* by Tolan.<sup>[147]</sup>

The XRR measurements presented in this work are performed with a Bruker D8 Advance Diffractometer with a copper anode. The X-rays are generated with a copper anode, using its Cu-K $_{\alpha}$  emission at  $\lambda = 1.54 \text{ \AA}$  selected by a Göbel mirror which also preshapes the beam. The shaped beam is collimated with slits (0.2 mm). A tantalum knife-edge decreases the beam footprint for the small angles (typically below 7°) to enhance the angular resolution of the measured signal. The reflected beam is further collimated with slits (0.1 mm and 0.05 mm), guided through an absorber to prevent oversaturation and its intensity detected with a scintillation detector. The angle-dependent reflectivity can be modeled using the software environment IGOR Pro (V6.37, WaveMetrics) with the plugin Motofit that allows modeling the films according to the Paratt algorithm.<sup>[158]</sup>

### 4.3.2 Grazing-Incidence X-ray Scattering (GIXS)

Grazing-incidence X-ray scattering (GIXS) methods are often used to obtain information about average structural features of thin organic films. Details on the theoretical background can be found in Section 2.4.1. Typical X-ray scattering experiments are performed in transmission, which is not a feasible method for thin films due to the small scattering volume. Especially for organic thin films with low scattering contrast, the grazing incidence geometry is preferred to increase the beam's footprint up to a few  $\text{cm}^2$  and therefore increase the total scattering volume significantly. Additionally, probing the sample under a shallow angle in reflection geometry yields further information about features in vertical direction.

GIXS can be divided into methods probing different length scales. Depending on the region of angles for which scattering is detected, structural features in the  $\text{\AA}$  to the  $\mu\text{m}$  region can be probed. In the scope of this work, a focus lies on the range of 1 nm – 100 nm accessible via grazing-incidence small-angle X-ray scattering (GISAXS), as explained in the following section. Grazing-incidence wide-angle X-ray scattering (GIWAXS) offers additional information about the crystal quality of the gold layers investigated during sputter deposition and will be explained in Section 4.3.4. Figure 4.12 illustrates the schematic setup of both experiments which can also be performed simultaneously. The incoming X-rays ( $\vec{k}_i$ ) hit the sample under the small angle  $\alpha_i < 1.0^\circ$

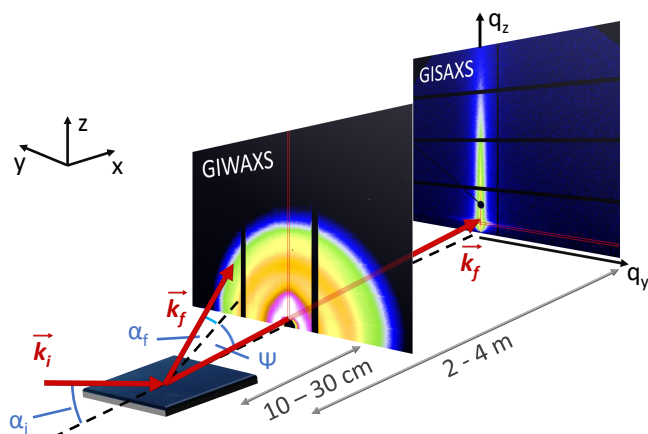


**Figure 4.12**

Schematic setup for grazing incidence X-ray scattering measurements. The incident X-ray beam  $\vec{k}_i$  impinges the sample under a shallow angle  $\alpha_i$  and is scattered due to the film's SLD variations. The scattering leads to a change in direction for the scattered signal ( $\vec{k}_f$  with the exit angle  $\alpha_f$  in the  $xz$ -plane and  $\psi$  in the  $xy$ -plane). 2D-detectors detect wide-angle scattering (GIWAXS) at a distance of 10 cm – 30 cm or small-angle scattering (GISAXS) at 2 m – 4 m distance. Beamstops are used to block the direct and specularly reflected light to prevent over-saturation of the photodetector.

and are scattered. The scattered photons leave the sample film with a changed momentum ( $\vec{k}_f$ ) and in a certain direction, described by the exit angles  $\alpha_f$  in the  $xz$ -plane and  $\psi$  in the  $xy$ -plane. The accessible length scales are determined by the size and placement of the respective photodetectors. Placing the detector at a larger sample-to-detector distance (SDD), smaller angles can be resolved, while placing it closer to the sample, a higher range of angles can be accessed. For GIWAXS (short SDDs of about 10 cm – 30 cm), wide angles can be detected corresponding to a high momentum transfer which in turn is related to small distances up to a few nanometers, thereby yielding information about the molecular arrangement and crystal packing. For GISAXS (large SDDs of about 2 m – 4 m), small angles below  $5^\circ$  are investigated, corresponding to length scales of around 1 nm up to 1  $\mu\text{m}$ . The technique is used to probe the inner morphology on the mesoscale, detecting the phase separation of the materials, their porosity, or the aggregation of domains. Depending on the chosen incident angle, the method can be more or less surface sensitive. For angles below the material-specific critical angle  $\alpha_c$ , the film is not penetrated, leading to a high surface sensitivity, while angles above  $\alpha_c$  are applied to probe the bulk film.

To follow certain processes in situ, the GISAXS and GIWAXS experiments have to be performed with a high temporal and spatial resolution which necessitates the use of synchrotron radiation. For the in-situ investigations discussed in the present thesis, the MiNaXS beamline P03 of the brilliant synchrotron light source PETRA III at DESY in Hamburg, Germany, is used.<sup>[214]</sup> The measurements are performed at

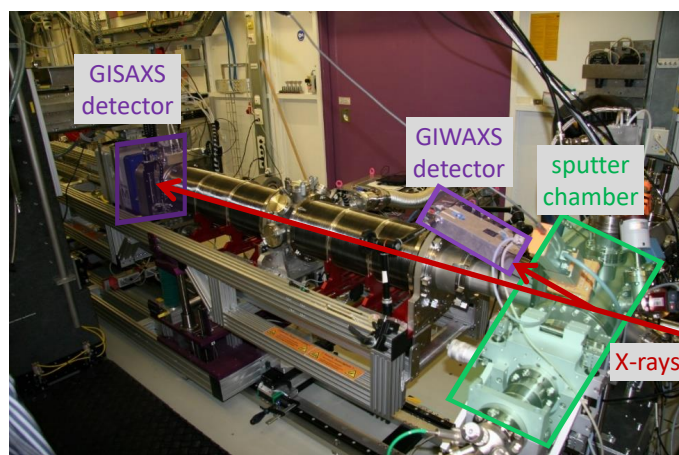


**Figure 4.13**

Setup at the MiNaXS beamline P03 (PETRA III at DESY, Hamburg) with a mobile sputter chamber installed in the path of X-rays injected from the synchrotron storage ring. The X-rays are scattered at the sample within the sputter chamber and detected by 2D detectors placed at different SDDs. The GISAXS detector is placed behind an evacuated flight tube to resolve small scattering angles. The GIWAXS detector is directly placed above the entrance of the flight tube to detect higher scattering angles.

an energy of 13.0 keV ( $\lambda = 0.953 \text{ \AA}$ ) with a micro-beam spot size on the sample. A typical setup is shown in Figure 4.13 with a mobile sputter chamber (described in Chapter 5) installed at the beamline. The chamber is installed in such a way that the X-ray beam is directed to the sample. The X-rays scattered in small angles are lead through an evacuated flight tube to reduce background noise due to scattering at air particles, before reaching the GISAXS detector placed at a large SDD behind the flight tube. X-rays scattered in larger angles reach the GIWAXS detector attached to the front end of the flight tube. The high X-ray flux at a synchrotron light source can be used to make sub-second measurements to follow processes in situ. However, the high flux also necessitates certain precautionary measures, as it might lead to sample degradation, so-called beam damage. For this purpose, test measurements are usually performed to check for the stability of samples under a certain total illumination time. For this, a whole series of short measurements can be taken at one spot of the sample, while simultaneously monitoring the data for beam-induced changes. During the in-situ measurements, the X-ray beam is typically scanned over the sample surface, thereby keeping the local exposure to radiation below the critical dose to avoid beam damage. Scanning additionally verifies the homogeneity of the film and increases the probed sample volume, effectively increasing the statistical relevance of GIXS-based techniques.

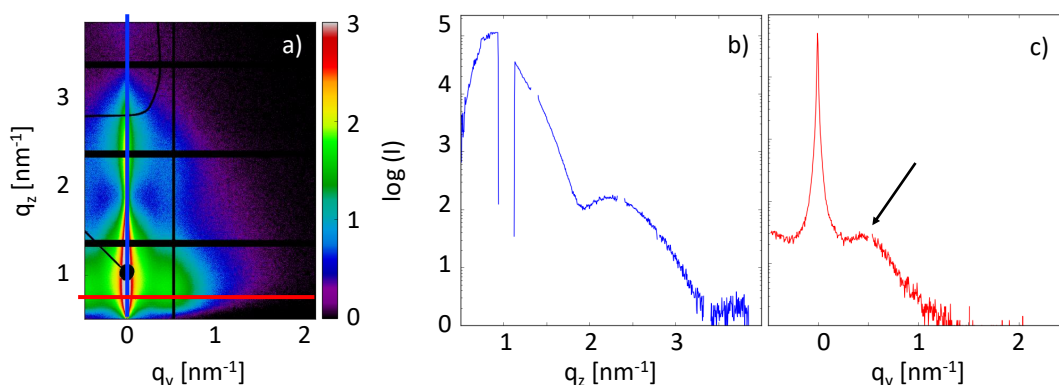


**Figure 4.14**

a) Exemplary 2D GISAXS scattering data with the respective ROIs for line cuts illustrated via colored lines. Black lines result from gaps between the detector elements, while the specular reflection is covered by a round beamstop to prevent over-saturation of the detector. b) The vertical line cut (blue) shows intensity modulations due to a certain film thickness of the sample. c) The horizontal line cut (red) exhibits a side peak due to Bragg-like scattering (indicated with an arrow) induced by clusters of a similar form and structure factor distributed on the substrate.

### 4.3.3 Grazing-Incidence Small-Angle X-ray Scattering (GISAXS)

GISAXS experiments are performed using the 2D detector Pilatus 1M (Dectris Ltd.) with a pixel size of  $172 \times 172 \mu\text{m}^2$ . The detector consists of  $1043 \times 981 \text{ px}^2$  and is divided into ten segments, which are also visible by the intersegment gaps in the data. Placing the detector in a large SDD of 2 m – 4 m allows to resolve small scattering angles and therefore mesoscale structural features. To reduce scattering in air on the long flight path of the X-rays, an evacuated flight tube is installed between the sample environment and the detector. The detector is protected from oversaturation by placing beamstops at the position of the direct and the specularly reflected beam.

To analyze the 2D data, the scattering intensity in specific regions of interest is processed via the software DPDAK v1.3.1<sup>[215]</sup> and fitted using an appropriate model. For data analysis, the 2D data are reduced to 1D cuts integrated in vertical or horizontal direction. Custom-made macros are implemented for further fitting the data. Line integrals are performed as illustrated in Figure 4.14 in the respective directions with blue and red lines. From the line cuts of the 2D GISAXS data with defined integration width, information about the film composition parallel and perpendicular to the substrate can be obtained. Vertical line cuts (illustrated in blue) are analyzed to acquire information about the film profile such as the film thickness. To gain insights into the lateral structures of the samples, horizontal line cuts (red line) at the Yoneda position of the material of interest are made. This Yoneda region is defined by a material's critical angle of total reflection  $\alpha_c$  and is similar for many organic materials (see also

Section 2.4.3).<sup>[154]</sup> Incident angles above  $\alpha_c$  will allow for the X-rays to penetrate the film to a certain extent. The created evanescent wave within the film couples out at the critical edge of the material, leading to the observed highest scattering intensity at the Yoneda position. By adjusting the incident angle, the penetration depth can be controlled, making it possible to choose a mode sensitive to the film bulk or its surface, respectively. Typically, the angle is chosen such that it is larger than the respective sample material's  $\alpha_c$ , but smaller than the  $\alpha_c$  of the substrate material to probe the sample without contributions from the substrate. However, this is not always possible. In particular for the sputtering experiments discussed in Chapter 5 and Chapter 6, the  $\alpha_c$  of the investigated gold films is higher than the critical angles of the organic film and the silicon substrate.

As discussed in Section 2.4.3, the scattering vector can be calculated according to Equation 2.29. Additionally, the small-angle approximation can be applied, as the incoming and scattering angles are all small. The incident angle can be derived geometrically from the SDD and pixel positions of the specular reflection ( $y_{\text{spec}}$ ) and direct beam  $y_{\text{DB}}$  via

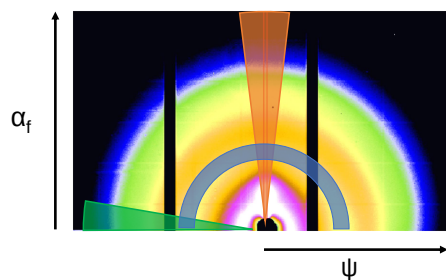
$$\alpha_i = \frac{1}{2} \arctan \left( \frac{(y_{\text{spec}} - y_{\text{DB}})}{\text{SDD}} \right), \quad (4.12)$$

Similar geometrical considerations lead to the respective lateral ( $\psi$ ) and vertical ( $\alpha_{i,f}$ ) deflection angles

$$\begin{pmatrix} \alpha_i + \alpha_f \\ \psi \end{pmatrix} = \begin{pmatrix} \arctan \left( \frac{(y - y_{\text{DB}})}{\text{SDD}} \right) \\ \arctan \left( \frac{(z - z_{\text{DB}})}{\text{SDD}} \right) \end{pmatrix}. \quad (4.13)$$

While the pixel positions can be obtained directly, the SDD needs to be determined via an initial measurement of a calibration sample, i.e. fresh silver behenate. Using the IGOR Pro macro package Nika, the SDD can be derived via the strong scattering peaks at well-defined angles.<sup>[216,217]</sup>

Data modeling is performed based on a model assuming spherical or cylindrical form factors with a Gaussian size distribution placed in a 1D paracrystalline lattice with a respective Gaussian distribution of mean distances represented by the structure factor. Additionally, scattering is assumed to only occur from objects of the same size, independent of the presence of other structures, using the local monodisperse approximation (LMA), while possible correlations are neglected (effective interface approximation (EIA)). Due to the reflection geometry, the framework of the distorted-wave Born approximation (DWBA) has to be applied. The instrument resolution limit for very low  $q_y$ -values is modeled with a Lorentzian resolution function. The model is applied using a Python 2.7 script written by Dr. Christoph J. Schaffer.<sup>[181]</sup> 2D GISAXS simulations are performed using the software BornAgain.<sup>[176]</sup>

**Figure 4.15**

Exemplary 2D GIWAXS data with the respective ROIs illustrated via colored areas. Radially integrated intensity profiles (red and green) yield information about in-plane and out-of-plane structures, respectively. From the azimuthally integrated intensity profile (grey-blue), information about the crystal orientation of a certain reflex, corresponding to a certain length scale, can be obtained.

#### 4.3.4 Grazing-Incidence Wide-Angle X-ray Scattering (GIWAXS)

In contrast to GISAXS, GIWAXS probes the signal at larger scattering angles and therefore structures on smaller length scales. The incoming X-ray beam is scattered at crystal lattice planes or in crystalline clusters of atoms in the thin film, leading to intensity maxima under the Bragg-angle  $\theta$  on the detector. Usually, the detector surface normal is assumed to be parallel to the incident beam. For the measurements presented in this work, however, the 2D GIWAXS detector (LAMBDA detector, pixel size  $55 \times 55 \mu\text{m}^2$ , X-Spectrum GmbH, Hamburg) is placed above the entrance of the GISAXS flight tube and tilted to an angle of about  $10^\circ - 20^\circ$  versus the sample horizon at a sample detector distance of 150 mm – 250 mm. To evaluate the collected data, the resulting geometrical distortions need to be corrected using a python-script. Afterward, subsequent intensity corrections and reshaping steps to account for the inaccessible  $q$ -space need to be performed, as described in more detail in Section 2.4.4. The data are reduced to 1D intensity profiles, to obtain quantitative information about the sample in the desired directions. For intensity corrections, reshaping and data reduction, the Matlab<sup>®</sup> based software GIXSGUI v1.7.1 is used.<sup>[169]</sup> Depending on the direction of integration, different information can be accessed. An exemplary intensity-corrected and reshaped 2D image with the respective ROIs is shown in Figure 4.15. The 2D data can be integrated in radial or azimuthal direction. From vertical, radially integrated intensity profiles (indicated in red) structural features perpendicular to the substrate can be obtained, while horizontal cuts (green) yield information about lateral structures. The crystal orientation can be estimated by azimuthal intensity profiles (grey-blue).

The small-angle approximation used for GISAXS is not viable for higher angles. Therefore, the  $q_x$ -component of the scattering vector  $\vec{q}$  cannot be neglected. When mapping the 2D scattering pattern in the typical  $q_r$ - $q_z$ -representation, the so-called missing wedge has to be taken into account, as discussed in Section 2.4.4. In brief, only signals fulfilling the Laue-condition – on the surface of the Ewald sphere – are collected. Transforming that information onto a 2D plane, while preserving the length of the vector  $q$ , leads to distortions that give rise to the missing wedge.  $\vec{q}$  exhibits a  $q_{xz}$ -component in the specular plane and a  $q_{xy}$ -component ( $q_r$ ) in the sample plane. This leads to a non-detectable region that is not accessible via diffuse scattering, as the bare

$q_z = \sqrt{(q^2 - q_x^2 - q_y^2)}$  component perpendicular to the sample surface is only accessible for  $q_y = q_x = 0$ . This condition is only fulfilled for zero lateral divergence ( $\psi_f = 0$ ) and specular reflection ( $\alpha_f = \alpha_i$ ). If the sample behaves like an in-plane powder, the reduced data are  $\sin(\chi)$  corrected to obtain pole figures that are representative of the amount of scattering material into the chi-direction of interest.<sup>[166]</sup> The material characteristic peaks are fitted using a combination of Pseudo-Voigt functions for each peak and an adequate background function depending on the noise from the exact sample environment. Usually, the Pseudo-Voigt functions show an almost Gaussian behavior, but very small Lorentzian parts play a role when fitting very early stages of film growth with very low intensities. From the fitting parameters, conclusions about the crystal properties such as the crystal size, distance, and distribution can be derived. The minimum crystal size is estimated using the Scherrer equation (see Equation 2.38).

# CHAPTER 5

## Influence of Polymer Side Chains on the Growth of Gold Electrodes during Sputter Deposition

The following chapter is based on the publication “Following in Situ the Deposition of Gold Electrodes on Low Band Gap Polymer Films” (Löhrer et al., *ACS Applied Materials & Interfaces*, 2020).<sup>[218]</sup> Reproduced with permission from the American Chemical Society.

Metal top electrodes such as gold are widely used in organic solar cells. The present chapter investigates the effect of side-chain engineering of the photoactive polymer on the structure formation of the gold electrode, comparing the low-bandgap polymers PTB7 and PTB7-Th. The growth of gold contacts on the polymer films is investigated with in-situ GISAXS and GIWAXS during the sputter deposition of gold. From grazing-incidence wide-angle X-ray scattering (GIWAXS) the crystal structure of the gold film is determined. Independent of the type of the side chain, gold crystals form in the very early stages and improve in size and crystallinity during the sputter deposition until the late stages. From grazing-incidence small-angle X-ray scattering (GISAXS), the nanoscale structure is determined, as discussed in detail in Section 2.4.3. Differences in terms of gold cluster size and growth phase limits for the two polymers are caused by the side-chain modification and result in a different surface coverage in the early phases. The changes in the diffusion and coalescence behavior of the forming gold nanoparticles cause differences in the morphology of the gold contact in the fully percolated regime, which is attributed to the different amount of thiophene rings of the side chains acting as nucleation sites.

## 5.1 Introduction

A major contribution to the increase in the performance of organic photovoltaic (OPV) devices has been made by the synthesis and optimization of highly efficient photoactive materials. This led to the development of whole families of polymers of the same backbone with different side chains and, accordingly, different energy levels and absorption spectra.<sup>[21]</sup> The bandgap tuning via side-chain engineering has been an immensely successful factor in finding new high-efficiency materials. A prominent example is the low-bandgap polymer mainly investigated in the present thesis, PTB7-Th as derivative of PTB7 (see also Section 3.1.1). PTB7-Th contains two 2-ethylhexyl-thienyl groups which are incorporated into the benzodithiophene unit of PTB7, substituting oxygen groups to improve the coplanarity of the backbone and to red-shift the respective absorption spectrum.<sup>[31]</sup> In comparison to power conversion efficiencies (PCEs) of around 9% for solar cells based on PTB7, this modification enabled PCE values beyond 10% when using PTB7-Th as donor material in the active layer.<sup>[13,23,184,197,219–221]</sup>

Although organic electronic devices are mostly based on purely organic or organic-inorganic hybrid materials, many electrodes are still made from pure metals due to their unrivaled electrical conductivity. This implies that the polymer-metal interface plays a vital role in the final device performance, as is detailed in Section 2.3. Research efforts have successfully established the application of ultrathin metal electrodes for semi-transparent solar cells.<sup>[222,223]</sup> Additionally, metal nanoparticles can be implemented in photovoltaic devices to enhance light-harvesting using various plasmonic effects.<sup>[224–226]</sup> The right choice of electrode can increase the morphological stability of optically active organic layers<sup>[21]</sup> or offer a better energy level alignment, e.g. via bandgap tuning.<sup>[25]</sup> The quality of the interface determines the extent of structural defects, which could increase the resistance and the chances of a short circuit.<sup>[10]</sup> For research purposes, these back contacts are mostly applied using lab-scale methods, for example, thermal evaporation. In industry, however, large-scale techniques, such as sputter deposition methods, are preferred.<sup>[29,30]</sup> Thus, understanding the formation of the polymer-metal interface via sputter deposition is of utmost importance for reproducible, optimized, and scalable organic electronic devices.

A powerful technique for the real-time investigation of the formation of the polymer-metal interface during the deposition process is *in situ* GISAXS.<sup>[142,164,227]</sup> Studies of gold sputtering on polystyrene-block-polyisoprene-block-polystyrene (P(S-*b*-I-*b*-S))<sup>[131]</sup> and poly(*N*-vinylcarbazole) (PVK)<sup>[132]</sup> gave basic insights into the fundamental growth mechanisms. This understanding was then expanded by studies on amorphous silicon and polystyrene (PS), which led to the definition of a growth model and the understanding of the role of the sputter deposition rate on the gold film formation up to industrially relevant deposition rates.<sup>[133,142,146]</sup> GISAXS offers the unique advantage of non-destructively following the metal growth *in situ* with a high time-resolution,

thereby gaining valuable information about each stage of the deposition without having to manipulate, slow down or pause the deposition process.

The utilization of side-chain-modified polymers for highly efficient organic solar cells raises the question of how the deposition behavior of sputtered metal electrodes is influenced by the chemical composition and nanostructure of the respective conductive polymers. To date, most of the investigations of electrode sputtering are performed on standard polymers and silicon substrates and the transfer of the found knowledge to materials relevant for organic photovoltaics is still missing. However, exactly such knowledge will be necessary for the efficient production of these solar cells based on modified low-bandgap polymers.

In the following chapter, the differences in growth behavior of a sputtered gold layer onto thin films of the two low-bandgap polymers PTB7 and PTB7-Th are investigated to study the effect of bandgap tuning via side-chain engineering on the formation of the metal contact. Both polymers have been studied intensively in terms of their photovoltaic properties,<sup>[197,228-232]</sup> but not with respect to their effect on the back electrode. The structural and morphological changes during the sputter deposition of gold atoms forming a thin gold layer on each of the polymer films will be discussed in the following. As shown in earlier experiments, the deposition rate has a pronounced effect on the growth mode of metal films.<sup>[142,233]</sup> Based on these findings, a sputter deposition rate was chosen which is industrially relevant, yet still enables time-resolved insights into the early stages of the growth process. The gold film deposition is divided into distinct growth phases, which are defined by their respective predominant nanoscale processes. The structure model is verified by model-based simulations of the different phases.

## 5.2 Experimental Details

To study the growth of the gold layer on top of PTB7 and PTB7-Th thin films, the polymer-metal interface during the growth of the nanogranular gold layer is monitored. General information can be found in Chapter 3 and Chapter 4, while experiment-specific details are given below.

**Materials and sample preparation:** Silicon wafers are cut into pieces of  $12 \times 15 \text{ mm}^2$ , cleaned using an acid bath, rinsed with deionized water, and dried under nitrogen flow.<sup>[193]</sup> After subsequent treatment with oxygen plasma for 10 min, the cleaned substrates are transferred to a glovebox for the sample preparation. Due to the sensitivity of the used polymers, the following steps are performed under an inert nitrogen atmosphere. PTB7 and PTB7-Th are each dissolved in chlorobenzene (CB) with a concentration of  $10 \text{ mg mL}^{-1}$  for PTB7 and  $15 \text{ mg mL}^{-1}$  for PTB7-Th and stirred for 15 h at  $60^\circ\text{C}$  to allow for complete dissolution. Samples are prepared via spin casting the respective polymer solution under an inert atmosphere on a cleaned silicon sub-

strate at 1000 rpm for 40 s. They are left to dry under nitrogen atmosphere for one day, before sealing them individually in sealed aluminum bags for the transport from the laboratory to the synchrotron facility.

**Sputter deposition:** For the deposition process, a custom-built sputter setup is used, as described in more detail in earlier publications.<sup>[142]</sup> The setup includes a high-vacuum chamber with a direct current (DC) magnetron sputter source, load-lock system, and several openings for additional characterization equipment. Inside the sputter chamber, a polymer thin-film sample is placed below a gold target, from which gold atoms can be sputtered and deposited onto the sample (see Figure 5.1). The average sputter rate can be controlled by varying the applied power and tracked using a quartz crystal microbalance. The vacuum needed for the sputtering process is created using a system of pumps, which leads to a base pressure in the range of  $1 \times 10^{-6}$  mbar. After applying an argon gas flow the working pressure is around  $5 \times 10^{-3}$  mbar. By application of a voltage of 335 V, an argon plasma is created, which enables the sputtering of gold atoms from the plasma-cleaned 2-inch gold target (99.999% purity, Kurt J. Lesker, United States). The nominal sputter rate of  $0.2 \text{ nm s}^{-1}$  is adjusted by applying a power of 14 W. After 103.5 s, the final layer thickness  $\delta_{Au,final} \approx 22 \text{ nm}$  is reached.

**In-situ scattering investigation:** To perform GISAXS and GIWAXS experiments with a high temporal and spatial resolution, the sputter deposition setup is implemented into the Micro- and Nano-focus X-ray Scattering (MiNaXS) beamline P03 of the brilliant synchrotron light source PETRA III at Deutsches Elektronen-Synchrotron (DESY) in Hamburg, Germany.<sup>[214]</sup> The measurements are performed at an energy of 13.0 keV ( $\lambda = 0.953 \text{ \AA}$ ) with a micro-beam spot size of  $31 \times 42 \mu\text{m}^2$  on the sample. To ensure the penetration of the complete gold film by the X-ray beam, an incident angle ( $\alpha_i = 0.446^\circ$ ) slightly above the critical angle of gold ( $\alpha_{c,Au} = 0.337^\circ$  at this energy) is chosen, thus obtaining information on the gold layer, its interface to the polymer, and the polymer thin film itself. Potential X-ray beam damage is prevented by scanning the sample continuously over a range of 2 mm with a rate of  $0.6 \text{ mm s}^{-1}$  in horizontal direction. The scattered X-rays are recorded with two 2D pixel detectors. The GISAXS detector is placed at a larger sample-to-detector distance (SDD) perpendicular to the direct beam. The GIWAXS detector is placed at a closer distance and at a tilted angle above the direct beam path to detect X-rays scattered at higher angles and thereby ensure observation of the corresponding Bragg angles of gold. Figure 5.1 schematically illustrates the experimental geometry. The X-ray beam (red) enters the sputter chamber through a Kapton<sup>®</sup> window and hits the sample at a small angle. It is specularly reflected (red) and scattered (green) due to structures present in the polymer and gold layers. The GISAXS detector is illustrated with an exemplary 2D scattering data placed at a larger distance from the sputter setup. Black areas originate from different sources: a) gaps between the detector elements, b) shadowing of

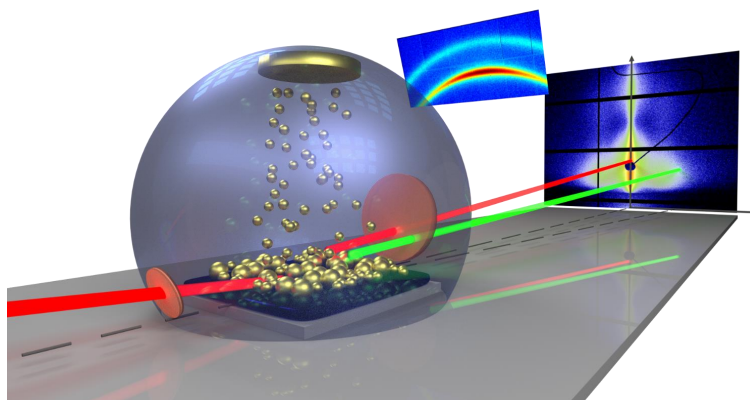


**Figure 5.1**

Schematic of the GISAXS experiment depicting the in-situ GISAXS and GIWAXS measurements during the deposition of gold on a thin-film sample in a sputter chamber. The incoming X-ray beam and the specularly reflected beam are depicted in red; an exemplary scattered X-ray beam caused by lateral structures in the forming gold film is shown in green. The grey sphere indicates the sputter chamber, the red circles the entry and exit windows. The sputtered gold atoms are shown as golden spheres. After leaving the sputter target, they impinge on and self-assemble at the substrate.

the evacuated small-angle X-ray scattering (SAXS) tube, and c) the beam stop placed on the position of the specular beam. The tilted GIWAXS detector is shown at a closer distance to the sputter setup (not to scale). An exemplary GIWAXS data from a later stage of the gold film growth is chosen for an illustration of the scattering pattern. The growth process is visible by the changes in the 2D scattering patterns taken during the gold deposition.

**In-situ GISAXS:** The data are recorded using the 2D detector Pilatus 1M (Dectris Ltd.) with a pixel size of  $172 \times 172 \mu\text{m}^2$  in an SDD of  $(2376 \pm 2)$  mm. With a frame rate of  $20 \text{ s}^{-1}$  and 103.5 s of deposition time, 2070 2D scattering data are acquired for each sample. To analyze the 2D data, the scattering intensity in specific regions of interest is integrated via the software Directly Programmable Data Analysis Kit (DP-DAK)<sup>[215]</sup> and fitted using an appropriate geometric model. 2D GISAXS simulations are performed using the software BornAgain.<sup>[176]</sup> Vertical line cuts either around  $q_y = 0$  ( $\pm 5$  px, so-called detector cuts) or from  $q_y = 0.1 \text{ nm}^{-1} - 2.5 \text{ nm}^{-1}$  (so-called off-detector cuts) are analyzed to acquire information about the film depth profile. To gain insights into the lateral structures of the samples, horizontal line cuts at the Yoneda position of a specific material are made. The Yoneda region is defined by a material's critical angle of total reflection and is very similar for many organic materials, as described in more detail in Section 2.4.3.<sup>[154]</sup> Bulk gold films show a much higher critical angle as compared to the polymers. However, as the gold deposition is investigated in situ, the gold layer initially exhibits a vastly decreased (optical) density and therefore de-

creased critical angle. During the deposition process, this critical angle increases with a growing electron density towards the bulk gold value of  $q_z = 0.90 \text{ nm}^{-1}$ . Therefore, a horizontal region of interest is chosen in such a way that it includes the Yoneda region of the polymers and ranges up to the finally reached gold Yoneda region with  $0.62 \text{ nm}^{-1} < q_z < 0.90 \text{ nm}^{-1}$ . The average film thickness of the samples before and after the deposition is obtained using static GISAXS data recorded on the pure polymer films and on the final gold layers.

**In-situ GIWAXS:** The data are acquired analogously to GISAXS data, with a few changes, as follows. During the sputter deposition process, 207 2D scattering data are acquired for each sample with a frame rate of  $2 \text{ s}^{-1}$ . The 2D GIWAXS detector (LAMBDA detector, pixel size  $55 \times 55 \mu\text{m}^2$ , X-Spectrum GmbH, Hamburg) is placed above the flight tube (connecting the sample chamber with the GISAXS detector) and tilted at an angle of about  $17.8^\circ$  versus the sample horizon at a sample detector distance of  $(183 \pm 2) \text{ mm}$  to detect the two important Bragg peaks at  $2.676 \text{ \AA}^{-1}$  (111) and  $3.088 \text{ \AA}^{-1}$  (200) for gold (space group  $Fm\bar{3}m$ ).<sup>[234]</sup> To evaluate the collected data, the tilt of  $17.8^\circ$  is corrected geometrically using a python script. Afterward, typical further intensity corrections and reshaping steps to account for the inaccessible q-space are performed using the MATLAB-based software GIXSGUI.<sup>[169]</sup> 1D vertical cuts are integrated for  $\chi$  between  $-15^\circ$  and  $+15^\circ$  and fitted using a constant background in combination with a Pseudo-Voigt function for each of the two Bragg peaks.

**Real-space imaging:** For investigating the surface morphology of the sputtered films, scanning electron microscopy (SEM) data are obtained using the high-resolution field emission SEM Zeiss Gemini Nvision 40 with 5 kV at 3.6 mm distance.

## 5.3 In-situ Characterization

For the in-situ investigation of the deposition process, GISAXS and GIWAXS are chosen as non-invasive methods for measurements with a high time resolution.<sup>[164,235]</sup>

### 5.3.1 Evolution of Crystallinity

The crystallinity of the deposited gold layer is tracked using GIWAXS. Representative 2D GIWAXS for specific stages of the film growth before, during, and after the gold layer deposition are plotted in Figure 5.2 for PTB7 and PTB7-Th, respectively. To enable comparisons to other experiments, the sputter deposition time can be converted to the effective film thickness  $\delta$  ( $10 \text{ s} \approx 2.1 \text{ nm} - 2.2 \text{ nm}$ , as discussed in Section 5.3.2). The 2D GIWAXS data show the pure polymer films ( $\delta = 0 \text{ nm}$ ), the five different growth phases ( $\delta \approx 0.2, 1, 2, 4$  and  $8 \text{ nm}$ ) as well as a late growth stage ( $\delta \approx 20 \text{ nm}$ ).

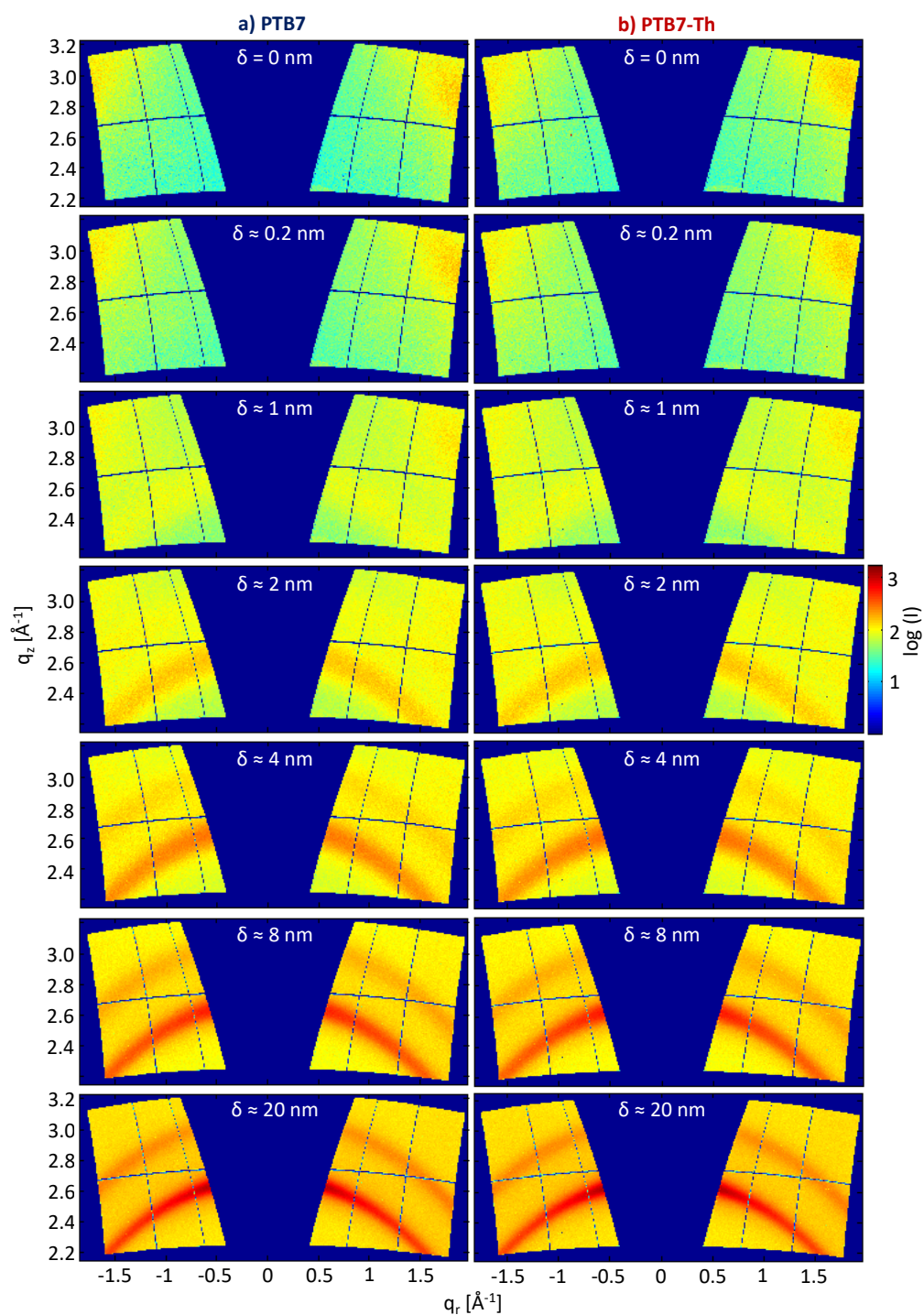


**Figure 5.2**

Exemplary 2D GIWAXS data for a) PTB7 and b) PTB7-Th, taken at specific stages of the film growth, corresponding to the pure polymer film (effective film thickness  $\delta = 0$  nm), the five different growth phases ( $\delta \approx 0.2, 1, 2, 4$  and  $8$  nm) as well as a late growth stage ( $\delta \approx 20$  nm). Intensity corrections and reshaping steps are performed using the MATLAB-based software GIXSGUI.<sup>[169]</sup>

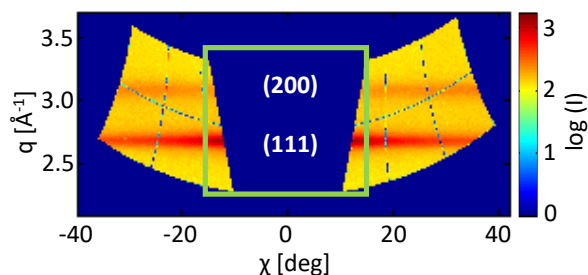


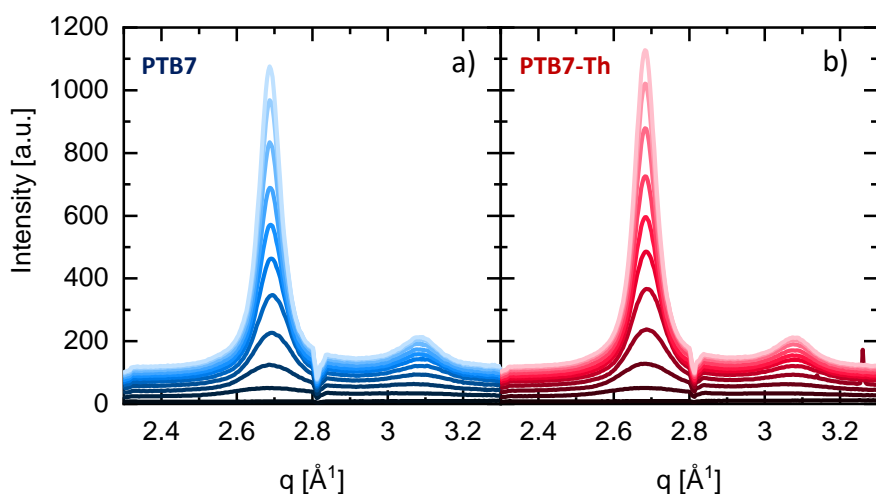
**Figure 5.3**

Exemplary region of interest for the vertical cuts (for  $\chi$  between  $-15^\circ$  and  $+15^\circ$ ) with visible gold Bragg peaks (111) and (200).

The definition of the respective growth phases will be discussed in Section 5.3.3. In general, GIWAXS data yield information on the crystalline structure and spacing of materials, here the deposited gold layers. The evolution of the structural features causes changes in the scattering patterns due to the growing gold layer. At first glance, these changes show a high similarity for both polymer samples.

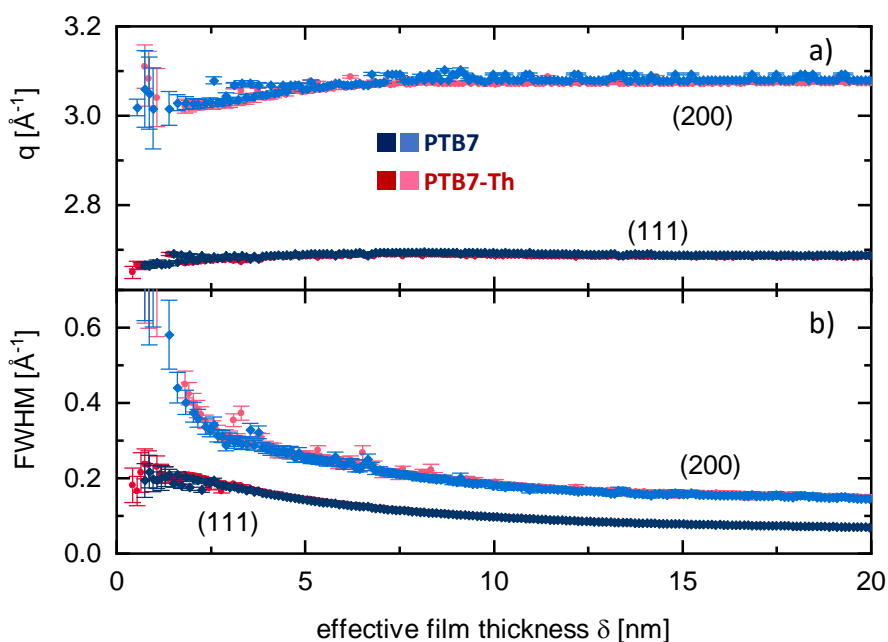
For further evaluation, the 2D data are reduced to 1D data by focusing on a certain region of interest (ROI). Intensity corrections and reshaping steps are performed using the MATLAB-based software GIXSGUI.<sup>[169]</sup> A typical ROI is sketched in Figure 5.3, with a vertical cut integrated over the azimuthal angle  $\chi$  from  $-15^\circ$  to  $+15^\circ$ . It is important to note the difference in representation of the data as compared to Figure 5.2. The two gold Bragg peaks (111) and (200) are clearly visible. The respective 1D data can be found in Figure 5.4 for PTB7 and PTB7-Th. Two Bragg peaks are visible for the vertical direction, namely the (111) peak at  $2.676 \text{ \AA}^{-1}$  and the (200) peak at  $3.088 \text{ \AA}^{-1}$ . Fitting these Bragg peaks with Pseudo-Voigt functions, their  $q$  position their width are extracted.

Figure 5.5 shows the changes of the  $q$  position and the full width at half maximum (FWHM) for the (111) and (200) Bragg peak as a function of effective gold film thickness  $\delta$ . The trends in peak position and FWHM illustrate the similar behavior of the gold films on both samples in terms of their crystalline structure. At the beginning of the deposition process, the  $q$  values for both peaks increase, indicating a decrease in lattice parameters, as expected for the formation of nanocrystals. For both polymers alike, the final  $q$  position – meaning the final gold lattice spacing – is established in a very early stage of the deposition process: after  $\delta \approx 3 \text{ nm}$  for the (111) Bragg peak and after  $\delta \approx 4 \text{ nm} - 5 \text{ nm}$  for the (200) peak. This difference can be attributed to the significantly lower intensity of the (200) peak. Only at a certain threshold intensity, the fit quality is high enough to give consistent  $q$  values. The FWHM exhibits an exponential decrease for both peaks, meaning that the crystal quality and size increase during the sputter deposition. Again due to its much lower intensity, the (200) peak is fitted with a broader FWHM. For the (111) peak, the exponential decrease starts after around  $\delta \approx 1.5 \text{ nm}$ . Summarily, the increase in crystallinity with the growing layer thickness is illustrated by the strong increase in the Bragg peak intensity and in the decrease of the FWHM.



**Figure 5.4**

Evolution of the gold crystallinity illustrated via exemplary vertical cake cuts (for  $\chi$  between  $-15^\circ$  and  $+15^\circ$ ) of the 2D GIWAXS data (taken every  $\delta \approx 2.1$  nm starting at  $\delta = 0$  nm) for a) PTB7 (blue, dark to light) and b) PTB7-Th (red, dark to light). The Bragg peaks can be fitted with Pseudo-Voigt functions to extract structural parameters.



**Figure 5.5**

The (111) and (200) Bragg peaks are fitted with Pseudo-Voigt functions plus constant background for all frames. The results are plotted over effective film thickness, showing no pronounced differences between the polymers PTB7 (blue) and PTB7-Th (red) for a) the  $q$  positions and b) the FWHM of the (111) and (200) Bragg peaks (illustrated in dark and light colors, respectively).

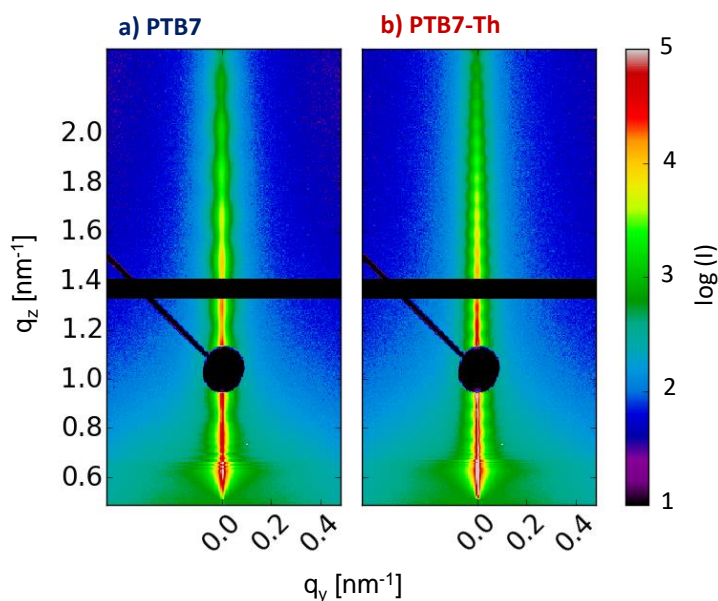


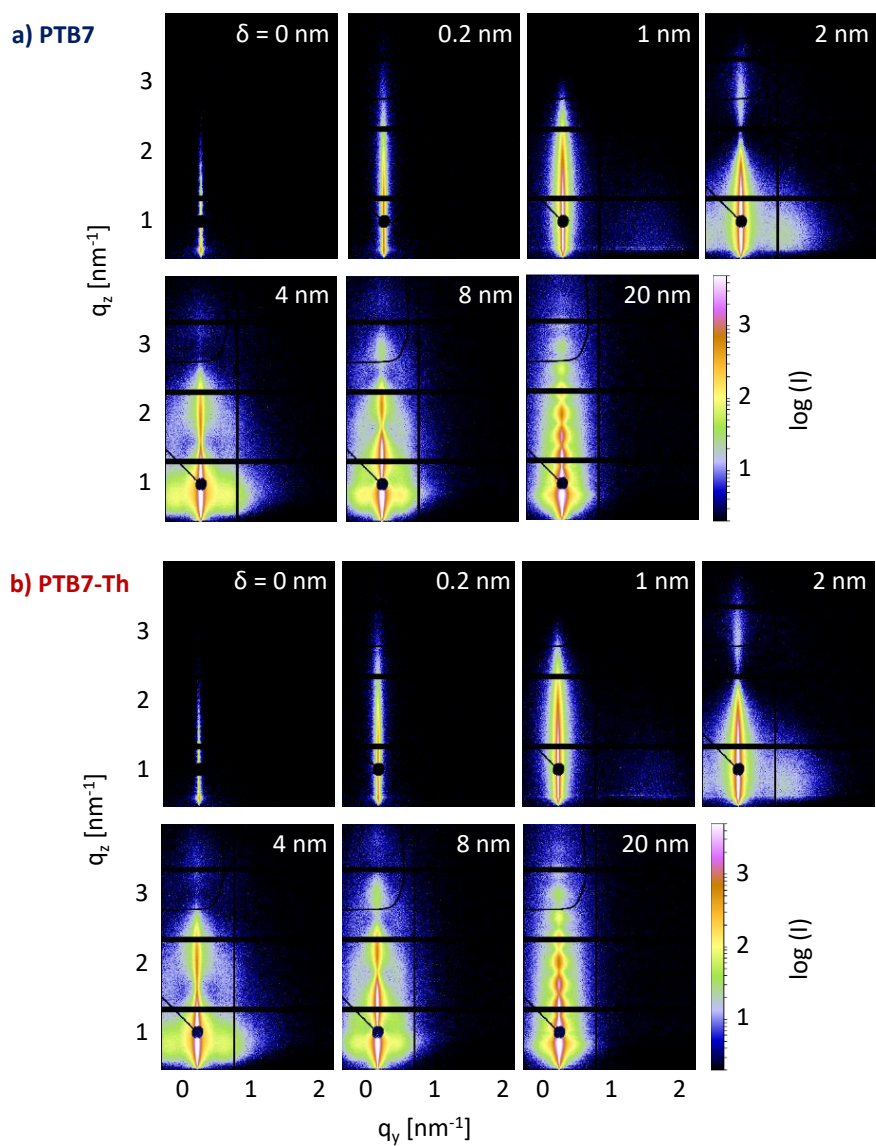
**Figure 5.6**

Initial 2D GISAXS data for a bare a) PTB7 and b) PTB7-Th thin film, summed up over  $11 \times 1$  s for an improved signal-to-noise ratio.

### 5.3.2 Film Thickness Evolution

Using GISAXS, information is obtained on the morphological changes such as the creation and growth of gold clusters. Before looking into the gold deposition process itself, the pure polymer films are investigated, illustrated with 2D data in Figure 5.6. As the pure polymer films show only weak scattering, eleven scattering data of 1 s duration each are summed to increase the statistics and to reduce the signal-to-noise ratio. No prominent scattering features are seen in horizontal direction, as is expected from homogeneous films of one material. The main scattering is visible in vertical direction, correlated to the film thickness, which will be discussed later in more detail.

After the initial measurements, the actual sputter deposition is followed using in-situ GISAXS. Similar to the GIWAXS data discussed before, representative 2D GISAXS data for specific stages of the film growth before, during, and after the gold layer deposition can be found in Figure 5.7 for PTB7 and PTB7-Th, respectively. At first glance, already significant changes in the scattering pattern are visible. The overall scattering intensity increases drastically and scattering features appear or change significantly. The trend is very similar for both observed samples. In the 2D GISAXS data, the in-plane evolution of gold clusters in terms of their average size and distance is visible in the  $q_y$ -direction, while the layer growth in vertical direction leads to the evolution of the intensity fringes in the  $q_z$ -direction. The chosen ROIs for horizontal and vertical line cuts are integrated along  $q_z$  and  $q_y$ , respectively, to obtain 1D data.

**Figure 5.7**

Exemplary 2D GISAXS data for a) PTB7 and b) PTB7-Th, taken at specific stages of the film growth, corresponding to the pure polymer film (effective gold film thickness  $\delta = 0$  nm), the five different growth phases ( $\delta \approx 0.2, 1, 2, 4$  and  $8$  nm) as well as a late growth stage ( $\delta \approx 20$  nm). In horizontal direction, the in-plane evolution of structures can be observed in form of intensity maxima, while in vertical direction, the formation of Kiessig fringes resulting from the gold layer is seen.

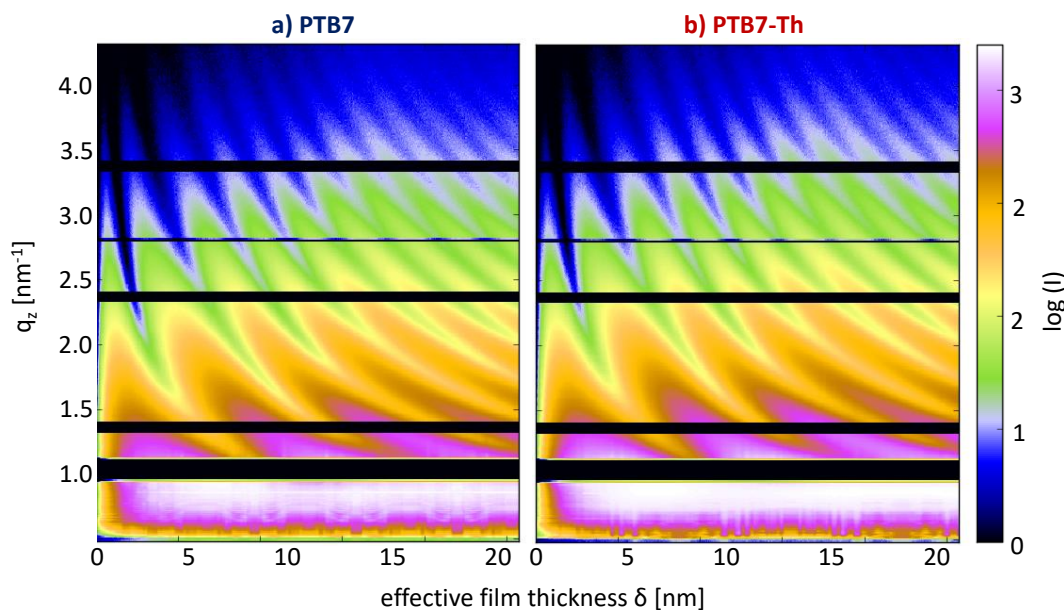


**Figure 5.8**

Contour mapping plots of the vertical line cuts integrated for every frame for a) PTB7 and b) PTB7-Th and plotted as a function of effective film thickness  $\delta$ .

Figure 5.8 shows the contour plots of the integrated vertical line cuts over effective film thickness  $\delta$  for both polymers in comparison. The observed intensity fringes illustrate the increasing thickness of the gold cluster layer during sputter deposition. In the lower  $q_z$ -range of the vertical line cuts, the Yoneda regions of the investigated materials can be observed. Especially for the first stages of deposition, a strong increase in intensity and a shift to higher  $q_z$ -values is visible.

Focusing on the region below  $q_z \approx 0.95 \text{ nm}^{-1}$ , the trend can be followed in more detail. Figure 5.9 illustrates the shift in maximum intensity from the Yoneda region of the polymers (at around  $0.63 \text{ nm}^{-1}$ ) towards the bulk gold value of  $0.902 \text{ nm}^{-1}$ . This shift and the general increase of the intensity are caused by the growing gold film thickness for the first 6 nm of effective gold film thickness. In later stages, additional intensity extrema due to the growing film thickness move from higher  $q_z$  values into the shown range, partly overlapping the gold Yoneda peak. Interestingly, the intensities for PTB7-Th increase much faster compared to those of PTB7, which hints at a rougher surface leading to more forward scattering for PTB7-Th.

The film growth itself can be followed using exemplary vertical line cuts, taken every  $\delta \approx 2.1 \text{ nm}$ , as shown in Figure 5.10 for PTB7 (blue) and PTB7-Th (red). Here, the evolution and shift of the maxima are even more prominent. The data are fitted using a combination of an exponential background with a Gaussian function for each peak and illustrated with black lines. The dark curves at the bottom of each diagram show the scattering intensity of the used pure polymers. The top curves are taken at the end of

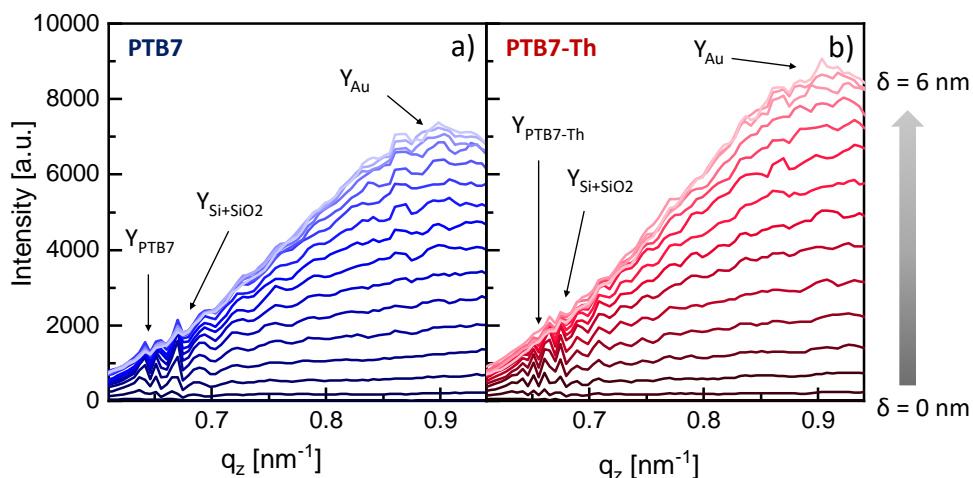


**Figure 5.9**

Evolution of the scattering intensity in vertical direction for a) PTB7 and b) PTB7-Th, illustrating the Yoneda peaks of the polymer layer in the first stages (dark curves, peaks at around  $q_z \approx 0.66 \text{ nm}^{-1} - 0.67 \text{ nm}^{-1}$ ) and the evolution of the strong Yoneda peak intensity of the thin gold layer evolving at  $q_z \approx 0.9 \text{ nm}^{-1}$  within the first 6 nm of effective film thickness.

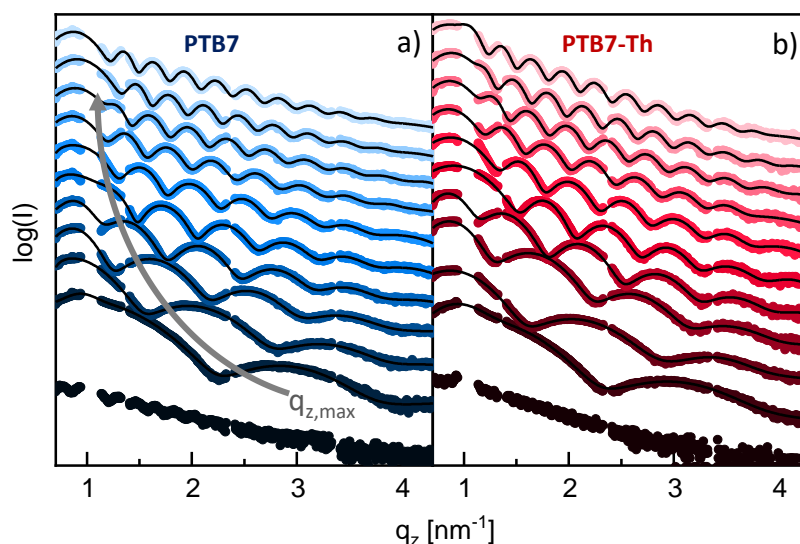


**Figure 5.10**

Structural evolution in vertical direction illustrated via exemplary integrated vertical line (detector) cuts of the GISAXS data at  $q_y = 0 \text{ nm}^{-1}$ , taken every  $\delta \approx 2.1 \text{ nm}$  starting at  $\delta = 0 \text{ nm}$ , and respective fits (black lines) for a) PTB7 (blue) and b) PTB7-Th (red). The intensities are plotted logarithmically for a better visualization of the maxima and shifted along the intensity axis for clarity.

the gold layer deposition and result from the final film structure. For the pure polymer films typical Kiessig fringes are caused by a combination of refraction and reflection of the incident wave due to the highly homogeneous film thickness.<sup>[160,236]</sup> From the intensity fringes, an average pure polymer film thickness of  $\delta_{polymer} \approx (35 \pm 2)$  nm for PTB7 and  $(84 \pm 2)$  nm for PTB7-Th is calculated, which is in accordance with profilometry measurements performed on identical polymer films:  $(40 \pm 5)$  nm and  $(80 \pm 5)$  nm, respectively. The difference in the film thickness is of no consequence for the discussed experiments, as the sputter deposition only affects the very first few nanometers of the polymer films.<sup>[130,237]</sup>

Starting the sputtering process leads to a pronounced increase in scattering intensity due to the deposition of the electronically dense, strongly scattering gold particles on the polymer films. The scattered intensity soon completely eclipses the Kiessig fringes of the original polymer film. A few seconds after the start of the deposition process, at an effective film thickness  $\delta \approx 1$  nm of the gold film, new intensity modulations arise due to the evolving gold film.<sup>[236]</sup> With ongoing gold sputter deposition, more and more intensity extrema occur and shift to smaller  $q_z$  values, thereby indicating a growth in the average film thickness. By fitting the intensity maxima using a combination of an exponential background with a Gaussian function for each peak, the evolution of the extrema can be followed. From these peak positions, the average film thickness  $\delta_{Au}$  for each growth stage can be deduced according to Equation 2.28

$$\delta_{Au} \approx \frac{2\pi}{\Delta q_z},$$

with  $\Delta q_z$  being the difference of two neighboring maxima or minima. The final film thickness can be determined from GISAXS data taken after the sputtering process to be  $\delta_{Au(final)} \approx (22.4 \pm 0.2)$  nm for PTB7 and  $(22.1 \pm 0.2)$  nm for PTB7-Th. With a sputtering time of 103.5 s, an identical effective film thickness growth rate of  $(0.22 \pm 0.02)$  nm s<sup>-1</sup> and  $(0.21 \pm 0.02)$  nm s<sup>-1</sup>, respectively, is calculated. These results are in good accordance with the actual sputter rate of 0.2 nm s<sup>-1</sup>, which is measured using a quartz crystal microbalance prior to the start of the deposition.

Figure 5.11 illustrates the evolution of the average gold film thickness  $\delta_{Au}$  as function of the effective film thickness  $\delta$ . While  $\delta_{Au}$  grows linearly for later stages after  $\delta \approx 3$  nm, a clear offset is visible at the beginning for both polymers. This already gives a hint towards the growth mechanism, with a preferred creation of gold clusters of a certain height  $H$  instead of a uniform monolayer on top of the polymer thin film. This cluster height  $H$  can be estimated using the first-order minima visible in vertical direction for  $0.01 \text{ nm}^{-1} < q_y < 2.5 \text{ nm}^{-1}$  (so-called off detector line cuts), which are related to the form factor and thereby the height of the clusters.

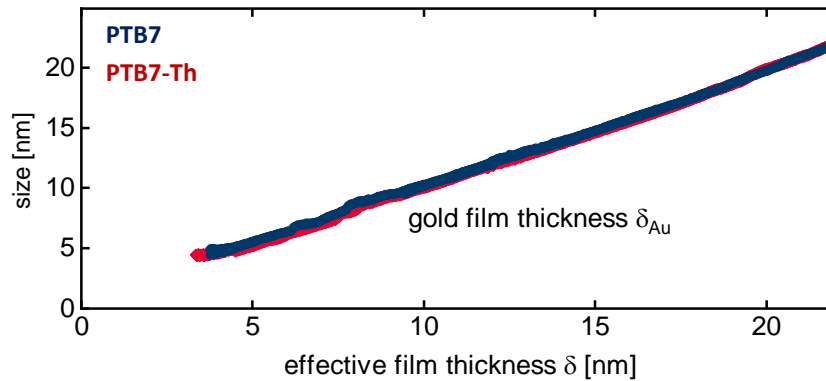


**Figure 5.11**

Average gold film thickness  $\delta_{Au}$  for PTB7 (blue) and PTB7-Th (red), as extracted from  $\Delta_{q_y, max}$  of the fitted detector cuts, plotted over the effective film thickness  $\delta$ .

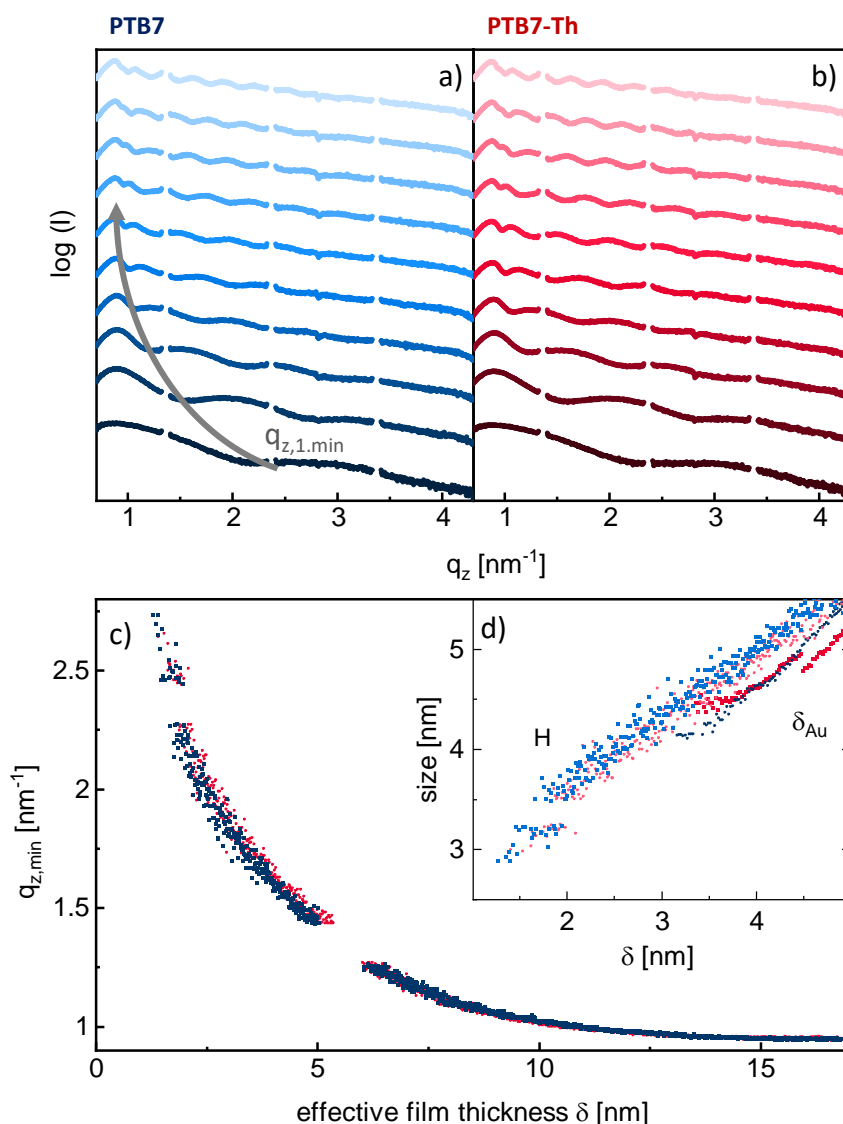
In Figure 5.12, exemplary off-detector cuts for PTB7 and PTB7-Th are plotted, illustrating the shift of the first-order minima to smaller  $q_z$ -values. Figure 5.12 c) shows the fitted  $q_{z,1.min}$  position during the deposition process. From the fitted  $q_{z,1.min}$  position in these so-called off-detector cuts,  $H$  can be deduced, as explained in the following. The first-order minimum in the off-detector cuts is directly related to the form factor – and therefore the height  $H$  – of the scattering clusters. The evolution of  $q_{z,1.min}$  as exponential function of effective film thickness

$$q_{z,1.min} \approx Ae^{\delta/t} + y_0 \quad (5.1)$$

is fitted for both polymers, resulting in  $A \approx 2.61$  and  $2.51$ ,  $t \approx 3.02$  and  $2.97$ ,  $y_0 \approx 0.93$  and  $0.94$  for PTB7 and PTB7-Th, respectively. From earlier work by Schwartzkopf et al. (see the corresponding Supporting Information), the simulated  $q_{z,1.min,sim}$  for hemispherical clusters of different heights in a distance of 20 nm are known.<sup>[133]</sup> Using the relation

$$q_{z,1.min,exp}(\delta) = q_{z,min,sim}(H) \quad (5.2)$$

of the fit functions, the cluster height  $H(\delta)$  can be extracted for  $\delta < 8$  nm. Figure 5.12 d) shows the evolution of  $H$  (light symbols) for the first 5 nm of effective film thickness in comparison to the average layer thickness  $\delta_{Au}$  (dark symbols), again pointing to the formation of islands in the very early stages of gold deposition.  $H$  is not only slightly larger than the respective average thickness  $\delta_{Au}$ , but shows a significant offset of about 2 nm, when linearly extrapolating to the beginning of the deposition process.

**Figure 5.12**

Structure evolution in vertical direction illustrated via exemplary integrated vertical line (off-detector) cuts of the GISAXS data at  $0.1 \text{ nm}^{-1} < q_y < 2.5 \text{ nm}^{-1}$ , taken every  $\delta \approx 2.1 \text{ nm}$  starting at  $\delta = 0 \text{ nm}$  for a) PTB7 and b) PTB7-Th. The intensities are plotted logarithmically for a better visualization of the maxima and shifted along the intensity axis for clarity. c) Position of the first-order minimum  $q_{z,1,min}$ , as extracted from the off-detector cuts for PTB7 (blue) and PTB7-Th (red), plotted over effective film thickness  $\delta$ . d) Average gold cluster height  $H$  (light symbols) for PTB7 (blue) and PTB7-Th (red), calculated from the  $q_{z,1,min}$  position, plotted over  $\delta$  in comparison to the early values for  $\delta_{Au}$  (dark symbols), which are shown in detail in Figure 5.11.

### 5.3.3 Morphological Evolution

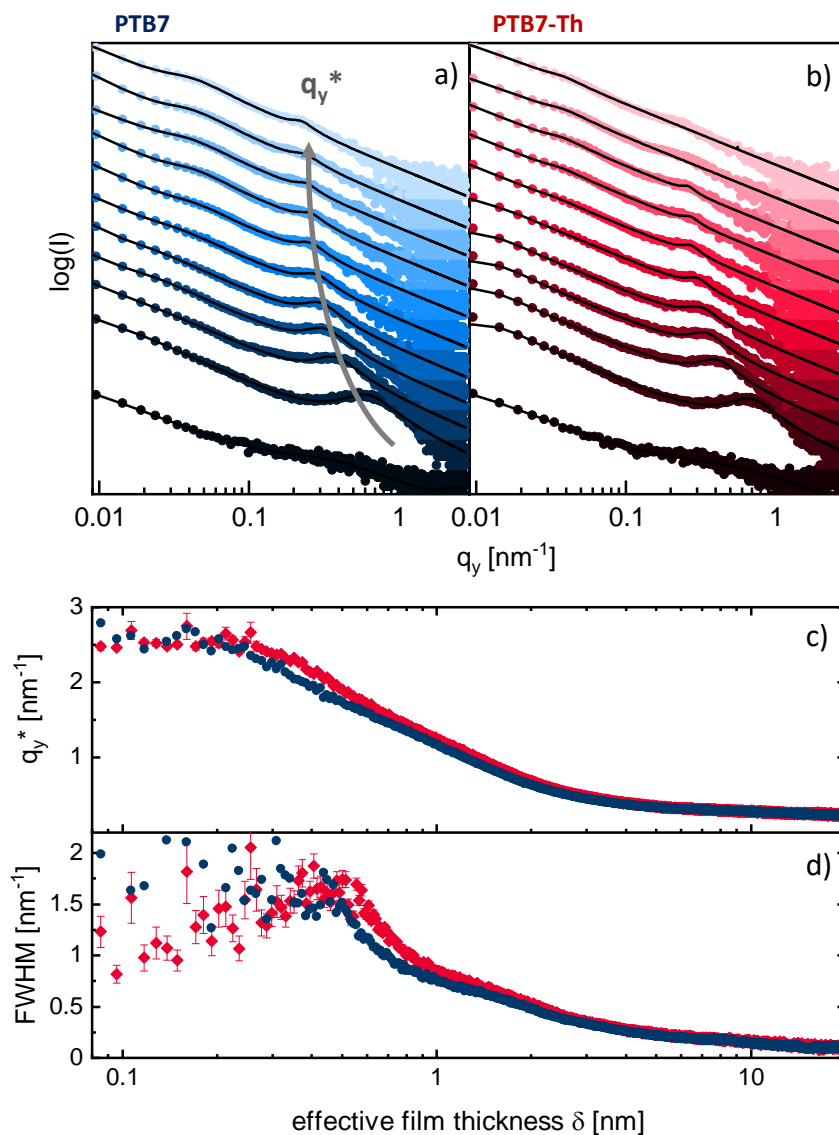
Figure 5.13 illustrates this island growth in lateral direction. Selected horizontal line cuts, taken every 2.1 nm of effective film thickness, are shown for PTB7 (blue) and PTB7-Th (red) with the respective fits (black lines, using a combination of Gaussian and Lorentzian functions for the intensity maxima). The black curves at the bottom of each diagram show the scattering intensity of the used pure polymers. The top curves are taken at the end of the layer deposition and show the final film structure. The pure polymer films show no pronounced scattering peaks in horizontal direction. Soon after starting the sputtering process, a broad maximum in intensity evolves at  $q_y^* \approx 2.6 \text{ nm}^{-1}$  and subsequently shifts to smaller  $q_y^*$  values, indicating the creation of gold clusters. In later stages of the film growth ( $\delta > 12 \text{ nm}$ ), a second, weaker maximum can be distinguished at a  $q_y^*$  value of about  $0.05 \text{ nm}^{-1}$ , indicating a second, larger scattering feature, for example coarse, ramified domains. The peak width is affected by the average cluster size and shape distribution as well as the disorder in the paracrystalline lattice. The width decreases rapidly during the sputtering process, which indicates a strong lateral growth of gold clusters. At first glance, both polymers show a similar trend. However, distinct differences especially for early stages can be found by tracking the fitted  $q_y^*$  position and the FWHM of the respective evolving peaks. Figure 5.13 c) and d) show plotted logarithmically over  $\delta$  to focus on these early differences. The fitted values exhibit only negligible errors for later stages, confirming the validity of the fitting procedure even for stages in which the peak is moving to very small  $q_y^*$  values. PTB7-Th shows a later onset of the change in FWHM than PTB7, suggesting that the gold layer on PTB7-Th displays less order and increased coarsening compared to the one on PTB7.

The average cluster center-to-center distance is determined via the relation

$$D \approx \frac{2\pi}{q_y^*} \quad (5.3)$$

from the fitted lateral peak position  $q_y^*$ . The evolution of the distance  $D$  as a function of the effective film thickness  $\delta$ , as extracted from the fits, is shown in Figure 5.14.  $D$  grows with pronounced changes of the growth rate for different phases, indicating several competing factors favoring an island growth mechanism. This can be explained by the strong affinity of gold atoms to each other as compared to their affinity to the polymer, which leads to a 3D cluster growth until the percolation limit is reached.

As discussed by Schwartzkopf et al. for inorganic as well as polymer substrates,<sup>[133,146]</sup> a geometrical model is applied to deduce parameters such as the average cluster radius, surface coverage, or cluster density of the deposited gold film. The gold clusters are assumed to be uniform, hemispherical, and arranged in a locally hexagonal pattern, as illustrated in Figure 5.15. Geometrical considerations lead to the following equations by which further important structural parameters can be calculated.

**Figure 5.13**

Structural evolution in horizontal direction illustrated via exemplary integrated horizontal line cuts taken every 2.1 nm starting at  $\delta = 0$  nm and respective fits (black curves) for a) PTB7 (blue) and b) PTB7-Th (red). The intensities are plotted logarithmically for a better visualization of the maxima and shifted along the intensity axis for clarity. The shift in the  $q_y^*$  position of the side maximum to smaller values is illustrated with the grey arrow. The fitted c)  $q_y^*$  position and d) FWHM of the gold side peak in lateral direction for PTB7 (blue) and PTB7-Th (red) over effective film thickness.

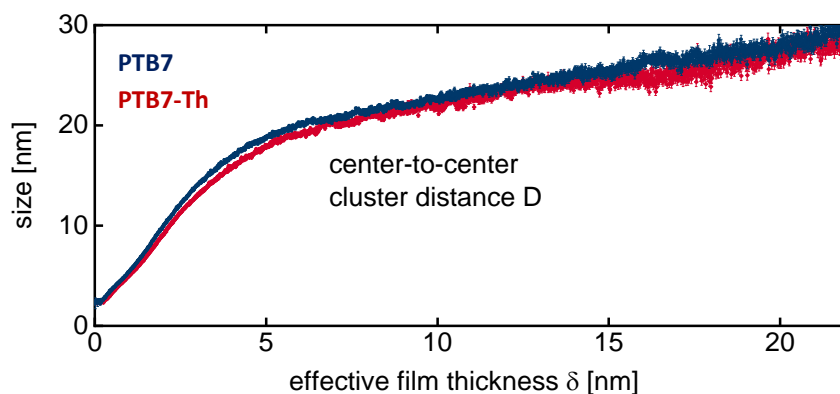


**Figure 5.14**

Average scattering cluster distance  $D$  for PTB7 (blue) and PTB7-Th (red), as extracted from fits of the horizontal line cuts, plotted over effective film thickness  $\delta$ .

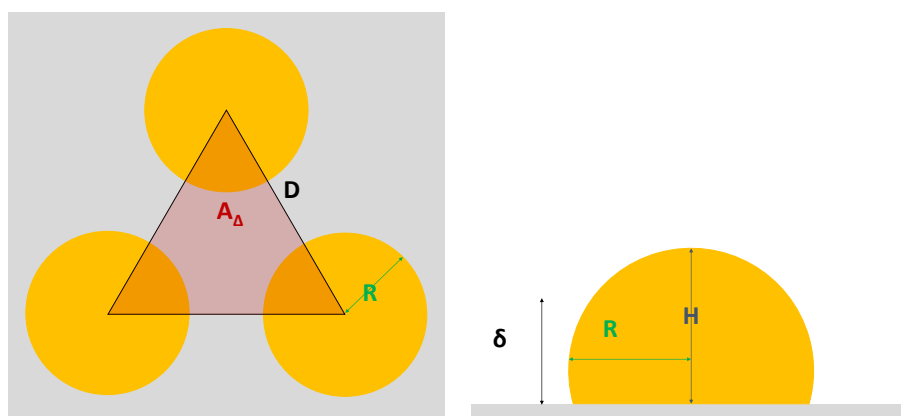


**Figure 5.15**

Geometric model of truncated spheres of gold with radius  $R$  arranged in a trigonal unit cell of side length (= cluster distance)  $D$ , surface area  $A_{\Delta}$  and height (= effective film thickness)  $\delta$ . The clusters are usually assumed to be hemispherical, but for certain purposes (see below), their cluster height  $H$  and contact angle plays a role.

The cluster volume  $V_c$  per unit cell

$$V_c = 3\frac{1}{6}V_{hemisphere} = \frac{\pi}{3}R^3, \quad (5.4)$$

with  $R$  = the average cluster radius, is chosen such that it equals the total volume of deposited material  $V_\Delta$  for the respective unit cell

$$V_\Delta = A_\Delta\delta = \frac{\sqrt{3}}{4}D^2\delta. \quad (5.5)$$

Equating both volumes, the cluster radius  $R$  can then be described by

$$R = \sqrt[3]{\frac{3^{3/2}}{4\pi}D^2\delta} \approx \left[ 3^{3/2}\pi\frac{\delta}{q_y^{*2}} \right]^{1/3}. \quad (5.6)$$

The ratio between the average cluster diameter ( $= 2R$ ) and distance ( $D$ ),  $2R/D$ , gives insights into different processes dominating different stages of the growth. Additionally, it defines the important percolation limit, for which  $2R/D$  reaches the value 1, meaning that clusters meet and build the first fully percolated gold layer. This point is not to be confused by a full surface coverage, which will only occur later in the process when also holes between the clusters are filled. The surface coverage  $\theta$  can be calculated by the ratio of the area covered by the clusters and the total unit cell area

$$\theta = \frac{A_c}{A_\Delta} = \frac{2\pi R^2}{\sqrt{3}D^2}, \quad (5.7)$$

although this only holds until the percolation limit ( $2R/D = 1$ ) is reached, after which the clusters would overlap. For later stages, the respective overlap integral between the clusters has to be subtracted until complete coverage is reached. The overlap integral can be calculated via

$$A_{overlap} = 6 \int_{D/2}^R \sqrt{R^2 - x^2} dx \quad (5.8)$$

and has to be subtracted from  $\theta$  for values of  $2R/D > 1$ . The model also allows determining the average cluster density  $\rho$

$$\rho = \frac{2}{\sqrt{3}D^2} \quad (5.9)$$

as well as the number of gold atoms per cluster  $N_{Au,c}$

$$N_{Au,c} = \frac{1}{2} \left( \frac{R}{r_{Au,atom}} \right)^3. \quad (5.10)$$

Figure 5.16 illustrates the structural changes during the layer formation and hence yields a detailed view of the growth mechanism. The structural features are plotted with respect to the effective gold film thickness in a logarithmic fashion to focus on the important early stages of the growth. Data for PTB7 are plotted in blue, for PTB7-Th in red. Figure 5.16 a) shows the average cluster distance  $D$  and the respective calculated average cluster radius  $R$ . The evolution of the ratio between average cluster diameter ( $2R$ ) and distance ( $D$ ) as well as changes in the surface coverage  $\theta$  are illustrated in Figure 5.16 b). Figure 5.16 c) follows the evolution in the cluster density  $\rho$  (per  $\text{cm}^2$ ) and the number of gold atoms per cluster. The structure evolution can be divided into different stages, as defined by the respective most dominant process and described in the following: I) nucleation, II) diffusion-mediated coalescence, III) adsorption-dominated growth with a) partial coalescence, and b) further growth of ramified clusters under size restrictions IV) layer growth.

2D GISAXS simulations (see Figure 5.17) confirm the geometrical model applied for the analysis. Using the calculated parameters  $R$ ,  $D$ , and  $\delta$  in combination with a 1D paracrystalline lattice,<sup>[238]</sup> the main features of the experimental scattering data are confirmed in these simulations. For the modeling of the 2D GISAXS data, the simulation software BornAgain is used.<sup>[176]</sup> Using python scripts, a model of the sample at a specific effective gold film thickness is defined and its theoretical scattering pattern simulated. Here, the model is based on a 2D distribution (1D paracrystalline) of gold clusters (approximated with truncated spheres) with a certain distance and diameter placed onto a polymer film above a silicon substrate. The scattering pattern is simulated using the distorted-wave Born approximation (DWBA). Deviations from the experimental data are expected because the modeling is based on the use of simple form factors and structure factors, whereas the real existing nanostructures might be more complex. The simulations were performed by Gabriele Semino in the frame of his Bachelor's thesis.<sup>[239]</sup>

**Phase I:** The initial nucleation and growth of the first gold clusters dominate the early stage of the growth process which is referred to as phase I. The average cluster distance  $D$  and cluster density  $\rho$  stay constant for an effective film thickness of up to  $\delta_{I \rightarrow II} \approx (0.21 \pm 0.02)$  nm for PTB7 and  $(0.25 \pm 0.02)$  nm for PTB7-Th (equivalent to less than a complete atomic monolayer). The later onset in the growth of  $D$  for PTB7-Th suggests that the gold nuclei on PTB7-Th are more immobilized in contrast to the gold nuclei on PTB7, which reduces the chances of colliding with other mobile nuclei or atoms and establishing larger clusters at larger distances. The parameters acquired during this early stage suggest that the processes differ from the growth of gold clusters for other experiments, where an initial decrease in the cluster distance  $D$  and increase of cluster density  $\rho$  is observed.<sup>[133,134,146]</sup> However, these differences might be due to the comparably high sputter rate, as the results are similar to the ones discussed for PS at the same sputter rate.<sup>[142]</sup> It should be noted that – in contrast to thermal evaporation –

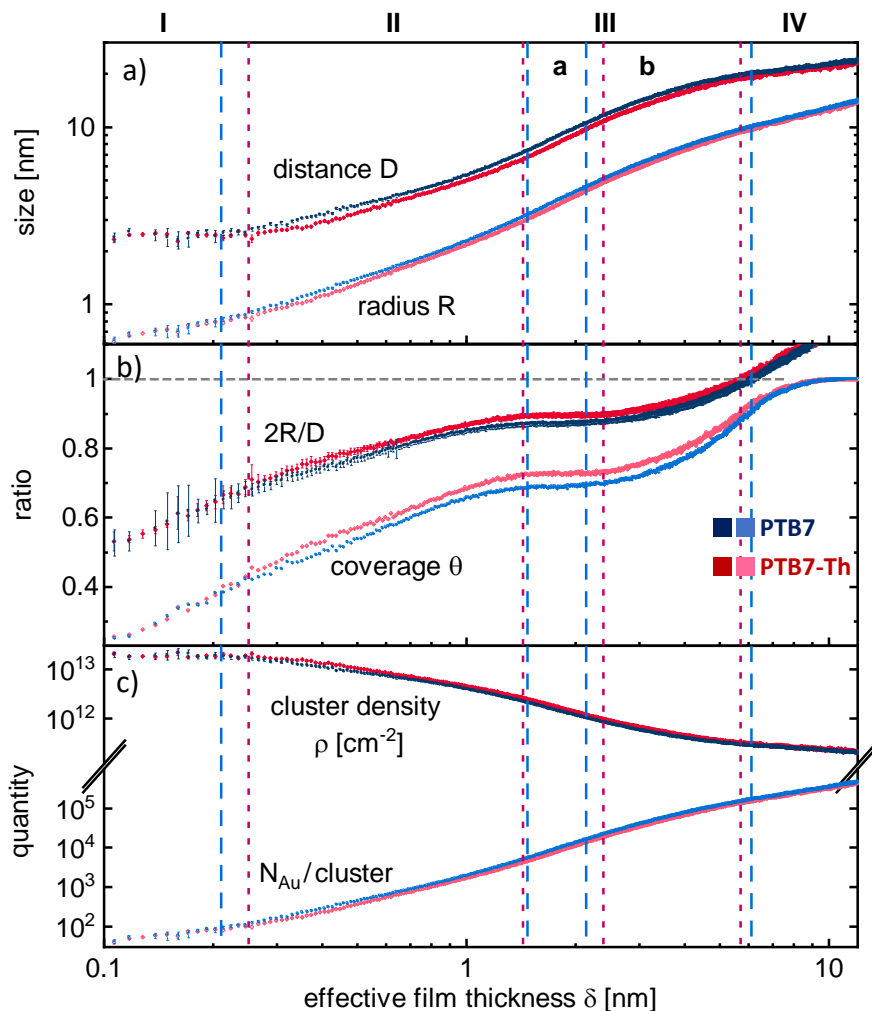


**Figure 5.16**

Structure evolution over effective film thickness shown by the a) average cluster distance  $D$  (dark symbols, extracted from fits) and radius  $R$  (light, calculated using the mentioned model) for PTB7 (blue) and PTB7-Th (red). The model additionally yields b) the ratio of the average cluster diameter to cluster distance  $2R/D$  (dark) and the surface coverage (light), as well as c) the cluster density (dark) and number of gold atoms per cluster (light). The structure evolution can be divided into different stages, as defined by the respective most dominant process: I) nucleation, II) diffusion-mediated coalescence, III) adsorption-dominated growth with a) partial coalescence and b) further growth of ramified clusters under size restrictions IV) layer growth. PTB7-Th shows overall smaller structures in terms of  $R$  and  $D$ .

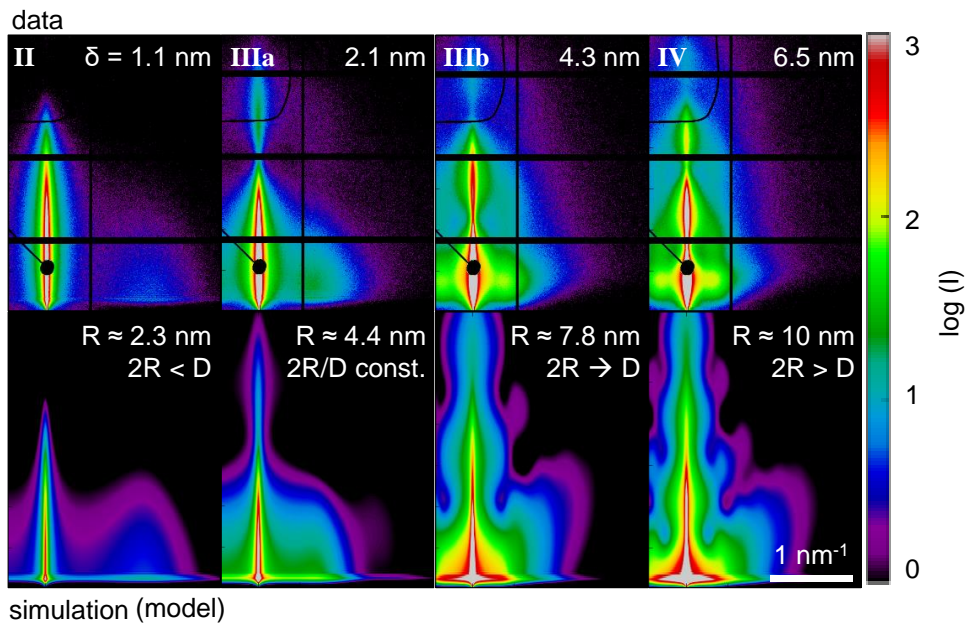


**Figure 5.17**

Experimental data for PTB7-Th vs. simulated data using the software BornAgain<sup>[176]</sup> and the model for the different growth phases as indicated with II, IIIa and IIIb, and IV.

sputtering creates gold particles of comparably high energy, which can lead to diffusion of gold atoms into the first few nm of the soft polymer film. The implantation of metal atoms or ions within the surface-near region of polymers has been examined and described extensively for metals such as gold or chromium.<sup>[133,240–242]</sup> The nucleation process is linked to this embedding and immobilization of the gold particles within the surface-near region of the polymer film. The nucleation is followed by a further 3D growth of gold clusters, as seen in the pronounced increase of the cluster radius  $R$ . The surface coverage  $\theta$  reaches about 40% towards the end of phase I with a very similar trend for both polymers.

**Phase II:** The onset of phase II can be distinguished clearly by the increase in cluster distance, which can be attributed to the merging of small mobile clusters, forming larger clusters with a lower cluster density. This behavior is typical for a diffusion-dominated process, in which larger clusters grow on the expense of smaller, more mobile ones via full coalescence. In phase II, the crystal lattice of the gold quickly decreases towards its equilibrium values, while the small-sized crystals still cause a broad FWHM of the corresponding Bragg peaks. As illustrated in Figure 5.18, the minimum crystallite size within the gold clusters – determined from the FWHM via the Scherrer formula (Equation 2.38) – stays constant during phase II. Towards the end of phase II, the surface coverage  $\theta$  reaches values of slightly below (PTB7) versus

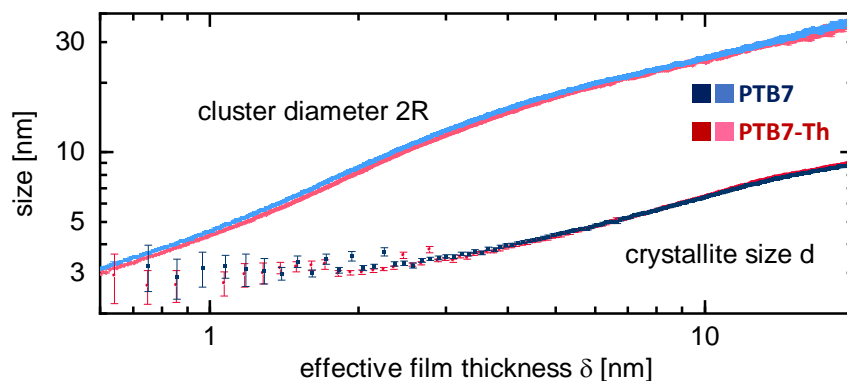


**Figure 5.18**

Changes in the minimum gold crystallite size  $d$  (dark symbols) over effective film thickness  $\delta$  in comparison to the gold cluster diameter  $2R$  (light symbols). The minimum crystallite size within the clusters can be determined from the FWHM of the (111) Bragg peak in the GIWAXS data using the Scherrer formula. While  $2R$  is growing quickly even in the very early stages of the deposition process,  $d$  stays constant during phase II and increases only moderately afterward.

slightly above (PTB7-Th) 70%, indicating a higher probability of gold atoms to attach to the surface of PTB7-Th as compared to that of PTB7. This phase is additionally characterized by a strong decrease in the ratio between the cluster height and cluster radius  $H/R$ , as shown in Figure 5.19. The ratio starts with values above 1, meaning that the clusters in phases I and II have contact angles above  $90^\circ$ , thereby reducing their interaction with the polymer surface. Towards phase III, the ratio reaches a value of about 1, indicating hemispherical clusters on the polymer surface.

**Phase III:** The strong increase in surface coverage  $\theta$  indicates the onset of phase III (at  $\delta_{II \rightarrow IIIa} \approx (1.47 \pm 0.02)$  nm for PTB7 and  $\delta_{II \rightarrow IIIa} \approx (1.43 \pm 0.02)$  nm for PTB7-Th, respectively), in which newly sputtered gold atoms have a significantly higher probability of reaching already existing, immobilized clusters than nucleating in new clusters. Both  $D$  and  $R$  continue their increase. However, the now constant  $2R/D$  ratio and  $\theta$  hint to a partial coalescence, with smaller clusters merging into larger, elongated clusters without fully coalescing. This hindered coalescence can be explained by the reduction in surface mobility of the clusters with increasing  $R$ . Reaching a certain critical radius  $R_c$ , the full relaxation of neighboring coarser clusters to a preferred symmetric state takes longer than the cluster growth due to deposition and adsorption of atoms. It should be noted that the partial coalescence for PTB7 and PTB7-Th is less pronounced than the partial coalescence witnessed during similar experiments on thin films of polymers without sulfur components, e.g. PS.<sup>[133,142]</sup>

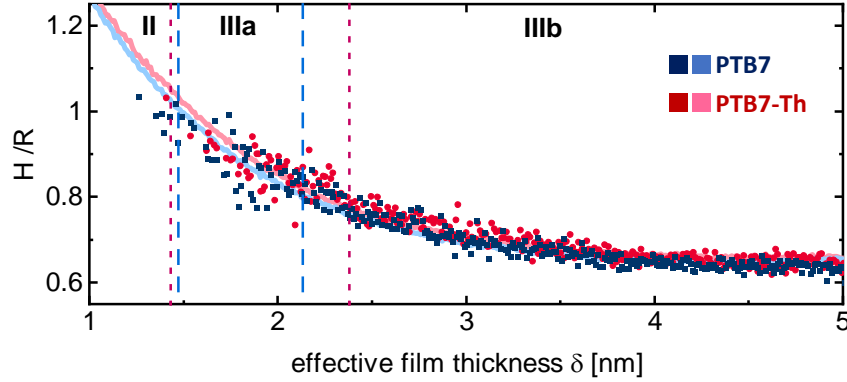


**Figure 5.19**

Changes in the  $H/R$  ratio for PTB7 (dark red) and PTB7-Th (dark blue) over effective film thickness  $\delta$ , illustrating the change in the form factor of the sputtered gold clusters. The values are extrapolated for smaller  $\delta$  by calculating  $H$  from the fitted  $q_{z,min}$  (see Figure 5.12) and shown in light blue for PTB7 and light red for PTB7-Th. The ratio  $H/R \approx 1$  marks the change from phase II to IIIa.

Additionally, the plateauing of the  $2R/D$  ratio and surface coverage is more pronounced for PTB7-Th in contrast to PTB7. One reason could be the reduced mobility of gold clusters on PTB7-Th, which could hinder the relaxation of partially coalesced and elongated clusters to a more favorable geometrical state. According to Jeffers et al., the gold mobility on amorphous surfaces can be described by the surface diffusion coefficient  $D_s$ .<sup>[243]</sup> This measure for surface mobility has been successfully correlated to the change in growth behavior of gold on polymer films using atomic force microscopy (AFM) and GISAXS studies.<sup>[133,244]</sup>

$D_s$  can be correlated to the respective critical radii  $R_c$  and cluster heights  $H_c$  for the critical film thicknesses  $\delta_c = \delta_{II \rightarrow IIIa}$  of PTB7 and PTB7-Th. According to the so-called kinetic freezing model by Jeffers et al., the full coalescence of two clusters is hindered when reaching a certain cluster radius, leading to partial coalescence and elongated structures.<sup>[243]</sup> The respective critical radius  $R_c$  depends on various parameters, such as the metal surface free energy  $\gamma$ , the metal atomic volume  $\omega$ , the deposition rate  $J$  and the Temperature  $T$ . It is, however, also correlated to the surface diffusion coefficient of the metal on the respective polymer  $D_s$  as well as the critical aspect ratio  $H/R = \alpha_c$  at the critical effective film thickness  $\delta_c$

$$R_c^4 = \frac{D_s \alpha_c \delta_c \gamma \omega^{(4/3)}}{k_B T J}. \quad (5.11)$$

Using the values for  $R_c$ ,  $\alpha_c$ , and  $\delta_c$  from the fitted experimental data at  $\delta_c = \delta_{II \rightarrow IIIa}$ ,

the relative surface diffusion coefficients for gold on PTB7 and PTB7-Th can be compared via the relation

$$D_s \approx \frac{R_c^4}{\alpha_c \delta_c}. \quad (5.12)$$

The values can additionally be compared to the ones extracted for gold sputter-deposited on PS under the same conditions (sputter setup, sputter rate, temperature, deposition rate, etc.). Even though the critical cluster height is not calculated for Au on PS, the  $H/R$  ratio can be estimated to be around or above 1. Using the critical thickness of partial coalescence  $\delta_{c,PS} = 1.6$  nm and a critical radius of around 2.8 nm,  $D_{s,PS}$  can be estimated to be within the same order of magnitude as PTB7 and PTB7-Th.

From this correlation, a significantly lower value for the gold mobility of PTB7-Th as compared to the one of PTB7 (ratio 0.64 : 1) can be deduced. At an effective layer thickness of  $\delta_{IIIa \rightarrow b} \approx (2.13 \pm 0.03)$  nm for PTB7 and  $(2.38 \pm 0.03)$  nm for PTB7-Th, respectively, the  $2R/D$  ratio and surface coverage increase again, indicating a change in growth behavior. The growth in distance  $D$  slows down significantly, until the percolation limit

$$2R/D = 1 \quad (5.13)$$

is reached. This decrease in growth can be attributed to the lateral size restrictions of the large clusters. A strong increase in surface coverage indicates that the immobilized clusters mainly grow by directly adsorbing newly sputtered atoms and filling the gaps between clusters.

**Phase IV:** The percolation limit is reached at  $\delta_{IIIb \rightarrow IV} \approx (6.10 \pm 0.05)$  nm for PTB7 and  $(5.70 \pm 0.05)$  nm for PTB7-Th, respectively. This difference can be mainly attributed to the fact that the  $2R/D$  ratio for PTB7-Th is slightly higher for the whole process, therefore reaching the value 1 earlier than the gold layer on PTB7. During phase IIIb, the crystal quality improves significantly, as seen from the decreasing FWHM of the Bragg peaks (see Figure 5.5).

Beyond the percolation threshold, the surface is soon fully covered.  $\theta$  reaches values of 1 at an effective film thickness  $\delta \approx 10.5$  nm for PTB7-Th and 10.0 nm for PTB7-Th, respectively. The fully connected clusters can only grow slowly by moving grain boundaries in phase IV. Even at an effective film thickness of around  $\delta \approx 22$  nm, the films still show domains with a calculated average distance  $D$  of around  $(30.1 \pm 0.5)$  nm for PTB7 and a slightly smaller distance of around  $(28.8 \pm 0.6)$  nm for PTB7-Th. However, the geometric model reaches its limits in this phase, as values for  $2R/D > 1$  would imply cluster diameters larger than the average cluster distance. For this reason, the surface coverage  $\theta$  is determined by additionally subtracting the overlap integrals of the clusters until the full coverage is reached.

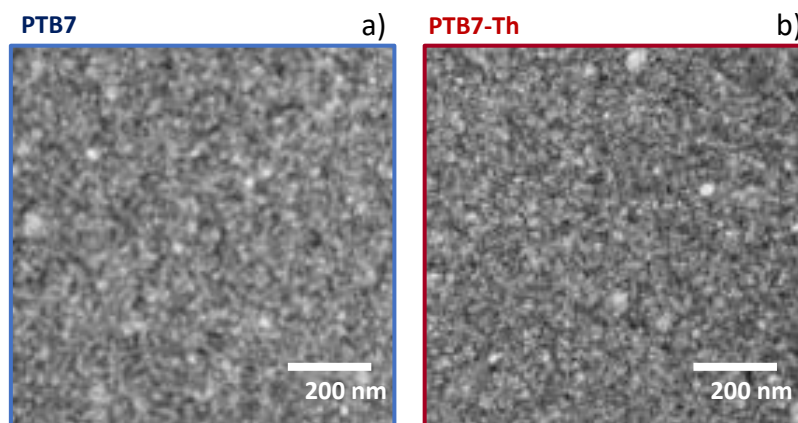


**Figure 5.20**

Surface morphology after sputter deposition probed with ex-situ SEM measurements shown for gold sputtered on a) PTB7 and b) PTB7-Th, respectively. Fully percolated gold films with coarse grain structures are seen.

SEM images taken ex situ after the deposition process are shown in Figure 5.20 for PTB7 and PTB7-Th. They confirm the presence of nanogranular gold films with visible, coarse gold clusters of about 40 nm in diameter and distance, albeit with a broad size distribution. These values are in accordance with the ones extracted from the GISAXS measurements. In comparison to earlier studies on PS,<sup>[133,142]</sup> the films based on the two discussed polymers show significantly smaller cluster distances  $D$  towards the end of the nucleation phase. This effect can be explained by a stronger affinity of the gold atoms to the thiophene groups of PTB7 and PTB7-Th, which are not present in PS. The affinity of gold to sulfur groups has been well-established<sup>[245–248]</sup> and is also reported for thiophene-containing materials.<sup>[249,250]</sup> The (sub-)nanometer-sized gold atoms and clusters build complexes with organic sulfur groups, exhibiting partially covalent bonds.<sup>[245]</sup> The binding strength between Au and S-groups is in the same range as the one between gold atoms, with values of  $40 \text{ kcal mol}^{-1} - 50 \text{ kcal mol}^{-1}$ .<sup>[247]</sup> The higher affinity might lead to a reduced mobility of gold atoms and small gold clusters on the polymer surface or within the gold enrichment layer near the surface. This enrichment layer is investigated and discussed in Chapter 6 and has also been observed for gold sputtered on PS<sup>[133]</sup> and PVK<sup>[132]</sup>. Indeed, comparing the surface diffusion coefficient  $D_s$  for both polymers, as described before, shows a correlation between the higher affinity of PTB7-Th and its respective lower  $D_s$ . The decreased mobility, in turn, results in a slower increase of the  $2R/D$  ratio. The surface coverage  $\theta$  reaches higher values for PTB7-Th versus PTB7 towards the end of phase II, indicating a higher probability of gold adatoms to attach to the surface of PTB7-Th compared to that of PTB7. This effect can be explained by the two additional thiophene rings in the side chains of PTB7-Th which might lead to an even further reduced mobility

of the gold atoms and therefore higher surface coverage at earlier stages. It can be concluded that side-chain engineering impacts the early growth stages which plays an important role when considering plasmon-based effects.<sup>[25,130,251–254]</sup>

A comprehensive layer growth model (shown in Figure 5.21) can be deduced from the described behavior. Phase I is defined by nucleation processes and a high mobility of the very small gold clusters. In phase II, the now nanometer-sized gold clusters at comparably large distances are still very mobile and grow mostly by incorporation of diffusing gold atoms and by merging with other small clusters and full coalescence, leading to larger clusters at higher distances. Above a certain cluster size, the surface mobility of the clusters is significantly reduced. Phase IIIa is characterized by partial coalescence of neighboring clusters, forming elongated structures, which leads to a further increase in the average cluster distance. In phase IIIb, the clusters grow mainly by incorporation of deposited clusters and filling gaps. The merging of immobile clusters leads to a non-continuous coverage of the surface with percolated, worm-like structures. Phase IV is reached at the so-called percolation limit, at which the average cluster diameter reaches the average cluster distance. Shortly after, a complete coverage of the surface can be assumed. Due to the now fully developed gold layer, the growth will become more layer-like, even though the domains grow further by moving their grain boundaries and are still visible at a thickness of 20 nm. Differences in the behavior of the two polymer thin films are illustrated, with PTB7-Th showing a higher tendency to immobilize gold nuclei and clusters, leading to several distinct features, namely the prolonged nucleation phase, the higher overall surface coverage, and the more pronounced plateauing in phase IIIa in comparison to the one of PTB7. It is interesting to note that the growth behavior in the isolated nanoparticle phase II for both polymers leads to a distinctly small grain size even after percolation.

## 5.4 Conclusion

The influence of a side-chain modification of state-of-the-art low-bandgap polymers (PTB7 versus PTB7-Th) on the formation of a gold layer during sputter deposition is investigated. The process is followed by in-situ GISAXS and GIWAXS measurements during DC magnetron sputter deposition. The nanogranularity of the gold nanoparticle layer is extracted and quantified, from isolated particles to the percolated gold contact in terms of cluster size, cluster distance, and surface coverage. By combining the observations of the lateral and vertical gold layer growth with simulations, a five-stage model of the electrode formation is derived. After the initial nucleation and subsequent diffusion of gold atoms and small, mobile clusters, a change to an adsorption-dominated process is observed, in which the immobilized larger clusters build elongated structures and size-restrictions set in, followed by the final layer growth. The tuning of side chains does indeed influence the growth kinetics of the gold electrodes differently in the different growth regimes, with more pronounced ef-

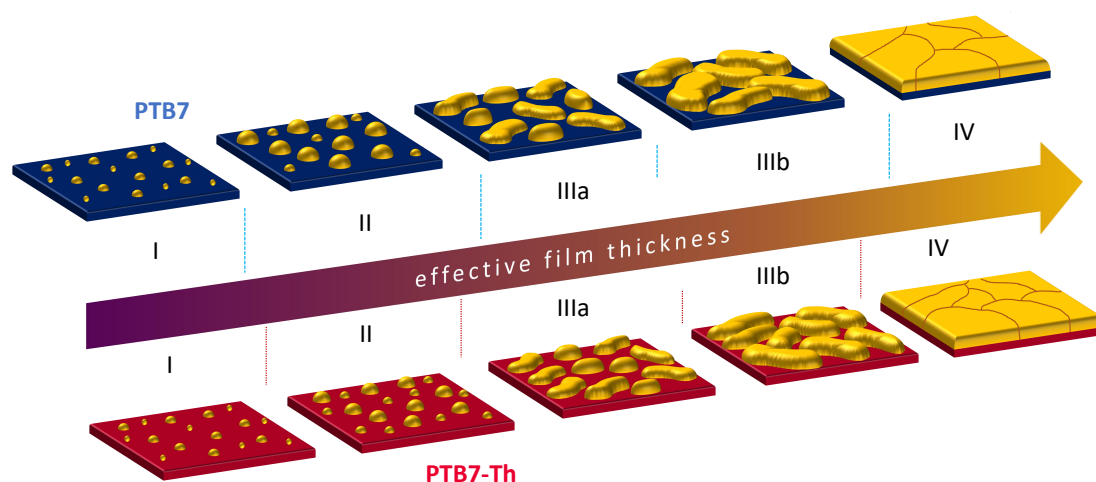


**Figure 5.21**

Derived growth model with five phases, I) the nucleation, II) the diffusion of gold adatoms and small clusters on the polymer film, III) the adsorption of further gold atoms with IIIa) partial coalescence and IIIb) further growth of coarse, ramified structures and IV) finally a layer growth. Differences in terms of cluster size and phase limits for the polymers (PTB7 in blue and PTB7-Th in red) are indicated. PTB7-Th shows a lower gold surface diffusion mobility, leading to prolonged nucleation and earlier onset of partial coalescence and an earlier percolation.

facts visible in the early stages of the growth. In the case of the side-chain modified low bandgap tuned polymer materials discussed here, this can directly be related to the sulfur content of the side chains. These findings provide a fundamental understanding of the layer growth dependence on bandgap-tuned polymers. They are an important step towards the controlled fabrication of high-efficiency solar cells and will be also of interest for other organic electronic devices with polymer-metal contacts.



# CHAPTER 6

## Effects of the Active Layer Morphology on the Gold Layer Growth

In the previous chapter, a distinct effect of polymer side-chains on the structure formation of gold electrodes was discussed. While surface chemistry certainly plays a role in the growth process, the morphology of the underlying layer can also affect the deposited electrode. The present chapter addresses the influence of the active layer morphology on a sputter-deposited gold electrode. For this purpose, thin films of PTB7-Th:PC<sub>71</sub>BM blends with and without the solvent additive 1,8-diodooctane (DIO) are investigated in comparison to the pristine PTB7-Th. Atomic force microscopy (AFM) and grazing-incidence small-angle X-ray scattering (GISAXS) data illustrate the initial morphology of the organic films, before following the gold deposition in situ using GISAXS and grazing-incidence wide-angle X-ray scattering (GIWAXS). Ex-situ X-ray reflectometry (XRR) after the deposition process gives insights into the final vertical film composition. The differences in the initial film surface roughness affect the created gold layer and translate into differences in the gold layer surface roughness. The addition of DIO to the active layer leads to a smoother gold film resembling the one deposited on the pure polymer, which likely benefits the device performance.

### 6.1 Introduction

The morphology of the active layer has for years been under investigation as a main factor affecting the performance of bulk-heterojunction (BHJ) OPVs.<sup>[19,22,23,184,255–257]</sup> While a randomly structured morphology is beneficial for solar cells due to easy,

low-cost processability, the structure needs to meet several prerequisites. The donor-acceptor interface needs to be reached by excitons within their lifetime. This lifetime can be translated into an average diffusion length, which defines the optimal distances between the donor-acceptor interfaces to enable efficient charge separation. The phases need to offer fully percolated paths for the separated charge carriers to reach the respective electrodes. Several methods have been investigated to tailor the morphology for enhancing the overall performance and/or stability of the active layer. One common method is the use of solvent additives, which have different effects, depending on the respective systems. The additives are chosen such that they offer a certain solubility for one or several of the used materials. They are added to the solution of the donor and acceptor materials in small quantities. Studies were performed for several material systems, illustrating the wide range of effects of additives,<sup>[27]</sup> from a heightened crystallinity of the polymer domains<sup>[257,258]</sup> to an enhanced phase separation<sup>[68,255,257-260]</sup> or decrease in excessive aggregates<sup>[184,260,261]</sup> as well as enhanced stability against aging during operation.<sup>[70,91]</sup>

In the previous chapter, the effect of the side-chains of the pure polymers PTB7 and PTB7-Th was investigated with regard to their effect on the sputter-deposited gold electrode applied on the respective polymer thin films. As electrodes for certain organic solar cells are applied directly on top of the respective BHJ active layer, a similar investigation on the effect of the active layer morphology on the applied electrode is of high interest. The effect of DIO on the PTB7-Th:PC<sub>71</sub>BM BHJ morphology has been investigated by several studies – without, however, taking electrode effects into account.<sup>[28,197,262,263]</sup> In our earlier work on solar cells based on this system, we found considerable effects of the additive on the initial morphology as well as the behavior under degradation, as described in more detail by Yang, Löhner et al.<sup>[70]</sup>

For the present chapter, typical PTB7-Th:PC<sub>71</sub>BM active layer blend films with and without the solvent additive DIO are prepared to investigate a potential effect of the changes in layer morphology on the formation of the sputter-deposited gold electrode. The films are additionally compared to films of the pristine polymer PTB7-Th as a reference. Initial ex-situ AFM and GISAXS measurements give insights into the surface topology and film morphology of the three sample types. The in-situ investigation during the gold deposition is performed via GISAXS and GIWAXS to follow the development of the gold-organic interface on a morphological as well as crystalline level. Ex-situ XRR after the experiment determines the vertical film profile of the active layers and their gold contacts. By combining these methods, the influence of the organic film morphology becomes evident, with the initial surface roughness and morphological composition affecting the developing gold film.

## 6.2 Experimental Details

General information on the sample preparation and characterization can be found in Chapter 3 and Chapter 4, respectively. In contrast to the experiments discussed in Chapter 5, a few slight changes are taken for the experiment, as noted in the following. The samples are deposited with a lower sputter rate to focus on the early stages of film growth. XRR measurements taken *ex situ* complement the findings.

**Materials and sample preparation:** Silicon wafers are cut into pieces of  $12 \times 15 \text{ mm}^2$  and acid cleaned, before transferring them to a glovebox for the sample preparation. Due to the sensitivity of the used materials, the following steps are performed under an inert nitrogen atmosphere. The sample preparation is slightly different for the three investigated samples. For the pristine polymer film, PTB7-Th is dissolved in pure chlorobenzene (CB) with a concentration of  $15 \text{ mg mL}^{-1}$  and stirred overnight at  $60^\circ\text{C}$  to allow for complete dissolution. For the active layer blend, PTB7-Th is dissolved either in pure CB or a CB:DIO mixture (97:3) with a concentration of  $15 \text{ mg mL}^{-1}$  and stirred for 2 h at  $60^\circ\text{C}$ . Subsequently, the respective solutions with or without additive are added to a corresponding amount of PC<sub>71</sub>BM ( $21 \text{ mg mL}^{-1}$ ) to achieve the total concentration of  $35 \text{ mg mL}^{-1}$ , and stirred overnight at  $60^\circ\text{C}$ . Thin films are prepared via spin casting the respective solution under an inert atmosphere on a cleaned silicon substrate at 1000 rpm for 40 s. They are left to dry at room temperature under a nitrogen atmosphere for one day, before sealing them individually in aluminum bags for the transport from the laboratory to the synchrotron facility.

**Real-space imaging:** To investigate the surface morphology of the organic thin films, AFM images are obtained using the nanoinfrared light (IR)2-FS instrument with QCL laser (Anasys Instruments, US). The measurements are performed in tapping mode using a gold-covered tip.

**Sputter deposition:** For the deposition process, the custom-built sputter setup is used, as described in more detail in the previous chapter.<sup>[146]</sup> The sputter chamber is evacuated to a base pressure of about  $1 \times 10^{-6}$  mbar. After applying an argon gas flow, the working pressure is around  $5 \times 10^{-3}$  mbar. The average sputter rate can be varied by applying a respective voltage and power. A low nominal sputter rate of  $0.036 \text{ nm s}^{-1}$  is adjusted by applying a power of 3 W. After 560 s, the final layer thickness  $\delta_{Au,final} \approx (22.1 \pm 0.3) \text{ nm}$  is reached.

**In-situ scattering investigation:** To perform GISAXS and GIWAXS experiments with a high temporal and spatial resolution, the sputter deposition setup is implemented into the Micro- and Nano-focus X-ray Scattering (MiNaXS) beamline P03 of the brilliant synchrotron light source PETRA III at Deutsches Elektronen-Synchrotron

(DESY) in Hamburg, Germany.<sup>[214]</sup> The measurements are performed at an energy of 13.0 keV ( $\lambda = 0.953 \text{ \AA}$ ) with a micro-beam spot size of about  $32 \times 42 \mu\text{m}^2$  on the sample. To ensure the penetration of the complete gold film by the X-ray beam, an incident angle ( $\alpha_i = 0.401^\circ$ ) slightly above the critical angle of gold ( $\alpha_{c,Au} = 0.337^\circ$  at this energy) is chosen, thus obtaining information on the gold layer, its interface to the polymer and the polymer thin film itself. Potential X-ray beam damage is prevented by scanning the sample continuously over a range of 2 mm with a rate of  $0.6 \text{ mm s}^{-1}$  in horizontal direction. Additionally, potential damage is monitored by taking a series of  $100 \times 1 \text{ s}$  images on a sample spot not investigated during the in-situ experiment, observing no changes in the scattering pattern. The scattered X-rays are recorded with two 2D pixel detectors, as described in more detail in Section 5.2.

**In-situ GISAXS:** The data are recorded using the 2D detector Pilatus 1M (Dectris Ltd.) with a pixel size of  $172 \times 172 \mu\text{m}^2$  in a sample-to-detector distance (SDD) of  $(2376 \pm 2) \text{ mm}$ . With a frame rate of  $20 \text{ s}^{-1}$  and a deposition time of 560 s, 11 200 2D scattering data are acquired for each measurement. To analyze the 2D data, the scattering intensity in specific regions of interest is integrated via the software Directly Programmable Data Analysis Kit (DPDAK)<sup>[215]</sup> and fitted using an appropriate geometric model. Vertical line cuts around  $q_y = 0 \text{ nm}^{-1}$  ( $\pm 5 \text{ px}$ , so-called detector cuts) are analyzed to acquire information about the film profile. To gain insights into the lateral structures of the samples, horizontal line cuts at the Yoneda position of a specific material are made. As the gold deposition is investigated in situ, the gold layer initially exhibits a vastly decreased (optical) density and therefore decreased critical angle. During the deposition process, this critical angle increases with a growing electron density towards the bulk gold value of  $q_z = 0.902 \text{ nm}^{-1}$ . Therefore, a horizontal region of interest is chosen in such a way that it includes the Yoneda region of the polymer and ranges up to the finally reached gold Yoneda region with  $0.62 \text{ nm}^{-1} < q_z < 0.90 \text{ nm}^{-1}$ . The average film thickness of the samples before and after the deposition is obtained using static GISAXS data recorded on the pure organic films as well as on the final gold layers.

**In-situ GIWAXS:** During the sputter deposition process, 1120 2D scattering data are acquired for each sample with a frame rate of  $2 \text{ s}^{-1}$ . The 2D GIWAXS detector (LAMBDA detector, pixel size  $55 \times 55 \mu\text{m}^2$ , X-Spectrum GmbH, Hamburg) is placed above the flight tube (connecting the sample chamber with the GISAXS detector) and tilted at an angle of about  $12^\circ$  versus the sample horizon at a sample detector distance of  $(178 \pm 3) \text{ mm}$  to detect the two most important gold Bragg peaks at  $2.676 \text{ \AA}^{-1}$  (111) and  $3.088 \text{ \AA}^{-1}$  (200). To evaluate the collected data, the tilt is corrected geometrically using a custom-made Python script. Afterward, typical further intensity corrections and reshaping steps to account for the inaccessible q-space are performed using the MATLAB-based software GIXSGUI, as described in Section 2.4.4.<sup>[169]</sup> 1D vertical cuts

are integrated for  $\chi$  between  $-20^\circ$  and  $+20^\circ$  and fitted using a constant background in combination with a Pseudo-Voigt function for each of the two Bragg peaks.

**Ex-situ XRR:** Ex-situ XRR measurements are taken with a D8 Advance Diffractometer by Bruker, using monochromatic Cu-K $_{\alpha}$  radiation with a wavelength of  $\lambda = 1.54 \text{ \AA}$ . The obtained data are modeled using the Igor-based software Motofit with a stack of different layers with different SLDs.<sup>[158]</sup>

## 6.3 Morphology of the Organic Thin Films

As three different samples are to be compared, films of the respective materials are initially investigated regarding their surface morphology using AFM. The method gives insights into the local topology of the respective films in a chosen region of up to several micrometers. Here, areas of  $2 \times 2 \mu\text{m}^2$  are investigated. Figure 6.1 illustrates the 2D height scan of the pristine PTB7-Th thin film in contrast to the surface of its blend with PC $_{71}$ BM with the solvent additive DIO, and without DIO. At first glance, distinct features are visible for the different films. The pristine PTB7-Th film shows a flat, homogeneous topology, as expected. Both blend films have a rougher surface but differ significantly in the shape and distribution of features. The influence of DIO is clearly visible, as it leads to a smoother PTB7-Th:PC $_{71}$ BM blend film with elongated, interconnected areas of the material phases. The blend without additive shows pronounced aggregates on the sample surface. Literature on the BHJ system based on PTB7-Th's sister polymer PTB7 has shown very similar findings, with a smoother film and elongated phase features for the blend processed with DIO and pronounced aggregation of PC $_{71}$ BM for the blend processed without additive.<sup>[184,260,261,264]</sup>

The differences between the films can also be expressed in terms of their respective averaged root mean square (rms) roughness  $\sigma$ , as calculated from the deviation from the mean height  $r_j$  for all considered points  $N$  via Equation 2.27:

$$\sigma_{rms} = \sqrt{\frac{1}{N} \sum_{j=1}^N r_j^2}$$

Indeed,  $\sigma$  is significantly lower for the pristine polymer film, with  $\sigma \approx 0.8 \text{ nm}$  for PTB7-Th,  $1.8 \text{ nm}$  for the blend with DIO, and  $2.5 \text{ nm}$  for the blend without DIO. However, this averaged value does not describe the local roughness or the lateral dimensions of the respective features. From the 2D data, typical length scales in lateral direction can be extracted by measuring the structure sizes and distances of the visible features. For the blend film with DIO, average diameters of the elongated structures are found to be between  $(100 \pm 10)$  and  $(150 \pm 20) \text{ nm}$ , while their center-to-center distances vary between  $(200 \pm 20)$  and  $(300 \pm 20) \text{ nm}$ . As the structures are elongated, higher values are

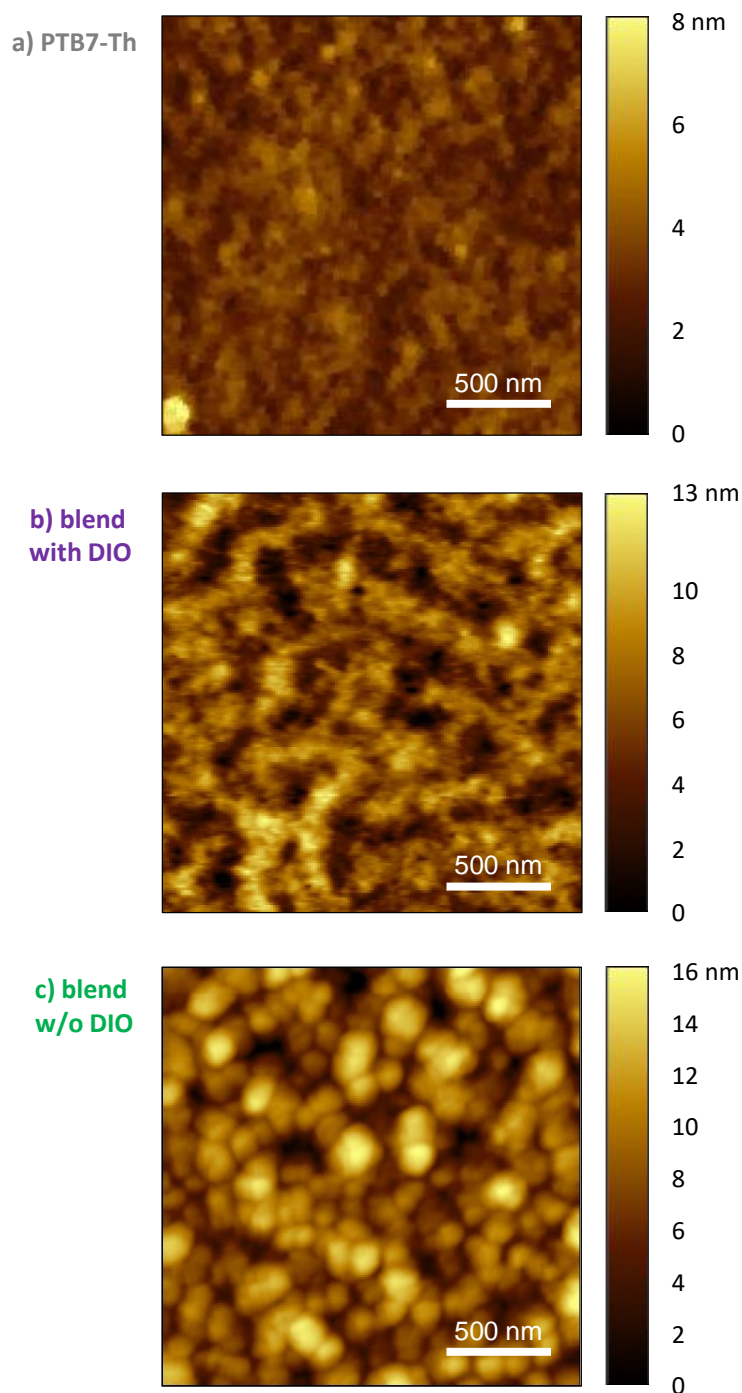


**Figure 6.1**

Surface topology of the pure organic thin films, probed with ex-situ AFM for a) pristine PTB7-Th, b) the PTB7-Th:PC<sub>71</sub>BM blend with DIO, and c) the PTB7-Th:PC<sub>71</sub>BM blend without DIO. Note the different height scales, as the polymer film is significantly smoother than both PTB7-Th:PC<sub>71</sub>BM blend films.

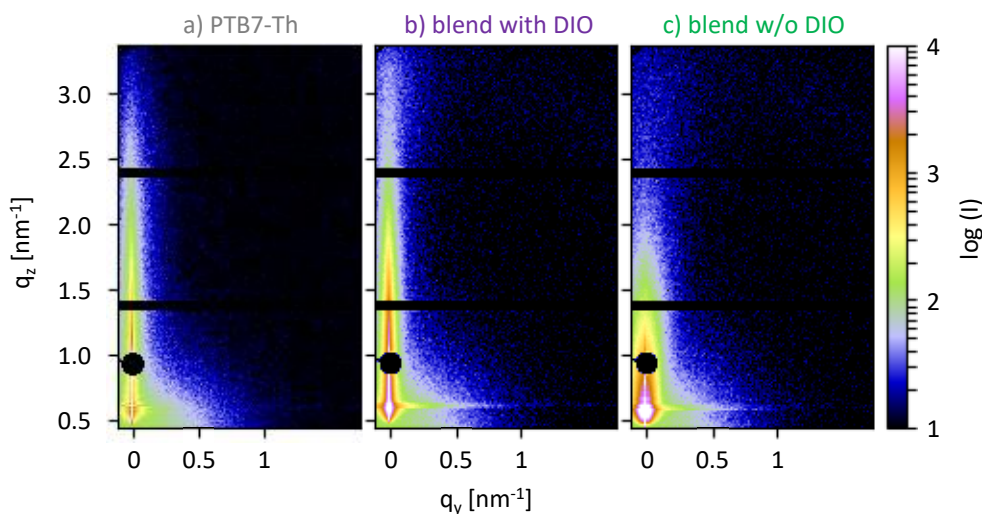


**Figure 6.2**

Initial 2D GISAXS data for a) a pristine PTB7-Th thin film, b) the PTB7-Th:PC<sub>71</sub>BM blend with DIO, and c) the blend without DIO, summed up over  $10 \times 1$  s for an improved signal-to-noise ratio. The black horizontal lines are caused by a gap between the detector modules. The black circle denotes the beamstop, which absorbs the specularly reflected beam of high intensity to protect the detector.

also measured with an emphasis on structures with sizes of  $(190 \pm 10)$  nm and center-to-center distances between  $(400 \pm 30)$  and  $(500 \pm 30)$  nm. The blend film without additive exhibits close-to spherical aggregates at its surface, which can be roughly divided into large (diameters of  $(200 \pm 20)$  nm), medium (diameter  $(130 \pm 10)$  nm), and small structures (diameter  $(90 \pm 10)$  nm) with average distances varying in a broad range between  $(150 \pm 10)$  and  $(400 \pm 30)$  nm. These PC<sub>71</sub>BM aggregates on the blend film are expected to influence the deposition of the electrode, as they provide a much rougher surface in the range of potential gold clusters.

While the AFM measurements investigate the surface topology, they are limited to a certain area and cannot easily distinguish different phases within an all-organic film. For this, GISAXS is a more suitable method to probe the inner thin film morphology. 2D GISAXS data for the different samples – acquired by summing  $10 \times 1$  s data for a better signal-to-noise ratio – are illustrated in Figure 6.2. All data show the typical Yoneda region with the highest scattering intensity due to the respective material critical angle at  $q_z \approx 0.6 \text{ nm}^{-1} - 0.7 \text{ nm}^{-1}$ . However, distinct differences can be seen for the different material systems. Both blend films exhibit an increased diffuse scattering in comparison to the pure polymer film. Additionally, the blend film without DIO shows a decreased intensity at higher  $q_z$  values in combination with increased intensity at higher  $q_y$  values. This effect can be attributed to the rougher surface, which leads to more diffuse scattering. The broadened intensity at small  $q_y$  values originates from

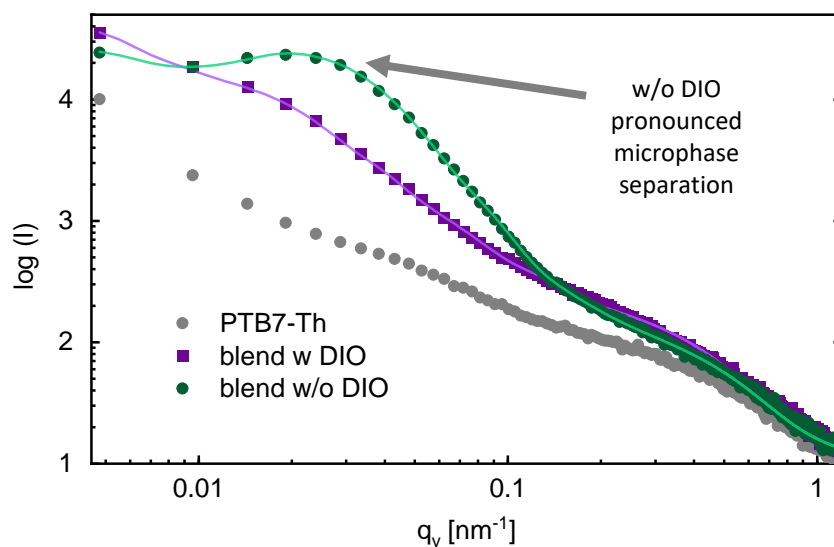


**Figure 6.3**

Integrated horizontal line cuts and respective modeled curved (light lines) for the PTB7-Th:PC<sub>71</sub>BM blend with DIO (purple) and without DIO (green). The intensity and  $q_y$  axis are plotted logarithmically for better visualization of the features.

the microphase separation within the blend, as has also been described by others for similar systems without additives.<sup>[27,231,260,261]</sup>

To better visualize the differences between the films, the respective data are integrated for horizontal line cuts in the polymer Yoneda region ( $q_z$  between  $0.6 \text{ nm}^{-1}$  and  $0.7 \text{ nm}^{-1}$ ), as illustrated in Figure 6.3. Data for the blend with DIO are plotted in purple and for the blend without DIO in green. For comparison, data of the pure polymer film are shown in grey, illustrating the much lower scattering intensity due to the missing phase contrast. The most striking difference between the blends is the pronounced intensity maximum at  $q_y = 0.02 \text{ nm}^{-1}$  for the blend film without DIO. The data for the blends are modeled to extract the average dimensions of the scattering polymer domains in the active layer. Due to the missing phase contrast, this model is not applicable for the pure polymer film. With a combination of three cylindrical structures (form factor) a 1D paracrystalline distribution (structure factor), the experimental data can be modeled. This model has been successfully applied to similar organic thin films, for example other BHJ solar cells, and is also used for organic solar cells discussed in the following chapter.<sup>[65,68,70,261]</sup> Based on the distorted-wave Born approximation (DWBA) to take the grazing incidence geometry into account, the local monodisperse approximation (LMA) is applied to model the scattering intensity via incoherent superposition of the intensities of the individual structures. The respective modeled structure parameters are listed in Table 6.1, showing a significant difference in large and medium structures.

**Table 6.1**

Structure parameters extracted from the models shown in Figure 6.3 for the PTB7-Th:PC<sub>71</sub>BM blend films.

| sample   | structures | diameter $2R$ [nm] | distance $D$ [nm] |
|----------|------------|--------------------|-------------------|
| with DIO | large      | $100 \pm 15$       | $540 \pm 20$      |
|          | medium     | $28 \pm 4$         | $136 \pm 10$      |
|          | small      | $6 \pm 2$          | $40 \pm 5$        |
| w/o DIO  | large      | $88 \pm 10$        | $190 \pm 20$      |
|          | medium     | $46 \pm 5$         | $160 \pm 15$      |
|          | small      | $4 \pm 2$          | $38 \pm 4$        |

The pronounced intensity peak for the blend without additive is assigned to structures (diameter  $2R = (88 \pm 10)$  nm) with a comparably small and defined structure factor (distances  $D = (190 \pm 20)$  nm). These largest structures are associated with the smallest aggregates found via AFM at the surface of the respective blend film, as discussed earlier. All larger structures seen via AFM cannot be resolved with the used GISAXS setup and contribute to the scattering intensity around  $q_y = 0$ . In contrast to the blend without additive, the blend with additive exhibits a much less defined shoulder due to the larger distribution of length scales in the system, which is comparable to other data usually seen for BHJ systems. This also mirrors the findings of the AFM data discussed before, with a large variation of length scales present at the film surface. The addition of the solvent additive leads to smaller medium structures, which benefits the exciton dissociation at the respective phase boundaries (see also Section 2.2 for more details).<sup>[27,261]</sup> Additionally, the larger distribution of length scales with elongated structures is also beneficial for solar cells, as they offer a higher chance for the charge carriers to reach the electrodes.

## 6.4 In-Situ Characterization

For the in-situ investigation of the sputter deposition, the samples are observed using GISAXS and GIWAXS. Many of the concepts used in the following are based on findings of the previous chapter and have been described in more detail in Section 5.3.

### 6.4.1 Island Growth

As mentioned before, the sputter rate has a significant impact on the deposited gold film. While lower sputter rates leave enough time for the gold particles at the surface to rearrange, this process cannot compete with higher sputter deposition rates, as investigated in more detail by Schwartzkopf et al. for gold on polystyrene (PS).<sup>[142]</sup>

The low deposition rate of  $0.036 \text{ nm s}^{-1}$  chosen for the following experiment allows for the particles and small clusters to rearrange on the polymer surface, leading to larger clusters at higher average cluster distance  $D$ , which leads to larger grains in the later film. As these processes depend on the thin film morphology, the low sputter rate is chosen for the following experiment to focus on potential differences between the blend films.

To investigate the gold deposition process on the different samples, representative 2D GISAXS data for effective film thicknesses  $\delta \approx 0.2, 1, 2, 4$  and  $8 \text{ nm}$  are plotted in Figure 6.4. Shown are data for thin films of pure PTB7-Th in comparison to its blend with PC<sub>71</sub>BM with and without DIO. The chosen values for  $\delta$  correspond to the growth phases, as defined in Chapter 5, which are also in general valid for the blend films, as will be clarified in the following. When comparing the 2D GISAXS data, a strong similarity between the different samples for all phases is visible. The electrode growth shows a similar process for all samples, with a cluster and island growth for the blends as well as the pristine polymer thin film. Only slight changes are visible in vertical direction. The sample without DIO continuously shows an increased diffuse scattering, which is in accordance with the initial 2D GISAXS and AFM data illustrating a higher surface roughness of the original blend film.

To get a better insight into the island growth, horizontal line cuts at the Yoneda region of the materials are plotted over effective film thickness for all three samples in Figure 6.5. Here again, the region of interest (ROI) is chosen to include all important Yoneda regions, from the polymer at around  $q_z = 0.65 \text{ nm}^{-1}$  to the final value for the closed gold film  $q_z = 0.90 \text{ nm}^{-1}$ , to follow the formation of the gold clusters from the very beginning. The early gold film has a vastly decreased density and therefore a critical angle still dominated by the polymer that rises with increasing film thickness. The contour plots show a clear increase in intensity at  $q_y = 0$  over the first few nm of effective film thickness. Symmetric side maxima emerge from a very early stage, corresponding to small gold clusters that are built via nucleation in the first few seconds of the deposition process. The maxima evolve at a similar position for all three samples, and move to smaller  $q_y$  values until almost merging with the intensity at  $q_y = 0$ .

The 1D data are fitted using a combination of a Gaussian for the intensity at  $q_y = 0$  and two symmetric Lorentzian functions for the evolving lateral peaks. For the blend films, an additional double Lorentzian peak is needed to fit the broadened intensity at low  $q_y$ , modeling the large structures also visible in the AFM data (see Figure 6.1). The fitted  $q_y$  position, full width at half maximum (FWHM), and intensity of the cluster side peaks is shown in Figure 6.6 for all three samples. Data for the blend with DIO are plotted in purple and for the blend without DIO in green. The fitted values exhibit only negligible errors for later stages, confirming the validity of the fitting procedure even for stages in which the peak is moving to very small  $q_y$  values. The  $q_y^*$  position

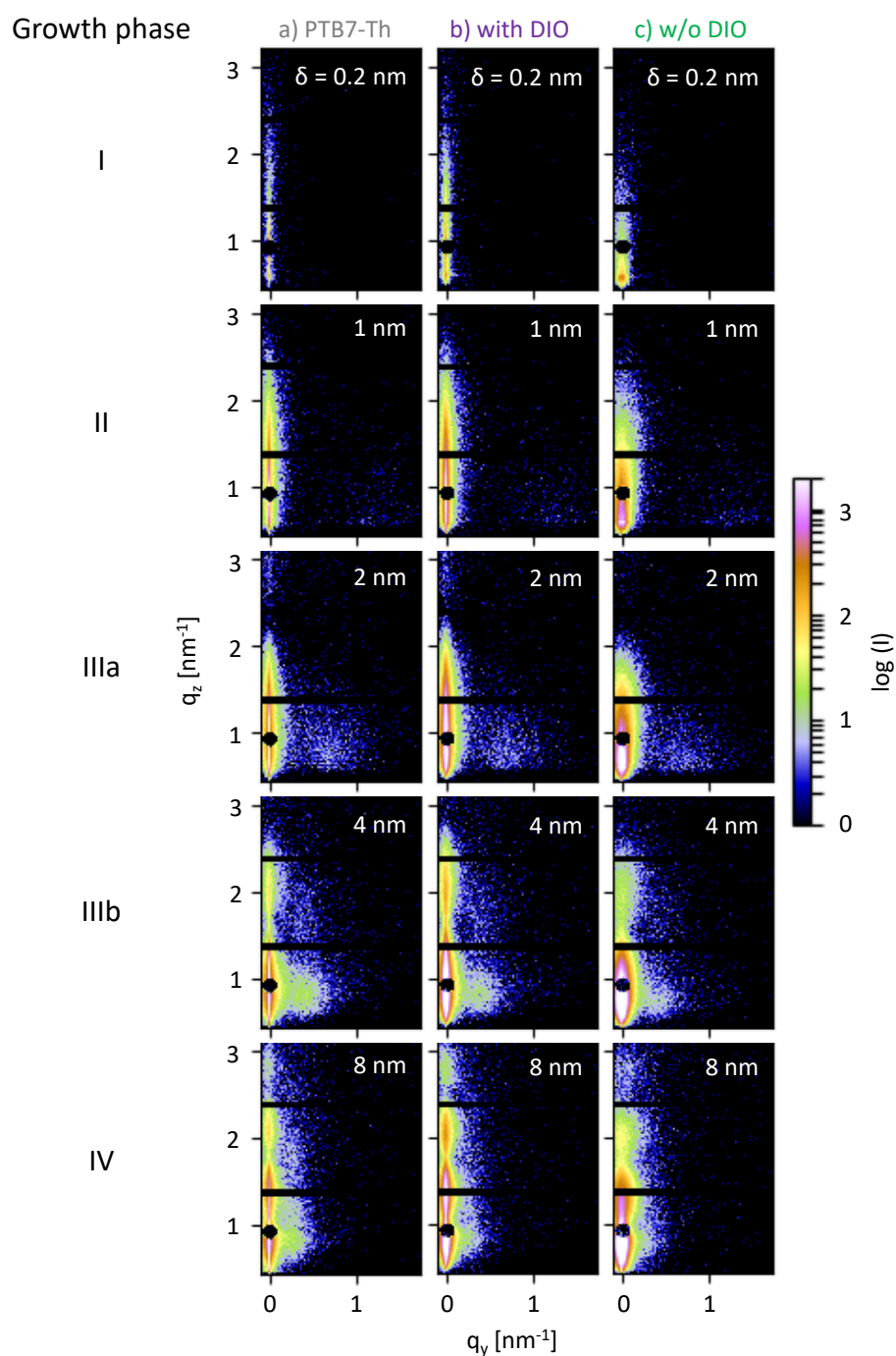


**Figure 6.4**

Exemplary 2D GISAXS data for a) pristine PTB7-Th, b) the PTB7-Th:PC<sub>71</sub>BM blend with DIO, and c) the blend without DIO, taken at specific points in time, corresponding to effective thicknesses in different growth phases ( $\delta \approx 0.2, 1, 2, 4$  and  $8$  nm), as discussed in detail in Chapter 5. In horizontal ( $q_y$ ) direction, the in-plane evolution of structures can be observed in form of intensity maxima. The formation of Kiessig fringes resulting from the gold layer is visible in vertical direction.

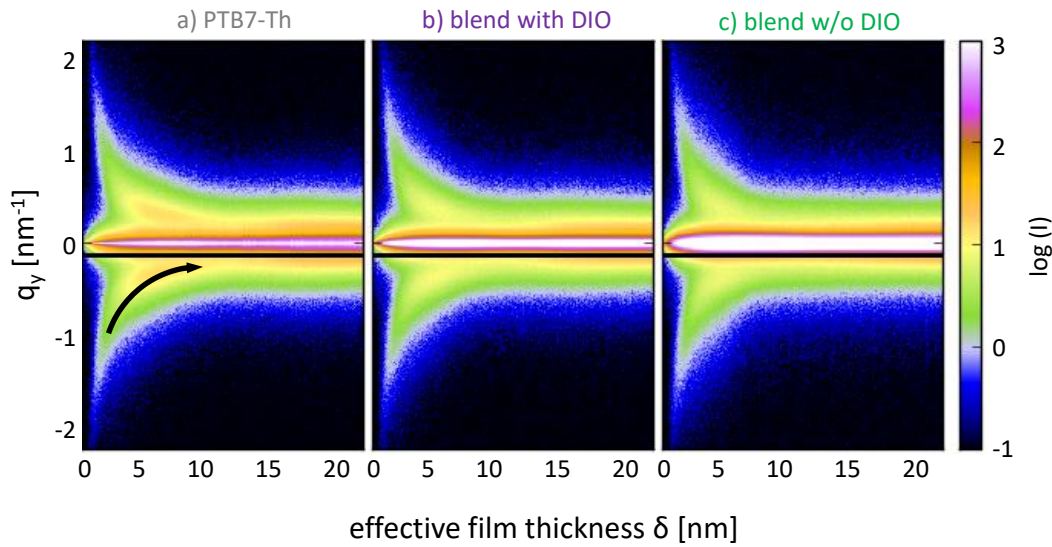


**Figure 6.5**

Contour mapping plots of the horizontal line cuts for every frame for a) pristine PTB7-Th, b) the PTB7-Th:PC<sub>71</sub>BM blend with DIO, and c) the blend without DIO, plotted as a function of effective film thickness.

of the side maxima derives from the Bragg-like scattering of the gold clusters and can be converted to the average cluster distance  $D$  via the relation

$$D \approx \frac{2\pi}{q_y^*}.$$

The decrease in  $q_y^*$  indicates an increase in  $D$  for all samples. The peak width or FWHM is affected by the average cluster size and shape distribution as well as the disorder in the paracrystalline lattice. The width decreases rapidly during the sputtering process, which indicates a strong lateral growth of gold clusters. The peak intensity depends on the scattering contrast of the material phases within the sample. While the  $q_y$  position and FWHM have similar trends for all samples, the intensity of the side maxima shows pronounced differences. Due to its smoother surface, the gold clusters on the pure polymer film have significantly higher contrast, leading to a higher intensity for the cluster peak. The blends exhibit a rougher morphology, resulting in more diffuse scattering and less defined contrast of the gold clusters.

Using the model discussed in more detail in Chapter 5, the cluster radius  $R$  and other structural parameters can be calculated for the respective samples. The values are plotted over effective film thickness in Figure 6.7, giving a similar general trend for all three samples. Subfigure a) shows the average cluster distance  $D$  and the respective calculated average cluster radius  $R$ . The evolution of the ratio between average cluster diameter ( $2R$ ) and distance ( $D$ ) as well as changes in the surface

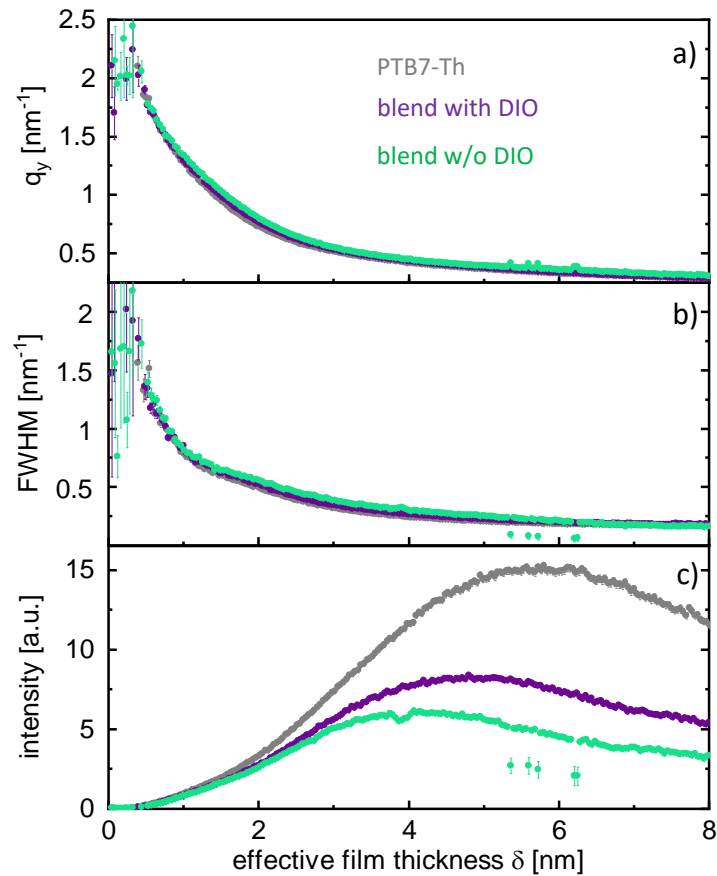


**Figure 6.6**

Evolution of the fitted a)  $q_y^*$  position, b) FWHM, and c) intensity of the gold side peak in lateral direction for PTB7-Th (grey) and the PTB7-Th:PC<sub>71</sub>BM blend with DIO (purple) and without DIO (green) over effective film thickness.

coverage  $\theta$  are illustrated in Subfigure b). Subfigure c) follows the evolution in the cluster density  $\rho$  (per  $\text{cm}^2$ ) and the number of gold atoms per cluster. As seen in the previous chapter for the pure polymer samples, the parameters show pronounced changes for different phases. The island growth mechanism can be explained by the strong affinity of gold atoms to each other as compared to their affinity to the organic films, which leads to a 3D cluster growth until the percolation limit is reached. More details on the different growth phases and the respective dominating processes have been discussed in Section 5.3.3.

Apart from this general similarity in the growth, some important differences between the blends can be distinguished.  $D$  and  $R$  of the pure polymer and the blend with DIO overlap or are very close for most of the growth. The blend without DIO shows significant deviations, with lower overall  $D$  and  $R$ , but higher  $2R/D$  ratio and surface coverage  $\theta$ . These findings suggest that the addition of DIO leads to a growth behavior

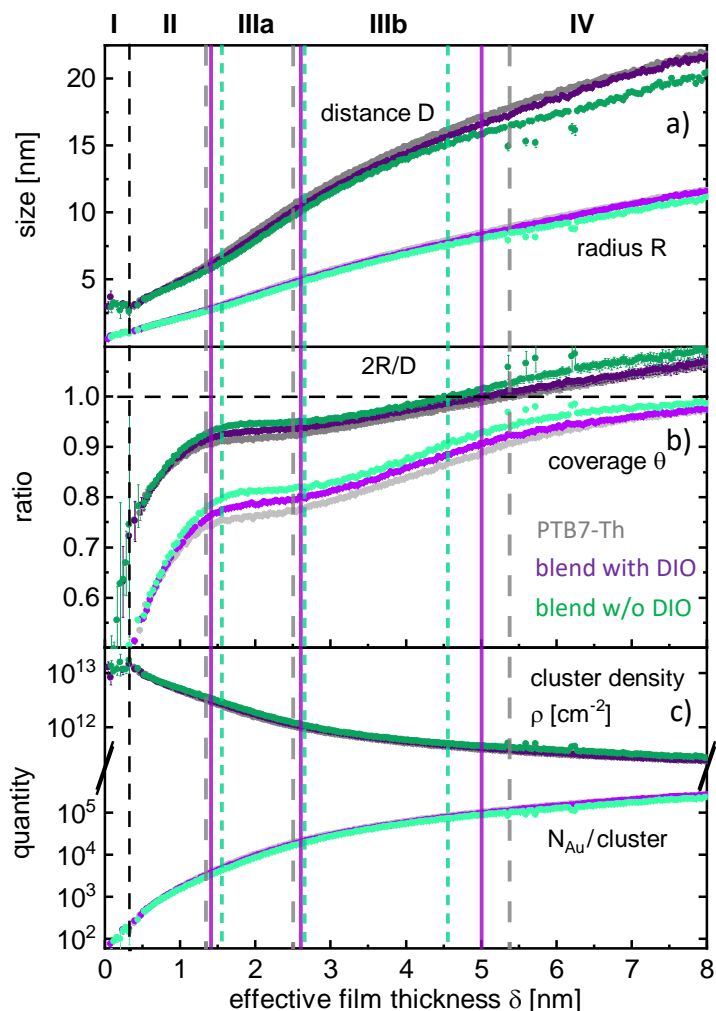


**Figure 6.7**

Structure evolution over effective film thickness shown by the a) average cluster distance  $D$  (dark symbols, extracted from fits) and radius  $R$  (light, calculated) for PTB7-Th (grey) and the PTB7-Th:PC<sub>71</sub>BM blend with DIO (purple) and without DIO (green). The model additionally yields b) the ratio of the average cluster diameter to average cluster distance  $2R/D$  (dark) and the surface coverage (light) and c) the cluster density (dark) and number of gold atoms per cluster (light). The structure evolution can be divided into different stages, as defined by the respective most dominant process: I) nucleation, II) diffusion-mediated coalescence, III) adsorption-dominated growth with a) partial coalescence and b) further growth of ramified clusters under size restrictions, and IV) layer growth.

**Table 6.2**

Phase limits for the three samples, as extracted from the data shown in Figure 6.7.

| phase limit             | effective film thickness $\delta_{Au}$ [nm] |                 |                 |
|-------------------------|---|-----------------|-----------------|
|                         | PTB7-Th                                     | blend with DIO  | blend w/o DIO   |
| I $\rightarrow$ II      | $0.32 \pm 0.03$                             | $0.32 \pm 0.03$ | $0.32 \pm 0.03$ |
| II $\rightarrow$ IIIa   | $1.35 \pm 0.02$                             | $1.41 \pm 0.02$ | $1.56 \pm 0.02$ |
| IIIa $\rightarrow$ IIIb | $2.51 \pm 0.05$                             | $2.61 \pm 0.05$ | $2.66 \pm 0.05$ |
| IIIb $\rightarrow$ IV   | $5.38 \pm 0.08$                             | $5.01 \pm 0.08$ | $4.56 \pm 0.08$ |

more closely resembling the one on the pure PTB7-Th film, which can be explained by different factors. Firstly, the blend with DIO shows an overall smoother surface than the one without, as was also shown in the initial AFM and GISAXS data. Secondly, the addition of DIO leads to a preferential PTB7-Th enrichment layer near the surface, as is shown for similar systems in the literature.<sup>[66,231,265,266]</sup> Both factors make the blend with DIO behave more like the pristine polymer film. The dashed lines indicate the approximate phase limits, as defined in Section 5.3.3. The exact values for the three samples are listed in Table 6.2, showing distinct differences between the films.

Comparing the three samples, differences regarding the phases can be determined. The onset of phase IIIa, which is characterized by an almost constant  $2R/D$  ratio, is directly connected to the cluster radius  $R$  on the respective samples. With higher  $R$ , the cluster surface mobility is decreased. At a certain critical radius  $R_c$ , calculated via Equation 5.11, merging smaller clusters build elongated rather than fully coalesced larger clusters, as the coalescence takes longer than the deposition and adsorption of atoms (see also Section 5.3.3 for more details on the surface mobility and  $R_c$ ). Gold sputtered on the polymer film, exhibiting overall larger  $R$ , reaches this limit earlier than the blends. Due to the higher surface coverage of the gold layer on the blend films, the respective percolation limit is reached significantly earlier than on the polymer sample. Here again, the blend with additive shows a value in between the pristine polymer film and the blend film without additive. As the same model is used for the three samples, all those effects mainly arise from the variance in  $D$ .

The difference is established already at an early stage when the surface morphology of the underlying films has a considerable effect on the gold layer growth. In literature, a connection could be found between the respective organic block dimensions of various block-copolymers and length scales found for the applied metal film.<sup>[130,131,134]</sup> For those systems, the contrast for the features present in the organic film was significantly enhanced when applying a thin layer of gold or silver. For the blend films discussed in the present, no such clear correlation can be found, as the contrast for the organic features shown in the initial GISAXS data (Figure 6.3) is not enhanced by the gold deposition. Other work has investigated the influence of films based on CdSe and PbS

nanocrystals, finding a templating effect of the nanocrystal pattern on the applied gold layer.<sup>[267,268]</sup> As the blend films investigated in the present chapter are based on less-ordered, all-organic materials, no pronounced templating effect is expected even for the PC<sub>71</sub>BM aggregates in the blend film without DIO. Yet a certain preferential accumulation of gold in the pores between aggregates can be assumed for later phases of the layer growth due to reduced mobilities in the confined spaces. Additionally, the roughness of the blend films affects the calculated structure parameters. For the geometric model, a smooth substrate is assumed, which works well in generally explaining the trend in the parameters. However, a higher surface roughness increases the total surface area available for the deposited gold particles, thereby also increasing the actual distance between clusters  $D(\text{roughsurface})$  with an additional vertical component, as also described for gold sputter-deposited on comparably rough films of P3P6T<sup>1</sup>:TiO<sub>2</sub><sup>2</sup>+PEDOT:PSS films.<sup>[269]</sup> Due to the higher distances, nuclei and small clusters have a smaller chance to meet and merge to bigger clusters, which again leads to a decreased growth in  $D$  and  $R$ .

## 6.4.2 Layer Growth

Aside from the lateral structures within the photoactive layer and gold electrode, the vertical film composition plays a crucial role in the performance of organic electronic devices. The incorporation of gold particles and clusters within the soft organic film leads to a gold enrichment layer, which affects the electrical properties of the layer stack. The vertical film profile can be investigated using information from the in-situ GISAXS experiment, as also explained in the previous chapter. Figure 6.8 illustrates the final 2D GISAXS data of the deposited gold film on the three samples. The total gold film thickness can be calculated via Equation 2.28

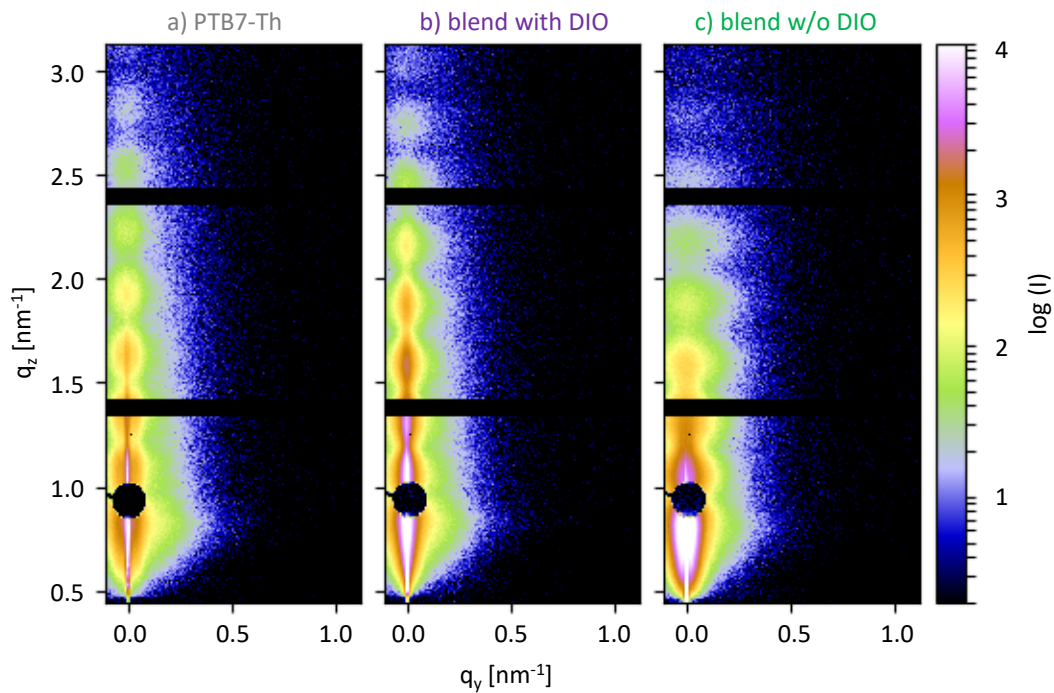
$$\delta_{Au} \approx \frac{2\pi}{\Delta q_z},$$

as discussed in Section 5.3.2, to be  $\delta_{Au(\text{final})} = (21.5 \pm 0.2)$  nm for the pure PTB7-Th sample,  $(22.3 \pm 0.2)$  nm for the blend with DIO, and  $(22.4 \pm 0.2)$  nm for the blend without DIO. The variance in the final film thickness may result from several factors, such as differences in the film roughness and gold-polymer interfaces. Here again, a stronger overall scattering is visible for the blend sample without additive, corresponding to the higher surface roughness of the underlying blend film. The blend films seem to induce a gold layer of higher roughness, which leads to more forward scattering and is discussed in more detail in the following.

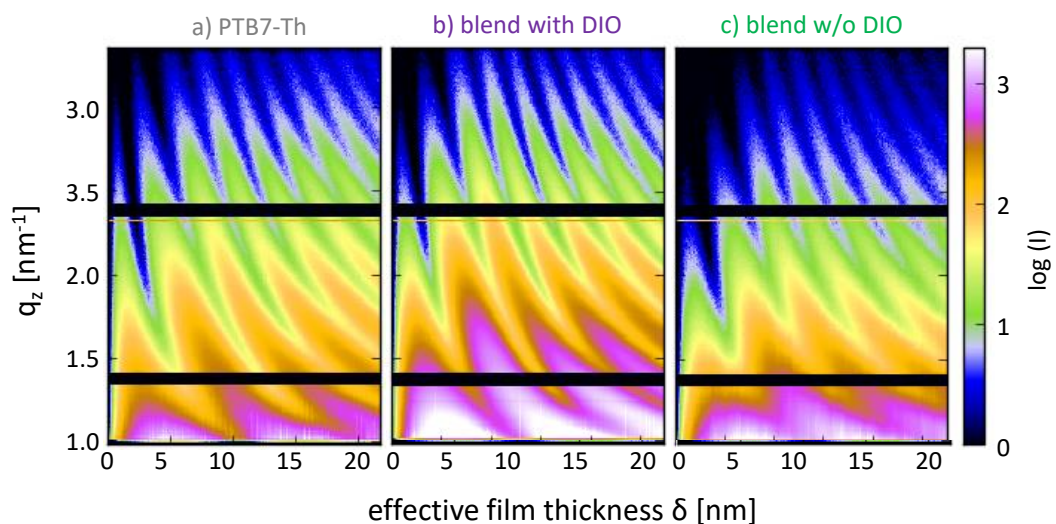
In vertical direction, the gold layer growth can be easily followed by the evolution of the intensity maxima to smaller  $q_z$  values. Figure 6.9 illustrates this effect by plotting the vertical cuts taken at  $q_y = 0 \text{ nm}^{-1}$  over time for all three samples. In principle,

<sup>1</sup>P3P6T: poly[3-(potassium-6-hexanoate)thiophene-2,5-diyl]

<sup>2</sup>TiO<sub>2</sub>: titanium dioxide

**Figure 6.8**

Final 2D GISAXS data taken after the full gold sputter deposition process for a) pristine PTB7-Th and PTB7-Th:PC<sub>71</sub>BM blends b) with DIO and c) without DIO.

**Figure 6.9**

Contour mapping plots of the vertical line cuts for every frame for a) pristine PTB7-Th, b) the PTB7-Th:PC<sub>71</sub>BM blend with DIO and c) the blend without DIO, and plotted as a function of effective film thickness  $\delta$ .

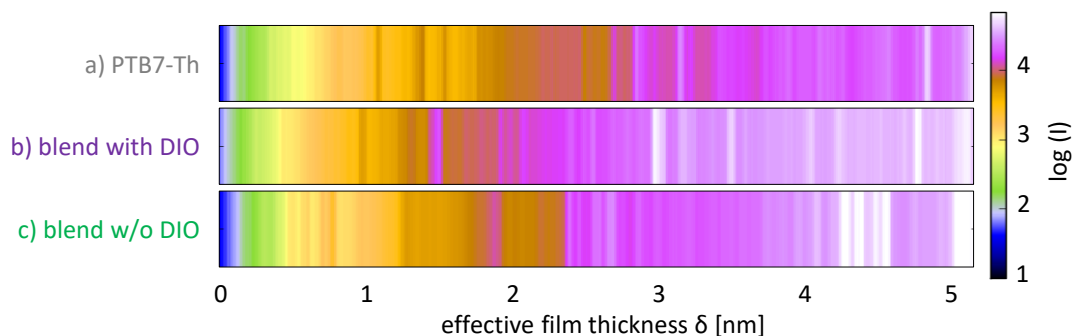


**Figure 6.10**

Change in intensity around the gold Yoneda at  $q_y = 0$  (integrated between  $0.8 \text{ nm}^{-1} < q_z < 0.9 \text{ nm}^{-1}$ ) for every frame for a) pristine PTB7-Th and PTB7-Th:PC<sub>71</sub>BM blends b) with DIO and c) without DIO, and plotted as a function of effective film thickness  $\delta$ .

the layer growth looks very similar, with an interestingly lower intensity at higher  $q_z$  values for the blend without DIO. This can be explained by the initial intensity of the film showing less pronounced scattering in  $q_z$  direction due to the higher roughness, which templates the gold scattering intensity to a certain degree. However, as the gold scattering intensity soon surpasses the scattering of the organic film below it, this cannot fully explain the effect at higher effective film thicknesses. It can be deduced, that the surface of the gold film shows a higher roughness with more diffuse scattering. Indeed, going back to the 2D GISAXS data discussed in Section 6.4.1, we see a higher intensity for  $q_y \neq 0$  for the blend film without DIO.

The difference in intensity around the gold Yoneda for the different samples is especially visible when focusing on the region of  $0.8 \text{ nm}^{-1} < q_z < 0.9 \text{ nm}^{-1}$  for  $q_y = 0$  (integrated over three pixels). Figure 6.10 plots this integrated intensity for PTB7-Th versus its blend with PC<sub>71</sub>BM with and without DIO over effective film thickness. For all samples, a very low initial intensity in this region is visible, as no gold has been applied and therefore no significant scattering occurs under the respective angles. However, a clear difference can be distinguished for the next few nm of the gold layer growth. The intensity for the blend with DIO increases strongly in earlier stages, while the increase in intensity (corresponding to a growing gold layer with higher density) is delayed for the pristine polymer and its blend without DIO. However, the blend without DIO shows a later strong increase in intensity corresponding to a higher surface roughness of the sample. Both blend samples exhibit a rougher gold film as compared to the pristine PTB7-Th sample, resulting in higher overall intensities.

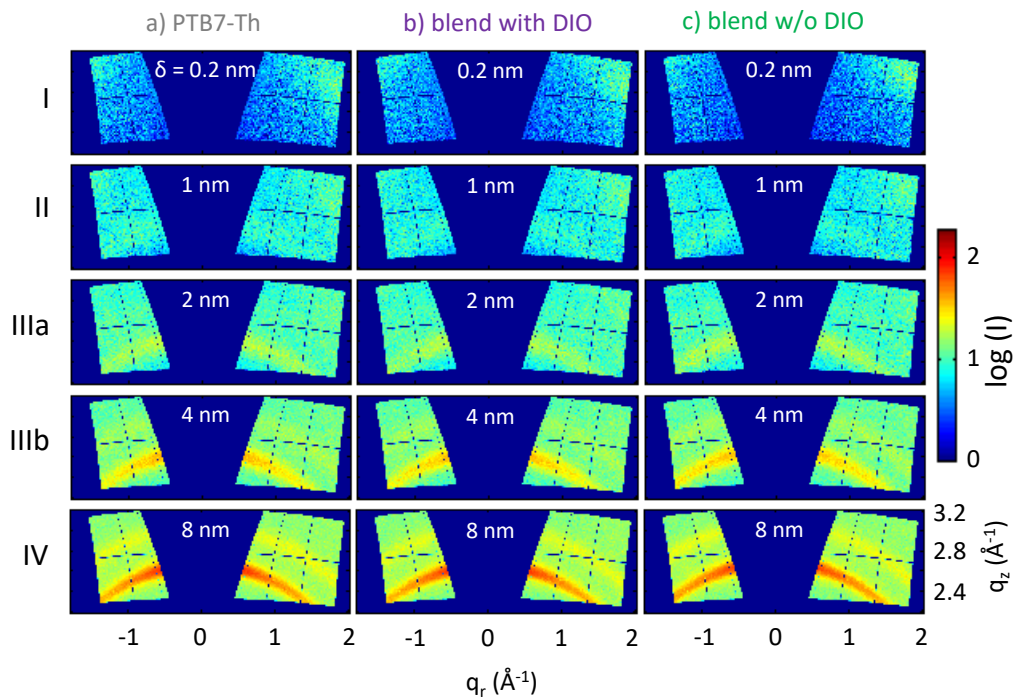


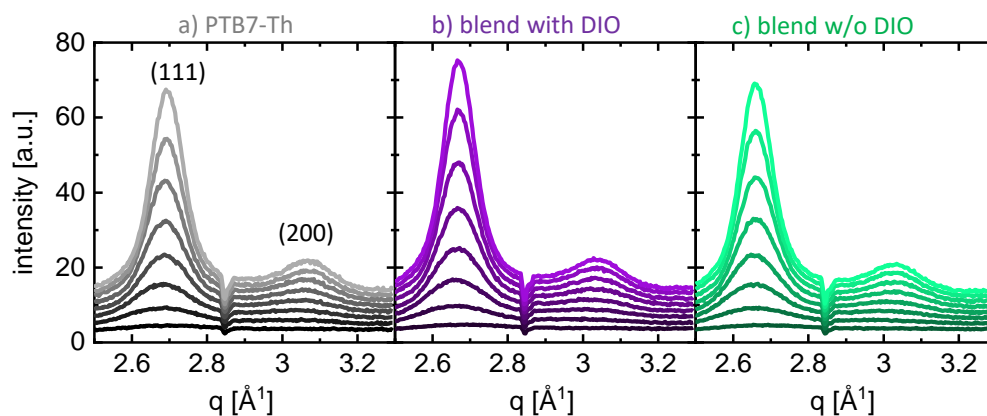
**Figure 6.11**

Exemplary 2D GIWAXS data for a) PTB7-Th, b) the PTB7-Th:PC<sub>71</sub>BM blend with DIO, and c) the blend without DIO, taken at specific effective thicknesses in different growth phases ( $\delta \approx 0.2, 1, 2, 4$  and  $8$  nm). Vertical cake cuts are taken, integrating over angles  $\chi$  between  $-20^\circ$  and  $+20^\circ$ . Intensity corrections and reshaping steps are performed using the MATLAB-based software GIXSGUI.<sup>[169]</sup>

### 6.4.3 Gold Layer Crystallinity

Parallel to the GISAXS investigation, GIWAXS measurements are performed in situ during the sputtering process to investigate the crystalline structure of the evolving gold film. Representative 2D GIWAXS data for different stages during the layer deposition are plotted in Figure 6.11 for the pure PTB7-Th film and its blend with and without DIO. Illustrated are data from different growth phases ( $\delta \approx 0.2, 1, 2, 4$  and  $8$  nm), showing the increase in overall scattering intensity and the appearance of the two scattering Bragg peaks also discussed in the previous chapter.

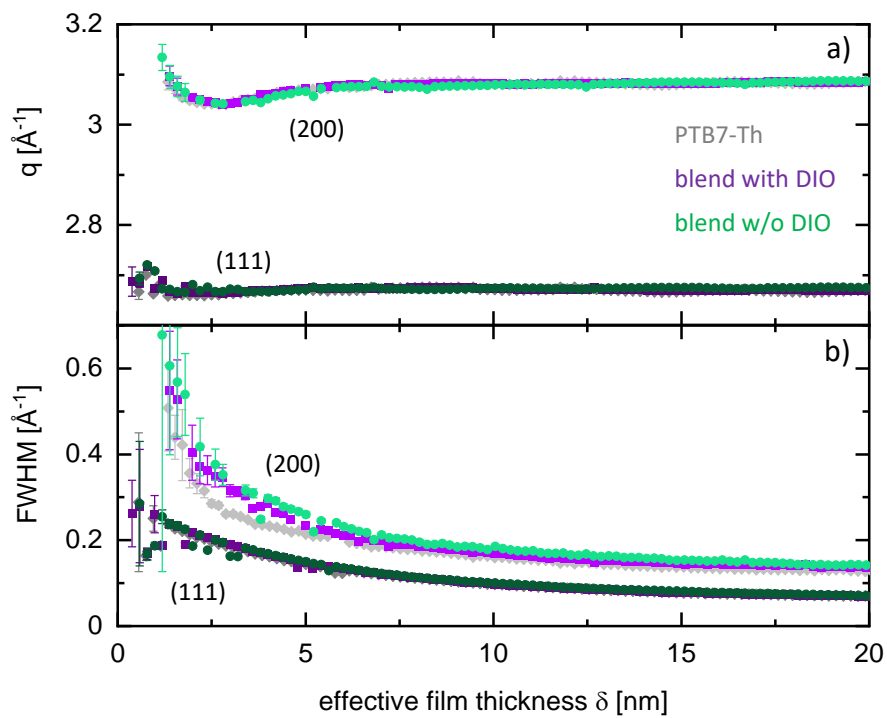
The 2D data are reduced to 1D data in a certain ROI to see the developing Bragg peaks in vertical direction. Intensity corrections and reshaping steps are performed using the MATLAB-based softer GIXSGUI.<sup>[169]</sup> Exemplary vertical cake cuts are integrated over the azimuthal angle  $\chi$  from  $-20^\circ$  to  $+20^\circ$  and plotted in Figure 6.12 for the three samples. Two Bragg peaks are visible for the vertical direction, namely the (111) peak at  $2.676 \text{ \AA}^{-1}$  and the (200) peak at  $3.088 \text{ \AA}^{-1}$ . All three samples show a similar increase in intensity for the two Bragg peaks, as also discussed in more detail in the



**Figure 6.12**

Evolution of the crystallinity of the gold layer illustrated via exemplary integrated vertical cake cuts (for  $\chi$  between  $-20^\circ$  to  $+20^\circ$ ) of the 2D GIWAXS data taken every 2.1 nm starting at  $\delta = 0$  nm for PTB7-Th (grey) and the PTB7-Th:PC<sub>71</sub>BM blend films with DIO (purple) and without DIO (green).

previous chapter. For all three samples, the final  $q$  position – meaning the final gold lattice spacing – is established in a very early stage of the deposition process, while the FWHM continues its decrease. As discussed in the previous chapter, the FWHM is inversely correlated to the crystal size via the Scherrer formula (Equation 2.38), thereby indicating an increase in crystal size. The peaks are fitted with Pseudo-Voigt functions plus constant background to track their  $q$  positions and FWHM over effective film thickness, as illustrated in Figure 6.13. Similar to the previous chapter, the final  $q$  position – meaning the final gold lattice spacing – is established after  $\delta \approx 2$  nm for the (111) peak and after about  $\delta \approx 4$  nm for the (200) peak for all samples alike. The FWHM of the peaks also shows a trend similar to the one seen for the pure polymers in the previous chapter with an exponential decrease illustrating the increase in crystal quality and size. The slightly larger values for the blend films can be explained by their rougher surface, which disturbs the crystal growth. Summarily, both the increase in  $q$  position and decrease in FWHM result from an increase in crystal quality and crystal size, showing that also on the blend films, the gold clusters form crystal structures at the early stages of the layer growth.

**Figure 6.13**

The (111) and (200) Bragg peaks shown in Figure 6.12 are fitted with Pseudo-Voigt functions plus constant background for all frames. The results are plotted over effective film thickness for PTB7-Th (grey) and the PTB7-Th:PC<sub>71</sub>BM blend films with DIO (purple) and without DIO (green). No pronounced differences are visible between the samples for a) the  $q$  positions and b) the FWHM of the (111) and (200) Bragg peaks (illustrated in dark and light colors, respectively).

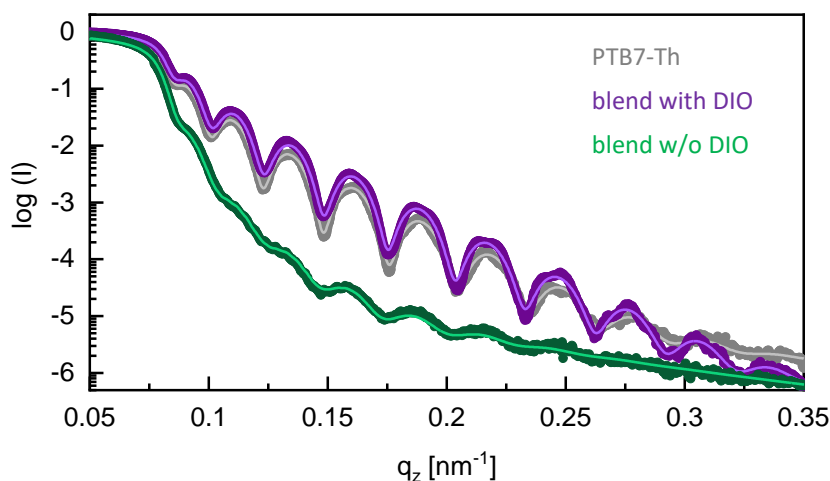


**Figure 6.14**

XRR data (points) and corresponding fits (lines) for gold sputtered on films of pristine PTB7-Th (grey) and PTB7-Th:PC<sub>71</sub>BM blends with DIO (purple) and without DIO (green).

## 6.5 Ex-Situ XRR

To acquire more information about the vertical film composition and gold incorporated within the organic layer, the films are investigated ex situ using XRR. This method is especially valuable in probing enrichment layers. Due to the strong difference in scattering length density (SLD) depending on the electron density of the gold versus the organic materials, a high contrast between the different layers is to be expected. This effect was also shown in earlier work for similar systems.<sup>[133,270]</sup> Due to its high SLD, even small amounts of incorporated gold particles within the organic layer will drastically increase the averaged SLD of the respective part of the layer.<sup>[271]</sup> The measurements are taken ex situ at the in-house instrument – several days after the sputter deposition – which has to be taken into account when directly comparing the results with the in-situ GISAXS data on the gold layer thickness. The XRR curves and fits for all three samples are illustrated in Figure 6.14. Similar to the vertical film profile in the GISAXS data, the XRR profiles show the prominent Kiessig fringes of the respective gold layers. The fringes for all three samples are similar in width and position due to the similar final gold film thickness. Especially the samples based on the pure polymer and its blend with DIO look highly similar, while the blend without additive shows a pronounced decrease in intensity towards higher  $q_z$  values. This effect can be assigned to the higher roughness of the layers within this sample, which also induces a rougher top surface of the gold film. For all samples, the data can be modeled using the Igor-based software Motofit with a stack of different layers with different SLDs.<sup>[158]</sup> The modeled fits for the data are shown as highlighted lines in Figure 6.14 for the

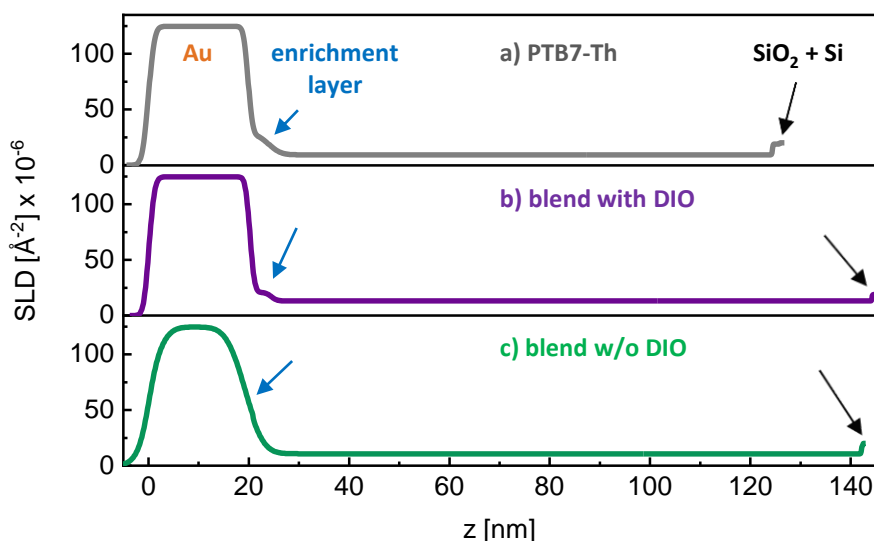


**Figure 6.15**

SLD profiles for the samples, as extracted from the fits in Figure 6.14 for gold sputtered on films of pristine PTB7-Th (grey) and PTB7-Th:PC<sub>71</sub>BM blends with DIO (purple) and without DIO (green).  $z = 0$  nm corresponds to the gold/air interface.

three samples. For this model, a stack of layers of different material composition is assumed, which is also illustrated in the SLD profiles shown in Figure 6.15. Generally, the layers are stacked in the following order from top to bottom, with characteristic differences between the three samples:

Au / enrichment layer (Au in org.) / organic layer / SiO<sub>2</sub> / Si

The substrate for all samples is simulated with an infinite Si layer coated by a thin SiO<sub>2</sub> layer (below 2 nm) with low roughness. The following organic layer consists of either the pure polymer PTB7-Th or its mixture with PC<sub>71</sub>BM. For the blends, the SLD results from a combination of the SLDs of both materials. Between the organic layer and the top gold film, an additional enrichment layer is implemented to model the gold enrichment layer within the soft organic material. This intermixing layer consists of mainly organic components with low gold content. In our earlier work, we found an enrichment layer of around 3.5 nm thickness with a gold content of around or less than 7%.<sup>[270]</sup> As the applied sputter rate is higher for the data presented here, those values are expected to be somewhat higher. Indeed, for the pure polymer film, the SLD for this intermixing layer suggests a gold content of up to 10% for a slightly higher layer thickness of about 4 nm. In comparison to the blend with additive, the pure polymer film shows a higher SLD for the intermixing layer. This might be due to the higher affinity of gold to the thiophene groups of PTB7-Th in comparison to other organic groups (see the previous chapter for more details). The changes in SLD

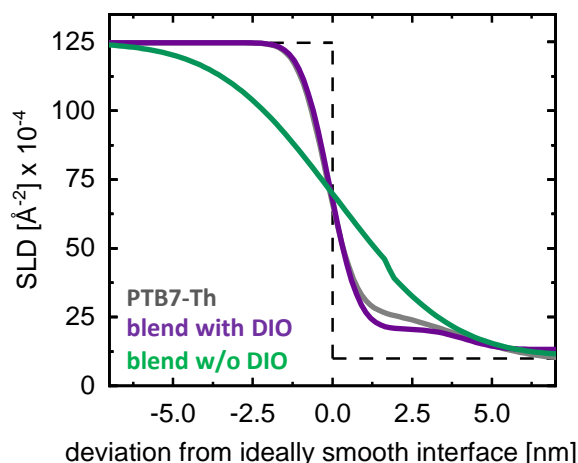


**Figure 6.16**

Zoom into the SLD profiles around the polymer-metal interface for gold sputtered on films of pristine PTB7-Th (grey) and PTB7-Th:PC<sub>71</sub>BM blends with DIO (purple) and without DIO (green). The dashed line at 0 nm corresponds to an ideally smooth polymer-metal interface.

around the polymer-metal interface are highlighted in Figure 6.16. A hypothetical, ideally smooth polymer-metal interface serves as a basis of comparison (shown with a dashed line). Both the pure polymer film and the blend with additive exhibit a rather steep decrease in SLD around the hypothetical interface line due to the comparably low interface roughness. The gold enrichment layer for both samples can be distinguished as a shoulder between 0.5 nm and 5 nm. In contrast, the blend without DIO exhibits a comparably slight SLD gradient in a range of over 10 nm around the interface line due to the higher interface roughness, thereby masking the enrichment layer.

For both the blend with additive and the pure polymer film, the described model can fit the experimental data very well. However, the blend without DIO shows a more complicated curve, which can be explained by several factors. As discussed before, it is known that the absence of DIO leads to an accumulation of fullerene clusters at the surface of the blend film, which increases the layer roughness and is expected to lead to a pronounced gold-organic intermixing layer.<sup>[184,260,261,264]</sup> Secondly, this higher roughness will translate to an increase in roughness for the gold layer deposited on top, which leads to significant differences in intensity for the XRR curve at higher  $q_z$  values. By increasing the intermixing layer thickness and the roughness for the upper layers, the model can qualitatively explain the experimental data. Looking at the SLD profile, the higher layer roughness is clearly visible in the much smoother increase from the organic film over a larger intermixing layer to the bulk gold film, meaning that the gold layer is not only incorporated within the organic film but also fills the rough surface between the PC<sub>71</sub>BM aggregates. Additionally, the gold film shows a clearly increased top roughness compared to PTB7-Th and the blend with DIO.

## 6.6 Growth Model

Taking all results from the discussed measurements into account, a comprehensive layer growth model can be deduced. In contrast to the growth model introduced in Chapter 5, also the vertical film profile is addressed, as the XRR measurements in combination with the AFM data yield additional information about the film roughness and incorporation of gold. The model is shown schematically in Figure 6.17, illustrating the differences between the three investigated samples. The initial organic thin films are based on either pristine PTB7-Th (shown in blue) or its blend with PC<sub>71</sub>BM (red). The effect of DIO is taken into account, as the blend with additive shows a thin upper PTB7-Th layer, while the blend without additive exhibits large PC<sub>71</sub>BM aggregates on top. The difference in roughness is shown schematically. Note that the pure polymer film is, of course, not completely flat, but shows vastly decreased peak-to-valley heights in comparison to the blend films. Additionally, PC<sub>71</sub>BM domains and gold clusters are marked by spheres or spheroids for simplification. Phase I is defined by nucleation processes and a high mobility of the very small gold clusters. They are distributed rather evenly on the available surface, but also implemented into the soft organic layer. In phase II, the now nanometer-sized gold clusters at comparably large distances are still very mobile. They grow mostly by incorporation of diffusing gold atoms and by merging with other small clusters and full coalescence, leading to larger clusters at higher distances. Here, the effect of the higher surface roughness of the blend without additive plays a role, as the clusters will accumulate in the spaces between PC<sub>71</sub>BM aggregates. Above a certain cluster size, the surface mobility of the clusters is significantly reduced. Phase IIIa is characterized by partial coalescence of neighboring clusters, forming elongated structures, which leads to a further increase in the average cluster distance  $D$ . This increase is hindered slightly for the blend without additive, which might be due to space limitations of the clusters between the PC<sub>71</sub>BM aggregates. In phase IIIb, the clusters grow mainly by incorporation of deposited clusters and filling gaps. The merging of immobile clusters leads to a non-continuous coverage of the surface with percolated, worm-like structures. For this later phase, the influence of the underlying organic layer should not play a major role in the processes within the gold layer. However, the effective film thickness is still significantly lower than typical heights for the PC<sub>71</sub>BM aggregates on the blend without DIO, so that the gold layer is still affected in terms of roughness and surface coverage. Towards the end of phase III,  $D$  grows significantly less than for the other samples, hinting at space restrictions due to the PC<sub>71</sub>BM aggregates. Phase IV is reached at the percolation limit and characterized by a severely space-limited grain growth for all samples. The final films show a bulk gold layer at all samples, with a higher roughness and intermixing layer for the blend without DIO, compared to the other two films.

Summarily, the gold film growth shows a similar behavior on all three samples, with similar growth stages at similar effective film thicknesses. However, differences in the

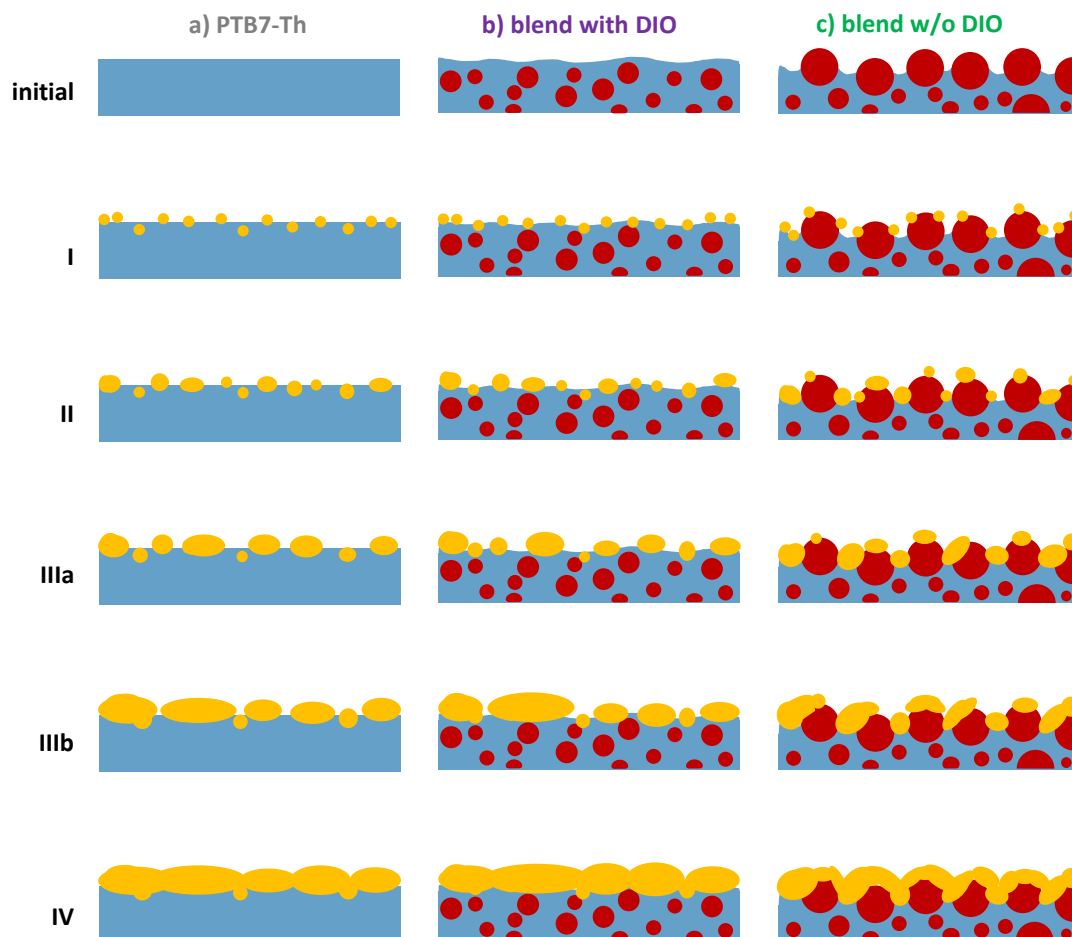


**Figure 6.17**

Growth model for the three different samples derived from combined results of the different measurements. Shown are the initial state and the five growth phases: I) the nucleation, II) the diffusion of gold adatoms and small clusters on the polymer film, III) the adsorption of further gold atoms with a) partial coalescence and b) further growth of coarse, ramified structures and IV) finally a layer growth. The layers consist of PTB7-Th (blue) and PC<sub>71</sub>BM (red), with gold shown in orange. The blend without DIO exhibits a rough layer of PC<sub>71</sub>BM agglomerates that lead to an increased gold film roughness. Note that several simplifications have to be made to illustrate the general concept.

film morphology play a small, yet important role. The blend processed with additive exhibits a smoother film with comparably more PTB7-Th at its surface, making it behave similarly to the pure polymer film in all measurements. The blend processed without additive is characterized by its increased roughness with pronounced PC<sub>71</sub>BM aggregates, which lead to a larger intermixing layer and a higher roughness of the gold surface. Both features most probably affect the quality of the gold contact for a device and have to be taken into account, when thinking about enhancing the device performance. It can be assumed that the addition of DIO, apart from enhancing the inner morphology of the photoactive layer, enhances the contact quality of a respective electrode significantly, because it enables the growth of a smoother gold contact with larger grains and overall fewer grain boundaries.

## 6.7 Conclusion

This chapter follows the sputter deposition of a thin gold layer on top of different organic thin films. Based on results acquired in the previous chapter for pure polymer thin films, the investigation focuses on morphological effects of blend films based on PTB7-Th in combination with the fullerene derivative PC<sub>71</sub>BM. The blend films are processed either with or without the solvent additive DIO which has pronounced effects on the active layer morphology. Processing with additive leads to a film with a better intermixing of smaller, elongated domains and a smoother surface. Processing without additive results in a film with larger, coarser domains and pronounced aggregates of PC<sub>71</sub>BM at the surface. While the overall growth mechanism is similar for all investigated films and resembles the one seen for the pure polymer films in the previous chapter, the differences in the initial film morphology also affect the deposited gold film in several ways. The blend processed with DIO behaves quite similarly to a pure PTB7-Th film investigated as a reference due to its comparably low roughness and the PTB7-Th enrichment layer at its surface. In contrast, for the blend processed without additive, a significantly larger gold-organic intermixing layer is found, as the gold film fills up spaces between the PC<sub>71</sub>BM aggregates. The aggregates additionally impose space restrictions on the growing gold clusters and increase the roughness of the final gold film significantly. Based on these findings, the quality of the resulting gold layer can be assumed to be higher for the blend film processed with solvent additive. The additive does not only enhance the photovoltaic properties of the active layer but also leads to a smoother gold-organic interface with larger grains and fewer grain boundaries which potentially enhances the charge carrier extraction.



# CHAPTER 7

## Light-Induced and Oxygen-Mediated Aging Processes in PTB7-Th-based Photoactive Layers

The following chapter is based on the publication “Light-Induced and Oxygen-Mediated Degradation Processes in Photoactive Layers Based on PTB7-Th” (Löhner et al., *Advanced Photonics Research*, 2020).<sup>[272]</sup>  
Reproduced with permission from John Wiley & Sons, Inc..

Low-bandgap polymers are sensitive to various degradation processes, which strongly decrease their lifetime (see also Section 2.2.3). The chemical and physical changes occurring in the low-bandgap polymer PTB7-Th and its blend with the fullerene derivative PC<sub>71</sub>BM are followed during irradiation-induced aging by a combination of various characterization methods. The active layer morphology is investigated using atomic force microscopy (AFM) and in-operando grazing-incidence small-angle X-ray scattering (GISAXS), indicating morphological alterations and material loss due to chemical modifications. Optical spectroscopy gives insights into these chemical processes which lead to significant absorption losses under ambient conditions. Independent of the energy of the absorbed photons, but only in combination with oxygen, the excitation of the polymer leads to a fatal increase in oxidation probability. Fourier-transform infrared (FTIR) data highlight the sensitivity of the conjugated polymer backbone to oxidation, a result of lost conjugation and therefore absorption capability. With combined AFM height and infrared light (IR) mapping, the chemical degradation and material loss are confirmed on a nanoscale. Although the chemical structure is seriously damaged, the blend morphology is not undergoing major changes.

## 7.1 Introduction

With the rise of organic photovoltaic (OPV) as a potential competitor to conventional solar cells, research efforts have focused on the two major issues that still hinder a widespread use, namely the comparably low initial power conversion efficiency (PCE) and insufficient long-term stability of purely organic devices. With efficiencies now safely above the industrially relevant threshold for different device architectures,<sup>[273–276]</sup> degradation processes are still a significant issue for most material systems.<sup>[16–18]</sup> Focusing on aging processes within the active layer of the devices, several degradation pathways have been distinguished by existing studies:<sup>[20,24,26]</sup> extrinsic degradation can be triggered by temperature, electromagnetic radiation and/or chemical reaction with pollutants such as oxygen and water, while intrinsic aging is caused by morphological changes and/or modification of the chemical structure within the materials. The morphological degradation of various material systems for use in organic solar cells was investigated using real-space imaging and scattering techniques.<sup>[63,66,67,71,88]</sup> In particular, the morphological aging process was followed in situ during operation of the respective solar cells using X-ray scattering methods in earlier works of our group.<sup>[65,68–70,89,90]</sup> Chemical reactions, on the other hand, were investigated using spectroscopy methods such as ultraviolet/visible (UV/vis) absorption or photoluminescence (PL) as well as Raman and FTIR spectroscopy (see Section 4.1).<sup>[74,92–94]</sup> However, research so far has neglected potential interconnections between chemical and structural changes.

In the present chapter, the influence of irradiation-induced aging processes within thin films of the common solar cell material PTB7-Th and its blend with the fullerene derivative PC<sub>71</sub>BM is investigated. From the large variety of recent solar cell materials, the low-bandgap system PTB7-Th:PC<sub>71</sub>BM can be understood as a next-generation model system in organic solar cells – given the rather large body of existing work – following the famous classical model system P3HT:PCBM with larger bandgap and the PTB7:PCBM system.<sup>[28,113,188,197,265,277–281]</sup> In a recently published study, PTB7-Th:PC<sub>71</sub>BM solar cells even served as exemplary low-bandgap system successfully operating under space applications on a rocket flight.<sup>[282]</sup> Indeed, PTB7-Th is investigated here as a stand-in for a range of irradiation-sensitive low-bandgap polymers.<sup>[67,88,93,107–111]</sup> The changes in morphology and chemistry are followed using a range of different measurement techniques, namely optical and FTIR spectroscopy as well as in-operando GISAXS, but also real-space imaging such as AFM combined with nanoscale IR spectroscopy (see Section 4.2.5 for details on this method).

Combining these complementary techniques gives a comprehensive picture of the processes taking place during photodegradation of PTB7-Th and PTB7-Th:PC<sub>71</sub>BM. The in-operando GISAXS measurements on PTB7-Th:PC<sub>71</sub>BM-based solar cells enable insights into morphological changes within the active layer during operation. In contrast to other systems investigated earlier,<sup>[65,68]</sup> the loss in PCE cannot be correlated to significant changes in the domain sizes. However, changes in scattering contrast and

surface roughness indicate chemical modifications. These modifications are corroborated by UV/vis absorption spectroscopy applied before and during irradiation under ambient conditions with various light sources. A pronounced degradation under ultraviolet (UV) light is visible, as expected from earlier work.<sup>[110-113]</sup> However, even red light can be harmful to low-bandgap materials such as PTB7-Th which shows the highest absorbance in this wavelength region. The degradation is found to be directly connected to the photon count of the light source irrespective of the absorbed photon energy, as long as the energy exceeds the respective bandgap. FTIR measurements show a pronounced chemical aging for the illuminated thin films, indicating photo-oxidative processes damaging the conjugated polymer backbone and destroying the absorption ability of the material. Combined height and IR mapping using a nanoIR AFM setup as described in Section 4.2.5 allows seeing the chemical degradation on a nanoscale,<sup>[209]</sup> confirming the loss of material and changes in chemistry at the sample surface.

## 7.2 Experimental Details

To understand potential aging mechanisms, thin films and OPV devices of the low-bandgap polymer PTB7-Th and the fullerene-derivative PC<sub>71</sub>BM as well as their blend are prepared and investigated in different settings. General information can be found in Chapter 3 and Chapter 4, while experiment-specific details are given below.

**Materials and thin film preparation:** Depending on the investigation technique, either microscopy glass slides or silicon wafers are used as substrates. All substrates are cut to the desired dimensions and cleaned for 15 min in an acid bath. For the preparation of the thin film samples, the cleaned substrates are transferred into a glovebox. The sample preparation is performed under a nitrogen atmosphere to avoid degradation via oxygen and water. The investigated materials are dissolved in chlorobenzene (CB) with a concentration of 14 mg mL<sup>-1</sup> for PTB7-Th, 21 mg mL<sup>-1</sup> for PC<sub>71</sub>BM or 35 mg mL<sup>-1</sup> for their blend (weight ratio 2 : 3). The solutions are stirred overnight at 70 °C, before casting them on the pre-cleaned substrates. The pristine active layer thin films are deposited without further functional layers to better compare the spectroscopy data with the discussed literature. For most experiments, the organic films are spin-cast on glass or silicon substrates, achieving films of 100 nm – 120 nm thickness, as measured via profilometry. For the FTIR investigation with enhanced signal-to-noise ratio, the solutions of the photoactive organic materials are drop-cast on cleaned silicon substrates to achieve thicker films (several tens of micrometers) and a certain thickness gradient throughout the sample to avoid interference. All samples are left to dry for about one day before further investigations.

**Solar cell preparation:** Solar cells are prepared according to routines described in the literature and detailed in Section 3.3.<sup>[197,198]</sup> ITO-coated glass substrates are cleaned and treated with oxygen plasma, before coating them with a PEDOT:PSS film. The active layer solution is prepared under an inert nitrogen atmosphere in a glovebox system, as described above. PTB7-Th ( $14 \text{ mg mL}^{-1}$ ) and PC<sub>71</sub>BM ( $21 \text{ mg mL}^{-1}$ ) are dissolved in ortho-dichlorobenzene (o-DCB) (with 3 vol % of 1,8-diiodooctane (DIO) as solvent additive) and stirred overnight at  $70^\circ\text{C}$ , before spin-casting the solution on the substrates and leaving the samples to dry overnight. Aluminum electrodes are applied in a custom-built thermal evaporation chamber with a pressure of about  $2 \times 10^{-5}$  mbar. Afterward, the devices are reintroduced into the glovebox and sealed under a nitrogen atmosphere for their transport to the synchrotron X-ray source. It should be noted, that for this experiment, the solar cell is intentionally designed without any blocking or encapsulation layer above the active layer for two reasons. On the one hand, the shortness of the assigned measurement time at the X-ray source makes it necessary to probe the solar cell under accelerated degradation conditions. On the other hand, without any additional layers on top of the solar cell, the active layer morphology can be probed directly without any complications.

**In-operando GISAXS measurement:** For the in-operando GISAXS measurements, the custom-built solar cell measurement chamber (for more details see the publication of Schaffer et al.<sup>[65]</sup>) is implemented into the MiNaXS beamline P03 of the PETRA III storage ring at DESY (Hamburg, Germany),<sup>[214]</sup> using a micro-focused X-ray beam ( $22 \times 25 \mu\text{m}^2$ ) with a wavelength of  $0.96 \text{ \AA}$ . In the chamber, a solar cell device is illuminated with a 150 W Xenon lamp (Perkin Elmer PX5) with an intensity of  $100 \text{ mW cm}^{-2}$ , while constantly collecting current-voltage (I/V) curves. The chamber is evacuated to a vacuum of about 0.2 mbar, which should significantly decrease photo-oxidative processes due to a decrease in available oxygen. The sample holder is cooled using a Peltier element to keep the device at a temperature of about  $25^\circ\text{C}$  upon illumination. GISAXS data are taken at certain intervals before, during, and after the illumination experiment to simultaneously probe the active layer morphology, using a Pilatus 1M detector with a sample-to-detector distance of  $(3790 \pm 20) \text{ mm}$  and an incident angle of  $0.367^\circ$ . Data acquisition times are optimized to avoid radiation damage by the intense X-ray beam. Radiation damage tests are performed via continuously irradiating an exemplary region of the sample with X-rays for  $90 \times 1 \text{ s}^2$ . No significant changes are visible in the scattering pattern during and after the illumination. During the in-operando experiment, the total data acquisition time of around 15 s is far below 90 s to ensure the absence of X-ray-induced changes on the samples. GISAXS measurements are done at selected times during the operation with a counting time of 1 s per image. For the data analysis, the 2D GISAXS data are analyzed with line cuts. Horizontal line cuts are done at the Yoneda position of the polymer PTB7-Th (integrating over three pixels for better statistics). Vertical line cuts are performed at  $q_y = 0 \text{ nm}^{-1}$ .

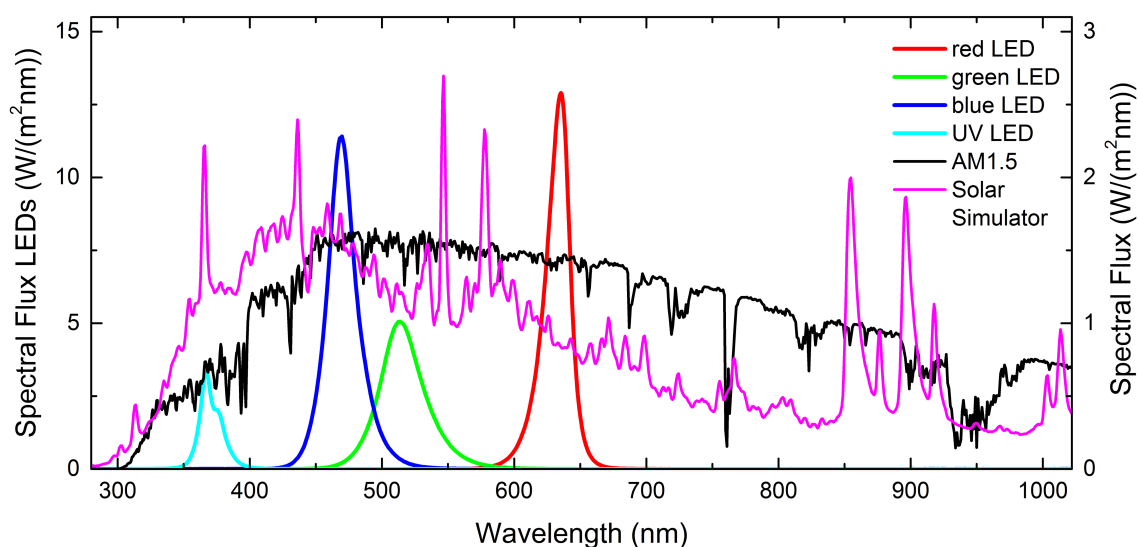


**Figure 7.1**

Emission spectra of the used illumination sources and the solar AM1.5 spectrum.

**Degradation experiments:** The freshly prepared samples are deliberately degraded using a variety of light sources in different environments, using either a broad spectrum simulating artificial sunlight or different light-emitting diodes (LEDs) targeting more specific wavelength regions. The emission spectra of all illumination devices are visualized in comparison to the solar spectrum (AM 1.5) in Figure 7.1. To simulate the broad AM1.5 solar radiation under ambient conditions, samples are placed on a solar simulator (SolarConstant 1200, K.H. Steuernagel Lichttechnik GmbH, Germany) calibrated to a power density of  $1000 \text{ W cm}^{-2}$  at the sample. To focus on certain wavelength regions, samples are placed inside a custom-built illumination setup (designed by Julian Fischer<sup>[283]</sup>, see Figure 7.2) within the FTIR spectrometer (Equinox 55, Bruker, Germany) under dry airflow. Several LEDs are placed at the same distance from the sample holder, which is placed in a copper holder to dissipate the heat. The samples are illuminated using one or several LEDs (Cree XP-E2 (red, green, blue) and/or 3x Nichia SMD LED UV NCSU275) for the photo-degradation. The respective parameters of the used LEDs are listed in Table 7.1. The spectra were measured by Christoph Senfter in the frame of his Master's thesis.<sup>[284]</sup>

**Sample Encapsulation:** For some aging experiments, samples are encapsulated with an additional glass slide to prevent chemical degradation due to ambient air during illumination. To encapsulate the films, a glass slide of the same proportions as the sample substrate is covered at all its sides with a thin film of a two-component epoxy resin (890578, MBFZ TOOLCRAFT GmbH, provided by Conrad Electronic SE). The freshly prepared sample is placed onto the slide and weighted with a copper block for three hours to finalize the encapsulation.

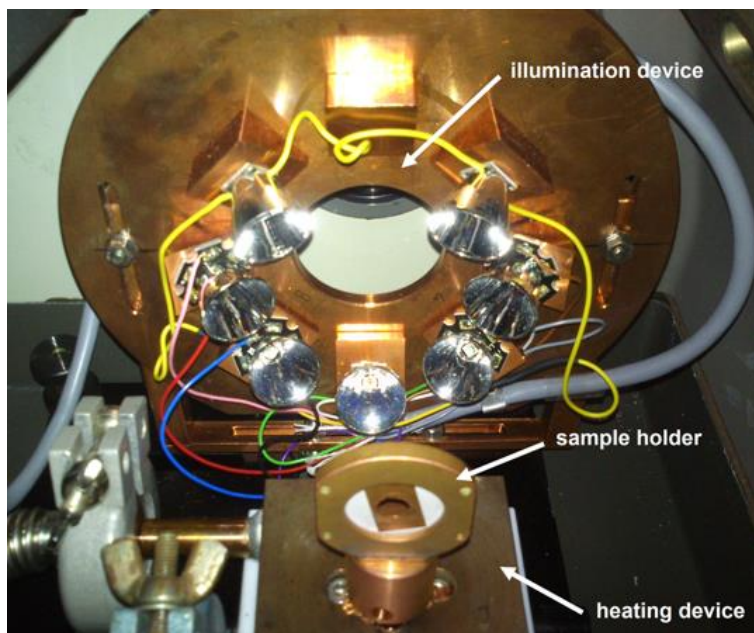


**Figure 7.2**

Illumination setup implemented inside the FTIR spectrometer. The setup consists of several LEDs placed equidistantly from the sample holder. The spectrometer can be flushed with dry air to reduce contaminants like water and CO<sub>2</sub>.

**Table 7.1**

LED sources used for illumination with corresponding wavelengths and intensities.

| LED color | wavelength [nm] | intensity [W/m] |
|-----------|-----------------|-----------------|
| red       | 634             | 305.4           |
| green     | 512             | 218.2           |
| blue      | 468             | 334.8           |
| UV        | 365             | 61.4            |

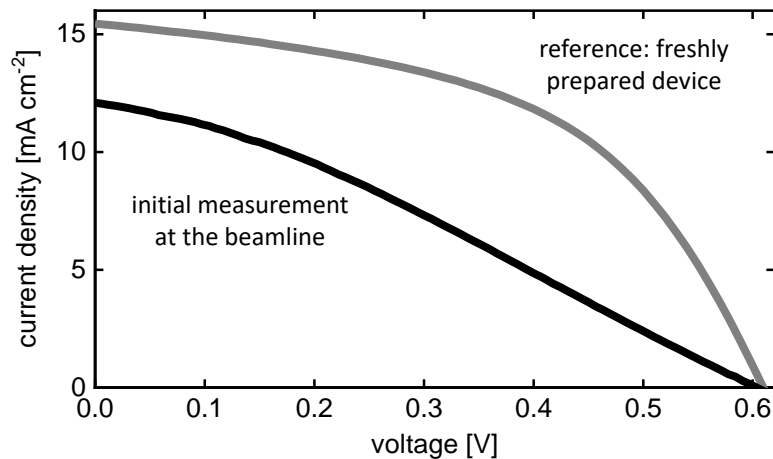


**Figure 7.3**

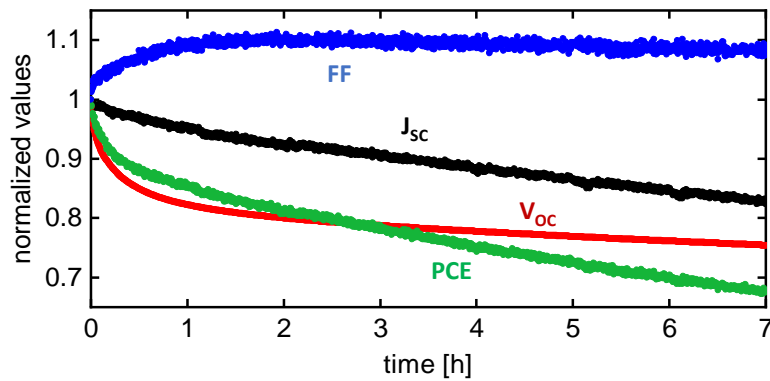
Initial IV-curve of the PTB7-Th:PC<sub>71</sub>BM based solar cell before the in-operando measurement in comparison to a fresh device measured directly after preparation.

## 7.3 In-Operando Solar Cell Characterization

For the in-operando GISAXS experiment, PTB7-Th:PC<sub>71</sub>BM bulk-heterojunction (BHJ) solar cells are prepared on an ITO-covered glass substrate, with a PEDOT:PSS blocking layer and without device encapsulation. The measurement is performed at the MiNaXS beamline P03 at DESY, Hamburg,<sup>[214]</sup> to achieve the required high spatial and temporal resolution. In the in-operando experiment, a solar cell is illuminated using a mobile solar simulator setup while measuring its photovoltaic response until the PCE decreases below 70 % of its initial value. Simultaneously, GISAXS data are acquired to probe the thin film morphology of the active layer during operation. Similar experiments on other OPV systems correlated changes in the PCE with changes in the sizes and distances of the respective domain structure in the active layer.<sup>[65,68]</sup>

### 7.3.1 Development of the Photovoltaic Properties

For the in-operando measurement, the solar cell has to be transported to the beamline and stored for several days after preparation. To investigate the influence of this procedure on the device, an identical solar cell is prepared and measured directly at the lab. The photovoltaic response of the freshly prepared reference PTB7-Th:PC<sub>71</sub>BM solar cell during an I/V-measurement is compared to the initial response of the device measured at the beamline in Figure 7.3. A pronounced difference in the curves is visible, with a significant loss in  $J_{sc}$  and fill factor (FF) as compared to the fresh device. The freshly prepared device exhibits values typical for non-optimized PTB7-Th:PC<sub>71</sub>BM solar cells in conventional architecture and after further treatment like encapsulation:  $J_{sc} = 15.5 \text{ mA cm}^{-2}$ ,  $V_{oc} = 0.61 \text{ V}$ ,  $\text{FF} = 50.7 \%$  and  $\text{PCE} = 4.77 \%$ .<sup>[198]</sup> In contrast, the

**Figure 7.4**

Evolution of the normalized OPV parameters over time during the in-operando measurement.

initial response of the solar cell device investigated here shows significant losses in all of the parameters except the  $V_{oc} = 0.61$  V. While  $J_{sc} = 12.1$  mA cm<sup>-2</sup> still reaches 78 % of the value for the fresh device, the FF = 31 % and the PCE = 2.29 % are significantly lower than expected. This can be explained by several factors. On the one hand, residual DIO is removed via vacuum treatment before applying the Al contacts to reduce the effect of additive evaporation during operation described in other works.<sup>[68,70]</sup> However, this harsh treatment may have led to effects similar to the evaporation of additive during the in-operando experiments described by Schaffer et al. and Yang et al., leading to an early decrease in FF and especially PCE. On the other hand, the preparation routine involves (short) exposition to ambient conditions and light during the transfers between the glovebox system and the thermal evaporation setup. This in itself would not greatly affect devices measured timely after preparation. However, the device measured in-operando had to be transported and stored in a small transport container for a week before the measurement was performed so that some additional pre-degradation could not be avoided. This effect was also seen for inherently more stable P3HT-based solar cells and is even more pronounced for PTB7-Th due to its sensitivity, as discussed in the following.<sup>[65,90]</sup> To exclude effects of heating during the solar cell operation, the sample holder is cooled using a Peltier element to limit the heating of the sample to a minimum. After an initial increase in temperature over the first hour, the temperature stabilizes at around 25 °C. Figure 7.4 illustrates the temporal evolution of the most important photovoltaic parameters normalized to their initial values. The FF exhibits an initial increase, which has also been seen for other devices and can be assigned to the initial burn-in effect.<sup>[65,90]</sup> The open-circuit voltage  $V_{oc}$  shows a significant initial loss within the first hour of operation and a less pronounced decrease afterward while the short-circuit current  $J_{sc}$  decreases linearly with time. The combination of both effects leads to a significant decrease in PCE within a few hours.

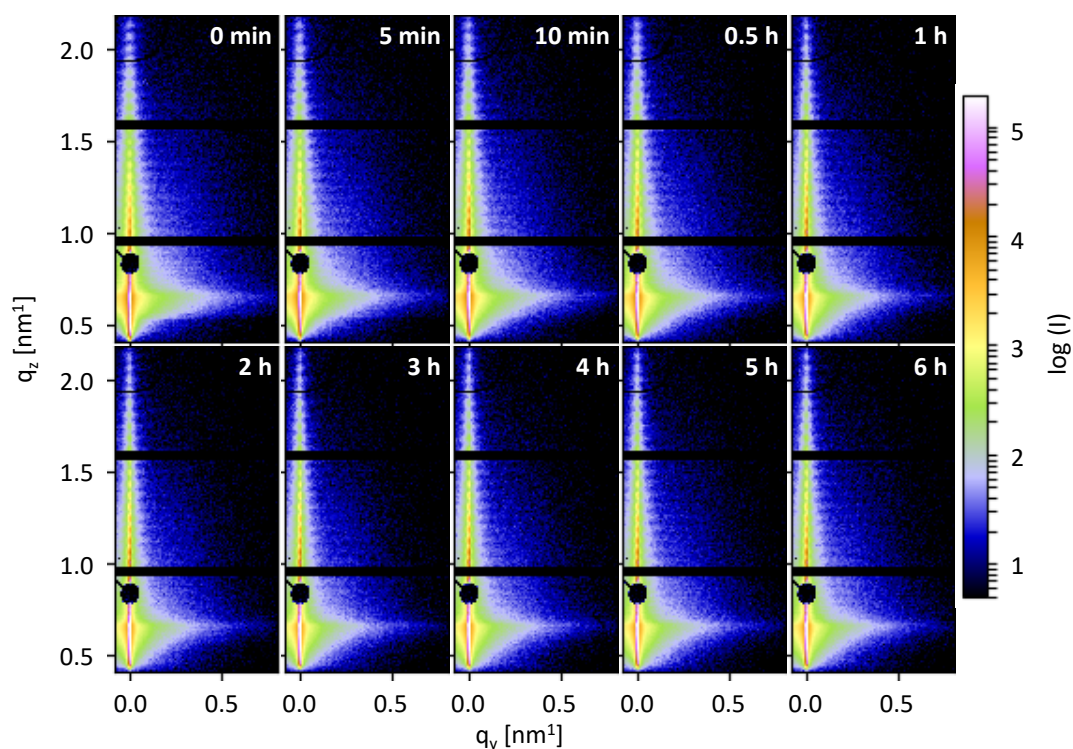


**Figure 7.5**

Exemplary 2D GISAXS data taken before and during the in-operando measurement of the solar cell under illumination. The black horizontal lines are caused by a gap between the detector modules. The black circle denotes the beamstop, which absorbs the specularly reflected beam of high intensity. Clearly visible are the intensity maxima in vertical direction caused by the homogeneous film thickness.

### 7.3.2 In-Operando GISAXS Measurement

To reveal the morphological changes within the photoactive layer, in-operando GISAXS measurements are performed. The related 2D GISAXS data are shown in Figure 7.5. For an in-depth data analysis, the 2D GISAXS data are reduced to 1D horizontal and vertical line cuts. The horizontal line cuts are performed in the so-called Yoneda region of PTB7-Th for which the highest scattering signal of PTB7-Th is detected. The respective scattering intensity for each measurement during operation is plotted in Figure 7.6 with the experimental data shown as black symbols and the respective fits as red lines. While the principle shape of the scattering curves stays constant, a slight shift in the intensity is visible, with a small decrease in intensity at higher  $q_y$  values in combination with an increase in intensity at very low  $q_y$  values. The curves are fitted using a model to extract the average sizes and distances of scattering polymer domains present in the active layer. The X-ray scattering arises due to different structures present in the probed thin films. These structures are modeled using ap-

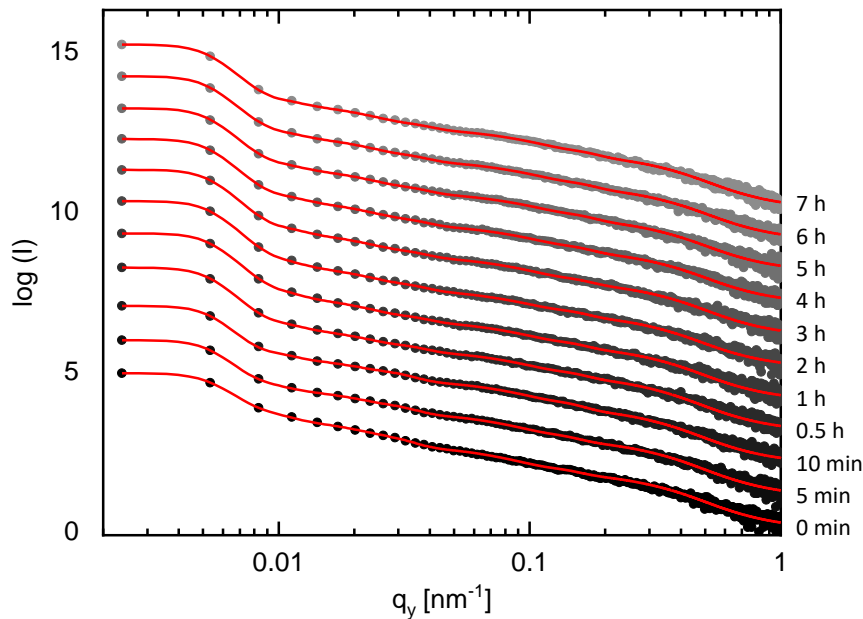


**Figure 7.6**

Horizontal line cuts of the 2D GISAXS data (black symbols) during operation of the solar cell with the corresponding model fits (red lines). The curves are plotted logarithmically and shifted along the intensity axis for clarity with increasing time.

appropriate form and structure factors to describe their diffuse scattering. Here, a model is used that had been successfully applied to other BHJ solar cells and similar systems before.<sup>[65,68,70]</sup> It is based on the distorted-wave Born approximation (DWBA) to take the grazing incidence geometry into account. Additionally, the effective interface approximation (EIA) is used. As the sample exhibits rather polydisperse scattering structures, a combination of three different lateral structures is used, applying averaged form factors of cylindrical shape with different radii. The local monodisperse approximation (LMA) is applied to model the scattering intensity via incoherent superposition of the intensities of the individual structures. The model parameters can be found in Figure 7.7. Indeed, the respective scattering intensities ( $I_1$ ,  $I_2$ , and  $I_3$  for the modeled domains and  $I_0$  at low  $q_y$  values beyond the resolution limit) show the most pronounced changes while the domain distances and sizes change only slightly, which is in contrast to other, similar systems investigated before.<sup>[65,68]</sup> Initial average radii for the modeled structures are  $R_1 = (75 \pm 5)$  nm,  $R_2 = (18 \pm 2)$  nm, and  $R_3 = (2.6 \pm 0.3)$  nm with virtually no changes for  $R_1$  and  $R_3$  and only a slight decrease of about 10% for  $R_1$  after the first hour.

For OPV systems such as P3HT:PCBM solar cells in conventional device architecture, a dominant decrease in  $J_{sc}$  was directly connected to an increase of polymer domain sizes and distances which caused a loss in donor-acceptor interface and therefore reduced the chance of exciton splitting.<sup>[65]</sup> Inverting the device structure for

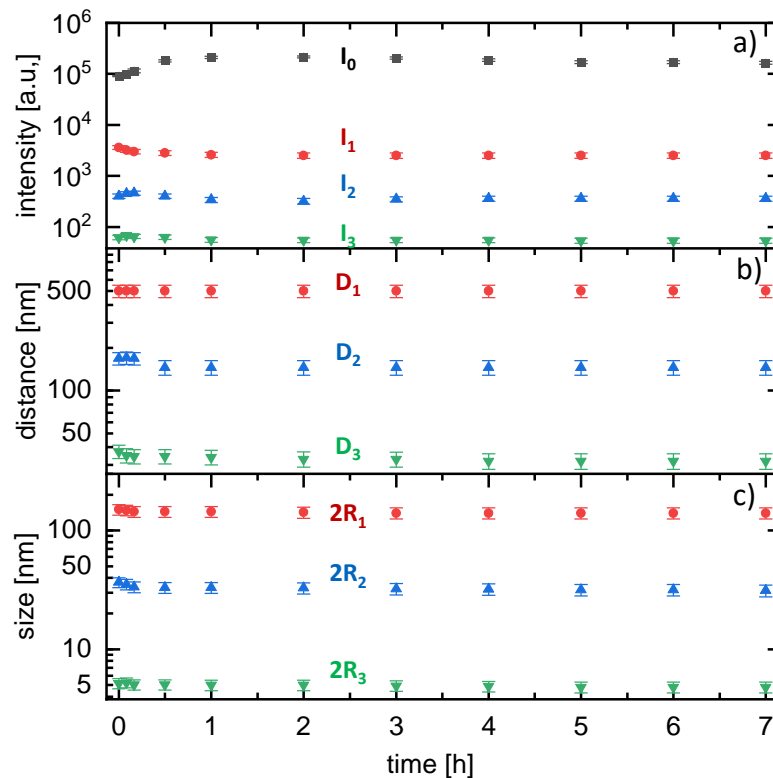


**Figure 7.7**

Parameters used for the fits: (a) intensities, (b) distances, and (c) diameters of the modeled structures in the active layer. Especially during the first hour of operation, an increase in intensity at lower  $q_y$  values ( $I_0$ ) is visible, while the intensity at larger  $q_y$  values ( $I_1$ ,  $I_2$ ,  $I_3$ , corresponding to the three modeled structures) decreases initially.

P3HT:PCBM solar cells, on the other hand, led to significantly less decrease in  $J_{sc}$  corresponding to the stabilized morphology.<sup>[89]</sup> In low-bandgap PCPDTBT:PC<sub>71</sub>BM solar cells, the evaporation of the processing additive led to a decrease in the domain sizes and formation of islands and traps which was attributed to being the reason for the observed dominant loss in FF.<sup>[68]</sup> Even though a slight decrease in domain size for intermediate structures ( $R_2$ ) is visible, this cannot be connected to a simultaneous loss in FF and occurs in structures larger than the ones discussed for PCPDTBT:PC<sub>71</sub>BM solar cells. From the use of DIO as solvent additive in the PTB7-Th:PC<sub>71</sub>BM system studied here, a decrease in the characteristic domain sizes might be expected if DIO is leaving the active layer, as was shown in earlier work on inverted PTB7-Th:PC<sub>71</sub>BM solar cells.<sup>[70]</sup> In the present work, however, no significant amount of residual DIO can evaporate, as the solar cell was treated with a prolonged vacuum before applying the back electrodes to minimize residual DIO inside the active layer. Moreover, the PTB7-Th:PC<sub>71</sub>BM based system studied here differs from the previous study not only

in the amount of residual DIO but also in the device architecture and type of interlayer, which are known to influence the film morphology and device stability.<sup>[65,89,285–287]</sup>

Neither of the processes reported in the literature before and discussed above seems to have a significant effect on the present system. The intensities for the three modeled polymer domains  $I_1$ ,  $I_2$ , and  $I_3$  in comparison to the intensity  $I_0$  at low  $q_y$  indicative of domains beyond the resolution limit show significant changes. Especially during the first hour of operation,  $I_0$  increases more than two-fold, while  $I_1$  decreases more than 30%. The changes in scattering intensity indicate that the three modeled domains lose some of their scattering contrast while the pronounced intensity increase beyond the resolution limit suggests an increase in scattering contrast for very large lateral structures. The trend in domain scattering intensity corresponds well with the initial decrease and later tapering off in  $V_{oc}$ . Several factors can influence the scattering contrast, namely the material composition of the respective domains, the domain abundance, or polydispersity.<sup>[288]</sup> A merging of large clusters  $R_1$  to even larger clusters beyond the resolution limit might account for the loss in  $I_1$  in combination with the increase in  $I_0$ , yet this would not significantly change the observed OPV parameters, as the length scales far exceed the exciton diffusion length. Additionally, an increase in surface roughness could lead to an increased forward scattering in vertical direction.<sup>[164]</sup>

This increased scattering is corroborated by vertical cuts of the 2D GISAXS data taken at  $q_y = 0 \text{ nm}^{-1}$  which show an increase in intensity for smaller  $q_z$  values, as illustrated in Figure 7.8. The interference fringes in  $q_z$  direction (for  $q_y$  close to 0) arise from the active layer exhibiting a surface roughness strongly correlated to its interface with the PEDOT:PSS layer, leading to a waveguide effect. The layer thickness  $d$  is estimated from the distance of neighboring minima or maxima via<sup>[164,288]</sup>

$$d = \frac{2\pi}{\Delta q_z}. \quad (7.1)$$

The pronounced fringes caused by the correlated roughness remain constant during the process, indicating a constant, homogeneous film thickness of around 100 nm within the active layer. As no significant changes in the active layer morphology can be found, chemical modifications might also be responsible for the change in scattering contrast of the domains.

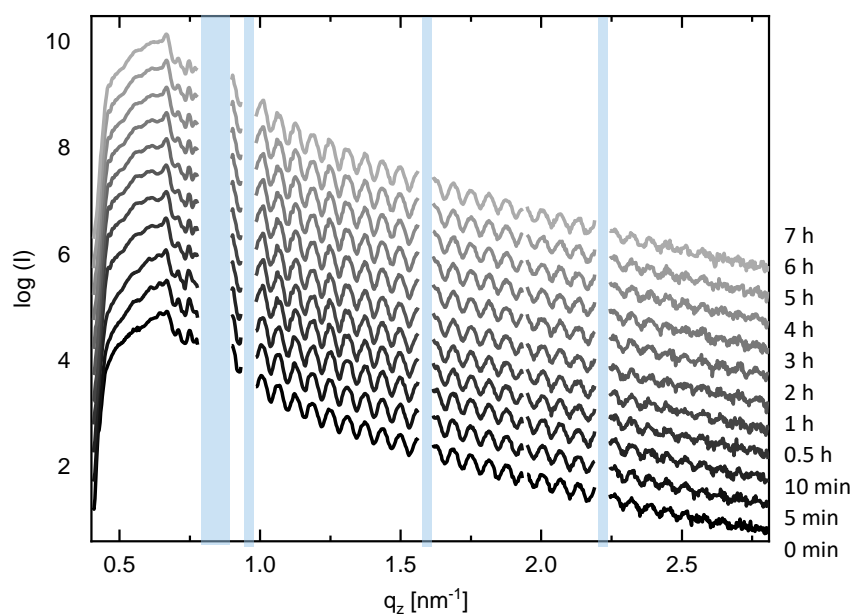


**Figure 7.8**

Intensity of the vertical cuts of the 2D GISAXS data during operation of the solar cell. The curves are plotted logarithmically and shifted along the intensity axis for clarity with increasing time. Areas shaded in light blue denote  $q_z$  values inaccessible due to the applied beamstop and gaps between the detector elements. Except for a slight increase in overall intensity over time, no significant changes can be deduced. Especially the distance between the extrema of the interference fringes  $\Delta q_z$  deriving from the active layer with a correlated surface roughness stays constant, indicating a constant film thickness of about 100 nm.

## 7.4 Following the Light-Induced Aging of Thin-Film Samples

To look into chemical alterations in more detail, thin-film samples of PTB7-Th are investigated concerning their optical and chemical properties using UV/vis and FTIR spectroscopy as well as nano IR mapping. For these measurements, freshly prepared samples are left to dry overnight under a nitrogen atmosphere in a glovebox before starting the initial measurements.

### 7.4.1 Optical Absorption

UV/vis absorbance spectra of the fresh samples illustrate the material characteristic absorption features of the investigated materials. Figure 7.9 shows typical absorbance curves (bold) for PC<sub>71</sub>BM (orange), PTB7-Th (dark blue), and their blend (turquoise). After these initial measurements, the samples are inserted into a custom-built setup for controlled illumination under a dry airflow. The setup consists of several LEDs of

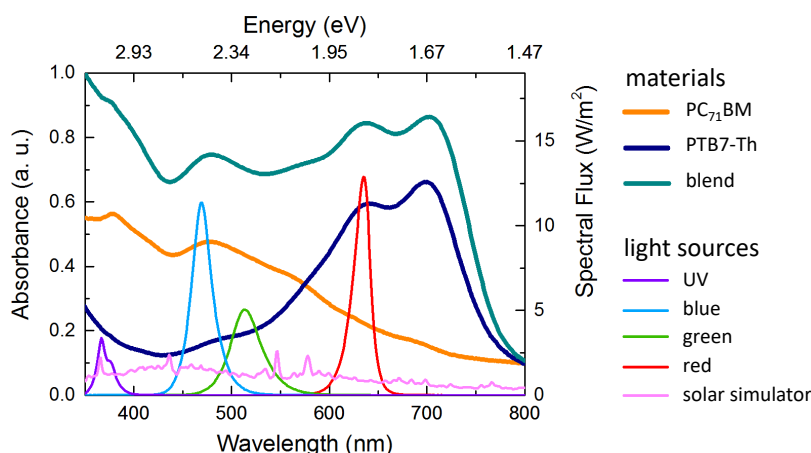


**Figure 7.9**

UV/vis absorbance spectra of the investigated pure PC<sub>71</sub>BM (orange) and PTB7-Th (dark blue) films and their blend (turquoise) in comparison to the spectral flux for the used illumination sources with 365, 468, 512, and 634 nm (indicated with the respective colored curves). For UV light, three LED sources are combined to increase the total intensity.

different wavelengths all placed at the same distance from the sample holder (see also Figure 7.2). Figure 7.9 additionally illustrates the wavelength-dependent spectral flux density  $F_\lambda$  of the used LEDs (denoted with the respective colors) in comparison to the one of the solar simulator (pink).

Optical absorbance spectra of thin films produced from solutions of pure PC<sub>71</sub>BM, pure PTB7-Th and the blend of both materials on glass substrates are shown in Figure 7.10 to emphasize changes with increasing illumination time between 0 and 23.5 h, as indicated. While the absorption for PC<sub>71</sub>BM stays almost constant over the course of one day, the other samples degrade significantly even after only 0.5 h of illumination. The trend is particularly visible for the pure PTB7-Th film, for which almost no absorbance can be measured after one day of illumination. For the blend film, the most pronounced losses are found for wavelength regions mostly connected to the polymer, with the spectrum showing a high similarity to the one of pure PC<sub>71</sub>BM after 3.5 h. Indeed, the blend seems to show a faster initial decrease in the polymer peak intensity as compared to the pure polymer. This will be discussed later in more detail.

At later stages of illumination, even the absorbance peak at around 500 nm derived from PC<sub>71</sub>BM decreases significantly, showing a loss in stability for the fullerene derivative when combined with the polymer, as has been discussed in other works.<sup>[74,92,289]</sup> As the pristine PC<sub>71</sub>BM film does not show significant degradation over the discussed time,<sup>[290]</sup> the following sections will focus on the pure polymer and its blend. Interestingly, the absorption maximum at 720 nm decreases significantly faster compared to the one at 640 nm and both peaks show a slight blue shift. This effect has also been observed for other materials before.<sup>[71,98,291]</sup> The maximum at higher wavelengths can

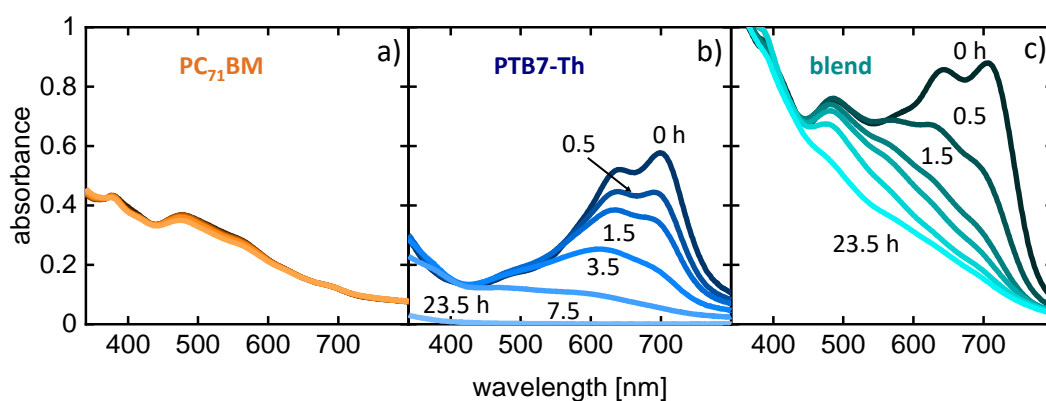


**Figure 7.10**

UV/vis absorption spectra of thin films of the pure materials (a) PC<sub>71</sub>BM and (b) PTB7-Th and (c) the PTB7-Th:PC<sub>71</sub>BM blend before illumination (dark color lines) with all LEDs and at certain intervals of illumination time (lighter colors).

be attributed to the chromophore length which depends on the conjugation within the aromatic polymer backbone and its inter-molecular interactions within the polymer aggregates.<sup>[228]</sup> It seems that in a first stage, this chromophore length is considerably decreased, causing the blue shift and loss in absorption. However, the simultaneous, albeit slower, decrease in the maximum at higher wavelengths results from a concurrent breaking of conjugation occurring on longer time scales.<sup>[74,94]</sup>

UV radiation is well-known to cause significant aging and loss in performance of sensitive photoactive organic materials.<sup>[110–113]</sup> To confirm if the elimination of UV light from the illumination setup could hinder the degradation process, the aging experiment is repeated for pure PTB7-Th and its blend, this time using either a single red, green or blue LED (634, 512 and 468 nm, respectively) or a combination of three UV LEDs (365 nm, see also Table 7.1 for the respective power output).

In Figure 7.11, the respective normalized absorbance spectra of PTB7-Th (a-f, blue) and its blend (g-l, green) are plotted individually for each illumination experiment, with small curves in violet (for UV light), blue, green, and red indicating the normalized spectral flux density of the applied LEDs in comparison to the simulated solar cell spectrum (pink). Even at first glance, a pronounced decrease in absorbance is visible for all applied wavelengths, which suggests that high-energy UV light is not chiefly responsible for the observed degradation process. Indeed, the strongest decrease in absorbance is induced by blue and even red light, which could be related to the higher flux of the respective LEDs in comparison to the UV LED. Additionally, another trend can be distinguished: depending on the maximum wavelength of the applied LED, a stronger decrease in absorbance in the corresponding wavelength region of the sample is visible. Blue light leads to a more pronounced reduction in the range of 450 nm, while red light affects this area only marginally but leads to more pronounced losses in the region around 650 nm.

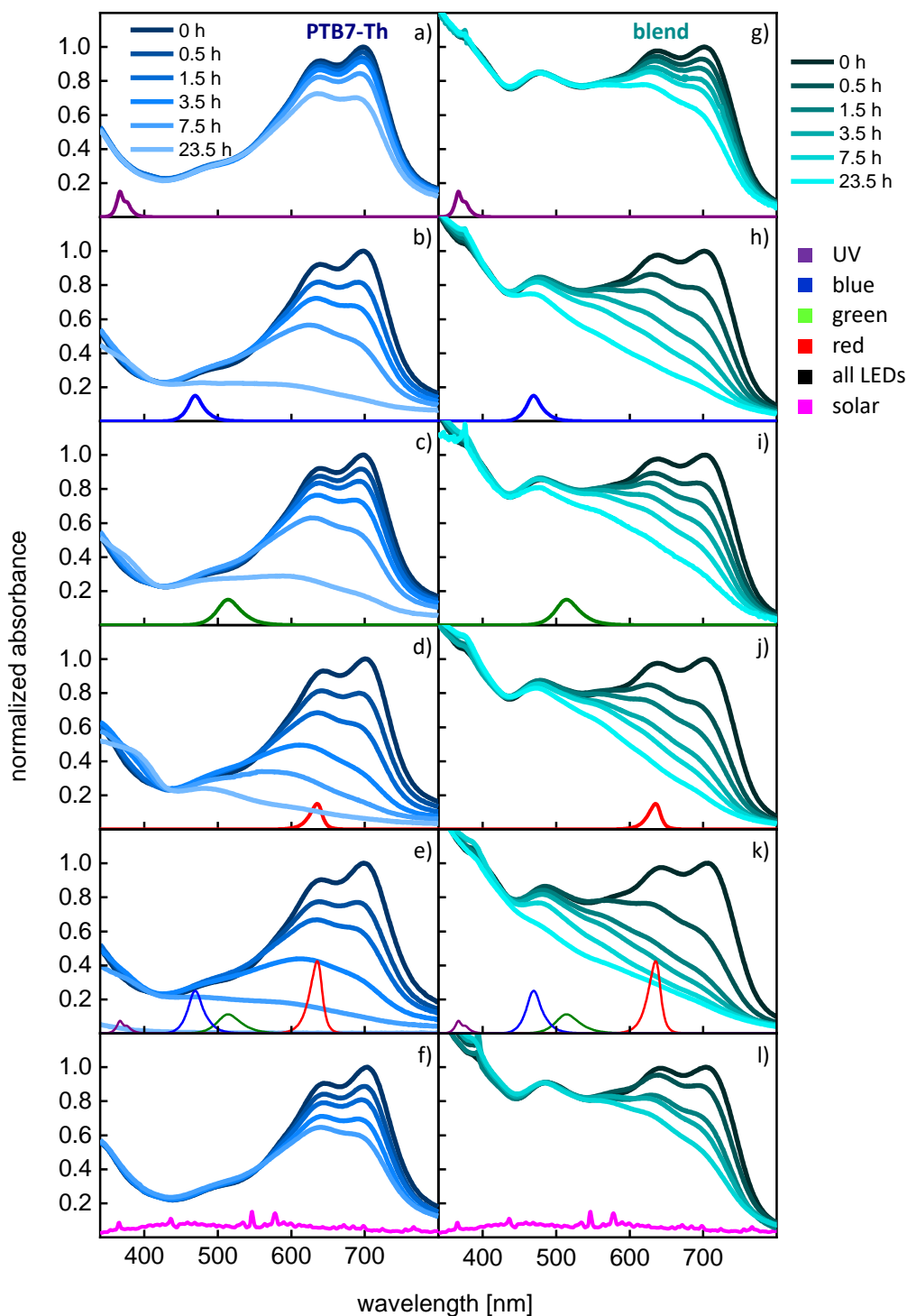


**Figure 7.11**

UV/vis absorption spectra collected before and during illumination of (a-f) pure PTB7-Th and (g-l) its blend with PC<sub>71</sub>BM with LEDs of different wavelengths (indicated with the respective colors in each subfigure): (a,g) 365, (b,h) 468, (c,i) 512, (d,j) 634 nm, (e,k) all LEDs, and (f,l) solar simulator.

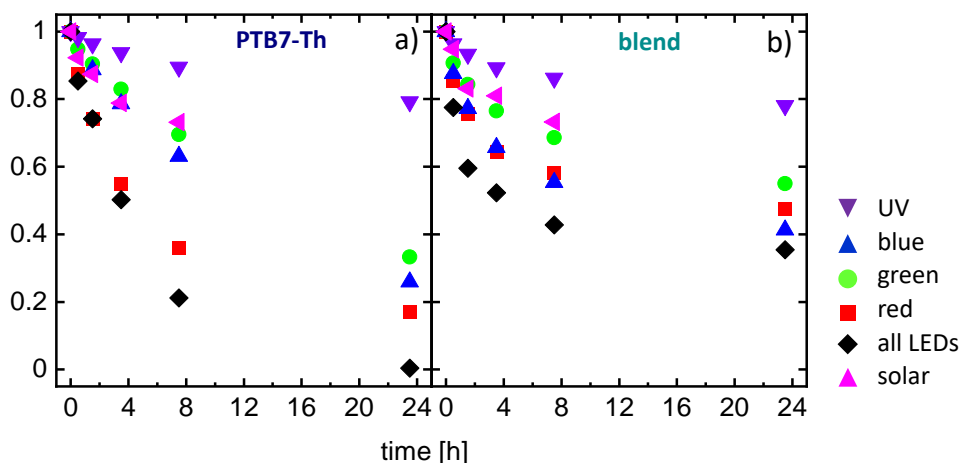


**Figure 7.12**

Evolution of the normalized integrated absorption peak area over time for illumination with different light sources for a) the pure polymer film in comparison to b) the blend film. The light sources are indicated by different colors.

To get a more comprehensive understanding of the effect that light of different wavelengths has on the overall degradation of the investigated materials, the areas below the absorbance curves are integrated over the important wavelength range between 500 nm and 800 nm to get one value of absorbance for each point in time, making comparisons easier. Figure 7.12 shows the evolution of the normalized integrated areas over time. The overall absorption of the polymer for illumination with LEDs in the visible range is, as expected, significantly more affected than the one of the blend, as the PC<sub>71</sub>BM absorption in the latter shows only slight losses. However, a pronounced initial decay for all illumination pathways is visible for the blend. This is in accordance with other works describing a destabilizing effect of PCBM on low-bandgap polymers,<sup>[67,92,93,107,108,279,292]</sup> in contrast to other polymers that are rather stabilized by blending with fullerene derivatives.<sup>[293,294]</sup> The exact processes are still under debate, although several competing mechanisms have been proposed, all connected to the difference in electron affinity between the polymer and the fullerene derivative.<sup>[75,106,295]</sup> While PC<sub>71</sub>BM exhibits radical scavenging properties due to its higher electron affinity, it can increase the creation of triplet states within the polymer via non-geminate recombination, which again can lead to the creation of more reactive oxygen species. Interestingly, the type of illumination seems to have a pronounced effect, with pure UV radiation and the solar simulator inducing the smallest decrease, while red and blue light seem to be the chief degradation agents when comparing their effect to the one of all LEDs combined.

Clearly, illumination over time alone is not a sufficient measure of the degradation process. Therefore, the accumulated spectral flux density  $F_\lambda$  (= emitted energy dose per area) of the respective light source for each measurement is used to better compare

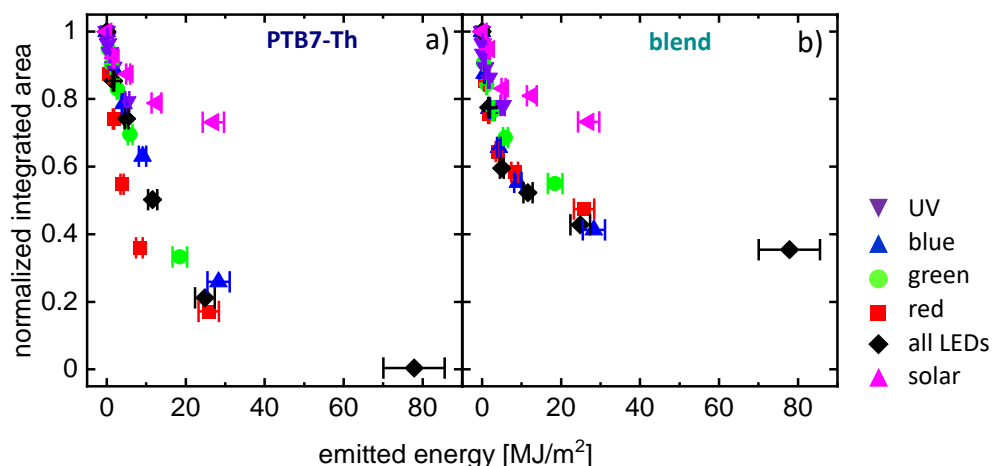


**Figure 7.13**

Evolution of the normalized integrated absorption peak area versus the emitted energy dose of the respective light source for illumination with different light sources for a) the pure polymer film in comparison to b) the blend film. The light sources are indicated by different colors.

the different light sources in terms of emitted energy. The integrated absorbance over the emitted energy dose of each light source is plotted in Figure 7.13. A pronounced correlation of the decrease in overall absorbance with increasing emitted energy dose is visible, with a similar trend for the used LEDs. However, the solar simulator radiation and red LED show unexpected results, with the former having only a weak influence, while the latter induces comparably strong aging. To explain these differences, a look at the respective spectral flux density  $F_\lambda$  of the different light sources in comparison to the spectral absorbance of the materials can help (see again Figure 7.9). While e.g. the red and blue LED show a similar  $F_\lambda$ , more photons are absorbed especially by the polymer in the red wavelength region due to its low bandgap. On the other hand, the solar simulator has a widespread power spectrum, including in wavelength regions for which the absorption of the materials is low.

Therefore, the accumulated number of absorbed photons per area (= absorbed photon dose) instead of the emitted energy dose is used to compare the different light sources in Figure 7.14. The absorbed photon dose is calculated from the emission spectra of the respective light sources and the measured absorbance spectra of the investigated materials. The absorbed spectral photon irradiance  $E_\lambda$  for any given sample at any given measurement time can be determined using its absorbance  $A_\lambda$  and the emitted spectral flux density  $F_\lambda$  of the used light source

$$E_\lambda = F_\lambda(1 - 10^{-A_\lambda}). \quad (7.2)$$

This equation can be converted to the number of absorbed photons of the respective energy. Integrating over the whole spectrum gives the total amount of absorbed

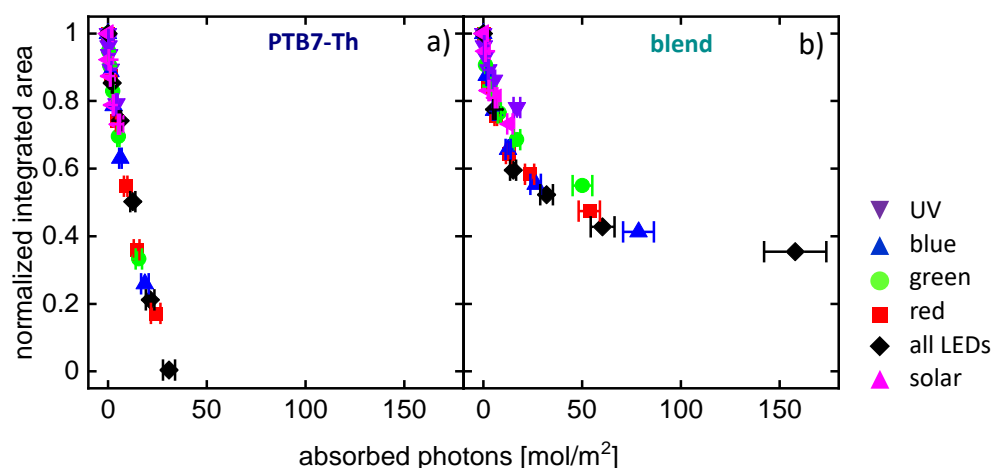


**Figure 7.14**

Evolution of the normalized integrated absorption peak area versus the absorbed photon dose of the respective light source for illumination with different light sources for a) the pure polymer film in comparison to b) the blend film. The light sources are indicated by different colors.

photon dose for this measurement. The data points for each measurement are fitted over time to get the number of absorbed photons in the intervals between every two measurements.

Using this measure, an almost linear degradation with the absorbed photon dose is observable for the pure polymer, indicating that each single absorbed photon – irrespective of its energy – has the same probability of inducing chemical degradation. For the blend, a similar trend can be seen for the first stage of degradation, until most of the absorbance due to the polymer is lost. Both samples initially show very similar behavior in terms of degradation over absorbed photon dose. The strong correlation of loss in absorbance with the number of absorbed photons irrespective of their energy hints at a process also suggested by Xie et al.<sup>[279]</sup> As soon as the chromophores of the polymer absorb a photon of sufficient energy, they are transferred into an excited state. Non-geminate recombination of separated charges can generate triplet states which subsequently increase the formation of highly reactive singlet oxygen expected to be the main oxidizing agent.<sup>[292,295,296]</sup>

These findings can be corroborated by additional aging experiments performed by variation of two parameters: Freshly prepared samples of the pure polymer and its blend are either stored in the dark under ambient conditions or encapsulated before illumination with all LEDs. The resulting UV/vis absorption spectra taken before and during the storage or illumination can be found in Figure 7.15 and show a vast improvement in the stability of the samples in all cases. This clearly shows that the main aging process needs a combination of excitation of the chromophores and the availability of an oxidizing agent (namely oxygen). Even though encapsulation

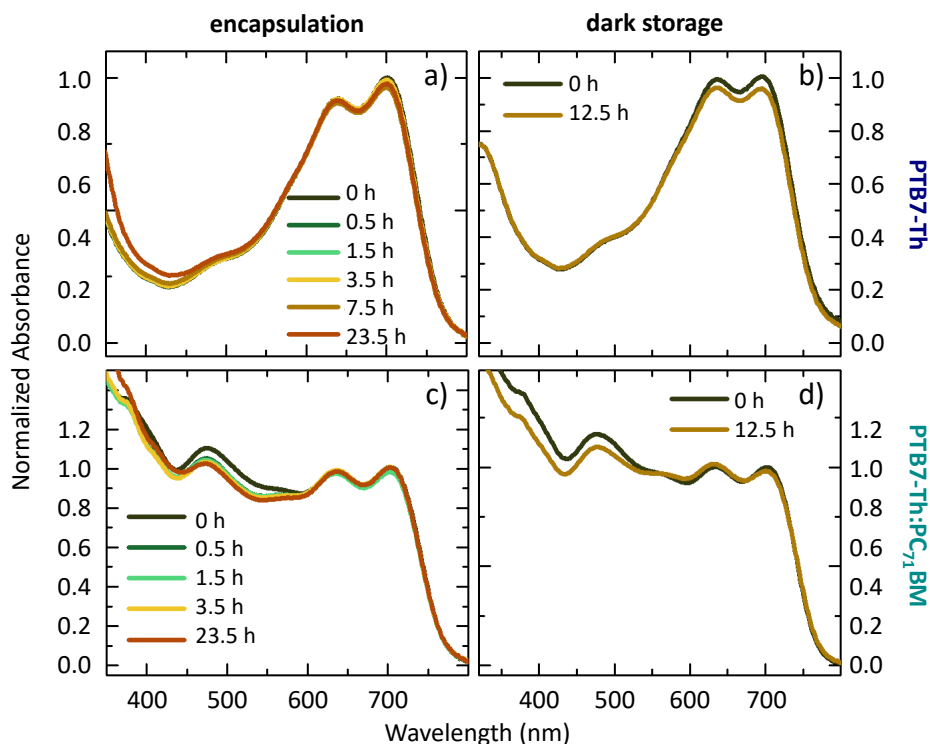


**Figure 7.15**

UV/vis absorbance spectra of thin films of (a,b) pure PTB7-Th and (c,d) the PTB7-Th:PC<sub>71</sub>BM blend under different conditions. (a,c) Samples encapsulated and illuminated exactly as the non-encapsulated films discussed before and shown in Figure 7.11. (b,d) Samples stored under normal atmospheric conditions (including air and water) without illumination.

can hinder some external degradation, this is not always sufficient to prevent aging. Photolysis, the irradiation performed in absence of oxygen, can still lead to long-term losses, albeit in a matter of hours rather than minutes.<sup>[71,291]</sup> On the other hand, residual solvent additive or small quantities of impurities acquired during processing might accelerate the degradation.<sup>[74,75]</sup> The small losses visible for the samples stored in the dark can be assigned to the short time in which they are illuminated (without encapsulation) while performing the spectroscopy measurements.<sup>[75]</sup> Similar processes can be assumed to be also responsible for the loss in PCE of the investigated solar cell, as some contamination and irradiation during the preparation process of the solar cells and implementation into the in-operando measurement setup could not be avoided.

**Table 7.2**

Prominent IR absorption peaks visible for pristine PTB7-Th films and the PTB7-Th:PC<sub>71</sub>BM blend. The respective vibration modes are assigned based on literature values and IR tables.<sup>[67,74,75,297,298]</sup>  $\nu$  denotes stretching vibrations,  $\delta$  bending modes.

| wavenumber (cm <sup>-1</sup> ) | assigned mode(s)   | trend |
|--------------------------------|--|-------|
| 2955                           | $\nu_{as}$ -CH <sub>3</sub>  | ↓     |
| 2943                           | PC <sub>71</sub> BM  | —     |
| 2926                           | $\nu_{as}$ -CH <sub>2</sub>  | ↓     |
| 2900                           | $\nu$ -CH (hidden peak)  | ↓     |
| 2870                           | $\nu_s$ -CH <sub>3</sub>   | ↓     |
| 2856                           | $\nu_s$ -CH <sub>2</sub>   | ↓     |
| 1857                           | $\nu$ -C=O (product)   | ↑     |
| 1786                           | $\nu$ -C=O (product)   | ↑     |
| 1738                           | PC <sub>71</sub> BM  | —     |
| 1730                           | $\nu$ -C=O (thienothiophene (TT) side-chain)                         | ↓     |
| 1704                           | $\nu$ -C=O (TT side-chain)   | ↓     |
| 1567                           | $\nu$ -C=C (TT-associated)   | ↓     |
| 1486                           | $\nu$ -C=C (benzodithiophene (BDT)-associated)                       | ↓     |
| 1460                           | $\delta$ -CH <sub>3</sub> + $\delta$ -CH <sub>2</sub> (+ $\nu$ -C=C) | ↓     |
| 1430                           | $\delta$ -CH <sub>2</sub> + C <sub>70</sub> (+ $\nu$ -C=C)           | ↓     |
| 1400                           | $\nu$ -C-F   | ↓     |
| 1377                           | $\delta$ -CH <sub>3</sub>  | ↓     |
| 1295                           | $\nu$ -C-O-C + $\delta$ -CH <sub>2</sub>                             | ↓     |
| 1252                           | $\nu$ -C-O-C   | ↓     |
| 1185                           | $\nu$ -C-O-C + $\delta$ -CH <sub>n</sub> + aromatic C-H              | ↑     |
| 1154                           | $\delta$ -CH <sub>3</sub> + $\delta$ -CH <sub>2</sub>                | ↓     |
| 1097                           | $\delta$ -CH in-plane (Th)   | —     |
| 1062                           | $\nu$ -C-O-C   | ↓     |

## 7.4.2 Chemical Structure

To elucidate the chemical changes of the polymer during and after illumination, FTIR spectroscopy measurements are performed. Initial high-resolution FTIR data of pristine films of PTB7-Th, PC<sub>71</sub>BM, and their blend are found in Figure 7.16. To enhance the signal-to-noise ratio for these data, films of a higher film thickness drop-cast on silicon substrates are used. Each of the peaks visible in the spectra can be assigned to one or several specific vibration modes present in the sample. Table 7.2 gives an overview of prominent absorption bands with their respective vibration modes and the functional unit they arise from for a range between 3000 cm<sup>-1</sup> – 1000 cm<sup>-1</sup>.

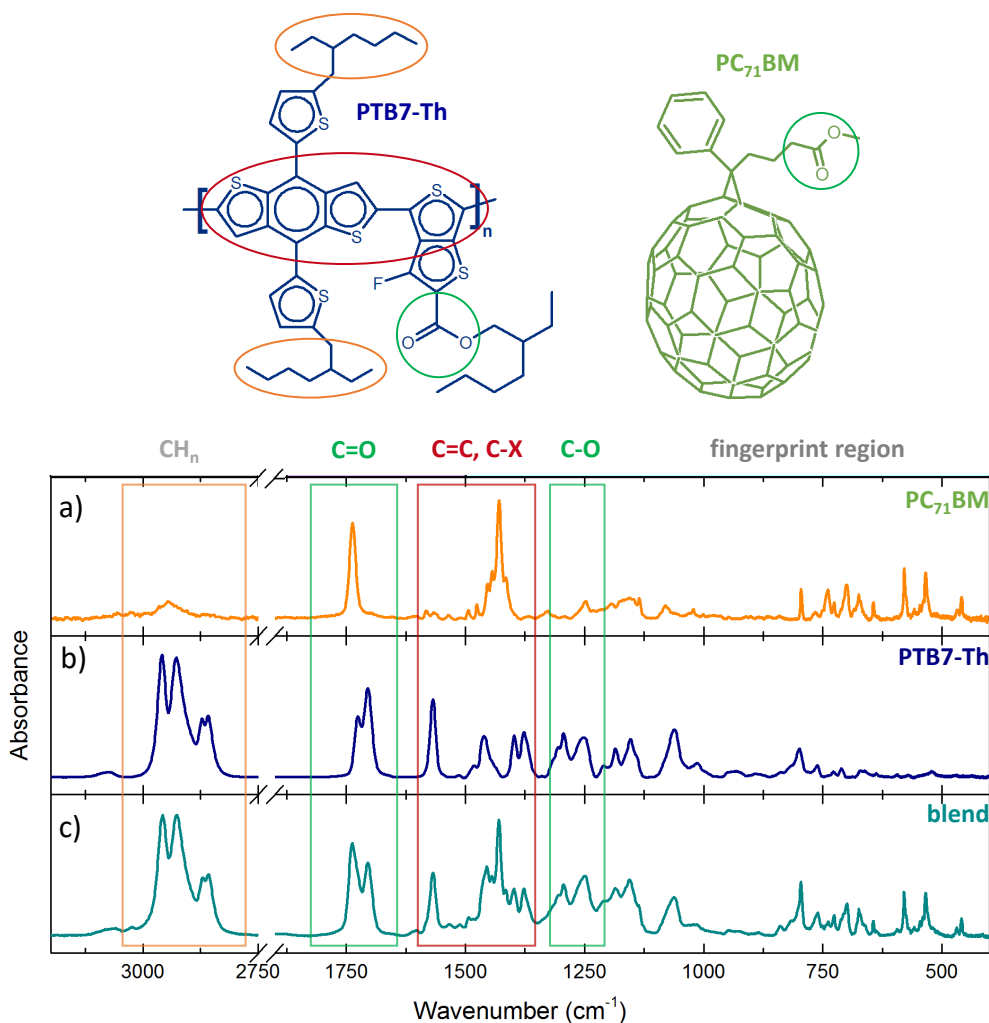


**Figure 7.16**

Chemical structures of the used materials and FTIR spectra taken before illumination of thin films made from (a) pure PTB7-Th, (b) pure PC<sub>71</sub>BM, and (c) the PTB7-Th:PC<sub>71</sub>BM blend. Indicated are the regions typical for vibrations of the respective bonds of C, H and O atoms and the fingerprint region. These initial spectra are taken using drop-cast films due to their higher thickness which significantly enhanced the signal-to-noise ratio.

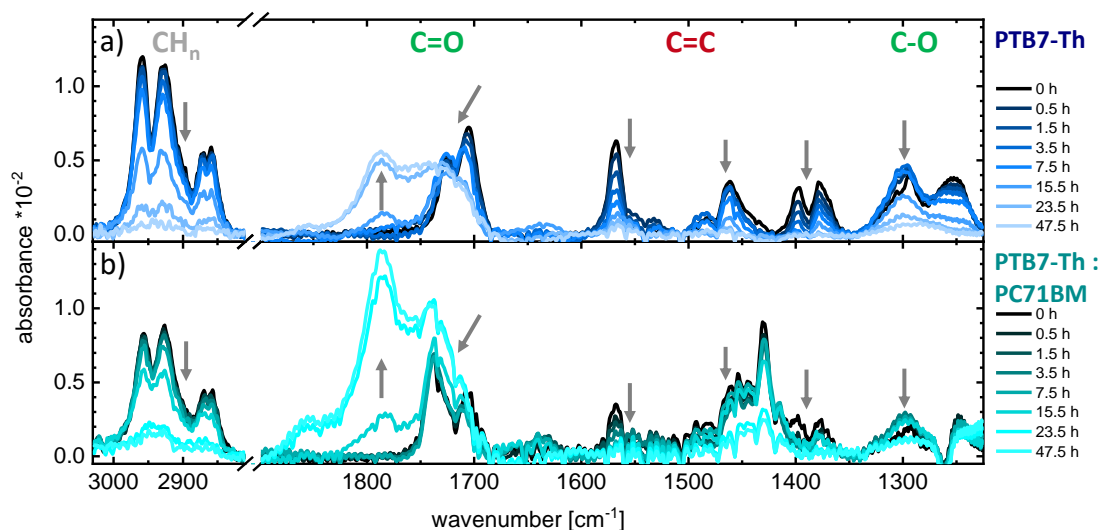


**Figure 7.17**

FTIR spectra for (a) PTB7-Th (blue) and (b) with the PTB7-Th:PC<sub>71</sub>BM blend (green) taken before, during, and after illumination with all LEDs, as indicated by progressively lighter colors. Changes in the peak intensity (and position) are marked by the respective arrows, indicating the creation or loss of C=O bonds and the loss of C=C bonds.

For following the degradation via FTIR, spin-cast films are investigated to keep the results comparable to the ones already discussed for the optical absorbance. Figure 7.17 illustrates the changes in the IR absorbance over time for PTB7-Th and the blend during illumination with all LEDs. The peaks are tracked over time similarly to the procedure used for the UV/vis absorbance values. The changes in IR absorbance upon illumination are quite pronounced for both samples. Most of the vibration bands assigned to C=C bonds in the conjugated backbone as well as alkyl groups in the side chains disappear almost completely. Meanwhile, the existing C=O bands associated with the ester groups show a blue shift and additional C=O vibration peaks arise at higher wavenumbers. In the blend film, also the bands assigned to PC<sub>71</sub>BM are affected, although less so than the ones of the polymer.

To get a more quantitative picture, the IR absorbance peaks are fitted using a combination of Gaussians for each of the absorption peaks with the general form

$$y = \frac{A}{\sigma\sqrt{2\pi}} \exp\left(-\frac{(x - \mu)^2}{2\sigma^2}\right). \quad (7.3)$$

Figure 7.18 illustrates the changes in IR absorbance for the most prominent vibration modes, as extracted from these fits and normalized to their maximum values, over time (the dotted lines are guides to the eye). A strong and early decrease in absorbance is visible for the bands connected to the conjugated polymer backbone and associated functional groups, while the creation of new C=O bands is delayed

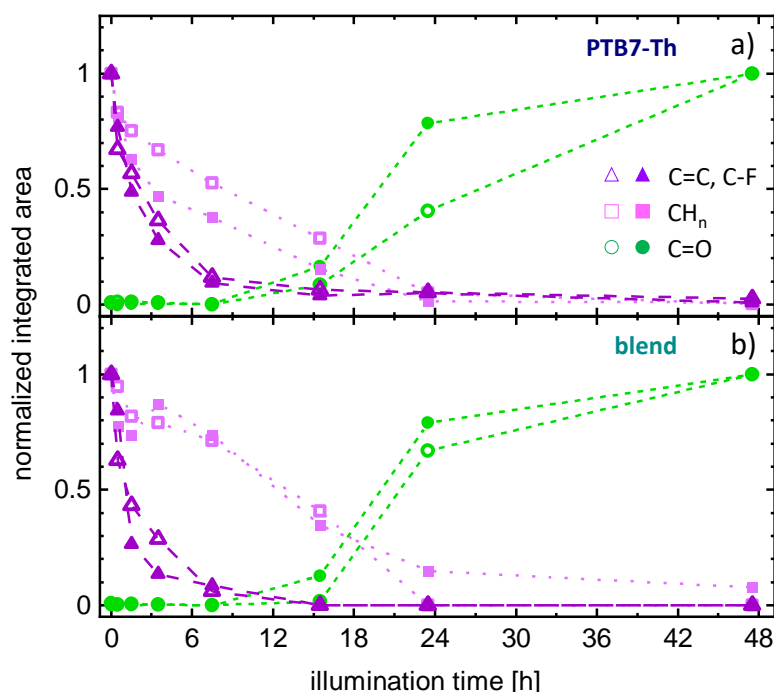


**Figure 7.18**

Comparison of the change in IR-absorbance for exemplary, prominent peaks for (a) pure PTB7-Th versus (b) the PTB7-Th:PC<sub>71</sub>BM blend, plotted over illumination time. The dotted lines are guides to the eye. Depicted in violet are vibration modes of the conjugated backbone ( $\blacktriangle$  1568  $\text{cm}^{-1}$ ) and the connected C-F bond ( $\triangle$  1396  $\text{cm}^{-1}$ ). Light pink values are derived from CH<sub>3</sub> ( $\square$  1379  $\text{cm}^{-1}$ ) and CH<sub>2</sub> ( $\blacksquare$  1462  $\text{cm}^{-1}$ ) vibrations and green illustrates intensity values of newly created C=O bonds ( $\circ$  1858  $\text{cm}^{-1}$ ,  $\bullet$  1785  $\text{cm}^{-1}$ ).

and starts several hours later. The PTB7-Th backbone consists of two alternating units, the electron donor TT and the acceptor BDT, as detailed in Section 3.1.1. The peaks for the stretching modes of the conjugated backbone (1568  $\text{cm}^{-1}$ ) and the C-F bond connected to the TT unit (1396  $\text{cm}^{-1}$ ) are shown in violet. For the polymer as well as the blend, they exhibit the most pronounced decay and virtually vanish in 8 h. Thus, as confirmed by other studies on PTB7 and PTB7-Th<sup>[68,90,94]</sup> and in contrast to polymers like P3HT,<sup>[71,98]</sup> the conjugated backbone is clearly the most sensitive reaction site within this process. Exemplary bending modes of the alkyl groups in the side chains (1460 and 1377  $\text{cm}^{-1}$ ), both depicted in light pink, show a rather linear decrease until they almost vanish after one day. A similar behavior is also found for the stretching vibrations of these alkyl groups (3000  $\text{cm}^{-1}$  – 2800  $\text{cm}^{-1}$ ). The interpretation of this linear decrease is complicated by the fact that vibration modes of the conjugated backbone might also contribute to absorption in the wavenumber region between 1500  $\text{cm}^{-1}$  – 1350  $\text{cm}^{-1}$ . For the blend film, the slower decrease of the alkyl bands might be due to the overlap with the pronounced C<sub>70</sub> vibrations at 1430  $\text{cm}^{-1}$

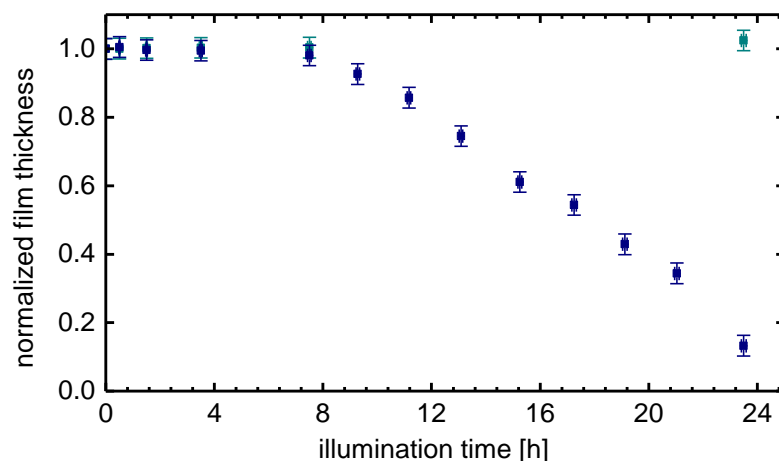


**Figure 7.19**

Comparison of the thickness evolution of thin films of pure PTB7-Th (blue) and the PTB7-Th:PC<sub>71</sub>BM blend (green) over time.

and  $2943\text{ cm}^{-1}$ , which only decrease in later stages of the degradation process. Overall, the decrease in the alkyl vibration bands hints at a significant side-chain cleavage and even the evaporation of created volatile products from the film.<sup>[299]</sup>

The extent of side-chain cleavage depends not only on the type of polymer but also on the applied aging conditions. It is important to note that a comparably high-intensity illumination was used including UV irradiation under close-to ambient conditions (albeit with dry air) for up to 48 h, while other groups chose significantly lower intensities for only a few hours in earlier studies. The chemical degradation initiates a significant loss of order within the side chains and the polymer backbone, leading to a loss in molecular packing with a subsequent blue-shift and loss of UV/vis absorption, as discussed in Figure 7.10.<sup>[74,228]</sup>

The side-chain cleavage is supported by additional measurements of the sample film thickness via profilometry, as illustrated in Figure 7.19. While the blend film thickness remains constant over the entire measurement time (similar to the in-operando solar cell measurement, see Figure 7.8), the polymer film shows a very different behavior. After keeping a constant film thickness for around 8 hours, a linear decline in thickness is visible for later stages of aging, until the film has not even 20 % of its original thickness after one day. The immense loss in thickness is a clear sign of the loss of material. It should be noted that this process only starts after about 8 hours, which is in accordance with a two-phase degradation process. In a first phase, the backbone is oxidized, leading to losses in chromophore length and conjugation, without completely destroying the molecules. Only later in the process – coinciding with the beginning creation of new C=O bonds at the cost of a drastic loss of C=C bonds – the material loss becomes visible, indicating that side-chains are broken from

the backbone due to oxidation. The constant film thickness within the blend film can be explained by several factors. PC<sub>71</sub>BM is known to incorporate oxygen within its phase, leading to swelling which might counteract possible thickness losses.<sup>[294]</sup> Additionally, it could lead to a containment of volatile products within the blend film. The pronounced initial losses in UV/vis spectroscopy (Figure 5) within the first 8 hours of illumination can be correlated to the initial breaking of the conjugation length. It is interesting to note that the new C=O bonds (illustrated in green) only emerge after several hours of illumination. It seems that the initial oxidation step does not lead to carbonyl or carboxyl groups directly, but creates an intermediate that does not show in the respective wavenumber region. Other groups have suggested that oxygen, as a dienophile, attacks the electron-rich regions within the thiophene rings of the BDT unit of the polymer<sup>[92]</sup> and creates intermediate cyclic peroxides, which in a later step are converted into carbonyl groups.<sup>[75,94]</sup>

### 7.4.3 Surface Morphology and Chemistry

Potential changes in the surface morphology and roughness are investigated with AFM. 2D AFM data of the pristine active layer film and a sample illuminated under a solar simulator for one day can be found in Figure 7.20. Similar to the findings discussed for the in-operando GISAXS study, no pronounced differences in the surface morphology of the active layer are distinguishable. The lateral size of visible (elevated) domains decreases slightly, with diameters of  $(200 \pm 40)$  nm for the fresh versus  $(185 \pm 35)$  nm for the aged sample while the surface after illumination shows an increase in average root mean square (rms) roughness (8 nm) as compared to the pristine sample (5 nm). The aged sample seems to have lost material on the surface which increases the contrast between the elevated and deeper domains. This could explain the increased scattering intensity at very low  $q_y$  values found in the GISAXS study due to an increased contrast between large domains and an increased surface roughness. However, a simple morphological change on these large length scales should not affect the OPV behavior significantly, as they exceed the exciton diffusion length. On the other hand,

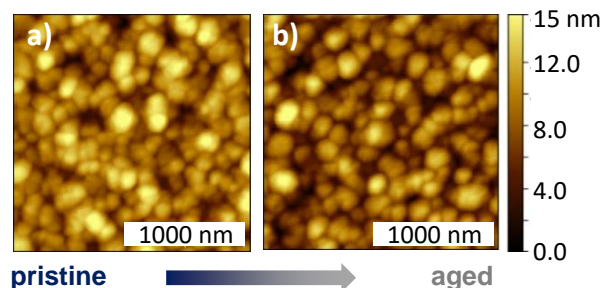


**Figure 7.20**

AFM height images of (a) the pristine active layer versus (b) an aged active layer film.

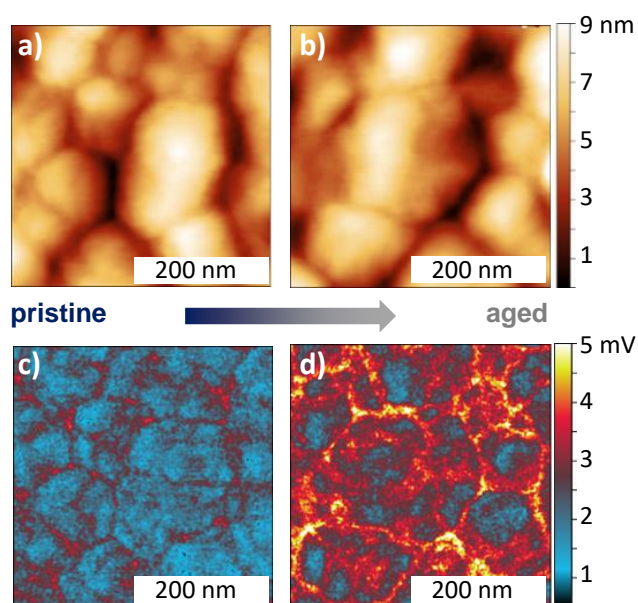


**Figure 7.21**

Comparison of (a,c) a pristine thin film stored in the dark with (b,d) an aged (illuminated) thin film of the PTB7-Th:PC<sub>71</sub>BM blend. (a,b) Topology showing the surface of the investigated films via AFM height scans, (c,d) simultaneously mapped area using IR wavenumber of 1740 cm<sup>-1</sup>. Differences in the surface chemistry between the aged and the pristine sample can be seen in the intensity at 1740 cm<sup>-1</sup>, indicating the amount of PC<sub>71</sub>BM at the surface, equating a lower surface coverage with PTB7-Th as compared to the pristine film. Measurements were performed by Anasys Instruments, US.

a loss of material at the surface due to evaporation again corroborates the findings gathered from the FTIR spectroscopy data.

To further elucidate the chemical degradation on a nanoscale, non-illuminated (pristine) and illuminated (aged) blend films are probed using AFM in combination with IR mapping. This method has been successfully used for other applications and offers a detailed view of the chemical changes happening at the sample surface.<sup>[209,300]</sup> As already mentioned, the surface topographies of the pristine and the aged samples are similar. Zooming into regions of  $1 \times 1 \mu\text{m}^2$  with AFM, the elevated structures appear to be rather polygonal than spherical (see Figure 7.21a) and b) for the pristine and aged sample, respectively). In the AFM-IR experiment, IR intensity maps are measured simultaneously at 1740 cm<sup>-1</sup> (see Figure 7.21c) and d) for the pristine and aged sample, respectively). Even though the surface topology of both samples does not differ significantly, the IR mapping shows pronounced differences. While for the non-degraded blend lower absorption at 1740 cm<sup>-1</sup>, especially over most elevated areas, is visible, the degraded blend film shows an increased overall absorption, particularly at the edges of the domains. At a wavenumber of 1740 cm<sup>-1</sup>, PC<sub>71</sub>BM-rich domains at

the sample surface will absorb significantly more radiation than PTB7-Th rich areas. As can be seen in the initial FTIR measurements on pristine samples (see Figure 7.16) and the FTIR data taken during degradation (see Figure 7.17), PC<sub>71</sub>BM has a pronounced C=O vibration band at 1740 cm<sup>-1</sup>. Theoretically, an increase at 1740 cm<sup>-1</sup> could also be due to degradation products (C=O bands) at the polymer forming at higher wavenumbers. However, degradation of the pure PTB7-Th film showed a rather constant value at this wavenumber over the entire process. It is known, that the polymer tends to accumulate near the surface under the typical production conditions and is, therefore, mainly present at the surface of the pristine sample. From this finding, it can be concluded that the aged sample exhibits a higher amount of PC<sub>71</sub>BM on its surface due to the loss of formerly accumulated PTB7-Th. These results are in accordance with the other findings, indicating the creation of volatile reaction products that leave the organic film, for example due to cleavage of side-chains.<sup>[75,109]</sup>

## 7.5 Conclusion

In this chapter, thin films of PTB7-Th and PC<sub>71</sub>BM used as active layers in organic solar cells are investigated during photodegradation by combining various methods to determine morphological and chemical changes relevant for the photovoltaic performance. In-operando GISAXS shows a correlation between the loss in the device efficiency and morphological changes. Alterations in surface roughness and scattering contrast also seen via AFM indicate structural changes and material loss. UV/vis absorption shows significant and wavelength-independent losses during illumination in oxygen atmosphere, evidencing that excitation of the polymer PTB7-Th – independent of the energy of the absorbed photons – leads to a strong increase in the oxidation probability. The sensitivity of the polymer backbone towards oxidation, causing a reduction in conjugation length, is evident from the FTIR data. Applying combined AFM height and IR mapping, the chemical degradation and material loss are proven on a nanoscale. Thus, it is shown that chemical changes during photodegradation influence the morphology on a nanoscale and have a significant effect on the active layer in various ways, leading to a fatal loss in efficiency. As a consequence, encapsulation is required for further work with PTB7-Th and similar polymers, as even traces of contaminants from the fabrication process will have to be taken into account for potential applications. The observed sensitivity to photons regardless of their respective energy and the finding that the blend morphology is not undergoing major changes although the chemical structure is seriously damaged will be interesting aspects to study in other OPV systems such as non-fullerene blends.

# CHAPTER 8

## Conclusion & Outlook

The widespread use of organic photovoltaics is still hindered by their comparably low initial efficiency and insufficient long-term stability. These parameters are significantly affected by the chemistry and morphology of the photoactive layer as well as the contact to applied electrodes. An in-depth understanding of the contributing factors is a vital step towards enhancing the solar cell performance. This work presents investigations of the interrelation between structural and photovoltaic parameters within solar cell systems, focusing on the photoactive layer itself and its interface to the metal back electrode. A range of different characterization methods is applied to acquire a deeper understanding of the properties of the respective material systems. Dynamic structural changes play a key role during the deposition of electrode materials as well as for degradation processes. Therefore, these changes are followed in situ using suitable X-ray scattering methods at a synchrotron radiation source to yield a high time resolution. The techniques of choice are GISAXS and GIWAXS, offering data with a high statistical relevance. Complementary spectroscopy and microscopy measurements illuminate the relations between different properties of the investigated systems and processes.

Interfaces between organic and metallic layers are inherently present in most organic solar cells, as the metal electrodes offer unparalleled advantages over other materials in terms of their electrical conductivity. In industrial settings, metal contacts are typically applied using sputter deposition methods. While the general concepts of metal layer formation are known, the effects of differences in the chemistry and morphology of an organic substrate in the layer growth are not yet fully understood.

As the affinity of the deposited metal to certain materials or functional groups varies, differences in the chemistry can impact the formation of the metal layer. Side-chain modifications are a typical way of tuning the optical bandgap of photoactive polymers and thereby optimizing the solar cell efficiency. In the scope of this work, the influence of differences in the side chains of the state-of-the-art low-bandgap polymers PTB7 and PTB7-Th on the formation of a gold layer are investigated. The growth process is followed in situ using GISAXS and GIWAXS, illuminating the formation of nanocrystalline gold clusters and subsequent island growth. From the first isolated gold nuclei to the percolated gold layer, information about the average cluster size and distance as well as the surface coverage are extracted and quantified. Combining observations about changes in the lateral and vertical structures, a five-stage model of the electrode formation is derived. The initial nucleation is followed by a diffusion-dominated growth of small, mobile clusters. With growing size, the cluster mobility is decreased, leading to primarily adsorption-driven further growth of immobilized larger clusters and to elongated structures. Size restrictions dominate the subsequent grain growth process. The slight modifications in the side-chains influence the growth kinetics especially in the early stages of the growth. Indeed, the substitution of oxygen with thiophene rings leads to a decrease in gold cluster size and distance, as gold exhibits lower mobilities on the surface due to its higher affinity to the sulfur groups. Using in-situ observations, these small effects are uncovered and the final difference in grain size is explained, providing a fundamental understanding of the layer growth dependence on bandgap-tuned polymers. Thus, when optimizing the bandgap of photoactive materials, potential effects on the contact have to be taken into account.

The morphology of the photoactive layer has a pronounced influence on the performance of organic photovoltaics. Solvent additives are used to enhance the solar cell efficiency by modifying the active layer morphology during processing. Building on the findings for pure PTB7-Th, mixed photoactive layers with PC<sub>71</sub>BM are explored, investigating the effects of the solvent additive DIO on the active layer morphology and on the formation of an applied gold layer. The blend films are processed either with or without DIO, illustrating differences in the inner film morphology and surface roughness. Processing without the additive results in films with larger, coarser domains and pronounced aggregates of PC<sub>71</sub>BM at the surface; adding DIO leads to smoother films with a better intermixing of smaller, elongated domains. The gold layer formation on the active layer films is investigated in situ using GISAXS and GIWAXS. Additional XRR measurements probe the vertical film profile. The general growth mechanism is similar for blends with and without the additive and comparable to the one on the pure polymer film. However, the differences in the initial film morphology clearly affect the deposited gold layer. The blend processed with DIO shows a behavior similar to the one of the pure polymer sample due to its PTB7-Th enrichment layer at the surface with comparably low surface roughness. In contrast, the blend without additive exhibits aggregates of PC<sub>71</sub>BM at its rough surface, affecting the gold layer

---

growth in several ways. Due to the gold filling the spaces between the aggregates, a significantly thicker intermixing layer is created. Additionally, the aggregates impose space restrictions on the growing gold clusters and increase the roughness of the final gold film. Therefore, the additive does not only enhance the photovoltaic properties of the active layer, but also leads to a smoother gold-organic interface with larger grains and fewer grain boundaries which potentially enhances the charge carrier extraction. Generally, the electrode contact needs to be taken into account when optimizing the active layer morphology.

Increasing the initial solar cell efficiency is a necessary, yet not sufficient measure to make them viable for widespread applications without a certain long-term stability. In particular solar cells based on low-bandgap polymers are sensitive to various degradation processes, which strongly decrease their lifetime. This work focuses on potential degradation pathways during irradiation-induced aging of active layer films of PTB7-Th and PC<sub>71</sub>BM. Various complementary methods are combined to determine the structural and chemical properties before, during, and after the illumination with different light sources. In-operando GISAXS is used to follow morphological changes within the active layer of a working solar cell, while simultaneously tracking its photovoltaic performance. While the loss in device efficiency cannot be correlated to significant differences in the phase separation, it is connected to alterations in the surface roughness and scattering contrast which indicate a material loss at the film surface. Structural changes happening on a molecular scale are probed with spectroscopic methods to evaluate the extent of light-induced oxidation processes leading to degradation. Significant and wavelength-independent losses in the optical absorption occur during illumination in an oxygen atmosphere, evidencing that the excitation of PTB7-Th – independent of the energy of the absorbed photons – leads to a strong increase in the oxidation probability. Pronounced oxidation and breaking of bonds are evidence for the sensitivity of the polymer towards photo-oxidation, causing a reduction in the conjugation length and therefore loss in optical absorption and conductivity. The chemical degradation and material loss are additionally proven on a nanoscale at the film surface by combining atomic force microscopy with infrared mapping. The changes during photodegradation influence the morphology and significantly affect the active layer in various ways, leading to a fatal loss of efficiency. Encapsulation can limit the aging and is required for further work with sensitive materials such as PTB7-Th, as even traces of contaminants from the fabrication process have to be taken into account for potential applications.

The combined findings from the present work address efficiency and stability issues from different morphological and chemical viewpoints and are an important step towards the controlled fabrication of high-efficiency solar cells. Additionally, they are of interest for other organic electronic devices based on irradiation-sensitive polymers or exhibiting polymer-metal contacts. Investigating the influence of chemical and morphological features of the organic layer on the electrode formation process supports

the industrialization of the process in a wide range of applications. For the reliable, long-term operation of organic electronic devices, the understanding gained from the investigations of the aging mechanism is of utmost importance. In particular, both chemical and morphological changes should be considered, as they are interrelated and may only jointly explain the observed effects. Interesting aspects for further study in other photoactive material systems are the high sensitivity of the low-bandgap polymer to photons regardless of their respective energy as well as the finding that the blend morphology is not undergoing major changes although the chemical structure is seriously damaged. While recent research efforts have focused on optimizing individual parameters in solar cells, this work recommends a more holistic approach for the future search for promising photovoltaic systems.

# Bibliography

- [1] *Statistisches Jahrbuch 2019*. Statistisches Bundesamt, 2019.
- [2] Baobing Fan, Xiaoyan Du, Feng Liu, Wenkai Zhong, Lei Ying, Ruihao Xie, Xiaofeng Tang, Kang An, Jingming Xin, Ning Li, Wei Ma, Christoph J. Brabec, Fei Huang, and Yong Cao. “Fine-tuning of the chemical structure of photoactive materials for highly efficient organic photovoltaics”. In: *Nature Energy* 3.12 (2018), pp. 1051–1058. DOI: 10.1038/s41560-018-0263-4.
- [3] Zhe Li, Kar Ho Chiu, Raja Shahid Ashraf, Sarah Fearn, Rajeev Dattani, Him Cheng Wong, Ching-Hong Tan, Jiaying Wu, João T. Cabral, and James R. Durrant. “Toward Improved Lifetimes of Organic Solar Cells under Thermal Stress: Substrate-Dependent Morphological Stability of PCDTBT:PCBM Films and Devices”. In: *Scientific Reports* 5 (2015), p. 15149. DOI: 10.1038/srep15149.
- [4] Craig H. Peters, I. T. Sachs-Quintana, John P. Kastrop, Serge Beaupré, Mario Leclerc, and Michael D. McGehee. “High Efficiency Polymer Solar Cells with Long Operating Lifetimes”. In: *Advanced Energy Materials* 1.4 (2011), pp. 491–494. DOI: 10.1002/aenm.201100138.
- [5] C. K. Chiang, C. R. Fincher, Y. W. Park, Alan J. Heeger, H. Shirakawa, E. J. Louis, S. C. Gau, and Alan G. MacDiarmid. “Electrical Conductivity in Doped Polyacetylene”. In: *Physical Review Letters* 39.17 (1977), pp. 1098–1101. DOI: 10.1103/PhysRevLett.39.1098.
- [6] Letian Dou, Jingbi You, Ziruo Hong, Zheng Xu, Gang Li, Robert A. Street, and Yang Yang. “25th anniversary article: a decade of organic/polymeric photovoltaic research”. In: *Advanced Materials* 25.46 (2013), pp. 6642–6671. DOI: 10.1002/adma.201302563.
- [7] Markus C. Scharber. “On the Efficiency Limit of Conjugated Polymer:Fullerene-Based Bulk Heterojunction Solar Cells”. In: *Advanced Materials* 28.10 (2016), pp. 1994–2001. DOI: 10.1002/adma.201504914.
- [8] Jianhui Hou, Olle Inganäs, Richard H. Friend, and Feng Gao. “Organic solar cells based on non-fullerene acceptors”. In: *Nature Materials* 17.2 (2018), pp. 119–128. DOI: 10.1038/nmat5063.

- [9] Caitlin McDowell, Maged Abdelsamie, Michael F. Toney, and Guillermo C. Bazan. “Solvent Additives: Key Morphology-Directing Agents for Solution-Processed Organic Solar Cells”. In: *Advanced Materials* 30.33 (2018), e1707114. DOI: 10.1002/adma.201707114.
- [10] E. B. L. Pedersen, Dechan Angmo, H. F. Dam, K. T. S. Thydén, T. R. Andersen, E. T. B. Skjønsvjell, Frederik C. Krebs, M. Holler, A. Diaz, M. Guizar-Sicairos, D. W. Breiby, and J. W. Andreasen. “Improving organic tandem solar cells based on water-processed nanoparticles by quantitative 3D nanoimaging”. In: *Nanoscale* 7.32 (2015), pp. 13765–13774. DOI: 10.1039/c5nr02824h.
- [11] Frederik C. Krebs. “Polymer solar cell modules prepared using roll-to-roll methods: Knife-over-edge coating, slot-die coating and screen printing”. In: *Solar Energy Materials and Solar Cells* 93.4 (2009), pp. 465–475. DOI: 10.1016/j.solmat.2008.12.012.
- [12] Roar Søndergaard, Markus Hösel, Dechan Angmo, Thue T. Larsen-Olsen, and Frederik C. Krebs. “Roll-to-roll fabrication of polymer solar cells”. In: *Materials Today* 15.1-2 (2012), pp. 36–49. DOI: 10.1016/S1369-7021(12)70019-6.
- [13] Sih-Hao Liao, Hong-Jyun Jhuo, Po-Nan Yeh, Yu-Shan Cheng, Yi-Lun Li, Yu-Hsuan Lee, Sunil Sharma, and Show-An Chen. “Single junction inverted polymer solar cell reaching power conversion efficiency 10.31% by employing dual-doped zinc oxide nano-film as cathode interlayer”. In: *Scientific Reports* 4 (2014), p. 6813. DOI: 10.1038/srep06813.
- [14] Baobing Fan, Difei Zhang, Meijing Li, Wenkai Zhong, Zhaomiyi Zeng, Lei Ying, Fei Huang, and Yong Cao. “Achieving over 16% efficiency for single-junction organic solar cells”. In: *Science China Chemistry* 62.6 (2019), pp. 746–752. DOI: 10.1007/s11426-019-9457-5.
- [15] Lingxian Meng, Yamin Zhang, Xiangjian Wan, Chenxi Li, Xin Zhang, Yanbo Wang, Xin Ke, Zuo Xiao, Liming Ding, Ruoxi Xia, Hin-Lap Yip, Yong Cao, and Yongsheng Chen. “Organic and solution-processed tandem solar cells with 17.3% efficiency”. In: *Science* 361.6407 (2018), pp. 1094–1098. DOI: 10.1126/science.aat2612.
- [16] Nadia Grossiord, Jan M. Kroon, Ronn Andriessen, and Paul W.M. Blom. “Degradation mechanisms in organic photovoltaic devices”. In: *Organic Electronics* 13.3 (2012), pp. 432–456. DOI: 10.1016/j.orgel.2011.11.027.
- [17] William R. Mateker and Michael D. McGehee. “Progress in Understanding Degradation Mechanisms and Improving Stability in Organic Photovoltaics”. In: *Advanced Materials* 29.10 (2017). DOI: 10.1002/adma.201603940.

- [18] Saqib Rafique, Shahino M. Abdullah, Khaulah Sulaiman, and Mitsumasa Iwamoto. “Fundamentals of bulk heterojunction organic solar cells: An overview of stability/degradation issues and strategies for improvement”. In: *Renewable and Sustainable Energy Reviews* 84 (2018), pp. 43–53. DOI: 10.1016/j.rser.2017.12.008.
- [19] Gilles Dennler, Markus C. Scharber, and Christoph J. Brabec. “Polymer-Fullerene Bulk-Heterojunction Solar Cells”. In: *Advanced Materials* 21.13 (2009), pp. 1323–1338. DOI: 10.1002/adma.200801283.
- [20] Jea Uk Lee, Jae Woong Jung, Jea Woong Jo, and Won Ho Jo. “Degradation and stability of polymer-based solar cells”. In: *Journal of Materials Chemistry* 22.46 (2012), p. 24265. DOI: 10.1039/c2jm33645f.
- [21] Yongfang Li. “Molecular design of photovoltaic materials for polymer solar cells: toward suitable electronic energy levels and broad absorption”. In: *Accounts of Chemical Research* 45.5 (2012), pp. 723–733. DOI: 10.1021/ar2002446.
- [22] Hongping Yan, Brian A. Collins, Eliot Gann, Cheng Wang, Harald Ade, and Christopher R. McNeill. “Correlating the efficiency and nanomorphology of polymer blend solar cells utilizing resonant soft X-ray scattering”. In: *ACS Nano* 6.1 (2012), pp. 677–688. DOI: 10.1021/nn204150f.
- [23] Zhicai He, Biao Xiao, Feng Liu, Hongbin Wu, Yali Yang, Steven Xiao, Cheng Wang, Thomas P. Russell, and Yong Cao. “Single-junction polymer solar cells with high efficiency and photovoltage”. In: *Nature Photonics* 9.3 (2015), pp. 174–179. DOI: 10.1038/nphoton.2015.6.
- [24] William R. Mateker, Thomas Heumueller, Rongrong Cheacharoen, I. T. Sachs-Quintana, Michael D. McGehee, Julien Warnan, Pierre M. Beaujuge, Xiaofeng Liu, and Guillermo C. Bazan. “Molecular Packing and Arrangement Govern the Photo-Oxidative Stability of Organic Photovoltaic Materials”. In: *Chemistry of Materials* 27.18 (2015), pp. 6345–6353. DOI: 10.1021/acs.chemmater.5b02341.
- [25] Smita Mukherjee, Sreeanta Chakraborty, Aniruddha Samanta, Jiten Ghosh, and Anoop Kr Mukhopadhyay. “Band gap tuning in gold nanoparticle decorated TiO<sub>2</sub> films: effect of Au nanoparticle concentration”. In: *Materials Research Express* 4.6 (2017), p. 065016. DOI: 10.1088/2053-1591/aa73fb.
- [26] Nutifafa Y. Doumon, Mikhail V. Dryzhov, Félix V. Houard, Vincent M. Le Corre, Azadeh Rahimi Chatri, Panagiotis Christodoulis, and L. Jan Anton Koster. “Photostability of Fullerene and Non-Fullerene Polymer Solar Cells: The Role of the Acceptor”. In: *ACS Applied Materials & Interfaces* 11.8 (2019), pp. 8310–8318. DOI: 10.1021/acsami.8b20493.

- [27] Hsueh-Chung Liao, Chun-Chih Ho, Chun-Yu Chang, Meng-Huan Jao, Seth B. Darling, and Wei-Fang Su. “Additives for morphology control in high-efficiency organic solar cells”. In: *Materials Today* 16.9 (2013), pp. 326–336. DOI: 10.1016/j.mattod.2013.08.013.
- [28] Ling Zhao, Suling Zhao, Zheng Xu, Qianqian Yang, Di Huang, and Xurong Xu. “A simple method to adjust the morphology of gradient three-dimensional PTB7-Th:PC71BM polymer solar cells”. In: *Nanoscale* 7.12 (2015), pp. 5537–5544. DOI: 10.1039/c5nr00148j.
- [29] Franz Faupel, Vladimir Zaporozhchenko, Thomas Strunskus, and Mady Elbahri. “Metal-Polymer Nanocomposites for Functional Applications”. In: *Advanced Engineering Materials* 12.12 (2010), pp. 1177–1190. DOI: 10.1002/adem.201000231.
- [30] Matthew J. Griffith, Nathan A. Cooling, Ben Vaughan, Kane M. O’Donnell, Mohammed F. Al-Mudhaffer, Alaa Al-Ahmad, Mahir Noori, Furqan Almyahi, Warwick J. Belcher, and Paul C. Dastoor. “Roll-to-Roll Sputter Coating of Aluminum Cathodes for Large-Scale Fabrication of Organic Photovoltaic Devices”. In: *Energy Technology* 3.4 (2015), pp. 428–436. DOI: 10.1002/ente.201402174.
- [31] Yen-Ju Hsieh, Yu-Ching Huang, Wei-Shin Liu, Yu-An Su, Cheng-Si Tsao, Syang-Peng Rwei, and Leeyih Wang. “Insights into the Morphological Instability of Bulk Heterojunction PTB7-Th/PCBM Solar Cells upon High-Temperature Aging”. In: *ACS Applied Materials & Interfaces* 9.17 (2017), pp. 14808–14816. DOI: 10.1021/acsami.7b01296.
- [32] Leslie H. Sperling. *Introduction to Physical Polymer Science*. 3. ed. A Wiley-Interscience publication. Wiley-VCH, 2005. DOI: 10.1002/0471757128.
- [33] A. D. Jenkins, P. Kratochvíl, R. F.T. Stepto, and U. W. Suter. “Glossary of basic terms in polymer science (IUPAC Recommendations 1996)”. In: *Pure and Applied Chemistry* 68.12 (1996), pp. 2287–2311.
- [34] Niyazi S. Sariciftci, L. Smilowitz, Alan J. Heeger, and F. Wudl. “Photoinduced electron transfer from a conducting polymer to buckminsterfullerene”. In: *Science* 258.5087 (1992), pp. 1474–1476. DOI: 10.1126/science.258.5087.1474.
- [35] Paul J. Flory. “Thermodynamics of High Polymer Solutions”. In: *The Journal of Chemical Physics* 10.1 (1942), pp. 51–61. DOI: 10.1063/1.1723621.
- [36] Maurice L. Huggins. “Theory of Solutions of High Polymers 1”. In: *Journal of the American Chemical Society* 64.7 (1942), pp. 1712–1719. DOI: 10.1021/ja01259a068.
- [37] Martin Pope and Charles E. Swenberg. *Electronic processes in organic crystals and polymers*. 2. ed. Vol. 56. Monographs on the physics and chemistry of materials. Oxford Univ. Press, 1999.

- [38] Wolfgang Brütting and Chihaya Adachi, eds. *Physics of organic semiconductors*. 2., completely new rev. ed. Wiley-VCH, 2012.
- [39] Anna Köhler and Heinz Bässler. *Electronic processes in organic semiconductors. An introduction*. Wiley-VCH, 2015.
- [40] Tomas Johansson, Wendimagegn Mammo, Mattias Svensson, Mats R. Andersson, and Olle Inganäs. “Electrochemical bandgaps of substituted polythiophenes”. In: *Journal of Materials Chemistry* 13.6 (2003), pp. 1316–1323. DOI: 10.1039/B301403G.
- [41] Renee Kroon, Martijn Lenes, Jan C. Hummelen, Paul W.M. Blom, and Bert de Boer. “Small Bandgap Polymers for Organic Solar Cells (Polymer Material Development in the Last 5 Years)”. In: *Polymer Reviews* 48.3 (2008), pp. 531–582. DOI: 10.1080/15583720802231833.
- [42] Matthew Wright and Ashraf Uddin. “Organic—inorganic hybrid solar cells: A comparative review”. In: *Solar Energy Materials and Solar Cells* 107 (2012), pp. 87–111. DOI: 10.1016/j.solmat.2012.07.006.
- [43] Markus C. Scharber, D. Mühlbacher, M. Koppe, P. Denk, C. Waldauf, Alan J. Heeger, and Christoph J. Brabec. “Design Rules for Donors in Bulk-Heterojunction Solar Cells—Towards 10 % Energy-Conversion Efficiency”. In: *Advanced Materials* 18.6 (2006), pp. 789–794. DOI: 10.1002/adma.200501717.
- [44] W. P. Su, J. R. Schrieffer, and Alan J. Heeger. “Solitons in Polyacetylene”. In: *Physical Review Letters* 42.25 (1979), pp. 1698–1701. DOI: 10.1103/PhysRevLett.42.1698.
- [45] P. M. Borsenberger, L. Pautmeier, and Heinz Bässler. “Charge transport in disordered molecular solids”. In: *The Journal of Chemical Physics* 94.8 (1991), pp. 5447–5454. DOI: 10.1063/1.460506.
- [46] Heinz Bässler. “Charge Transport in Disordered Organic Photoconductors a Monte Carlo Simulation Study”. In: *Physica Status Solidi (b)* 175.1 (1993), pp. 15–56. DOI: 10.1002/pssb.2221750102.
- [47] Georges Hadziioannou and George G. Malliaras, eds. *Semiconducting polymers. Chemistry, physics and engineering*. [2. ed.] Wiley-VCH, 2007.
- [48] Krishna Feron, Warwick J. Belcher, Christopher J. Fell, and Paul C. Dastoor. “Organic solar cells: understanding the role of Förster resonance energy transfer”. In: *International Journal of Molecular Sciences* 13.12 (2012), pp. 17019–17047. DOI: 10.3390/ijms131217019.
- [49] R. A. Marcus. “On the Theory of Oxidation–Reduction Reactions Involving Electron Transfer. I”. In: *The Journal of Chemical Physics* 24.5 (1956), pp. 966–978. DOI: 10.1063/1.1742723.

- [50] Allen Miller and Elihu Abrahams. “Impurity Conduction at Low Concentrations”. In: *Physical Review* 120.3 (1960), pp. 745–755. DOI: 10.1103/PhysRev.120.745.
- [51] Carsten Deibel and Vladimir Dyakonov. “Polymer–fullerene bulk heterojunction solar cells”. In: *Reports on Progress in Physics* 73.9 (2010), p. 096401. DOI: 10.1088/0034-4885/73/9/096401.
- [52] Harald Hoppe and Niyazi S. Sariciftci. “Organic solar cells: An overview”. In: *Journal of Materials Research* 19.7 (2004), pp. 1924–1945. DOI: 10.1557/JMR.2004.0252.
- [53] Christoph J. Brabec, Ullrich Scherf, and Vladimir Dyakonov, eds. *Organic photovoltaics. Materials, device physics, and manufacturing technologies*. 2. ed. Wiley-VCH, 2014.
- [54] M. C. J. M. Vissenberg and M. Matters. “Theory of the field-effect mobility in amorphous organic transistors”. In: *Physical Review B: Condensed Matter and Materials Physics* 57.20 (1998), p. 12964. DOI: 10.1103/PhysRevB.57.12964.
- [55] Dirk Hertel and Heinz Bässler. “Photoconduction in amorphous organic solids”. In: *ChemPhysChem* 9.5 (2008), pp. 666–688. DOI: 10.1002/cphc.200700575.
- [56] Neil W. Ashcroft and N. David Mermin. *Solid state physics*. Brooks/Cole Thomson Learning, 2012.
- [57] Th. Förster. “Zwischenmolekulare Energiewanderung und Fluoreszenz”. In: *Annalen der Physik* 437.1-2 (1948), pp. 55–75. DOI: 10.1002/andp.19484370105.
- [58] Wichard J. D. Beenken. “Excitons in conjugated polymers: Do we need a paradigm change?” In: *Physica Status Solidi (a)* 206.12 (2009), pp. 2750–2756. DOI: 10.1002/pssa.200925297.
- [59] Paul E. Shaw, Arvydas Ruseckas, and Ifor D. W. Samuel. “Exciton Diffusion Measurements in Poly(3-hexylthiophene)”. In: *Advanced Materials* 20.18 (2008), pp. 3516–3520. DOI: 10.1002/adma.200800982.
- [60] J. Campbell Scott and George G. Malliaras. “Charge injection and recombination at the metal–organic interface”. In: *Chemical Physics Letters* 299.2 (1999), pp. 115–119. DOI: 10.1016/S0009-2614(98)01277-9.
- [61] R. Sokel and R. C. Hughes. “Numerical analysis of transient photoconductivity in insulators”. In: *Journal of Applied Physics* 53.11 (1982), pp. 7414–7424. DOI: 10.1063/1.330111.
- [62] Harald Hoppe, M. Niggemann, C. Winder, J. Kraut, R. Hiesgen, A. Hirsch, D. Meissner, and Niyazi S. Sariciftci. “Nanoscale Morphology of Conjugated Polymer/Fullerene-Based Bulk- Heterojunction Solar Cells”. In: *Advanced Functional Materials* 14.10 (2004), pp. 1005–1011. DOI: 10.1002/adfm.200305026.

- 
- [63] Matthieu Manceau, Agnès Rivaton, Jean-Luc Gardette, Stéphane Guillerez, and Noëlla Lemaître. “Light-induced degradation of the P3HT-based solar cells active layer”. In: *Solar Energy Materials and Solar Cells* 95.5 (2011), pp. 1315–1325. DOI: 10.1016/j.solmat.2010.09.021.
- [64] Matthias A. Ruderer and Peter Müller-Buschbaum. “Morphology of polymer-based bulk heterojunction films for organic photovoltaics”. In: *Soft Matter* 7.12 (2011), p. 5482. DOI: 10.1039/c0sm01502d.
- [65] Christoph J. Schaffer, Claudia M. Palumbiny, Martin A. Niedermeier, Christian Jendrzejewski, Gonzalo Santoro, Stephan V. Roth, and Peter Müller-Buschbaum. “A direct evidence of morphological degradation on a nanometer scale in polymer solar cells”. In: *Advanced Materials* 25.46 (2013), pp. 6760–6764. DOI: 10.1002/adma.201302854.
- [66] L. Ciammaruchi, Fulvio G. Brunetti, and I. Visoly-Fisher. “Solvent effects on the morphology and stability of PTB7:PCBM based solar cells”. In: *Solar Energy* 137 (2016), pp. 490–499. DOI: 10.1016/j.solener.2016.08.018.
- [67] Hyo Sang Lee, Hyeng Gun Song, Hyeseung Jung, Myung Hwa Kim, Changsoon Cho, Jung-Yong Lee, Sungnam Park, Hae Jung Son, Hui-Jun Yun, Soon-Ki Kwon, Yun-Hi Kim, and BongSoo Kim. “Effects of Backbone Planarity and Tightly Packed Alkyl Chains in the Donor–Acceptor Polymers for High Photostability”. In: *Macromolecules* 49.20 (2016), pp. 7844–7856. DOI: 10.1021/acs.macromol.6b01580.
- [68] Christoph J. Schaffer, Claudia M. Palumbiny, Martin A. Niedermeier, Christian Burger, Gonzalo Santoro, Stephan V. Roth, and Peter Müller-Buschbaum. “Morphological Degradation in Low Bandgap Polymer Solar Cells - An In Operando Study”. In: *Advanced Energy Materials* 6.19 (2016), p. 1600712. DOI: 10.1002/aenm.201600712.
- [69] Lin Song, Weijia Wang, Stephan Pröllner, Daniel Moseguí González, Johannes Schlipf, Christoph J. Schaffer, Kristina Peters, Eva M. Herzig, Sigrid Bernstorff, Thomas Bein, Dina Fattakhova-Rohlfing, and Peter Müller-Buschbaum. “In Situ Study of Degradation in P3HT–Titania-Based Solid-State Dye-Sensitized Solar Cells”. In: *ACS Energy Letters* 2.5 (2017), pp. 991–997. DOI: 10.1021/acsenerylett.7b00117.
- [70] Dan Yang, Franziska C. Löhner, Volker Körstgens, Armin Schreiber, Sigrid Bernstorff, Jillian M. Buriak, and Peter Müller-Buschbaum. “In-Operando Study of the Effects of Solvent Additives on the Stability of Organic Solar Cells Based on PTB7-Th:PC 71 BM”. In: *ACS Energy Letters* 4.2 (2019), pp. 464–470. DOI: 10.1021/acsenerylett.8b02311.

- [71] Agnès Rivaton, Sylvain Chambon, Matthieu Manceau, Jean-Luc Gardette, Noëlla Lemaître, and Stéphane Guillerez. “Light-induced degradation of the active layer of polymer-based solar cells”. In: *Polymer Degradation and Stability* 95.3 (2010), pp. 278–284. DOI: 10.1016/j.polymdegradstab.2009.11.021.
- [72] Jurgen Kesters, Pieter Verstappen, Jorne Raymakers, Wouter Vanormelingen, Jeroen Drijkoningen, Jan D’Haen, Jean Manca, Laurence Lutsen, Dirk Vanderzande, and Wouter Maes. “Enhanced Organic Solar Cell Stability by Polymer (PCPDTBT) Side Chain Functionalization”. In: *Chemistry of Materials* 27.4 (2015), pp. 1332–1341. DOI: 10.1021/cm504391k.
- [73] Tarek M. Abdel-Fattah, Enas M. Younes, Gon Namkoong, E. M. El-Maghraby, Adly H. Elsayed, and A. H. Abo Elazm. “Stability study of low and high band gap polymer and air stability of PTB7:PC71BM bulk heterojunction organic photovoltaic cells with encapsulation technique”. In: *Synthetic Metals* 209 (2015), pp. 348–354. DOI: 10.1016/j.synthmet.2015.08.005.
- [74] Bertrand J. Tremolet de Villers, Kathryn A. O’Hara, David P. Ostrowski, Perry H. Biddle, Sean E. Shaheen, Michael L. Chabinyc, Dana C. Olson, and Nikos Kopidakis. “Removal of Residual Diiodooctane Improves Photostability of High-Performance Organic Solar Cell Polymers”. In: *Chemistry of Materials* 28.3 (2016), pp. 876–884. DOI: 10.1021/acs.chemmater.5b04346.
- [75] Anthony Perthué, Thérèse Gorisse, Hugo Santos Silva, Didier Bégué, Agnès Rivaton, and Guillaume Wantz. “Influence of traces of oxidized polymer on the performances of bulk heterojunction solar cells”. In: *Materials Chemistry Frontiers* 3.8 (2019), pp. 1632–1641. DOI: 10.1039/C9QM00191C.
- [76] Frederik C. Krebs. *Stability and Degradation of Organic and Polymer Solar Cells*. John Wiley & Sons, Ltd, 2012. DOI: 10.1002/9781119942436.
- [77] Mikkel Jørgensen, Kion Norrman, Suren A. Gevorgyan, Thomas Tromholt, Birgitta Andreasen, and Frederik C. Krebs. “Stability of polymer solar cells”. In: *Advanced Materials* 24.5 (2012), pp. 580–612. DOI: 10.1002/adma.201104187.
- [78] J. McElvain, H. Antoniadis, M. R. Hueschen, J. N. Miller, D. M. Roitman, J. R. Sheats, and R. L. Moon. “Formation and growth of black spots in organic light-emitting diodes”. In: *Journal of Applied Physics* 80.10 (1996), pp. 6002–6007. DOI: 10.1063/1.363598.
- [79] M. Schaer, F. Nüesch, D. Berner, W. Leo, and L. Zuppiroli. “Water Vapor and Oxygen Degradation Mechanisms in Organic Light Emitting Diodes”. In: *Advanced Functional Materials* 11.2 (2001), pp. 116–121. DOI: 10.1002/1616-3028(200104)11:2<116::AID-ADFM116>3.0.CO;2-B.

- 
- [80] Wei Wang, Shuang Fang Lim, and Soo Jin Chua. “Bubble formation and growth in organic light-emitting diodes composed of a polymeric emitter and a calcium cathode”. In: *Journal of Applied Physics* 91.9 (2002), pp. 5712–5715. DOI: 10.1063/1.1467395.
- [81] R. Czerw, D. L. Carroll, H. S. Woo, Y. B. Kim, and J. W. Park. “Nanoscale observation of failures in organic light-emitting diodes”. In: *Journal of Applied Physics* 96.1 (2004), pp. 641–644. DOI: 10.1063/1.1759398.
- [82] Frederik C. Krebs, Jon E. Carlé, N. Cruysbagger, M. Andersen, M. Lilliedal, M. Hammond, and S. Hvidt. “Lifetimes of organic photovoltaics: photochemistry, atmosphere effects and barrier layers in ITO-MEHPPV:PCBM-aluminium devices”. In: *Solar Energy Materials and Solar Cells* 86.4 (2005), pp. 499–516. DOI: 10.1016/j.solmat.2004.09.002.
- [83] M. Seeland, R. Rösch, and Harald Hoppe. “Luminescence imaging of polymer solar cells: Visualization of progressing degradation”. In: *Journal of Applied Physics* 109.6 (2011), p. 064513. DOI: 10.1063/1.3553864.
- [84] M. P. de Jong, L. J. van IJzendoorn, and M. J. A. de Voigt. “Stability of the interface between indium-tin-oxide and poly(3,4-ethylenedioxythiophene)/poly(styrenesulfonate) in polymer light-emitting diodes”. In: *Applied Physics Letters* 77.14 (2000), pp. 2255–2257. DOI: 10.1063/1.1315344.
- [85] Min Chul Suh, Ho Kyoon Chung, Sang-Yeol Kim, Jang Hyuk Kwon, and Byung Doo Chin. “Cathode diffusion and degradation mechanism of polymeric light emitting devices”. In: *Chemical Physics Letters* 413.1-3 (2005), pp. 205–209. DOI: 10.1016/j.cplett.2005.07.082.
- [86] Sabine Bertho, Griet Janssen, Thomas J. Cleij, Bert Conings, Wouter Moons, Abay Gadisa, Jan D’Haen, Etienne Goovaerts, Laurence Lutsen, Jean Manca, and Dirk Vanderzande. “Effect of temperature on the morphological and photovoltaic stability of bulk heterojunction polymer:fullerene solar cells”. In: *Solar Energy Materials and Solar Cells* 92.7 (2008), pp. 753–760. DOI: 10.1016/j.solmat.2008.01.006.
- [87] Bert Conings, Sabine Bertho, Koen Vandewal, Alessia Senes, Jan D’Haen, Jean Manca, and René A. J. Janssen. “Modeling the temperature induced degradation kinetics of the short circuit current in organic bulk heterojunction solar cells”. In: *Applied Physics Letters* 96.16 (2010), p. 163301. DOI: 10.1063/1.3391669.
- [88] Xiao Wang, Hans-Joachim Egelhaaf, Hans-Georg Mack, Hamed Azimi, Christoph J. Brabec, Alfred J. Meixner, and Dai Zhang. “Morphology Related Photodegradation of Low-Band-Gap Polymer Blends”. In: *Advanced Energy Materials* 4.17 (2014), p. 1400497. DOI: 10.1002/aenm.201400497.

- [89] Weijia Wang, Christoph J. Schaffer, Lin Song, Volker Körstgens, Stephan Pröller, Efi Dwi Indari, Tianyi Wang, Amr Abdelsamie, Sigrid Bernstorff, and Peter Müller-Buschbaum. “In operando morphology investigation of inverted bulk heterojunction organic solar cells by GISAXS”. In: *Journal of Materials Chemistry A* 3.16 (2015), pp. 8324–8331. DOI: 10.1039/C5TA01109D.
- [90] Daniel Moseguí González, Christoph J. Schaffer, Stephan Pröller, Johannes Schlipf, Lin Song, Sigrid Bernstorff, Eva M. Herzig, and Peter Müller-Buschbaum. “Codependence between Crystalline and Photovoltage Evolutions in P3HT:PCBM Solar Cells Probed with in-Operando GIWAXS”. In: *ACS Applied Materials & Interfaces* 9.4 (2017), pp. 3282–3287. DOI: 10.1021/acsami.6b15661.
- [91] Dan Yang, Franziska C. Löhner, Volker Körstgens, Armin Schreiber, Bing Cao, Sigrid Bernstorff, and Peter Müller-Buschbaum. “In Operando GISAXS and GIWAXS Stability Study of Organic Solar Cells Based on PffBT4T-2OD:PC71BM with and without Solvent Additive”. In: *Advanced Science* 7.16 (2020), p. 2001117. DOI: 10.1002/advs.202001117.
- [92] Joseph Razzell-Hollis, Jessica Wade, Wing Chung Tsoi, Ying Soon, James R. Durrant, and Ji-Seon Kim. “Photochemical stability of high efficiency PTB7:PC70 BM solar cell blends”. In: *Journal of Materials Chemistry A* 2.47 (2014), pp. 20189–20195. DOI: 10.1039/C4TA05641H.
- [93] Ulf Dettinger, Hans-Joachim Egelhaaf, Christoph J. Brabec, Florian Latteyer, Heiko Peisert, and Thomas Chassé. “FTIR Study of the Impact of PC[60]BM on the Photodegradation of the Low Band Gap Polymer PCPDTBT under O<sub>2</sub> Environment”. In: *Chemistry of Materials* 27.7 (2015), pp. 2299–2308. DOI: 10.1021/acs.chemmater.5b00268.
- [94] Sangjun Kim, Md Al Mamunur Rashid, Taewon Ko, Kyusang Ahn, Yukyung Shin, Sanghee Nah, Myung Hwa Kim, BongSoo Kim, Kyungwon Kwak, and Minhaeng Cho. “New Insights into the Photodegradation Mechanism of the PTB7-Th Film: Photooxidation of  $\pi$ -Conjugated Backbone upon Sunlight Illumination”. In: *The Journal of Physical Chemistry C* 124.5 (2020), pp. 2762–2770. DOI: 10.1021/acs.jpcc.9b09954.
- [95] Mohamed S. A. Abdou and Steven Holdcroft. “Mechanisms of photodegradation of poly(3-alkylthiophenes) in solution”. In: *Macromolecules* 26.11 (1993), pp. 2954–2962. DOI: 10.1021/ma00063a047.
- [96] Sylvain Chambon, Agnès Rivaton, Jean-Luc Gardette, Muriel Firon, and Laurence Lutsen. “Aging of a donor conjugated polymer: Photochemical studies of the degradation of poly[2-methoxy-5-(3*I*,7*I*-dimethyloctyloxy)-1,4-phenylenevinylene]”. In: *Journal of Polymer Science Part A: Polymer Chemistry* 45.2 (2007), pp. 317–331. DOI: 10.1002/pola.21815.

- [97] Sylvain Chambon, Matthieu Manceau, Muriel Firon, Stéphane Cros, Agnès Rivaton, and Jean-Luc Gardette. “Photo-oxidation in an 18O<sub>2</sub> atmosphere: A powerful tool to elucidate the mechanism of UV–visible light oxidation of polymers – Application to the photodegradation of MDMO-PPV”. In: *Polymer* 49.15 (2008), pp. 3288–3294. DOI: 10.1016/j.polymer.2008.04.001.
- [98] Matthieu Manceau, Agnès Rivaton, Jean-Luc Gardette, Stéphane Guillerez, and Noëlla Lemaître. “The mechanism of photo- and thermooxidation of poly(3-hexylthiophene) (P3HT) reconsidered”. In: *Polymer Degradation and Stability* 94.6 (2009), pp. 898–907. DOI: 10.1016/j.polyimdeggradstab.2009.03.005.
- [99] Sylvain Chambon, Agnès Rivaton, Jean-Luc Gardette, and Muriel Firon. “Reactive intermediates in the initiation step of the photo-oxidation of MDMO-PPV”. In: *Journal of Polymer Science Part A: Polymer Chemistry* 47.22 (2009), pp. 6044–6052. DOI: 10.1002/pola.23628.
- [100] Holger Hintz, Hans-Joachim Egelhaaf, H. Peisert, and Thomas Chassé. “Photo-oxidation and ozonization of poly(3-hexylthiophene) thin films as studied by UV/VIS and photoelectron spectroscopy”. In: *Polymer Degradation and Stability* 95.5 (2010), pp. 818–825. DOI: 10.1016/j.polyimdeggradstab.2010.02.004.
- [101] Holger Hintz, Hans-Joachim Egelhaaf, Larry Lüer, Jens A. Hauch, Heiko Peisert, and Thomas Chassé. “Photodegradation of P3HT—A Systematic Study of Environmental Factors”. In: *Chemistry of Materials* 23.2 (2011), pp. 145–154. DOI: 10.1021/cm102373k.
- [102] Mohamed S. A. Abdou, Gerardo A. Diaz-Guijada, M. Isabel Arroyo, and Steven Holdcroft. “Photoimaging of electronically conducting polymeric networks”. In: *Chemistry of Materials* 3.6 (1991), pp. 1003–1006. DOI: 10.1021/cm00018a009.
- [103] R. Pacios, A. J. Chatten, K. Kawano, James R. Durrant, Donal D. C. Bradley, and Jenny Nelson. “Effects of Photo-oxidation on the Performance of Poly[2-methoxy-5-(3*I*,7*I*-dimethyloctyloxy)-1,4-phenylene vinylene]:[6,6]-Phenyl C61-Butyric Acid Methyl Ester Solar Cells”. In: *Advanced Functional Materials* 16.16 (2006), pp. 2117–2126. DOI: 10.1002/adfm.200500714.
- [104] Matthieu Manceau, Agnès Rivaton, and Jean-Luc Gardette. “Involvement of Singlet Oxygen in the Solid-State Photochemistry of P3HT”. In: *Macromolecular Rapid Communications* 29.22 (2008), pp. 1823–1827. DOI: 10.1002/marc.200800421.
- [105] Matthieu Manceau, Sylvain Chambon, Agnès Rivaton, Jean-Luc Gardette, Stéphane Guillerez, and Noëlla Lemaître. “Effects of long-term UV–visible light irradiation in the absence of oxygen on P3HT and P3HT:PCBM blend”. In: *Solar Energy Materials and Solar Cells* 94.10 (2010), pp. 1572–1577. DOI: 10.1016/j.solmat.2010.03.012.

- [106] Eric T. Hoke, I. T. Sachs-Quintana, Matthew T. Lloyd, Isaac V. Kauvar, William R. Mateker, Alexandre M. Nardes, Craig H. Peters, Nikos Kopidakis, and Michael D. McGehee. “The Role of Electron Affinity in Determining Whether Fullerenes Catalyze or Inhibit Photooxidation of Polymers for Solar Cells”. In: *Advanced Energy Materials* 2.11 (2012), pp. 1351–1357. DOI: 10.1002/aenm.201200169.
- [107] Matthieu Manceau, Eva Bundgaard, Jon E. Carlé, Ole Hagemann, Martin Helgesen, Roar Søndergaard, Mikkel Jørgensen, and Frederik C. Krebs. “Photochemical stability of  $\pi$ -conjugated polymers for polymer solar cells: a rule of thumb”. In: *Journal of Materials Chemistry* 21.12 (2011), p. 4132. DOI: 10.1039/c0jm03105d.
- [108] Salima Alem, Salem Wakim, Jianping Lu, Gilles Robertson, Jianfu Ding, and Ye Tao. “Degradation mechanism of benzodithiophene-based conjugated polymers when exposed to light in air”. In: *ACS Applied Materials & Interfaces* 4.6 (2012), pp. 2993–2998. DOI: 10.1021/am300362b.
- [109] Aurélien Tournebize, Pierre-Olivier Bussière, Pascal Wong-Wah-Chung, Sandrine Thérias, Agnès Rivaton, Jean-Luc Gardette, Serge Beaupré, and Mario Leclerc. “Impact of UV-Visible Light on the Morphological and Photochemical Behavior of a Low-Bandgap Poly(2,7-Carbazole) Derivative for Use in High-Performance Solar Cells”. In: *Advanced Energy Materials* 3.4 (2013), pp. 478–487. DOI: 10.1002/aenm.201200662.
- [110] Andrej Classen, Thomas Heumueller, Isabell Wabra, Johannes Gerner, Yakun He, Lukas Einsiedler, Ning Li, Gebhard J. Matt, Andres Osvet, Xiaoyan Du, Andreas Hirsch, and Christoph J. Brabec. “Revealing Hidden UV Instabilities in Organic Solar Cells by Correlating Device and Material Stability”. In: *Advanced Energy Materials* 9.39 (2019), p. 1902124. DOI: 10.1002/aenm.201902124.
- [111] Jay B. Patel, Priti Tiwana, Nico Seidler, Graham E. Morse, Owen R. Lozman, Michael B. Johnston, and Laura M. Herz. “Effect of Ultraviolet Radiation on Organic Photovoltaic Materials and Devices”. In: *ACS Applied Materials & Interfaces* 11.24 (2019), pp. 21543–21551. DOI: 10.1021/acsami.9b04828.
- [112] Subarna Babu Sapkota, Martin Fischer, Birger Zimmermann, and Uli Würfel. “Analysis of the degradation mechanism of ITO-free organic solar cells under UV radiation”. In: *Solar Energy Materials and Solar Cells* 121 (2014), pp. 43–48. DOI: 10.1016/j.solmat.2013.10.021.
- [113] Jaehoon Jeong, Jooyeok Seo, Sungho Nam, Hyemi Han, Hwajeong Kim, Thomas D. Anthopoulos, Donal D. C. Bradley, and Youngkyoo Kim. “Significant Stability Enhancement in High-Efficiency Polymer:Fullerene Bulk Heterojunction Solar Cells by Blocking Ultraviolet Photons from Solar Light”. In: *Advanced Science* 3.4 (2016), p. 1500269. DOI: 10.1002/advs.201500269.

- 
- [114] John A. Venables and G. D. T. Spiller. “Nucleation and Growth of Thin Films”. In: *Surface Mobilities on Solid Materials*. Ed. by Vu Thien Binh. Springer, 1983, pp. 341–404. DOI: 10.1007/978-1-4684-4343-1\_16.
- [115] John A. Venables. *Introduction to Surface and Thin Film Processes*. Cambridge University Press, 2010. DOI: 10.1017/CB09780511755651.
- [116] Gunar M. Kaune. “Strukturierung von anorganisch-organischen Hybridsystemen für Anwendungen in der Photovoltaik”. TU München, Chair for Functional Materials. Doctoral Thesis. 2010.
- [117] Mario Einax, Wolfgang Dieterich, and Philipp Maass. “Colloquium: Cluster growth on surfaces: Densities, size distributions, and morphologies”. In: *Reviews of Modern Physics* 85.3 (2013), p. 921. DOI: 10.1103/RevModPhys.85.921.
- [118] Matthias Schwartzkopf. “In situ  $\mu$ GISAXS Untersuchungen der Wachstumskinetik von Goldclustern”. Doctoral Thesis. 2013.
- [119] Alexandre de Castro Maciel, Reifenberger, Choi, and Andres. “Size-dependent melting temperature of individual nanometer-sized metallic clusters”. In: *Physical Review B, Condensed Matter* 42.13 (1990), pp. 8548–8556. DOI: 10.1103/physrevb.42.8548.
- [120] Günter Schmid and Benedetto Corain. “Nanoparticulated Gold: Syntheses, Structures, Electronics, and Reactivities”. In: *European Journal of Inorganic Chemistry* 2003.17 (2003), pp. 3081–3098. DOI: 10.1002/ejic.200300187.
- [121] G. Nimtz, P. Marquardt, and H. Gleiter. “Size-induced metal-insulator transition in metals and semiconductors”. In: *Journal of Crystal Growth* 86.1-4 (1988), pp. 66–71. DOI: 10.1016/0022-0248(90)90700-U.
- [122] R. H. Doremus. “Optical Properties of Thin Metallic Films in Island Form”. In: *Journal of Applied Physics* 37.7 (1966), pp. 2775–2781. DOI: 10.1063/1.1782121.
- [123] B. Gompf, J. Beister, T. Brandt, J. Pflaum, and Martin Dressel. “Nanometer-thick Au-films as antireflection coating for infrared light”. In: *Optics Letters* 32.11 (2007), pp. 1578–1580. DOI: 10.1364/ol.32.001578.
- [124] Martin Hövel, Bruno Gompf, and Martin Dressel. “Dielectric properties of ultrathin metal films around the percolation threshold”. In: *Physical Review B: Condensed Matter and Materials Physics* 81.3 (2010). DOI: 10.1103/PhysRevB.81.035402.
- [125] Jakub Siegel, Olexiy Lyutakov, Vladimír Rybka, Zdeňka Kolská, and Václav Svorčík. “Properties of gold nanostructures sputtered on glass”. In: *Nanoscale Research Letters* 6.1 (2011), p. 96. DOI: 10.1186/1556-276X-6-96.

- [126] Kazuhiko Seki, Naoki Hayashi, Hiroshi Oji, Eisuke Ito, Yukio Ouchi, and Hisao Ishii. “Electronic structure of organic/metal interfaces”. In: *Thin Solid Films* 393.1-2 (2001), pp. 298–303. DOI: 10.1016/S0040-6090(01)01094-X.
- [127] P. Dannetun, M. Boman, S. Stafström, W. R. Salaneck, R. Lazzaroni, C. Fredriksson, Jean-Luc Brédas, R. Zamboni, and C. Taliani. “The chemical and electronic structure of the interface between aluminum and polythiophene semiconductors”. In: *The Journal of Chemical Physics* 99.1 (1993), pp. 664–672. DOI: 10.1063/1.466217.
- [128] Gunar M. Kaune, Ezzeldin Metwalli, Robert Meier, Volker Körstgens, Kai Schlage, Sebastien Couet, Ralf Röhlsberger, Stephan V. Roth, and Peter Müller-Buschbaum. “Growth and morphology of sputtered aluminum thin films on P3HT surfaces”. In: *ACS Applied Materials & Interfaces* 3.4 (2011), pp. 1055–1062. DOI: 10.1021/am101195m.
- [129] Simon J. Schaper, Franziska C. Löhner, Senlin Xia, Christina Geiger, Matthias Schwartzkopf, Pallavi Pandit, Jan Rubeck, Björn Fricke, Susann Frenzke, Alexander Martin Hinz, Niko Carstens, Oleksandr Polonskyi, Thomas Strunskus, Franz Faupel, Stephan V. Roth, and Peter Müller-Buschbaum. “Revealing the growth of copper on polystyrene-block-poly(ethylene oxide) diblock copolymer thin films with in situ GISAXS”. In: *Nanoscale* 13.23 (2021), pp. 10555–10565. DOI: 10.1039/D1NR01480C.
- [130] Marc Gensch, Matthias Schwartzkopf, Wiebke Ohm, Calvin J. Brett, Pallavi Pandit, Sarathlal Koyiloth Vayalil, Lorenz Bießmann, Lucas P. Kreuzer, Jonas Drewes, Oleksandr Polonskyi, Thomas Strunskus, Franz Faupel, Andreas Stierle, Peter Müller-Buschbaum, and Stephan V. Roth. “Correlating Nanostructure, Optical and Electronic Properties of Nanogranular Silver Layers during Polymer-Template-Assisted Sputter Deposition”. In: *ACS Applied Materials & Interfaces* 11.32 (2019), pp. 29416–29426. DOI: 10.1021/acami.9b08594.
- [131] Ezzeldin Metwalli, Sebastien Couet, Kai Schlage, R. Röhlsberger, V. Körstgens, Matthias A. Ruderer, W. Wang, Gunar M. Kaune, Stephan V. Roth, and Peter Müller-Buschbaum. “In situ GISAXS investigation of gold sputtering onto a polymer template”. In: *Langmuir* 24.8 (2008), pp. 4265–4272. DOI: 10.1021/la7038587.
- [132] Gunar M. Kaune, Matthias A. Ruderer, Ezzeldin Metwalli, Weinan Wang, Sebastien Couet, Kai Schlage, Ralf Röhlsberger, Stephan V. Roth, and Peter Müller-Buschbaum. “In situ GISAXS study of gold film growth on conducting polymer films”. In: *ACS Applied Materials & Interfaces* 1.2 (2009), pp. 353–360. DOI: 10.1021/am8000727.

- [133] Matthias Schwartzkopf, Gonzalo Santoro, Calvin J. Brett, André Rothkirch, Oleksandr Polonskyi, Alexander Martin Hinz, Ezzeldin Metwalli, Yuan Yao, Thomas Strunskus, Franz Faupel, Peter Müller-Buschbaum, and Stephan V. Roth. “Real-Time Monitoring of Morphology and Optical Properties during Sputter Deposition for Tailoring Metal-Polymer Interfaces”. In: *ACS Applied Materials & Interfaces* 7.24 (2015), p. 13547. DOI: 10.1021/acsami.5b02901.
- [134] Stephan V. Roth, Gonzalo Santoro, Johannes F. H. Risch, Shun Yu, Matthias Schwartzkopf, Torsten Boese, Ralph Döhrmann, Peng Zhang, Bastian Besner, Philipp Bremer, Dieter Rukser, Michael A. Rübhausen, Nick J. Terrill, Paul A. Staniec, Yuan Yao, Ezzeldin Metwalli, and Peter Müller-Buschbaum. “Patterned Diblock Co-Polymer Thin Films as Templates for Advanced Anisotropic Metal Nanostructures”. In: *ACS Applied Materials & Interfaces* 7.23 (2015), pp. 12470–12477. DOI: 10.1021/am507727f.
- [135] Marie-Christine Daniel and Didier Astruc. “Gold nanoparticles: assembly, supramolecular chemistry, quantum-size-related properties, and applications toward biology, catalysis, and nanotechnology”. In: *Chemical Reviews* 104.1 (2004), pp. 293–346. DOI: 10.1021/cr030698.
- [136] Pekka Pyykkö. “Theoretical chemistry of gold”. In: *Angewandte Chemie (International Edition)* 43.34 (2004), pp. 4412–4456. DOI: 10.1002/anie.200300624.
- [137] Yi-Cheun Yeh, Brian Creran, and Vincent M. Rotello. “Gold nanoparticles: preparation, properties, and applications in bionanotechnology”. In: *Nanoscale* 4.6 (2012), pp. 1871–1880. DOI: 10.1039/c1nr11188d.
- [138] G. Bräuer, B. Szyszka, M. Vergöhl, and R. Bandorf. “Magnetron sputtering – Milestones of 30 years”. In: *Vacuum* 84.12 (2010), pp. 1354–1359. DOI: 10.1016/j.vacuum.2009.12.014.
- [139] P. J. Martin. “Ion-based methods for optical thin film deposition”. In: *Journal of Materials Science* 21.1 (1986), pp. 1–25. DOI: 10.1007/BF01144693.
- [140] M. Rühle and H. Gleiter, eds. *Interface Controlled Materials*. Wiley-VCH, 2000. DOI: 10.1002/352760622X.
- [141] John A. Thornton. “Influence of substrate temperature and deposition rate on structure of thick sputtered Cu coatings”. In: *Journal of Vacuum Science and Technology* 12.4 (1975), pp. 830–835. DOI: 10.1116/1.568682.
- [142] Matthias Schwartzkopf, Alexander Martin Hinz, Oleksandr Polonskyi, Thomas Strunskus, Franziska C. Löhner, Volker Körstgens, Peter Müller-Buschbaum, Franz Faupel, and Stephan V. Roth. “Role of Sputter Deposition Rate in Tailoring Nanogranular Gold Structures on Polymer Surfaces”. In: *ACS Applied Materials & Interfaces* 9.6 (2017), pp. 5629–5637. DOI: 10.1021/acsami.6b15172.

- [143] L. Rosenthal, A. Filinov, M. Bonitz, Vladimir Zaporozhchenko, and Franz Faupel. “Diffusion and Growth of Metal Clusters in Nanocomposites: A Kinetic Monte Carlo Study”. In: *Contributions to Plasma Physics* 51.10 (2011), pp. 971–980. DOI: 10.1002/ctpp.201100034.
- [144] R. Weber, I. Grotkopp, J. Stettner, Metin Tolan, and W. Press. “Embedding of Gold Nanoclusters on Polystyrene Surfaces: Influence of the Surface Modification on the Glass Transition”. In: *Macromolecules* 36.24 (2003), pp. 9100–9106. DOI: 10.1021/ma034880o.
- [145] Ernst Bauer. “Phänomenologische Theorie der Kristallabscheidung an Oberflächen. I”. In: *Zeitschrift für Kristallographie* 110.1-6 (1958), pp. 372–394. DOI: 10.1524/zkri.1958.110.1-6.372.
- [146] Matthias Schwartzkopf, Adeline Buffet, Volker Körstgens, Ezzeldin Metwalli, Kai Schlage, Gunthard Benecke, Jan Perlich, Monika Rawolle, André Rothkirch, Berit Heidmann, Gerd Herzog, Peter Müller-Buschbaum, Ralf Röhlberger, Rainer Gehrke, Norbert Striebeck, and Stephan V. Roth. “From atoms to layers: in situ gold cluster growth kinetics during sputter deposition”. In: *Nanoscale* 5.11 (2013), pp. 5053–5062. DOI: 10.1039/c3nr34216f.
- [147] Metin Tolan. *X-Ray Scattering from Soft-Matter Thin Films*. Vol. 148. Springer, 1999. DOI: 10.1007/BFB0112834.
- [148] B. L. Henke, E. M. Gullikson, and J. C. Davis. “X-Ray Interactions: Photoabsorption, Scattering, Transmission, and Reflection at  $E = 50\text{--}30,000$  eV,  $Z = 1\text{--}92$ ”. In: *Atomic Data and Nuclear Data Tables* 54.2 (1993), pp. 181–342. DOI: 10.1006/adnd.1993.1013.
- [149] Jean Daillant and Alain Gibaud, eds. *X-ray and neutron reflectivity. Principles and applications*. 2. ed. Vol. 770. Springer, 2009.
- [150] *Atomic Scattering Factors*. 13.03.2021. URL: [https://henke.lbl.gov/optical\\_constants/asf.html](https://henke.lbl.gov/optical_constants/asf.html) (visited on 07/13/2021).
- [151] Peter Müller-Buschbaum. “Structure Determination in Thin Film Geometry Using Grazing Incidence Small-Angle Scattering”. In: *Polymer Surfaces and Interfaces*, pp. 17–46. DOI: 10.1007/978-3-540-73865-7\_2.
- [152] Gert R. Strobl. *The Physics of Polymers. Concepts for understanding their structures and behavior*. 3rd ed. Springer, 2007. DOI: 10.1007/978-3-540-68411-4.
- [153] Peter Müller-Buschbaum. “The active layer morphology of organic solar cells probed with grazing incidence scattering techniques”. In: *Advanced Materials* 26.46 (2014), pp. 7692–7709. DOI: 10.1002/adma.201304187.
- [154] Y. Yoneda. “Anomalous Surface Reflection of X Rays”. In: *Physical Review* 131.5 (1963), pp. 2010–2013. DOI: 10.1103/PhysRev.131.2010.

- 
- [155] Florin Abelès. “La théorie générale des couches minces”. In: *Journal de Physique et le Radium* 11.7 (1950), pp. 307–309. DOI: 10.1051/jphysrad:01950001107030700.
- [156] L. G. Parratt. “Surface Studies of Solids by Total Reflection of X-Rays”. In: *Physical Review* 95.2 (1954), pp. 359–369. DOI: 10.1103/PhysRev.95.359.
- [157] Oliver S. Heavens. *Optical properties of thin solid films*. Dover Publications, 1991.
- [158] Andrew Nelson. “Co-refinement of multiple-contrast neutron/X-ray reflectivity data using MOTOFIT”. In: *Journal of Applied Crystallography* 39.2 (2006), pp. 273–276. DOI: 10.1107/S0021889806005073.
- [159] L. Névoit and P. Croce. “Caractérisation des surfaces par réflexion rasante de rayons X. Application à l’étude du polissage de quelques verres silicates”. In: *Revue de Physique Appliquée* 15.3 (1980), pp. 761–779. DOI: 10.1051/rphysap:01980001503076100.
- [160] Heinz Kiessig. “Interferenz von Röntgenstrahlen an dünnen Schichten”. In: *Annalen der Physik* 402.7 (1931), pp. 769–788. DOI: 10.1002/andp.19314020702.
- [161] Peter Müller-Buschbaum. “GISAXS and GISANS as metrology technique for understanding the 3D morphology of block copolymer thin films”. In: *European Polymer Journal* 81 (2016). DOI: 10.1016/j.eurpolymj.2016.04.007.
- [162] Rémi Lazzari. “IsGISAXS : a program for grazing-incidence small-angle X-ray scattering analysis of supported islands”. In: *Journal of Applied Crystallography* 35.4 (2002), pp. 406–421. DOI: 10.1107/S0021889802006088.
- [163] O. Glatter and O. Kratky, eds. *Small angle X-ray scattering*. Academic Press, 1982.
- [164] Peter Müller-Buschbaum. “Grazing incidence small-angle X-ray scattering: an advanced scattering technique for the investigation of nanostructured polymer films”. In: *Analytical and Bioanalytical Chemistry* 376.1 (2003), pp. 3–10. DOI: 10.1007/s00216-003-1869-2.
- [165] Detlef-M. Smilgies. “Scherrer grain-size analysis adapted to grazing-incidence scattering with area detectors”. In: *Journal of Applied Crystallography* 42.6 (2009), pp. 1030–1034. DOI: 10.1107/S0021889809040126.
- [166] Jessy L. Baker, Leslie H. Jimison, Stefan C. B. Mannsfeld, Steven Volkman, Shong Yin, Vivek Subramanian, Alberto Salleo, A. Paul Alivisatos, and Michael F. Toney. “Quantification of thin film crystallographic orientation using X-ray diffraction with an area detector”. In: *Langmuir* 26.11 (2010), pp. 9146–9151. DOI: 10.1021/la904840q.

- [167] Dean M. DeLongchamp, R. Joseph Kline, and Andrew A. Herzing. “Nanoscale structure measurements for polymer-fullerene photovoltaics”. In: *Energy & Environmental Science* 5.3 (2012), p. 5980. DOI: 10.1039/C2EE02725A.
- [168] Jonathan Rivnay, Stefan C. B. Mannsfeld, Chad E. Miller, Alberto Salleo, and Michael F. Toney. “Quantitative determination of organic semiconductor microstructure from the molecular to device scale”. In: *Chemical Reviews* 112.10 (2012), pp. 5488–5519. DOI: 10.1021/cr3001109.
- [169] Zhang Jiang. “GIXSGUI : a MATLAB toolbox for grazing-incidence X-ray scattering data visualization and reduction, and indexing of buried three-dimensional periodic nanostructured films”. In: *Journal of Applied Crystallography* 48.3 (2015), pp. 917–926. DOI: 10.1107/S1600576715004434.
- [170] J. R. Levine, J. B. Cohen, Y. W. Chung, and P. Georgopoulos. “Grazing-incidence small-angle X-ray scattering: new tool for studying thin film growth”. In: *Journal of Applied Crystallography* 22.6 (1989), pp. 528–532. DOI: 10.1107/S002188988900717X.
- [171] Peter Müller-Buschbaum, P. Vanhoorne, V. Scheumann, and M. Stamm. “Observation of nano-dewetting structures”. In: *Europhysics Letters (EPL)* 40.6 (1997), pp. 655–660. DOI: 10.1209/ep1/i1997-00519-4.
- [172] George H. Vineyard. “Grazing-incidence diffraction and the distorted-wave approximation for the study of surfaces”. In: *Physical Review B: Condensed Matter and Materials Physics* 26.8 (1982), p. 4146. DOI: 10.1103/PhysRevB.26.4146.
- [173] S. Dietrich and H. Wagner. “Critical surface scattering of x-rays at grazing angles”. In: *Zeitschrift für Physik B Condensed Matter* 56.3 (1984), pp. 207–215. DOI: 10.1007/BF01304174.
- [174] David Babonneau. “FitGISAXS : software package for modelling and analysis of GISAXS data using IGOR Pro”. In: *Journal of Applied Crystallography* 43.4 (2010), pp. 929–936. DOI: 10.1107/S0021889810020352.
- [175] Slim T. Chourou, Abhinav Sarje, Xiaoye S. Li, Elaine R. Chan, and Alexander Hexemer. “HipGISAXS : a high-performance computing code for simulating grazing-incidence X-ray scattering data”. In: *Journal of Applied Crystallography* 46.6 (2013), pp. 1781–1795. DOI: 10.1107/S0021889813025843.
- [176] J. Burle, C. Durniak, J. M. Fisher, M. Ganeva, G. Pospelov, W. van Herck, J. Wuttke, and D. Yurov. *BornAgain - Software for Simulating and Fitting X-Ray and Neutron Small-Angle Scattering at Grazing Incidence*. 2018. URL: <http://www.bornagainproject.org/> (visited on 07/13/2021).
- [177] T. Salditt, T. H. Metzger, J. Peisl, and G. Goerigk. “Non-specular X-ray scattering from thin films and multilayers with small-angle scattering equipment”. In: *Journal of Physics D: Applied Physics* 28.4A (1995), A236–A240. DOI: 10.1088/0022-3727/28/4a/046.

- [178] A. Naudon, D. Babonneau, D. Thiaudière, and S. Lequien. “Grazing-incidence small-angle X-ray scattering applied to the characterization of aggregates in surface regions”. In: *Physica B: Condensed Matter* 283.1-3 (2000), pp. 69–74. DOI: 10.1016/S0921-4526(99)01894-3.
- [179] Sinha, Sirota, Garoff, and Stanley. “X-ray and neutron scattering from rough surfaces”. In: *Physical Review. B, Condensed Matter* 38.4 (1988), pp. 2297–2311. DOI: 10.1103/physrevb.38.2297.
- [180] R. Hosemann, W. Vogel, D. Weick, and F. J. Baltá-Calleja. “Novel aspects of the real paracrystal”. In: *Acta Crystallographica Section A* 37.1 (1981), pp. 85–91. DOI: 10.1107/S0567739481000156.
- [181] Christoph J. Schaffer. “Morphological degradation in polymer-fullerene solar cells”. TU München, Chair for Functional Materials. Doctoral Thesis. 2016.
- [182] Gilles Renaud, Rémi Lazzari, and Frédéric Leroy. “Probing surface and interface morphology with Grazing Incidence Small Angle X-Ray Scattering”. In: *Surface Science Reports* 64.8 (2009), p. 255. DOI: 10.1016/j.surfrep.2009.07.002.
- [183] Bernd Ebenhoch, Stuart A.J. Thomson, Kristijonas Genevičius, Gytis Juška, and Ifor D.W. Samuel. “Charge carrier mobility of the organic photovoltaic materials PTB7 and PC71BM and its influence on device performance”. In: *Organic Electronics* 22 (2015), p. 62. DOI: 10.1016/j.orgel.2015.03.013.
- [184] Yongye Liang, Zheng Xu, Jiangbin Xia, Szu-Ting Tsai, Yue Wu, Gang Li, Claire Ray, and Luping Yu. “For the bright future-bulk heterojunction polymer solar cells with power conversion efficiency of 7.4%”. In: *Advanced Materials* 22.20 (2010), E135–8. DOI: 10.1002/adma.200903528.
- [185] Kedar D. Deshmukh, Shyamal K. K. Prasad, Naresh Chandrasekaran, Amelia C. Y. Liu, Eliot Gann, Lars Thomsen, Dinesh Kabra, Justin M. Hodgkiss, and Christopher R. McNeill. “Critical Role of Pendant Group Substitution on the Performance of Efficient All-Polymer Solar Cells”. In: *Chemistry of Materials* 29.2 (2017), pp. 804–816. DOI: 10.1021/acs.chemmater.6b04791.
- [186] Shaoqing Zhang, Long Ye, Wenchao Zhao, Delong Liu, Huifeng Yao, and Jianhui Hou. “Side Chain Selection for Designing Highly Efficient Photovoltaic Polymers with 2D-Conjugated Structure”. In: *Macromolecules* 47.14 (2014), pp. 4653–4659. DOI: 10.1021/ma500829r.
- [187] Sebastian F. Hoefler, Thomas Rath, Nadiia Pastukhova, Egon Pavlica, Dorothea Scheunemann, Sebastian Wilken, Birgit Kunert, Roland Resel, Mathias Hobisch, Steven Xiao, Gvido Bratina, and Gregor Trimmel. “The effect of polymer molecular weight on the performance of PTB7-Th:O-IDTBR non-fullerene organic solar cells”. In: *Journal of Materials Chemistry A* 6.20 (2018), pp. 9506–9516. DOI: 10.1039/C8TA02467G.

- [188] Jaemin Kong, In-Wook Hwang, and Kwanghee Lee. “Top-down approach for nanophase reconstruction in bulk heterojunction solar cells”. In: *Advanced Materials* 26.36 (2014), pp. 6275–6283. DOI: 10.1002/adma.201402182.
- [189] J. Peet, A. B. Tamayo, X.-D. Dang, J. H. Seo, and T.-Q. Nguyen. “Small molecule sensitizers for near-infrared absorption in polymer bulk heterojunction solar cells”. In: *Applied Physics Letters* 93.16 (2008), p. 163306. DOI: 10.1063/1.3001802.
- [190] Youjun He and Yongfang Li. “Fullerene derivative acceptors for high performance polymer solar cells”. In: *Physical Chemistry Chemical Physics* 13.6 (2011), pp. 1970–1983. DOI: 10.1039/c0cp01178a.
- [191] Paul H. Wöbkenberg, Donal D. C. Bradley, David Kronholm, Jan C. Hummelen, Dago M. de Leeuw, Michael Cölle, and Thomas D. Anthopoulos. “High mobility n-channel organic field-effect transistors based on soluble C60 and C70 fullerene derivatives”. In: *Synthetic Metals* 158.11 (2008), pp. 468–472. DOI: 10.1016/j.synthmet.2008.03.016.
- [192] Sylvia J. Lou, Jodi M. Szarko, Tao Xu, Luping Yu, Tobin J. Marks, and Lin X. Chen. “Effects of additives on the morphology of solution phase aggregates formed by active layer components of high-efficiency organic solar cells”. In: *Journal of the American Chemical Society* 133.51 (2011), pp. 20661–20663. DOI: 10.1021/ja2085564.
- [193] Peter Müller-Buschbaum. “Influence of surface cleaning on dewetting of thin polystyrene films”. In: *The European Physical Journal. E, Soft Matter* 12.3 (2003), pp. 443–448. DOI: 10.1140/epje/e2004-00014-7.
- [194] David B. Hall, Patrick Underhill, and John M. Torkelson. “Spin coating of thin and ultrathin polymer films”. In: *Polymer Engineering & Science* 38.12 (1998), pp. 2039–2045. DOI: 10.1002/pen.10373.
- [195] Dirk W. Schubert and Thomas Dunkel. “Spin coating from a molecular point of view: its concentration regimes, influence of molar mass and distribution”. In: *Materials Research Innovations* 7.5 (2003), pp. 314–321. DOI: 10.1007/s10019-003-0270-2.
- [196] Chang Liu, Chao Yi, Kai Wang, Yali Yang, Ram S. Bhatta, Mesfin Tsige, Shuyong Xiao, and Xiong Gong. “Single-junction polymer solar cells with over 10% efficiency by a novel two-dimensional donor-acceptor conjugated copolymer”. In: *ACS Applied Materials & Interfaces* 7.8 (2015), pp. 4928–4935. DOI: 10.1021/am509047g.
- [197] Qun Wan, Xia Guo, Zaiyu Wang, Wanbin Li, Bing Guo, Wei Ma, Maojie Zhang, and Yongfang Li. “10.8% Efficiency Polymer Solar Cells Based on PTB7-Th and PC 71 BM via Binary Solvent Additives Treatment”. In: *Advanced Functional Materials* 26.36 (2016), pp. 6635–6640. DOI: 10.1002/adfm.201602181.

- [198] Xiaohui Liu, Hai-Qiao Wang, Yaru Li, Zhenzhen Gui, Shuaiqiang Ming, Khurram Usman, Wenjun Zhang, and Junfeng Fang. “Regular Organic Solar Cells with Efficiency over 10% and Promoted Stability by Ligand- and Thermal Annealing-Free Al-Doped ZnO Cathode Interlayer”. In: *Advanced Science* 4.8 (2017), p. 1700053. DOI: 10.1002/advs.201700053.
- [199] Robert Meier. “Novel Structuring Routines for Organic Photovoltaics”. TU München, Chair for Functional Materials. Doctoral Thesis. 2012.
- [200] J. Tauc, R. Grigorovici, and A. Vancu. “Optical Properties and Electronic Structure of Amorphous Germanium”. In: *Physica Status Solidi (b)* 15.2 (1966), pp. 627–637. DOI: 10.1002/pssb.19660150224.
- [201] Nader Ghobadi. “Band gap determination using absorption spectrum fitting procedure”. In: *International Nano Letters* 3.1 (2013). DOI: 10.1186/2228-5326-3-2.
- [202] G03 Committee, ed. *ASTM G173-03(2020), Standard Tables for Reference Solar Spectral Irradiances: Direct Normal and Hemispherical on 37° Tilted Surface*. West Conshohocken, PA: ASTM International. DOI: 10.1520/G0173-03R20. URL: <http://www.astm.org/cgi-bin/resolver.cgi?G173> (visited on 07/15/2021).
- [203] C. A. Gueymard, D. Myers, and Keith Emery. “Proposed reference irradiance spectra for solar energy systems testing”. In: *Solar Energy* 73.6 (2002), pp. 443–467. DOI: 10.1016/S0038-092X(03)00005-7.
- [204] M. D. Abramoff, Paulo J. Magalhães, and Sunanda J. Ram. “Image processing with ImageJ”. In: *Biophotonics International* 11.7 (2004), pp. 36–42.
- [205] Caroline A. Schneider, Wayne S. Rasband, and Kevin W. Eliceiri. “NIH Image to ImageJ: 25 years of image analysis”. In: *Nature Methods* 9.7 (2012), pp. 671–675. DOI: 10.1038/nmeth.2089.
- [206] D. Nečas and P. Klapetek. “Gwyddion: an open-source software for SPM data analysis”. In: *Open Physics* 10.1 (2012). DOI: 10.2478/s11534-011-0096-2.
- [207] Alexandre Dazzi, R. Prazeres, F. Glotin, and J. M. Ortega. “Local infrared microspectroscopy with subwavelength spatial resolution with an atomic force microscope tip used as a photothermal sensor”. In: *Optics Letters* 30.18 (2005), pp. 2388–2390. DOI: 10.1364/ol.30.002388.
- [208] Alexandre Dazzi, Craig B. Prater, Qichi Hu, D. Bruce Chase, John F. Rabolt, and Curtis A. Marcott. “AFM-IR: combining atomic force microscopy and infrared spectroscopy for nanoscale chemical characterization”. In: *Applied Spectroscopy* 66.12 (2012), pp. 1365–1384. DOI: 10.1366/12-06804.
- [209] Alexandre Dazzi and Craig B. Prater. “AFM-IR: Technology and Applications in Nanoscale Infrared Spectroscopy and Chemical Imaging”. In: *Chemical Reviews* 117.7 (2017), pp. 5146–5173. DOI: 10.1021/acs.chemrev.6b00448.

- [210] Feng Lu and Mikhail A. Belkin. “Infrared absorption nano-spectroscopy using sample photoexpansion induced by tunable quantum cascade lasers”. In: *Optics Express* 19.21 (2011), pp. 19942–19947. DOI: 10.1364/OE.19.019942.
- [211] Feng Lu, Mingzhou Jin, and Mikhail A. Belkin. “Tip-enhanced infrared nanospectroscopy via molecular expansion force detection”. In: *Nature Photonics* 8.4 (2014), pp. 307–312. DOI: 10.1038/nphoton.2013.373.
- [212] Andrea Centrone. “Infrared Imaging and Spectroscopy Beyond the Diffraction Limit”. In: *Annual Review of Analytical Chemistry* 8 (2015), pp. 101–126. DOI: 10.1146/annurev-anchem-071114-040435.
- [213] Anirban Roy, Qichi Hu, Debra Cook, Eoghan Dillon, and Kevin Kjoller. “Latest Advancements in Nanoscale IR Spectroscopy for Characterization and Failure Analysis of Electronic Devices”. In: *Photonics for Solar Energy Systems II*, pp. 610–612. DOI: 10.31399/asm.cp.istfa2017p0610.
- [214] Adeline Buffet, André Rothkirch, Ralph Döhrmann, Volker Körstgens, Mottakin M. Abul Kashem, Jan Perlich, Gerd Herzog, Matthias Schwartzkopf, Rainer Gehrke, Peter Müller-Buschbaum, and Stephan V. Roth. “P03, the microfocus and nanofocus X-ray scattering (MiNaXS) beamline of the PETRA III storage ring: the microfocus endstation”. In: *Journal of Synchrotron Radiation* 19.4 (2012), pp. 647–653. DOI: 10.1107/S0909049512016895.
- [215] Gunthard Benecke, Wolfgang Wagermaier, Chenghao Li, Matthias Schwartzkopf, Gero Flucke, Rebecca Hoerth, Ivo Zizak, Manfred Burghammer, Ezzeldin Metwalli, Peter Müller-Buschbaum, Martin Trebbin, Stephan Förster, Oskar Paris, Stephan V. Roth, and Peter Fratzl. “A customizable software for fast reduction and analysis of large X-ray scattering data sets: applications of the new DPDAK package to small-angle X-ray scattering and grazing-incidence small-angle X-ray scattering”. In: *Journal of Applied Crystallography* 47.5 (2014), pp. 1797–1803. DOI: 10.1107/S1600576714019773.
- [216] Fan Zhang, Jan Ilavsky, Gabrielle G. Long, John P. G. Quintana, Andrew J. Allen, and Pete R. Jemian. “Glassy Carbon as an Absolute Intensity Calibration Standard for Small-Angle Scattering”. In: *Metallurgical and Materials Transactions A* 41.5 (2010), pp. 1151–1158. DOI: 10.1007/s11661-009-9950-x.
- [217] Jan Ilavsky. “Nika : software for two-dimensional data reduction”. In: *Journal of Applied Crystallography* 45.2 (2012), pp. 324–328. DOI: 10.1107/S0021889812004037.
- [218] Franziska C. Löhner, Volker Körstgens, Gabriele Semino, Matthias Schwartzkopf, Alexander Martin Hinz, Oleksandr Polonskyi, Thomas Strunskus, Franz Faupel, Stephan V. Roth, and Peter Müller-Buschbaum. “Following in Situ the Deposition of Gold Electrodes on Low Band Gap Polymer Films”.

- In: *ACS Applied Materials & Interfaces* 12.1 (2020), pp. 1132–1141. DOI: 10.1021/acsmi.9b17590.
- [219] Zhicai He, Chengmei Zhong, Shijian Su, Miao Xu, Hongbin Wu, and Yong Cao. “Enhanced power-conversion efficiency in polymer solar cells using an inverted device structure”. In: *Nature Photonics* 6.9 (2012), pp. 591–595. DOI: 10.1038/nphoton.2012.190.
- [220] Sih-Hao Liao, Hong-Jyun Jhuo, Yu-Shan Cheng, and Show-An Chen. “Fullerene derivative-doped zinc oxide nanofilm as the cathode of inverted polymer solar cells with low-bandgap polymer (PTB7-Th) for high performance”. In: *Advanced Materials* 25.34 (2013), pp. 4766–4771. DOI: 10.1002/adma.201301476.
- [221] Luyao Lu and Luping Yu. “Understanding low bandgap polymer PTB7 and optimizing polymer solar cells based on it”. In: *Advanced Materials* 26.26 (2014), pp. 4413–4430. DOI: 10.1002/adma.201400384.
- [222] Jungheum Yun. “Ultrathin Metal films for Transparent Electrodes of Flexible Optoelectronic Devices”. In: *Advanced Functional Materials* 27.18 (2017), p. 1606641. DOI: 10.1002/adfm.201606641.
- [223] Guiying Xu, Liang Shen, Chaohua Cui, Shanpeng Wen, Rongming Xue, Weijie Chen, Haiyang Chen, Jingwen Zhang, Hongkun Li, Yaowen Li, and Yongfang Li. “High-Performance Colorful Semitransparent Polymer Solar Cells with Ultrathin Hybrid-Metal Electrodes and Fine-Tuned Dielectric Mirrors”. In: *Advanced Functional Materials* 27.15 (2017), p. 1605908. DOI: 10.1002/adfm.201605908.
- [224] Harry A. Atwater and Albert Polman. “Plasmonics for improved photovoltaic devices”. In: *Nature Materials* 9.3 (2010), pp. 205–213. DOI: 10.1038/nmat2629.
- [225] Emmanuel Stratakis and Emmanuel Kymakis. “Nanoparticle-based plasmonic organic photovoltaic devices”. In: *Materials Today* 16.4 (2013), pp. 133–146. DOI: 10.1016/j.mattod.2013.04.006.
- [226] Lin Feng, Mengsi Niu, Zhenchuan Wen, and Xiaotao Hao. “Recent Advances of Plasmonic Organic Solar Cells: Photophysical Investigations”. In: *Polymers* 10.2 (2018), p. 123. DOI: 10.3390/polym10020123.
- [227] Bärbel Krause, Susan Darma, Marthe Kaufholz, Hans Hellmuth Gräfe, Sven Ulrich, Miguel Mantilla, Ralf Weigel, Steffen Rembold, and Tilo Baumbach. “Modular deposition chamber for in situ X-ray experiments during RF and DC magnetron sputtering”. In: *Journal of Synchrotron Radiation* 19.2 (2012), pp. 216–222. DOI: 10.1107/S0909049511052320.
- [228] Fatima Bencheikh, David Duché, Carmen M. Ruiz, Jean-Jacques Simon, and Ludovic Escoubas. “Study of Optical Properties and Molecular Aggregation of Conjugated Low Band Gap Copolymers: PTB7 and PTB7-Th”. In: *The Journal of Physical Chemistry C* 119.43 (2015), pp. 24643–24648. DOI: 10.1021/acs.jpcc.5b07803.

- [229] Jia Sun, Zhuohan Zhang, Xinxing Yin, Jie Zhou, Linqiang Yang, Renyong Geng, Fujun Zhang, Rihong Zhu, Jiangsheng Yu, and Weihua Tang. “High performance non-fullerene polymer solar cells based on PTB7-Th as the electron donor with 10.42% efficiency”. In: *Journal of Materials Chemistry A* 6.6 (2018), pp. 2549–2554. DOI: 10.1039/C7TA10391C.
- [230] Lethy K. Jagadamma, Muhammad T. Sajjad, Victoria Savikhin, Michael F. Toney, and Ifor D. W. Samuel. “Correlating photovoltaic properties of a PTB7-Th:PC 71 BM blend to photophysics and microstructure as a function of thermal annealing”. In: *Journal of Materials Chemistry A* 5.28 (2017), pp. 14646–14657. DOI: 10.1039/C7TA03144K.
- [231] Feng Liu, Wei Zhao, John R. Tumbleston, Cheng Wang, Yu Gu, Dong Wang, Alejandro L. Briseno, Harald Ade, and Thomas P. Russell. “Understanding the Morphology of PTB7:PCBM Blends in Organic Photovoltaics”. In: *Advanced Energy Materials* 4.5 (2014), p. 1301377. DOI: 10.1002/aenm.201301377.
- [232] Xueping Yi, Bhoj Gautam, Iordania Constantinou, Yuanhang Cheng, Zhengxing Peng, Erik Klump, Xiaochu Ba, Carr Hoi Yi Ho, Chen Dong, Seth R. Marder, John R. Reynolds, Sai-Wing Tsang, Harald Ade, and Franky So. “Impact of Nonfullerene Molecular Architecture on Charge Generation, Transport, and Morphology in PTB7-Th-Based Organic Solar Cells”. In: *Advanced Functional Materials* 28.32 (2018), p. 1802702. DOI: 10.1002/adfm.201802702.
- [233] Johannes V. Barth, Giovanni Costantini, and Klaus Kern. “Engineering atomic and molecular nanostructures at surfaces”. In: *Nanoscience and Technology*, pp. 67–75. DOI: 10.1142/9789814287005\_0008.
- [234] J. Zemann. “Crystal structures, 2 nd edition. Vol. 1 by R. W. G. Wyckoff”. In: *Acta Crystallographica* 18.1 (1965), p. 139. DOI: 10.1107/S0365110X65000361.
- [235] Matthias Schwartzkopf and Stephan V. Roth. “Investigating Polymer-Metal Interfaces by Grazing Incidence Small-Angle X-Ray Scattering from Gradients to Real-Time Studies”. In: *Nanomaterials* 6.12 (2016). DOI: 10.3390/nano6120239.
- [236] D. Babonneau, S. Camelio, D. Lantiat, L. Simonot, and A. Michel. “Waveguiding and correlated roughness effects in layered nanocomposite thin films studied by grazing-incidence small-angle x-ray scattering”. In: *Physical Review B: Condensed Matter and Materials Physics* 80.15 (2009), p. 596. DOI: 10.1103/PhysRevB.80.155446.
- [237] George Amarandei, Colm O’Dwyer, Arousian Arshak, and David Corcoran. “The stability of thin polymer films as controlled by changes in uniformly sputtered gold”. In: *Soft Matter* 9.9 (2013), p. 2695. DOI: 10.1039/c3sm27130g.

- [238] R. Hosemann and S. N. Bagchi. “The interference theory of ideal paracrystals”. In: *Acta Crystallographica* 5.5 (1952), pp. 612–614. DOI: 10.1107/S0365110X52001702.
- [239] Gabriele Semino. “Analysis of GISAXS Data of Gold Nanostructures on a Polymer Film”. TU München, Chair for Functional Materials. Bachelor Thesis. 2016.
- [240] Jitesh Hora, Bastian Stoehr, Emmanuel Lepleux, Louis Pacheco, Peter J. Murphy, Drew R. Evans, and Eric Charrault. “Chemically Heterogeneous Nanowrinkling of Polymer Surfaces Induced by Low-Energy Cluster Implantation”. In: *The Journal of Physical Chemistry C* 123.21 (2019), pp. 13330–13336. DOI: 10.1021/acs.jpcc.9b02702.
- [241] F. S. Teixeira, W. W. R. Araújo, and M. C. Salvadori. “Spontaneous wrinkling of soft matter by energetic deposition of Cr and Au”. In: *Journal of Applied Physics* 119.14 (2016), p. 145305. DOI: 10.1063/1.4946036.
- [242] Michael Kiene, Thomas Strunskus, Ralf Peter, and Franz Faupel. “Evidence of Aggregation-Induced Copper Immobilization During Polyimide Metallization”. In: *Advanced Materials* 10.16 (1998), pp. 1357–1360. DOI: 10.1002/(SICI)1521-4095(199811)10:16<1357::AID-ADMA1357>3.0.CO;2-9.
- [243] G. Jeffers, M. A. Dubson, and P. M. Duxbury. “Island-to-percolation transition during growth of metal films”. In: *Journal of Applied Physics* 75.10 (1994), pp. 5016–5020. DOI: 10.1063/1.355742.
- [244] Francesco Ruffino, V. Torrisi, G. Marletta, and M. G. Grimaldi. “Growth morphology of nanoscale sputter-deposited Au films on amorphous soft polymeric substrates”. In: *Applied Physics A* 103.4 (2011), pp. 939–949. DOI: 10.1007/s00339-011-6413-1.
- [245] Hannu Häkkinen. “The gold-sulfur interface at the nanoscale”. In: *Nature Chemistry* 4.6 (2012), pp. 443–455. DOI: 10.1038/nchem.1352.
- [246] J. Christopher Love, Lara A. Estroff, Jennah K. Kriebel, Ralph G. Nuzzo, and George M. Whitesides. “Self-assembled monolayers of thiolates on metals as a form of nanotechnology”. In: *Chemical Reviews* 105.4 (2005), pp. 1103–1169. DOI: 10.1021/cr0300789.
- [247] Evangelina Pensa, Emiliano Cortés, Gastón Corthey, Pilar Carro, Carolina Vericat, Mariano H. Fonticelli, Guillermo Benítez, Aldo A. Rubert, and Roberto C. Salvarezza. “The chemistry of the sulfur-gold interface: in search of a unified model”. In: *Accounts of Chemical Research* 45.8 (2012), pp. 1183–1192. DOI: 10.1021/ar200260p.
- [248] Abraham Ulman. “Surface Absorption of Monolayers”. In: *MRS Bulletin* 20.6 (1995), pp. 46–51. DOI: 10.1557/S0883769400036976.

- [249] Cecilia M. Björström, Svante Nilsson, Andrzej Bernasik, Andrzej Budkowski, Mats R. Andersson, Kjell O. Magnusson, and Ellen Moons. “Vertical phase separation in spin-coated films of a low bandgap polyfluorene/PCBM blend—Effects of specific substrate interaction”. In: *Applied Surface Science* 253.8 (2007), pp. 3906–3912. DOI: 10.1016/j.apsusc.2006.08.024.
- [250] Toshihiko Matsuura, Masayoshi Nakajima, and Yuhei Shimoyama. “Growth of Self-Assembled Monolayer of Thiophene on Gold Surface: An Infrared Spectroscopic Study”. In: *Japanese Journal of Applied Physics* 40.1,12 (2001), pp. 6945–6950. DOI: 10.1143/JJAP.40.6945.
- [251] L. Britnell, R. M. Ribeiro, A. Eckmann, R. Jalil, B. D. Belle, A. Mishchenko, Y.-J. Kim, R. V. Gorbachev, T. Georgiou, S. V. Morozov, A. N. Grigorenko, A. K. Geim, C. Casiraghi, A. H. Castro Neto, and K. S. Novoselov. “Strong light-matter interactions in heterostructures of atomically thin films”. In: *Science* 340.6138 (2013), pp. 1311–1314. DOI: 10.1126/science.1235547.
- [252] Xiaohong Chen, Chunchang Zhao, Lewis Rothberg, and Man-Kit Ng. “Plasmon enhancement of bulk heterojunction organic photovoltaic devices by electrode modification”. In: *Applied Physics Letters* 93.12 (2008), p. 123302. DOI: 10.1063/1.2988190.
- [253] George Kakavelakis, Ioannis Vangelidis, Amelie Heuer-Jungemann, Antonios G. Kanaras, Elefterios Lidorikis, Emmanuel Stratakis, and Emmanuel Kymakis. “Plasmonic Backscattering Effect in High-Efficient Organic Photovoltaic Devices”. In: *Advanced Energy Materials* 6.2 (2016), p. 1501640. DOI: 10.1002/aenm.201501640.
- [254] Mengnan Yao, Ping Shen, Yan Liu, Boyuan Chen, Wenbin Guo, Shengping Ruan, and Liang Shen. “Performance Improvement of Polymer Solar Cells by Surface-Energy-Induced Dual Plasmon Resonance”. In: *ACS Applied Materials & Interfaces* 8.9 (2016), pp. 6183–6189. DOI: 10.1021/acsami.6b00297.
- [255] J. Peet, J. Y. Kim, N. E. Coates, W. L. Ma, Daniel Moses, Alan J. Heeger, and Guillermo C. Bazan. “Efficiency enhancement in low-bandgap polymer solar cells by processing with alkane dithiols”. In: *Nature Materials* 6.7 (2007), pp. 497–500. DOI: 10.1038/nmat1928.
- [256] Matthias A. Ruderer, Shuai Guo, Robert Meier, Hsin-Yin Chiang, Volker Körstgens, Johannes Wiedersich, Jan Perlich, Stephan V. Roth, and Peter Müller-Buschbaum. “Solvent-Induced Morphology in Polymer-Based Systems for Organic Photovoltaics”. In: *Advanced Functional Materials* 21.17 (2011), pp. 3382–3391. DOI: 10.1002/adfm.201100945.

- [257] Christoph J. Schaffer, Johannes Schlipf, Efi Dwi Indari, Bo Su, Sigrid Bernstorff, and Peter Müller-Buschbaum. “Effect of Blend Composition and Additives on the Morphology of PCPDTBT:PC71BM Thin Films for Organic Photovoltaics”. In: *ACS Applied Materials & Interfaces* 7.38 (2015), pp. 21347–21355. DOI: 10.1021/acsami.5b05939.
- [258] Weijia Wang, Lin Song, David Magerl, Daniel Moseguí González, Volker Körstgens, Martine Philipp, Jean-François Moulin, and Peter Müller-Buschbaum. “Influence of Solvent Additive 1,8-Octanedithiol on P3HT:PCBM Solar Cells”. In: *Advanced Functional Materials* 28.20 (2018), p. 1800209. DOI: 10.1002/adfm.201800209.
- [259] Jae Kwan Lee, Wan Li Ma, Christoph J. Brabec, Jonathan Yuen, Ji Sun Moon, Jin Young Kim, Kwanghee Lee, Guillermo C. Bazan, and Alan J. Heeger. “Processing additives for improved efficiency from bulk heterojunction solar cells”. In: *Journal of the American Chemical Society* 130.11 (2008), pp. 3619–3623. DOI: 10.1021/ja710079w.
- [260] Gabriel Bernardo, Hugo Gaspar, Gabriel E. Pérez, Alec S.D. Shackelford, Andrew J. Parnell, Markus Bleuel, Adélio Mendes, Stephen M. King, and Steven R. Parnell. “Impact of 1,8-diiodooctane on the morphology of organic photovoltaic (OPV) devices – A Small Angle Neutron Scattering (SANS) study”. In: *Polymer Testing* 82 (2020), p. 106305. DOI: 10.1016/j.polymertesting.2019.106305.
- [261] Shuai Guo, Weijia Wang, Eva M. Herzig, Anna Naumann, Gregory Tainter, Jan Perlich, and Peter Müller-Buschbaum. “Solvent-Morphology-Property Relationship of PTB7:PC71BM Polymer Solar Cells”. In: *ACS Applied Materials & Interfaces* 9.4 (2017), pp. 3740–3748. DOI: 10.1021/acsami.6b14926.
- [262] Ling Zhao, Suling Zhao, Zheng Xu, Bo Qiao, Di Huang, and Xurong Xu. “Two effects of 1,8-diiodooctane on PTB7-Th:PC71BM polymer solar cells”. In: *Organic Electronics* 34 (2016), pp. 188–192. DOI: 10.1016/j.orgel.2016.04.014.
- [263] F. L. Araújo, D. R. B. Amorim, B.B.M Torres, D. J. Coutinho, and R. M. Faria. “Effects of additive-solvents on the mobility and recombination of a solar cell based on PTB7-Th:PC71BM”. In: *Solar Energy* 177 (2019), pp. 284–292. DOI: 10.1016/j.solener.2018.11.027.
- [264] Di Huang, Yang Li, Zheng Xu, Suling Zhao, Ling Zhao, and Jiao Zhao. “Enhanced performance and morphological evolution of PTB7:PC71BM polymer solar cells by using solvent mixtures with different additives”. In: *Physical Chemistry Chemical Physics* 17.12 (2015), pp. 8053–8060. DOI: 10.1039/c4cp05826g.

- [265] Lin Song, Weijia Wang, Edoardo Barabino, Dan Yang, Volker Körstgens, Peng Zhang, Stephan V. Roth, and Peter Müller-Buschbaum. “Composition-Morphology Correlation in PTB7-Th/PC71BM Blend Films for Organic Solar Cells”. In: *ACS Applied Materials & Interfaces* 11.3 (2019), pp. 3125–3135. DOI: 10.1021/acsami.8b20316.
- [266] Jianfeng Li, Yufei Wang, Zezhou Liang, Ningning Wang, Junfeng Tong, Chunming Yang, Xichang Bao, and Yangjun Xia. “Enhanced Organic Photovoltaic Performance through Modulating Vertical Composition Distribution and Promoting Crystallinity of the Photoactive Layer by Diphenyl Sulfide Additives”. In: *ACS Applied Materials & Interfaces* 11.7 (2019), pp. 7022–7029. DOI: 10.1021/acsami.8b20466.
- [267] Neelima Paul, Ezzeldin Metwalli, Yuan Yao, Matthias Schwartzkopf, Shun Yu, Stephan V. Roth, Peter Müller-Buschbaum, and Amitesh Paul. “Templating growth of gold nanostructures with a CdSe quantum dot array”. In: *Nanoscale* 7.21 (2015), pp. 9703–9714. DOI: 10.1039/c5nr01121c.
- [268] Wei Chen, Suzhe Liang, Franziska C. Löhner, Simon J. Schaper, Nian Li, Wei Cao, Lucas P. Kreuzer, Haochen Liu, Haodong Tang, Volker Körstgens, Matthias Schwartzkopf, Kai Wang, Xiao Wei Sun, Stephan V. Roth, and Peter Müller-Buschbaum. “In situ Grazing-Incidence Small-Angle X-ray Scattering Observation of Gold Sputter Deposition on a PbS Quantum Dot Solid”. In: *ACS Applied Materials & Interfaces* 12.41 (2020), pp. 46942–46952. DOI: 10.1021/acsami.0c12732.
- [269] Adrian Haussmann. “Gold cluster growth kinetics at the metal-polymer interface of water-processed hybrid solar cells studied by in situ GISAXS sputter deposition”. TU München, Chair for Functional Materials. Master Thesis. 2017.
- [270] Lin Song, Martin A. Niedermeier, Volker Körstgens, Franziska C. Löhner, Yonghua Chen, Stephan V. Roth, and Peter Müller-Buschbaum. “In Situ Study of Sputtering Nanometer-Thick Gold Films onto 100-nm-Thick Spiro-OMeTAD Films: Implications for Perovskite Solar Cells”. In: *ACS Applied Nano Materials* 3.6 (2020), pp. 5987–5994. DOI: 10.1021/acsanm.0c01147.
- [271] Matthias Schwartzkopf, Sven-Jannik Wöhnert, Vivian Waclawek, Niko Carstens, André Rothkirch, Jan Rubeck, Marc Gensch, Jonas Drewes, Oleksandr Polonskyi, Thomas Strunskus, Alexander Martin Hinz, Simon J. Schaper, Volker Körstgens, Peter Müller-Buschbaum, Franz Faupel, and Stephan V. Roth. “Real-time insight into nanostructure evolution during the rapid formation of ultra-thin gold layers on polymers”. In: *Nanoscale Horizons* 6.2 (2021), pp. 132–138. DOI: 10.1039/d0nh00538j.

- [272] Franziska C. Löhner, Christoph Senfter, Christoph J. Schaffer, Johannes Schlipf, Daniel Moseguí González, Peng Zhang, Stephan V. Roth, and Peter Müller-Buschbaum. “Light-Induced and Oxygen-Mediated Degradation Processes in Photoactive Layers Based on PTB7-Th”. In: *Advanced Photonics Research* 1.1 (2020), p. 2000047. DOI: 10.1002/adpr.202000047.
- [273] Huiqiong Zhou, Yuan Zhang, Cheng-Kang Mai, Samuel D. Collins, Guillermo C. Bazan, Thuc-Quyen Nguyen, and Alan J. Heeger. “Polymer homo-tandem solar cells with best efficiency of 11.3%”. In: *Advanced Materials* 27.10 (2015), pp. 1767–1773. DOI: 10.1002/adma.201404220.
- [274] Shaoqing Zhang, Long Ye, and Jianhui Hou. “Breaking the 10% Efficiency Barrier in Organic Photovoltaics: Morphology and Device Optimization of Well-Known PBDTTT Polymers”. In: *Advanced Energy Materials* 6.11 (2016), p. 1502529. DOI: 10.1002/aenm.201502529.
- [275] Sarah Holliday, Yilin Li, and Christine K. Luscombe. “Recent advances in high performance donor-acceptor polymers for organic photovoltaics”. In: *Progress in Polymer Science* 70 (2017), pp. 34–51. DOI: 10.1016/j.progpolymsci.2017.03.003.
- [276] Samy Almosni, Amaury Delamarre, Zacharie Jehl, Daniel Suchet, Ludmila Cojocar, Maxime Giteau, Benoit Behaghel, Anatole Julian, Camille Ibrahim, Léa Tetry, Haibin Wang, Takaya Kubo, Satoshi Uchida, Hiroshi Segawa, Naoya Miyashita, Ryo Tamaki, Yasushi Shoji, Katsuhisa Yoshida, Nazmul Ahsan, Kentaro Watanabe, Tomoyuki Inoue, Masakazu Sugiyama, Yoshiaki Nakano, Tomofumi Hamamura, Thierry Toupance, Céline Olivier, Sylvain Chambon, Laurence Vignau, Camille Geffroy, Eric Cloutet, Georges Hadziioannou, Nicolas Cavasillas, Pierre Rale, Andrea Cattoni, Stéphane Collin, François Gibelli, Myriam Paire, Laurent Lombez, Damien Aureau, Muriel Bouttemy, Arnaud Etcheberry, Yoshitaka Okada, and Jean-François Guillemoles. “Material challenges for solar cells in the twenty-first century: directions in emerging technologies”. In: *Science and Technology of Advanced Materials* 19.1 (2018), pp. 336–369. DOI: 10.1080/14686996.2018.1433439.
- [277] Jing-De Chen, Chaohua Cui, Yan-Qing Li, Lei Zhou, Qing-Dong Ou, Chi Li, Yongfang Li, and Jian-Xin Tang. “Single-junction polymer solar cells exceeding 10% power conversion efficiency”. In: *Advanced Materials* 27.6 (2015), pp. 1035–1041. DOI: 10.1002/adma.201404535.
- [278] Wenchao Huang, Eliot Gann, Lars Thomsen, Cunku Dong, Yi-Bing Cheng, and Christopher R. McNeill. “Unraveling the Morphology of High Efficiency Polymer Solar Cells Based on the Donor Polymer PBDTTT-EFT”. In: *Advanced Energy Materials* 5.7 (2015), p. 1401259. DOI: 10.1002/aenm.201401259.

- [279] Yuanpeng Xie, Xiaotian Hu, Jingping Yin, Lin Zhang, Xiangchuan Meng, Guodong Xu, Qingyun Ai, Weihua Zhou, and Yiwang Chen. “Butanedithiol Solvent Additive Extracting Fullerenes from Donor Phase To Improve Performance and Photostability in Polymer Solar Cells”. In: *ACS Applied Materials & Interfaces* 9.11 (2017), pp. 9918–9925. DOI: 10.1021/acsami.6b16538.
- [280] Quan Liu, Johann Toudert, Feng Liu, Paola Mantilla–Perez, Miguel Montes Bajo, Thomas P. Russell, and Jordi Martorell. “Circumventing UV Light Induced Nanomorphology Disorder to Achieve Long Lifetime PTB7–Th:PCBM Based Solar Cells”. In: *Advanced Energy Materials* 7.21 (2017), p. 1701201. DOI: 10.1002/aenm.201701201.
- [281] Leiping Duan, Haimang Yi, Yu Zhang, Faiazul Haque, Cheng Xu, and Ashraf Uddin. “Comparative study of light- and thermal-induced degradation for both fullerene and non-fullerene-based organic solar cells”. In: *Sustainable Energy & Fuels* 3.3 (2019), pp. 723–735. DOI: 10.1039/C8SE00567B.
- [282] Lennart K. Reb, Michael Böhmer, Benjamin Predeschly, Sebastian Grott, Christian L. Weindl, Goran I. Ivandekic, Renjun Guo, Christoph Dreißigacker, Roman Gernhäuser, Andreas Meyer, and Peter Müller-Buschbaum. “Perovskite and Organic Solar Cells on a Rocket Flight”. In: *Joule* 4.9 (2020), pp. 1880–1892. DOI: 10.1016/j.joule.2020.07.004.
- [283] Julian B. Fischer. “In-situ degradation of thin films for organic photovoltaics”. TU München, Chair for Functional Materials. Bachelor Thesis. 2015.
- [284] Christoph Senfter. “Degradation Analysis of Low-Bandgap Organic Solar Cells”. TU München, Chair for Functional Materials. Master Thesis. 2016.
- [285] Souvik Kundu, Sankara Rao Gollu, Ramakant Sharma, Srinivas G, Adersh Ashok, A. R. Kulkarni, and D. Gupta. “Device stability of inverted and conventional bulk heterojunction solar cells with MoO<sub>3</sub> and ZnO nanoparticles as charge transport layers”. In: *Organic Electronics* 14.11 (2013), pp. 3083–3088. DOI: 10.1016/j.orgel.2013.07.016.
- [286] Shuai Guo, Matthias A. Ruderer, Monika Rawolle, Volker Körstgens, Christopher Birkenstock, Jan Perlich, and Peter Müller-Buschbaum. “Evolution of lateral structures during the functional stack build-up of P3HT:PCBM-based bulk heterojunction solar cells”. In: *ACS Applied Materials & Interfaces* 5.17 (2013), pp. 8581–8590. DOI: 10.1021/am402045p.
- [287] Weijia Wang, Stephan Pröller, Martin A. Niedermeier, Volker Körstgens, Martine Philipp, Bo Su, Daniel Moseguí González, Shun Yu, Stephan V. Roth, and Peter Müller-Buschbaum. “Development of the morphology during functional stack build-up of P3HT:PCBM bulk heterojunction solar cells with inverted geometry”. In: *ACS Applied Materials & Interfaces* 7.1 (2015), pp. 602–610. DOI: 10.1021/am5067749.

- [288] V. Holý and Tilo Baumbach. “Nonspecular x-ray reflection from rough multilayers”. In: *Physical Review B: Condensed Matter and Materials Physics* 49.15 (1994), pp. 10668–10676. DOI: 10.1103/physrevb.49.10668.
- [289] Thomas Tromholt, Morten V. Madsen, Jon E. Carlé, Martin Helgesen, and Frederik C. Krebs. “Photochemical stability of conjugated polymers, electron acceptors and blends for polymer solar cells resolved in terms of film thickness and absorbance”. In: *Journal of Materials Chemistry* 22.15 (2012), p. 7592. DOI: 10.1039/c2jm16340c.
- [290] Jing Guo, Yao Wu, Rui Sun, Wei Wang, Jie Guo, Qiang Wu, Xiaofeng Tang, Chenkai Sun, Zhenghui Luo, Kai Chang, Zhuohan Zhang, Jun Yuan, Tengfei Li, Weihua Tang, Erjun Zhou, Zuo Xiao, Liming Ding, Yingping Zou, Xiaowei Zhan, Chuluo Yang, Zhen Li, Christoph J. Brabec, Yongfang Li, and Jie Min. “Suppressing photo-oxidation of non-fullerene acceptors and their blends in organic solar cells by exploring material design and employing friendly stabilizers”. In: *Journal of Materials Chemistry A* 7.43 (2019), pp. 25088–25101. DOI: 10.1039/C9TA09961A.
- [291] Sylvain Chambon, Agnès Rivaton, Jean-Luc Gardette, and Muriel Firon. “Durability of MDMO-PPV and MDMO-PPV:PCBM blends under illumination in the absence of oxygen”. In: *Solar Energy Materials and Solar Cells* 92.7 (2008), pp. 785–792. DOI: 10.1016/j.solmat.2007.12.003.
- [292] Ying W. Soon, Hoduk Cho, Jonathan Low, Hugo Bronstein, Iain McCulloch, and James R. Durrant. “Correlating triplet yield, singlet oxygen generation and photochemical stability in polymer/fullerene blend films”. In: *Chemical Communications* 49.13 (2013), pp. 1291–1293. DOI: 10.1039/c2cc38243a.
- [293] Sylvain Chambon, Agnès Rivaton, Jean-Luc Gardette, and Muriel Firon. “Photo- and thermal degradation of MDMO-PPV:PCBM blends”. In: *Solar Energy Materials and Solar Cells* 91.5 (2007), pp. 394–398. DOI: 10.1016/j.solmat.2006.10.015.
- [294] Matthew O. Reese, Alexandre M. Nardes, Benjamin L. Rupert, Ross E. Larsen, Dana C. Olson, Matthew T. Lloyd, Sean E. Shaheen, David S. Ginley, Garry Rumbles, and Nikos Kopidakis. “Photoinduced Degradation of Polymer and Polymer-Fullerene Active Layers: Experiment and Theory”. In: *Advanced Functional Materials* 20.20 (2010), pp. 3476–3483. DOI: 10.1002/adfm.201001079.
- [295] Andreas Distler, Peter Kutka, Tobias Sauermann, Hans-Joachim Egelhaaf, Dirk M. Guldi, Daniele Di Nuzzo, Stefan C. J. Meskers, and René A. J. Janssen. “Effect of PCBM on the Photodegradation Kinetics of Polymers for Organic Photovoltaics”. In: *Chemistry of Materials* 24.22 (2012), pp. 4397–4405. DOI: 10.1021/cm302623p.

- [296] Saqib Rafique, Shahino M. Abdullah, Nafiseh Badiei, James McGettrick, Khue Tian Lai, Nur Adilah Roslan, Harrison Ka Hin Lee, Wing Chung Tsoi, and Lijie Li. “An insight into the air stability of the benchmark polymer:fullerene photovoltaic films and devices: A comparative study”. In: *Organic Electronics* 76 (2020), p. 105456. DOI: 10.1016/j.orgel.2019.105456.
- [297] Daimay Lin-Vien, Norman B. Colthup, William G. Fateley, and Jeanette G. Grasselli. *The Handbook of Infrared and Raman Characteristic Frequencies of Organic Molecules*. Academic Press, 1991.
- [298] Satvik Shah, Rana Biswas, Thomas Koschny, and Vikram Dalal. “Unusual infrared absorption increases in photo-degraded organic films”. In: *Nanoscale* 9.25 (2017), pp. 8665–8673. DOI: 10.1039/c7nr01132f.
- [299] Victoria Savikhin, Lethy K. Jagadamma, Lafe J. Purvis, Iain Robertson, Stefan D. Oosterhout, Christopher J. Douglas, Ifor D. W. Samuel, and Michael F. Toney. “Morphological, Chemical, and Electronic Changes of the Conjugated Polymer PTB7 with Thermal Annealing”. In: *iScience* 2 (2018), pp. 182–192. DOI: 10.1016/j.isci.2018.03.002.
- [300] Fuguang Tang, Peite Bao, and Zhaohui Su. “Analysis of Nanodomain Composition in High-Impact Polypropylene by Atomic Force Microscopy-Infrared”. In: *Analytical Chemistry* 88.9 (2016), pp. 4926–4930. DOI: 10.1021/acs.analchem.6b00798.

# List of Publications

## Peer-Reviewed Journal Articles

- S. J. Schaper, **F. C. Löhner**, S. Xia, C. Geiger, M. Schwartzkopf, P. Pandit, J. Rubeck, B. Fricke, S. Frenzke, A. Hinz, N. Carstens, O. Polonskyi, T. Strunskus, F. Faupel, S. V. Roth, P. Müller-Buschbaum: “Revealing the growth of copper on polystyrene-block-poly(ethylene oxide) diblock copolymer thin films with in situ GISAXS”, *Nanoscale* **13.23**, 10555—10565 (2021)
- **F. C. Löhner**, C. Senfter, C. J. Schaffer, J. Schlipf, D. Moseguí González, P. Zhang, S. V. Roth, P. Müller-Buschbaum: “Light-induced degradation processes in photoactive layers based on the low-bandgap polymer with benzodithiophene units PTB7-Th”, *Advanced Photonics Research* **1.1**, 2000047 (2020)
- W. Chen, S. Liang, **F. C. Löhner**, S. J. Schaper, N. Li, W. Cao, L. P. Kreuzer, H. Liu, H. Tang, V. Körstgens, M. Schwartzkopf, K. Wang, X. W. Sun, S. V. Roth, P. Müller-Buschbaum: “In situ Grazing-Incidence Small-Angle X-ray Scattering Observation of Gold Sputter Deposition on a PbS Quantum Dot Solid”, *ACS Applied Materials & Interfaces* **12.41**, 46942—46952 (2020)
- D. Yang, **F. C. Löhner**, V. Körstgens, A. Schreiber, B. Cao, S. Bernstorff, P. Müller-Buschbaum: “In Operando GISAXS and GIWAXS Stability Study of Organic Solar Cells Based on PffBT4T-2OD:PC71BM with and without Solvent Additive”, *Advanced Science* **7.16**, 42001117 (2020)
- L. Song, M. A. Niedermeier, V. Körstgens, **F. C. Löhner**, Y. Chen, S. V. Roth, P. Müller-Buschbaum: “In Situ Study of Sputtering Nanometer-Thick Gold Films onto 100 Nanometer-Thick Spiro-OMeTAD Films: Implications for Perovskite Solar Cells”, *ACS Applied Nano Materials* **3.6**, 5987—5994 (2020)
- **F. C. Löhner**, V. Körstgens, G. Semino, M. Schwartzkopf, A. Hinz, O. Polonskyi, T. Strunskus, F. Faupel, S. V. Roth, P. Müller-Buschbaum: “Following in Situ the Deposition of Gold Electrodes on Low-Bandgap Polymer Films”, *ACS Applied Materials & Interfaces* **1.12**, 1132—1141 (2019)
- D. Yang, **F. C. Löhner**, V. Körstgens, A. Schreiber, S. Bernstorff, J. M. Buriak, P. Müller-Buschbaum: “In-Operando Study of the Effects of Solvent Additives on the Stability of Organic Solar Cells Based on PTB7-Th:PC71BM”, *ACS Energy Letters* **4.2**, 464-470 (2019)

- L. Song, W. Wang, V. Körstgens, D. Moseguí González, **F. C. Löhner**, C. J. Schaffer, J. Schlipf, K. Peters, T. Bein, D. Fattakhova-Rohlfing, S. V. Roth, P. Müller-Buschbaum: “In situ study of spray deposited titania photoanodes for scalable fabrication of solid-state dye-sensitized solar cells”, *Nano Energy* **40**, 317-326 (2017)
- M. Tena-Solsona, B. Rieß, R. K. Grötsch, **F. C. Löhner**, C. Wanzke, B. Käs Dorf, A. R. Bausch, P. Müller-Buschbaum, O. Lieleg, J. Boekhoven: “Non-equilibrium dissipative supramolecular materials with a tunable lifetime”, *Nature Communications* **8.1**, 1-8 (2017)
- M. Schwartzkopf, A. Hinz, O. Polonskyi, T. Strunskus, **F. C. Löhner**, V. Körstgens, P. Müller-Buschbaum, F. Faupel, S. V. Roth: “Role of sputter deposition rate in tailoring nanogranular gold structures on polymer surfaces”, *ACS Applied Materials & Interfaces* **9.6**, 5629-5637 (2017)
- M. Al-Hussein, E. M. Herzig, M. Schindler, **F. C. Löhner**, C. M. Palumbiny, W. Wang, S. V. Roth, P. Müller-Buschbaum: “Comparative study of the nanomorphology of spray and spin coated PTB7 polymer: Fullerene films”, *Polymer Engineering & Science* **56.8**, 889-894 (2016)

## Scientific Reports

- F. C. Löhner, V. Körstgens, G. Semino, M. Schwartzkopf, A. Hinz, O. Polonskyi, T. Strunskus, F. Faupel, S. V. Roth, P. Müller-Buschbaum: “Following the sputter deposition of gold contacts on thin films of photoactive polymers”, *Lehrstuhl für Funktionelle Materialien, Annual Report*, 2019
- F. C. Löhner, V. Körstgens, M. Schwartzkopf, A. Hinz, O. Polonskyi, T. Strunskus, F. Faupel, S. V. Roth, P. Müller-Buschbaum: “Following the sputter deposition of gold contacts on thin films of photoactive polymers”, *Lehrstuhl für Funktionelle Materialien, Annual Report*, 2018
- F. C. Löhner, V. Körstgens, M. Schwartzkopf, A. Hinz, O. Polonskyi, T. Strunskus, F. Faupel, S. V. Roth, P. Müller-Buschbaum: “Sputter deposition of gold electrodes on photoactive polymer thin films for organic electronics”, *Lehrstuhl für Funktionelle Materialien, Annual Report*, 2017
- F. C. Löhner, V. Körstgens, M. Schwartzkopf, A. Hinz, O. Polonskyi, T. Strunskus, F. Faupel, S. V. Roth, P. Müller-Buschbaum: “In-situ GISAXS investigation of the structure evolution of metal clusters on organic thin films during sputter deposition”, *Lehrstuhl für Funktionelle Materialien, Annual Report*, 2016

- 
- F. C. Löhner, V. Körstgens, P. Zhang, S. V. Roth, P. Müller-Buschbaum: “Optical and morphological investigation of photoactive polymer films”, *Lehrstuhl für Funktionelle Materialien, Annual Report*, 2015
  - F. C. Löhner, S. Guo, P. Müller-Buschbaum: “Optical properties of the low band gap polymers PBDTT-FTTE and PTB7”, *Lehrstuhl für Funktionelle Materialien, Annual Report*, 2014

## Conference Talks

- F. C. Löhner, V. Körstgens, S. Schaper, M. Schwartzkopf, A. Hinz, O. Polonskyi, T. Strunskus, F. Faupel, S. V. Roth, P. Müller-Buschbaum: “Following the formation of metal electrodes on photoactive polymer thin films”, *DPG-Frühjahrstagung, Regensburg (Germany)*, 31 Mar – 05 Apr 2019
- F. C. Löhner, D. Yang, C. Schaffer, W. Wang, D. Moseguí González, S. V. Roth, S. Bernstorff, P. Müller-Buschbaum: “Understanding morphological degradation in organic photovoltaics with advanced scattering techniques”, *4th German SNI Conference, Garching (Germany)*, 17 – 19 Sep 2018
- F. C. Löhner, T. Widmann, L. Kreuzer: “Fourier Transform Infrared Spectroscopy”, *Polymer Physics Summer School 2018, Obertauern (Austria)*, 12- 15 Jun 2018
- F. C. Löhner, C. Senfter, P. Müller-Buschbaum: “Investigation of degradation processes in low bandgap polymers for organic photovoltaics”, *DPG-Frühjahrstagung, Berlin (Germany)*, 11 – 16 Mar 2018
- F. C. Löhner, V. Körstgens, M. Schwartzkopf, A. Hinz, O. Polonskyi, T. Strunskus, F. Faupel, S. V. Roth, P. Müller-Buschbaum: “Highly time-resolved insights into the sputter deposition of metal electrodes on polymer thin films for organic electronics”, *AVS 64th International Symposium and Exhibition, Tampa (USA)*, 19 – 27 Jun 2017
- F. C. Löhner, V. Körstgens, M. Schwartzkopf, A. Hinz, O. Polonskyi, T. Strunskus, F. Faupel, S. V. Roth, P. Müller-Buschbaum: “In-situ investigation of the sputter deposition of gold electrodes for organic electronics”, *8th International Workshop on Polymer Metal Nanocomposites, Prague (Czech Republic)*, 12 – 15 Sep 2017
- F. C. Löhner, V. Körstgens, M. Schwartzkopf, A. Hinz, O. Polonskyi, T. Strunskus, F. Faupel, S. V. Roth, P. Müller-Buschbaum: “Following the formation of metal electrodes for organic photovoltaics”, *3rd Internal Biennial Science Meeting of the MLZ, Grainau (Germany)*, 19 – 27 Jun 2017

- F. C. Löhner, V. Körstgens, M. Schwartzkopf, A. Hinz, O. Polonskyi, T. Strunskus, F. Faupel, S. V. Roth, P. Müller-Buschbaum: “Following the Formation of Metal Electrodes for Organic Photovoltaics”, *DPG-Frühjahrstagung, Dresden (Germany)*, 19 – 24 Mar 2017
- F. C. Löhner, N. Hohn, M. Coric: “Principles of Organic Solar Cells”, *Polymer Physics Summer School 2016, Obertauern (Austria)*, 21 – 24 Jun 2016
- F. C. Löhner, V. Körstgens, M. Schwartzkopf, A. Hinz, O. Polonskyi, T. Strunskus, F. Faupel, S. V. Roth, P. Müller-Buschbaum: “Metal electrodes in organic photovoltaics - why contact matters”, *6th Colloquium of the Munich School of Engineering, Garching (Germany)*, 7 Jul 2016
- F. C. Löhner, V. Körstgens, M. Schwartzkopf, A. Hinz, O. Polonskyi, T. Strunskus, F. Faupel, S. V. Roth, P. Müller-Buschbaum: “In-situ x-ray investigation of the structure formation of metal films on photoactive polymers”, *DPG-Frühjahrstagung, Regensburg (Germany)*, 6 – 11 Mar 2016

## Conference Poster Presentations

- F. C. Löhner, C. Senfter, P. Müller-Buschbaum: “Solar cell aging on a nanoscale – why even small changes can hurt”, *9th Colloquium of the Munich School of Engineering, Garching (Germany)*, 1 Aug 2019
- F. C. Löhner, V. Körstgens, M. Schwartzkopf, A. Hinz, O. Polonskyi, T. Strunskus, F. Faupel, S. V. Roth, P. Müller-Buschbaum: “In-situ investigation of the sputter deposition of metal contacts on polymer thin films”, *4th German SNI Conference, Garching (Germany)*, 17 – 19 Sep 2018
- F. C. Löhner, C. Senfter, P. Müller-Buschbaum: “Live fast, die young – understanding degradation processes in high-efficiency organic photovoltaics”, *8th Colloquium of the Munich School of Engineering, Garching (Germany)*, 19 Jul 2018
- F. C. Löhner, V. Körstgens, M. Schwartzkopf, A. Hinz, O. Polonskyi, T. Strunskus, F. Faupel, S. V. Roth, P. Müller-Buschbaum: “Following the formation of metal electrodes on photoactive polymer thin films”, *6th SolTech Conference: Solar Technologies go Hybrid, München (Germany)*, 4 – 5 Oct 2017
- F. C. Löhner, V. Körstgens, M. Schwartzkopf, A. Hinz, O. Polonskyi, T. Strunskus, F. Faupel, S. V. Roth, P. Müller-Buschbaum: “Investigating the formation of gold electrodes for organic solar cells”, *NIM Conference "Nanostructured functional Materials for sustainable Energy Provision", München (Germany)*, 26 – 28 Jul 2017

- 
- F. C. Löhner, V. Körstgens, M. Schwartzkopf, A. Hinz, O. Polonskyi, T. Strunskus, F. Faupel, S. V. Roth, P. Müller-Buschbaum: “Witnessing the formation of metal contacts on organic solar cells”, *7th Colloquium of the Munich School of Engineering, Garching (Germany)*, 13 Jul 2017
  - F. C. Löhner, V. Körstgens, M. Schwartzkopf, A. Hinz, O. Polonskyi, T. Strunskus, F. Faupel, S. V. Roth, P. Müller-Buschbaum: “In-situ GISAXS investigation of the structure evolution of metal contacts on polymer thin films”, *BornAgain School and User Meeting, München (Germany)*, 21 – 22 Nov 2016
  - F. C. Löhner, V. Körstgens, M. Schwartzkopf, A. Hinz, O. Polonskyi, T. Strunskus, F. Faupel, S. V. Roth, P. Müller-Buschbaum: “In-situ GISAXS investigation of the structure evolution of metal contacts on polymer thin films”, *DESY GISAXS Workshop 2016, Hamburg (Germany)*, 16 – 18 Nov 2016
  - F. C. Löhner, V. Körstgens, M. Schwartzkopf, A. Hinz, O. Polonskyi, T. Strunskus, F. Faupel, S. V. Roth, P. Müller-Buschbaum: “In-situ investigation of the structure evolution of metal electrodes for organic photovoltaics”, *4th International SolTech Conference in Munich, München (Germany)*, 5 – 8 Apr 2016
  - F. C. Löhner, V. Körstgens, P. Zhang, S. V. Roth, P. Müller-Buschbaum: “Optical and morphological investigation of photoactive low bandgap polymer films”, *DESY Photon Science Users’ Meeting 2016, Hamburg (Germany)*, 27 – 29 Jan 2016
  - F. C. Löhner, V. Körstgens, P. Müller-Buschbaum: “Low band gap polymers – the future in organic photovoltaics?”, *5th Colloquium of the Munich School of Engineering, Garching (Germany)*, 9 Jul 2015
  - F. C. Löhner, V. Körstgens, P. Müller-Buschbaum: “Characterization of the optical and morphological properties of high-efficiency polymers”, *Tag der Physikerinnen/Day of Female Physicists, Garching (Germany)*, 23 Jun 2015
  - F. C. Löhner, V. Körstgens, P. Müller-Buschbaum: “Characterization of the optical and morphological properties of high-efficiency polymers”, *2nd Internal Biennial Science Meeting of the MLZ, Grainau (Germany)*, 1 – 18 Jun 2015
  - F. C. Löhner, S. Guo, P. Müller-Buschbaum: “Characterization and comparison of the optical properties of high-efficiency polymers PBDTT-FTTE and PBT7”, *DPG-Frühjahrstagung, Berlin (Germany)*, 15 – 20 Mar 2015



# Acknowledgments

With deep gratitude, I am writing these lines acknowledging the support of countless people during the last years.

First, I would like to thank my supervisor, Peter Müller-Buschbaum, for giving me the time and space to develop my research projects, for many fruitful discussions, for the opportunity to attend international conferences and exciting beamtimes at synchrotron sources. Thank you especially for supporting my volunteer work in university politics by leaving me the freedom I needed for this important endeavor.

I was lucky to have collaborations projects with a whole bunch of great scientists whom I would like to thank for many astounding, sometimes fun or simply weird insights. Stephan Roth has been a source of encouragement and a true scientific mentor. Thank you for always being available when I didn't know how to get out of an excess data rabbit hole. When I was unexpectedly thrown into my first sputter beamtime, Matthias Schwartzkopf was incredibly supportive and took hours of his valuable time to teach me far more than the basics of his research. Thank you for your patience with newbies and your excellent explanation skills. I would like to thank the groups of Stephan Roth at DESY and of Franz Faupel at CAU Kiel for exciting beamtimes and conference meetings, but also for hard work and valuable input on publications and presentations.

This work would have never come into existence without my colleagues and friends from the Chair for Functional Materials. Thank you to the beamtime crews – Adrian, Armin, Christoph, Dan, Daniel, Johannes, Senlin, Simon, Volker, Wei – for sharing coffee, sleep deprivation, fancy meals, beamdumps, excitement at finally working out an error, creativity given impossible circumstances and simply the fun of doing science. Thank you especially to Volker for keeping it cool whenever my excitement got a little out of hand. Thank you to Carola, Marion and Susanna for the assistance on any administrative matters as well as always an open ear or kind word. Thank you to the E13 workshop for your helping hands, even though I still cannot manage a decent word of Bavarian. Thank you to my students – Akhil, Ali, Benedikt, Christian, Christoph, Christoph, Gabriele, Humi, Namitha, Razan, Sixin – for your new perspectives and your dedication. Thank you for excellent proofreading of my thesis to Anna, Christian, Christina, Christopher, Dominik, Jenny, Julian, Julija, Lennart, Lukas, Manuel, Sebastian, Simon, Stephan and Volker. Thank you to my office mates and friends – Anna, Christian, Christina, Christoph, Claudia, Dan, Daniel, Dominik, Jenny, Johannes, Julian, Julija, Kerstin, Kostas, Lennart, Lin, Lorenz, Lucas, Manuel,

## Acknowledgments

---

Marine, Mihael, Nitin, Nuri, Oliver, Sebastian, Senlin, Shambhavi, Simon, Stephan, Tobias, Volker, Wei, Weijia – for countless hours of discussions about anything and everything, for dancing and singing through the night, for early (very early...) bouldering sessions, for celebrating the nerdiest of ideas, for girls nights and for being there for each other. Thank you especially to Jenny, Mihi, Oli and Stephan for truly being family.

Research needs the right conditions to thrive. It was a pleasure and an honor working together with the members of the TUM Graduate Council in enhancing the university's structures for PhD researchers. Thank you to Chris for the great teamwork as speakers of the council, I am immensely proud of our work and excited to see where the TUM GC will head next. Thank you to Sindre for being a wonderful physics cospeaker. Working and thinking aloud with you has been incredibly educating and fun and I'm looking forward to witnessing your next projects, ideas and adventures. I found the right conditions to thrive despite these crazy times at the PhD Forum, you are the best thing to have come out of the isolation caused by the pandemic. Thank you all for being a wonderful bunch of humans and for seeing the person behind a name.

My social life was put on hold not only due to recent global events. I would like to thank all my amazing friends and family for their support in the last years. Thank you to my friends, old and new, for picking up our conversation no matter how long we didn't get to speak. I can't wait to catch up with you all at last. Thank you to my grandparents, who created the loving, big, boisterous family I had the honor of being born into. Thank you to my parents, who sparked and fostered my curiosity and love for learning and who always supported my endeavors. Thank you to my siblings for taking my weirdness with a laugh and a hug. Thank you all for never doubting my abilities, for supporting my goals and for simply being there for each other no matter what. During my PhD, I've been very fortunate to acquire a wonderful bonus family. Thank you for welcoming me with open arms and treating me as one of your own. This family was found through the best person I could wish for as a partner. Even had I nothing else to be thankful for, meeting Stephan would have been absolutely worth it. Words fail to carry all my love and thanks, but you know that already, don't you? I'm beyond excited to share the next adventures and my life with you, as I intend to hold you for the longest time!